Development of a Compton-TDCR system for application in radionuclide metrology

Vladislav Todorov Todorov

A dissertation
Submitted to the Department of Atomic Physics

In Partial Fulfilment of the
Requirements for the Degree of
Doctor of Philosophy

Under the supervision of
Assoc. Prof. Krasimir Mitev

Sofia, Bulgaria
July, 2026

Supervisor

Assoc. Prof. Dr. Krasimir Krumov Mitev
Department of Atomic Physics, Faculty of Physics, Sofia University "St. Kliment Ohridski"

Reviewers

Contents

1 Introduction

Metrology is the science of measurement and provides the conceptual and practical basis required to obtain results that are reliable, comparable, and traceable. It encompasses the definition of measurands, the realization and dissemination of units, the establishment of calibration chains, and the evaluation of measurement uncertainty. In modern measurement practice, traceability is achieved through an unbroken chain of calibrations linking a measurement result to a primary standard, together with a documented uncertainty budget. This metrological structure is essential whenever measurements must be compared across laboratories, instruments, or time, or when results support regulatory compliance and decision-making.

Radionuclide metrology provides the foundation for quantitative applications of ionizing radiation, including environmental monitoring, nuclear medicine, radiation protection, and fundamental research. Central to this discipline is the determination of activity with demonstrated traceability and well-quantified uncertainty. The measurand "activity" is defined as the mean number of disintegration of the radionuclide per unit of time. For many radionuclides — in particular low-energy β emitters and electron-capture nuclides — liquid scintillation counting remains the best measurement technique because it offers near-4π detection geometry, high efficiency, and low detection thresholds. Among primary methods based on liquid scintillation counting, the Triple-to-Double Coincidence Ratio (TDCR) technique has become widely adopted for absolute activity determination, relying on statistical and physical models that links measured coincidence counting rates to detection efficiency.

Historically, the earliest scintillation counters were visual instruments: individual scintillations on activated zinc sulfide screens produced by α particles were counted by an observer using a microscope in a dark room. Although the achievable count rates were limited by physiological constraints (typically of order of 60 events per minute), visual scintillation counting played an important role in nuclear research from its introduction by Crookes and Regener in 1908 until the 1930s [1]. A decisive advance followed the development of photomultiplier tubes with high gain and sensitivity to low light levels. Replacing the microscope and the human observer with a photomultiplier tube made it possible to convert scintillations into measurable electrical pulses, which could then be amplified and counted in a manner analogous to gas-filled detectors [1].

One of the first widely cited demonstration of organic scintillation detection was reported by Broser and Kallmann [2], who showed that large transparent blocks of naphthalene produce scintillations detectable with a photomultiplier under irradiation with β particles and γ rays. This was soon followed by early implementations of liquid organic scintillators [3]. Since these initial developments, organic scintillation counting has continuously progressed through advances in scintillator chemistry, detector instrumentation, statistical modeling, and analysis methods for quantitative activity determination. Broad overviews of these developments can be found in [1, 4, 5, 6, 7, 8].

A key milestone for radionuclide metrology was the development of absolute methods for pure β emitters using liquid scintillation counting. One of the earliest published attempts at direct activity determination of a pure β emitter using a two-PMT system and a statistical description of light detection was presented by Kolarov *et al.* [9]. This approach was subsequently extended to three-PMT systems, leading to the proposal of the Triple-to-Double Coincidence

Ratio method [10]. Since then, TDCR has been continuously refined and is now applied for primary standardization of pure β and electron-capture radionuclides in liquid scintillation sources [11], thereby providing traceable calibration sources for secondary measurement systems.

Despite its maturity, the TDCR analysis retains a well-known sensitivity to the scintillator response function, particularly for low-energy emitters where ionization quenching and non-proportional light yield are pronounced. In practice, this response is often parameterized by semi-empirical models (e.g. Birks-type relations) using an adjustable quenching parameter kB [11]. While effective in many cases, the applicability of such parameterizations depends on scintillator composition, the energy range of interest, and acquisition settings, and it can introduce systematic effects [12]. Consequently, an experimental method capable of characterizing the scintillator response as a function of deposited energy—under metrologically controlled conditions and within the same detection chain used for TDCR counting—is of significant interest for improving the robustness of primary activity measurements.

Compton-coincidence techniques with liquid scintillators [13, 14, 15, 16] provide a route to such an experimental characterization. By measuring the energy of a Compton-scattered γ ray in coincidence with the scintillation signal, the deposited energy of the corresponding Compton electron in the scintillator can be calculated. This enables the construction of an energy-dependent response function without relying solely on an assumed quenching model. When combined with TDCR counting, a Compton–TDCR system [15] offers the prospect of energy-selective scintillator characterization, reduced reliance on adjustable quenching parameters in TDCR efficiency calculations, and pathways toward model-independent ("zero-model") approaches [17] based on experimentally determined response functions.

Aim of the thesis

The aim of this thesis is to construct and commission a performant Compton-TDCR counting system. This aim is divided in several tasks:

- to study the photocathode response of the PMTs used in the TDCR channel and to verify their suitability for TDCR counting; to characterize the geometry of the γ-ray spectrometer and to optimize the acquisition setup for best attainable energy resolution;
- to develop and validate a Compton–TDCR system for studying scintillators response by combining of a TDCR liquid scintillation channel with a high-resolution γ-ray spectrometer and using dedicated coincidence logic for energy-selective gating of Compton events;
- to validate the TDCR channel measurements by comparing activity estimates of liquid scintillation samples with results obtained using three other TDCR systems;
- to perform measurements of scintillator response, to fit Birks' ionization-quenching formula to the experimental data, and to compare the resulting kB values with those obtained using efficiency variation techniques.

Main contributions

The main contributions of this thesis can be summarized as follows:

- development of a performant Compton–TDCR measurement system suitable for metrological use;
- tests of a coincidence acquisition scheme enabling efficient multi-ROI data collection in the γ spectrum;
- validation of TDCR counting performance using various radionuclide sources and established TDCR counters;
- application of the system to derive energy-dependent scintillation response functions relevant to low-energy β-emitter metrology.

Beyond the development and application of the Compton–TDCR system, this thesis also investigates the influence of the analytical correction for accidental coincidences [18] on the selection of the ionization-quenching parameter kB and on TDCR efficiency calculations, using both experimental data and Monte Carlo simulated list-mode files. The TDCR method is further applied to standardization of ^{222}Rn-in-water samples, which was proposed in [19], including the development of a practical sample preparation procedure. Finally, the permeability of ^{222}Rn in a plastic scintillator is used to evaluate the partition coefficient and diffusion length.

Structure of the thesis

Chapter 2 reviews the physical principles of scintillation, quenching, and coincidence counting, and introduces the TDCR formalism. The discussion follows the scintillation process from energy deposition in an organic medium to photon emission, summarizes scintillator and photomultiplier characteristics relevant to liquid scintillation counting, and outlines practical aspects of TDCR acquisition and analysis.

Original results are presented in Chapters 3 to 8 and appendix A.

Chapter 3 begins with studies of photocathode-response non-uniformity in several photomultiplier tubes, with emphasis on the PMTs selected for the Compton-TDCR system. The design and realization of the Compton–TDCR instrument are presented in Chapter 5, including the scintillation and γ detection channels, shielding and optical considerations, and the acquisition logic for coincidence gating. Performance validation, experimental results, Monte Carlo studies, and scintillator-response measurements are reported. The ionization-quenching parameter kB obtained by fitting Birks' equation to the measured response is compared with estimates from efficiency variation measurements. Chapter 6 presents the comparison of the TDCR channel of the newly developed system to three established TDCR counters and the results from efficiency variation with grey filters.

Chapters 7 and 8 present experimental and Monte Carlo simulation-based studies of the influence of the accidental coincidence correction on kB selection and TDCR efficiency calculations, with emphasis on low-energy β emitters. A practical application is described in Appendix A: standardization of ^{222}Rn-in-water samples, demonstrating that the TDCR method is well suited for this task and that relative activity uncertainties below 1% are achievable.

Liquid Scintillation Counting for Radionuclide Standardization

2

Liquid scintillation counting (LSC) determines the activity of a radionuclide dissolved in a scintillation cocktail by recording the rate of scintillation light pulses. The sample is typically prepared in a 20 mL glass or polyethylene vial and measured in a dedicated liquid scintillation (LS) counter, where one or more photomultiplier tubes (PMTs) view the vial inside an optical chamber. The counting rate n of the source of interest is evaluated by counting the pulses in a defined counting interval and the net counting rate n_0 is the background and dead-time corrected counting rate of the source. The detection efficiency ε links this rate to the activity A through $A = n_0/\varepsilon$. Because the radioactive material is effectively inside the sensitive volume, LSC can achieve high efficiencies—often close to 100% for α emitters and high-energy β emitters — whereas ε may be substantially lower for electron-capture (EC) nuclides and low-energy β emitters. For these cases, ε must be determined with high accuracy in order to obtain reliable activity estimates.

A common route to estimate ε is detector calibration using sources traceable to primary standards; however, the activity of many calibration sources is itself established by LSC, so the efficiency cannot be assumed a priori and this is not a primary method. This motivates the use of a detector-response model. Building on earlier work [4, 20, 9], the free-parameter model developed by Broda *et al.* [21] and Grau Malonda *et al.* [22] provides a statistical description of scintillation-light production and detection and forms the basis of modern LSC methods in radionuclide metrology. LSC is particularly well suited to calibrate pure EC and pure β emitters (e.g.^{3}H, ^{14}C, ^{55}Fe, ^{63}Ni), whose emissions are charged particles that have very limited range in matter.

This chapter introduces the physical principles of LSC as a primary technique for radionuclide standardization. The discussion starts with the scintillation mechanism in organic media and the processes that govern the time profile and non-linearity of the light yield (ionization quenching, delayed scintillation component kinetics, and energy-transfer/quenching effects). It then summarizes the role and performance requirements of PMTs and liquid scintillation counters, and presents the statistical (*the free parameter model*) model used to calculate counting efficiencies. The TDCR method is then described as a primary method for activity determination of β-emitters and electron-capture radionuclides. The chapter concludes with an introduction to Compton-coincidence approaches, which provide an experimental way to characterize scintillator response at low energies and thereby reduce reliance on purely parametric quenching descriptions.

2.1 Organic scintillators

Organic scintillators have a long history in ionizing-radiation detection, dating back to the pioneering work of Kallmann [2]. A major advance of that period was the demonstration that scintillation light produced in naphthalene crystals by β particles and γ rays could be detected with a photomultiplier. Naphthalene thus became one of the first widely used organic scintillators and among the first scintillators operated in a large-volume configuration.

Scintillation is a luminescence process, i.e. the emission of light with a characteristic spectrum

following absorption of radiation whose energy exceeds that of the emitted photons. In organic scintillators, luminescence arises primarily from aromatic molecules and is governed by their electronic structure. Because the molecules interact predominantly via weak van der Waals forces, they largely retain their electronic structure — and therefore their luminescent properties — regardless of the aggregation state of the medium [1].

2.1.1 Molecular basis of luminescence in aromatic compounds

The structure and optical response of organic scintillators are strongly linked to the valence electronic configuration of carbon. In the ground state, carbon has the configuration $1s^2 2s^2 2p^2$; upon excitation, a 2s electron can be promoted to the 2p level, enabling hybridization of the 2s and 2p orbitals into equivalent hybrid states [1, 23].

Three hybridization schemes are of primary relevance. In the sp^3 configuration, four equivalent orbitals are oriented tetrahedrally and form σ bonds as in methane (CH_4) and other saturated hydrocarbons, which typically do not exhibit luminescence. In the sp^2 configuration, three coplanar orbitals form σ bonds, while the remaining p orbitals overlap above and below the molecular plane to create delocalized π systems (e.g. the six-electron π bond in benzene; Fig. Figure 2.1). These π-electronic states are of particular importance because radiative transitions between them give rise to the luminescence underlying scintillation in aromatic compounds. In the sp configuration, characteristic of carbon–carbon triple bonds, two sp orbitals form σ bonds and two mutually perpendicular p orbitals generate two π bonds; such unsaturated structures may also exhibit luminescence [1, 23].

Organic scintillators are rarely used as single-component systems because the intrinsic emission and light transport properties of many pure organic liquids are not optimal for photomultiplier tube readout: their fluorescence is usually in the ultraviolet region which does not match the maximum PMT sensitivity and is often further degraded by self-absorption and non-radiative relaxation. A common solution is therefore to employ multicomponent mixtures. In a binary scintillator, a small fraction (typically $\sim$ 1% by volume) of a primary fluorophore — chosen for high fluorescence quantum yield and efficient excitation-energy transfer from the solvent — is dissolved in a bulk organic solvent. Since most of the energy deposited by an ionizing particle is initially absorbed by the solvent, intermolecular transfer processes convey a fraction of this excitation to the fluorophore [24], which then emits scintillation light with high probability. In many scintillation cocktails, a secondary fluorophore (typically $\sim$ 0.1%by volume) is added as a wavelength shifter to shift the emission toward longer wavelengths, thereby improving the spectral matching to the PMT response [1].

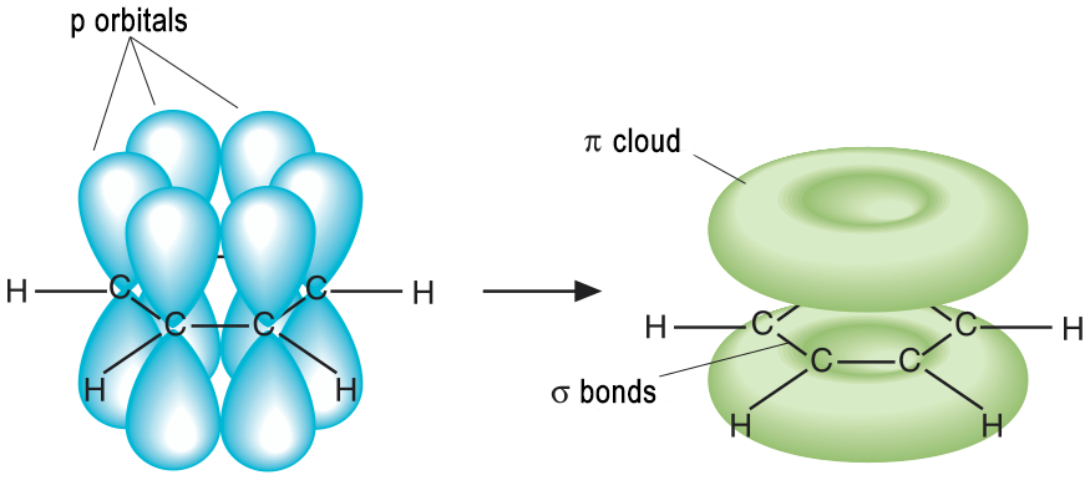

Figure 2.1: Left: benzene molecule showing the non-hybridized p-orbitals; right: the delocalized π-orbital (π-electron cloud) formed by overlap of the p-orbitals.

2.1.2 Track structure and excitation-density effects

A central element of the track-structure interpretation introduced by Voltz *et al.* [25, 26, 27] — widely used in the context of organic scintillation — is the explicit distinction between *primary* excitations and ionizations produced directly by the incident charged particle and *secondary-electron* excitations produced by atomic electrons ejected in close Coulomb collisions. Figure Figure 2.2 schematically illustrates a short segment of the ionization track left by a medium-energy, highly ionizing particle (e.g. a 10 MeV proton, deuteron, or α particle) immediately after it traverses the scintillator. Direct Coulomb interactions generate ionized and excited molecules within a narrow region surrounding the trajectory (the track core), typically extending only a few molecular dimensions from the path. In parallel, a fraction of collisions transfer sufficient energy to an atomic electron to eject it from the molecule; these energetic "knock-on" electrons are commonly referred to as δ electrons (or δ rays).

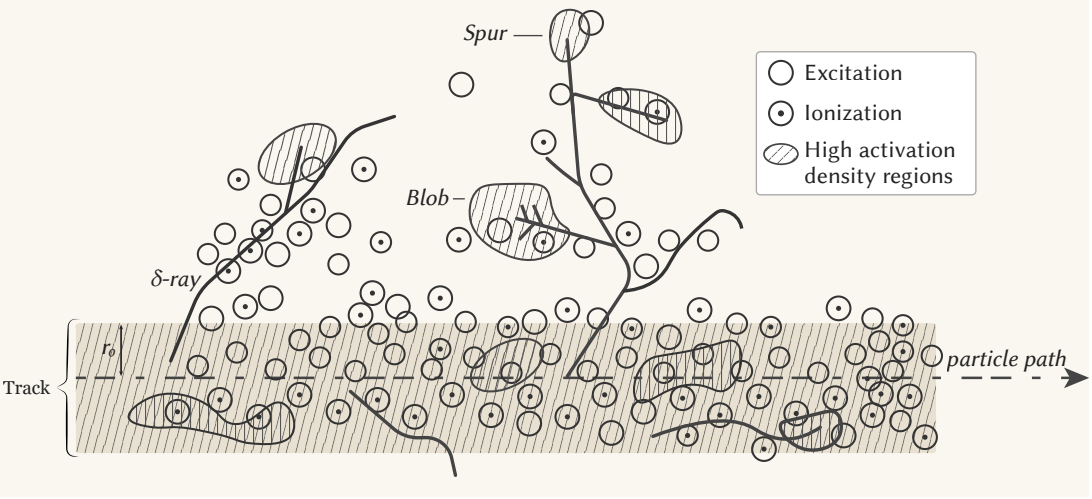

Figure 2.2: Schematic illustration of the spatial distribution of excitations produced by a charged particle [28].

The mean excitation density decreases with radial distance from the trajectory, while it

grows along the path as the stopping power ($\mathrm{d}E/\mathrm{d}x$) increases. For heavily ionizing particles it is therefore useful to introduce a dense core of radius r_0 (measured from the trajectory; Fig. Figure 2.2), within which the excitation density is highest. Fast secondary δ-rays can escape this core and produce additional energy deposition outside it, forming localized clusters commonly illustrated as spurs (approximately spherical regions) and blobs (more elongated regions). High-energy electrons β particles do not form a well-defined dense core and instead generate predominantly spur/blob-like structures. At the opposite extreme — when the ionization density is very high — the external spur/blob regions may overlap and approach a quasi-continuous annulus of elevated excitation density around the core [28].

For a given segment of the trajectory (as in Fig. Figure 2.2), the partition of deposited energy between the core and the surrounding region, and the corresponding excitation densities, depend on $\mathrm{d}E/\mathrm{d}x$, the particle charge Z, and its velocity. Each region contributes differently to the scintillation yield, and the total light output is obtained by integrating these contributions along the finite path length of the particle in the scintillator [28].

2.1.3 Singlet and triplet states; prompt and delayed emission

Energy deposition in organic scintillators produces electronic excitations (and ionizations) of the π-electron system, leading to the population of both singlet and triplet excited states. These states, in turn, give rise to prompt and delayed components of the scintillation emission [1].

In the ground state of benzene, the six π electrons occupy three bonding π molecular orbitals as three spin-paired electron pairs. Upon excitation to a singlet state (S_n), the electron spins remain paired and the total spin is $s = 0$. By contrast, a triplet state (T_n) involves two unpaired electrons with parallel spins, yielding $s = 1$ (Fig. Figure 2.3). The spin-projection quantum number takes the value $m_s = 0$ for a singlet and $m_s = -1,\ 0,\ +1$ for a triplet. Accordingly, triplet states are threefold degenerate in m_s, whereas singlet states are non-degenerate, which is often expressed as a 3:1 statistical weight in favour of triplets.

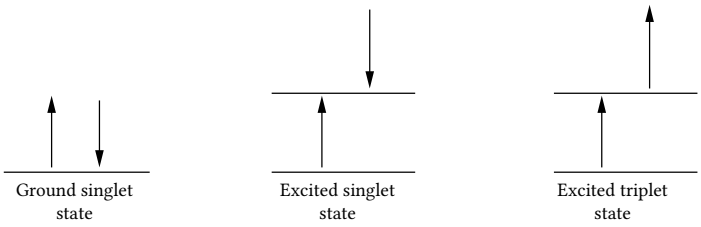

Figure 2.3: Spin orientation of the π electrons in the ground state, the excited singlet state, and the excited triplet state.

Under low excitation densities — where interactions between excited molecules are negligible — higher singlet excitations relax rapidly (typically $\lesssim 10^{-11}$ s) via non-radiative internal conversion to the lowest vibrational level of S_1. The excess energy is transferred to molecular vibrations through vibronic coupling and subsequently dissipated as heat. An analogous relaxation pathway applies for higher triplet states, $T_n \longrightarrow T_1$. Intersystem crossing refers to transitions between states of different multiplicity, $S_n \leftrightarrow T_n$, enabled by spin–orbit coupling and associated spin mixing [24].

Although triplet excitations have larger statistical weight, radiative decay from T_1 to S_0 is strongly suppressed by the spin-multiplicity selection rule. Consequently, emission associated with T_1 (phosphorescence) is typically weak and occurs on longer timescales than fluorescence

from S_1. As illustrated in Figure 2.4, T_1 can contribute to light output only if population is transferred back to the singlet manifold (e.g. by intersystem crossing), followed by radiative de-excitation.

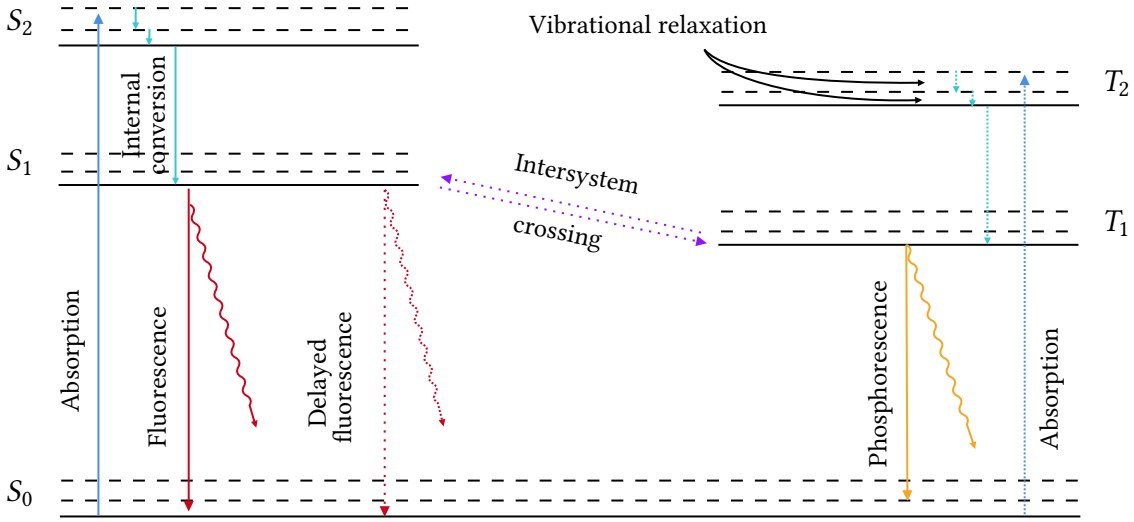

Figure 2.4: Scheme of the π-electron energy levels in organic scintillators. S_0 denotes the ground state, S_1 and S_2 the excited singlet states, and T_1 and T_2 the excited triplet states. The transition from S_1 to T_1 is indicated as intersystem crossing. Solid lines represent pathways leading to prompt fluorescence, whereas dashed lines denote pathways associated with delayed fluorescence [29].

Fluorescence (or *prompt fluorescence*) refers to photon emission associated with the radiative transition $S_1 \rightarrow S_0$. Emission from higher singlet states (S_n, $n > 1$) is generally negligible because internal conversion to S_1 is the dominant process which occurs on a much shorter timescale than the S_1 lifetime, which is typically $\sim 10^{-9}$–10^{-8} s [1].

Phosphorescence corresponds to radiative decay $T_1 \rightarrow S_0$. Owing to the required change in spin multiplicity, this transition is forbidden and therefore usually weak.

A more pronounced delayed component compared to the contribution of phosphorescence is *delayed fluorescence*. In this process, the T_1 states are converted back to the singlets states and subsequently emits via the same radiative transition as prompt fluorescence, $S_1 \rightarrow S_0$. The spectrum is therefore identical to prompt fluorescence, but the characteristic decay time is typically on the order of $\sim 10^{-6}$ s [30]. In organic scintillators, the dominant mechanism enabling this conversion is triplet–triplet annihilation, in which two molecules in T_1 interact to produce one molecule in S_1 and one molecule in the ground state. The intensity and decay kinetics of delayed fluorescence — typically much weaker than prompt fluorescence — depend on the energy gap between T_1 and S_1, the lifetime of T_1, temperature, and the frequency of T_1–T_1 encounters, which is governed by the spatial density of triplet excitations.

For oragnic binary scintillator systems (liquid and plastic), the overall process includes an additional energy-transfer step from solvent singlet states (S_1) to solute singlet states (F_1). At typical fluor concentrations this transfer is sufficiently fast that it does not significantly alter the emission kinetics.

After the formation of S_1 and T_1 states (within a few nanoseconds), the processes most relevant to LSC are often discussed using the following highly simplified reaction scheme, which neglects intermediate states and detailed kinetics [26, 31]:

1. $S_1 \rightarrow S_0$ or $S_1 + S_0 \rightarrow S_0 + S_0$ non-radiative relaxation of singlets;

2. $S_1 + S_0 \rightarrow S_0 + S_1$ energy transfer in the solvent;
3. $T_1 \rightarrow S_0$ non-radiative relaxation of triplets;
4. $S_1 + Q \rightarrow S_0 + Q$ singlet chemical quenching;
5. $T_1 + Q \rightarrow S_0 + Q$ triplet chemical quenching;
6. $T_1 + T_1 \rightarrow S_1 + S_0$ triplet–triplet annihilation followed by intersystem crossing;
7. $T_1 + T_1 \rightarrow T_1 + S_0$ triplet–triplet annihilation producing triplet and ground-state molecules;
8. $S_1 + F_0 \rightarrow F_1 + S_0$ Förster energy transfer to a fluorescent molecule;
9. $F_1 \rightarrow F_0 + h\nu$ fluorescence of the solute and photon emission;
10. $F_1 \rightarrow F_0$ non-radiative relaxation of the solute;
11. $F_1 + Q \rightarrow F_0 + Q$ chemical quenching of the solute.

In an LS cocktail, solvent molecules, primary-fluor molecules, and potential quenchers are essentially homogeneously distributed, whereas excited singlet and triplet states are generated predominantly near the charged-particle track (Fig. Figure 2.2). In this high-density region, fluorescence yield is reduced because additional non-radiative channels become accessible, including bimolecular interactions between excited species and energy transfer to quenchers.

In the track-structure model of Voltz *et al.* [26, 27], these *ionization quenching* processes compete with the rapid ($\sim 10^{-11}$–10^{-10} s) and otherwise efficient internal conversion from higher π-electronic states (S_n and T_n) to the lowest excited states (S_1 and T_1). The higher π-electronic S_n and T_n states undergo rapid non-radiative internal conversion and subsequent vibrational relaxation, reaching the lowest excited singlet and triplet states. The excess electronic energy is transferred to molecular vibrations and is effectively dissipated as heat. The model places the dominant ionization quenching *before* population of S_1, rather than as a depopulation process acting on S_1. This interpretation is supported by experimental evidence that the lifetime of the prompt component is largely independent of the excitation mode (photoexcitation, electrons, protons, or α particles), whereas the magnitude of the quenching effect increases with increasing $\mathrm{d}E/\mathrm{d}x$ [5].

Ion recombination provides an additional pathway for the formation of excited molecular states in organic scintillators. Following ionization, the initially produced molecular ions and electrons undergo thermalization, spatial redistribution, and eventual recombination. This process is not instantaneous and therefore occurs after the earliest, highest-density stage of the particle track, during which, ionization quenching is most effective. Consequently, excited states formed by recombination are generated after the local density of ionized and highly excited species has already decreased.

Recombination can populate both singlet and triplet states; however, it represents an important source of triplet excited states T_1, which may undergo triplet–triplet annihilation, producing an excited singlet state that decays radiatively and gives rise to delayed fluorescence. Since the triplet population relevant for this mechanism is formed later than the dominant early ionization-quenching stage, it is generally less strongly depleted by ionization quenching than the singlet population responsible for prompt fluorescence. The delayed component is therefore expected to show a weaker dependence on $\mathrm{d}E/\mathrm{d}x$ than the prompt component.

2.1.4 Time-dependence of the emission of scintillation light

The temporal evolution of scintillation emission in organic media is inherently multi-stage process and involves competing radiative and non-radiative pathways. Nevertheless, a number of established models provide practical descriptions of the total light output and its prompt and delayed components [32, 26, 28]. In early developments of these models, the experimental time resolution did not allow direct access to the earliest relaxation processes (e.g. ultrafast internal conversion from higher electronic states). Consequently, the time dependence of the scintillation intensity was formulated primarily in terms of the lowest excited singlet and triplet states, S_1 and T_1, and, for multicomponent scintillators, the lowest excited singlet state of the fluor, F_1.

For the prompt component, the emission intensity $I_p(t)$ is commonly found to follow an exponential decay, with a time constant equal to the mean lifetime of the emitting singlet state, τ_S (or τ_F for fluor emission) [1]:

$$I(t) = I_0 e^{-t/\tau_S}, \tag{2.1}$$

where $I(t)$ and I_0 denote the scintillation intensity at time t and at $t = 0$, respectively. In a binary scintillator, the prompt emission is not necessarily described by a single exponential because excitation energy is first created in the solvent and is then transferred to the solute (primary fluor) on a finite timescale. This additional transfer step modifies the time profile of the prompt component and can introduce a rise time and/or a sum of exponential terms, depending on the relative magnitudes of the transfer and fluorescence lifetimes. For a binary system, the prompt scintillation intensity $I_p''(t)$ may be written as [1]:

$$I_p''(t) = n_{0S} \frac{a_{SF}/\tau_{fS} + 1/\tau_{tSF}}{1/\tau_S - 1/\tau_F} \left(e^{-t/\tau_F} - e^{-t/\tau_S} \right) \tag{2.2}$$

where n_{0S} is the number of solvent molecules initially excited at $t = 0$, a_{SF} is the fraction of the solvent excitation transferred to the fluorophore, τ_{fS} is the intrinsic radiative lifetime of the solvent, τ_{tSF} is the characteristic time for non-radiative energy transfer from solvent to fluorophore, τ_F is the fluorescence decay time of the fluorophore, and τ_S denotes the mean lifetime of the solvent singlet state.

In a single-component scintillator, if excitation is effectively instantaneous and delayed components are neglected, the prompt fluorescence decay can often be approximated by a single exponential. Binary scintillators, however, generally exhibit a more complex time profile, with both a finite rise and a finite decay. This behavior arises because the excitation is produced mainly in the solvent and must first be transferred to the fluorophore before the observed fluorescence is emitted.

In the simplified sequential description, the solvent excitation acts as a feeding population for the fluorophore. As this population decreases with the characteristic time τ_S, the excited fluorophore population builds up and subsequently decays with the characteristic time τ_F. The resulting light pulse is therefore described by a combination, or difference, of exponential terms involving both τ_S and τ_F, rather than by a single exponential [1]. The leading part of the pulse reflects the build-up of fluorophore excitation, whereas the long-time tail is governed by the slower of the two characteristic times.

The delayed component of the scintillation light has been modelled in detail by King and Voltz [32] using a diffusion–kinetic approach that accounts for bimolecular reactions between triplet excitations leading to the formation of delayed singlet states. This approach was also used by Blanc *et al.* [29]. In this work, the local density of delayed singlet excitations, $c_S'(r, t)$,

obeys [32]:

$$\frac{\partial c'_S(r,t)}{\partial t} = D_S\,\nabla_r^2 c'_S(r,t) - \frac{1}{\tau_S}\,c'_S(r,t) + k_{tt}\,c_T^2(r,t)\,, \tag{2.3}$$

where D_S is the diffusion coefficient of the excited singlet states and τ_S is as defined above. The source term $k_{tt}\,c_T^2(r,t)$ describes the production rate of delayed singlets via triplet–triplet annihilation, i.e. the interaction of two molecules in the triplet state at a distance r from the particle track. It is typically assumed that $c'_S(r,0) = 0$, i.e. no delayed singlets are present immediately after excitation [32].

The initial spatial distribution of triplet excitations, $c_T(r,0)$, is treated differently depending on the stopping power of the incident radiation. Particles with high $\mathrm{d}E/\mathrm{d}x$ generate compact regions of high excitation density (spurs), whereas low $\mathrm{d}E/\mathrm{d}x$ particles produce spurs that are more widely separated. To obtain an analytical solution of Equation (2.3), King and Voltz assume a Gaussian form for $c_T(r,0)$ [32].

On the timescale relevant for delayed fluorescence, it is often sufficient to consider $t < \tau_T$, where τ_T is the triplet-state lifetime. In this regime, the dominant processes are triplet diffusion and bimolecular annihilation. For the pure diffusion problem (i.e. neglecting the annihilation term), the relaxation of the triplet density at the spur centre occurs on a characteristic timescale [32]:

$$t_a = \frac{r_0^2}{4D_T}, \tag{2.4}$$

where D_T is the diffusion coefficient of triplet excitations and r_0 denotes the characteristic initial spur radius.

Building on the King–Voltz formulation, Laustriat [28] investigated the delayed component for different media — pure organic crystals, liquid scintillators, and liquid scintillators with dissolved oxygen. For pure crystals, the delayed intensity is given by

$$I_d(t) = 2\pi\,\frac{\eta_S}{\tau_S}\,k_{tt}\int_0^L dL\int_0^t e^{-(t-\alpha)/\tau_s}\,d\alpha\int_0^\infty c_T^2(r,\alpha)\,r\,dr\,, \tag{2.5}$$

where η_S is the fluorescence quantum yield, L is the particle range and $c_T(r,t)$ is the local concentration of T_1 states at time t and distance r from the particle path.

For the asymptotic time region $t \gg \tau_S$ (i.e. after the prompt emission has effectively vanished), Equation (2.5) can be expressed as [28]:

$$I'_d(t) \simeq \eta_S\,\frac{N}{\left[1 + A\ln\left(1 + t/t_a\right)\right]^2\left(1 + t/t_a\right)}\,, \tag{2.6}$$

The parameters N and A arise from the solution of the coupled diffusion and triplet–triplet annihilation problem and should be regarded as effective, scintillator-dependent quantities unless a specific microscopic track-structure model is adopted. In particular, N sets the overall scale of the delayed component, while the dimensionless parameter A characterizes the efficiency of bimolecular triplet–triplet annihilation during diffusive expansion and therefore governs the shape of the long-time tail through the logarithmic depletion factor [28].

For an oxygen-free liquid scintillator, the delayed emission amplitude is further modulated by solvent–solute transfer, yielding a multiplicative factor $\varepsilon_{SF}\eta_F$, where ε_{SF} is the transfer

efficiency and η_F is the solute fluorescence quantum yield. In this case:

$$I'_d(t) = \varepsilon_{SF}\,\eta_F\,\frac{N}{\left[1 + A\ln\left(1 + t/t_a\right)\right]^2\left(1 + t/t_a\right)}\,. \tag{2.7}$$

In the presence of dissolved oxygen, triplet states are efficiently quenched, leading to a modified asymptotic expression [28]:

$$I_d(t) = \varepsilon_{SF}\,\eta_F\,\frac{Ne^{-2t/\tau_T}}{\left\{1 + Ae^{t_a/\tau_T}\left[Ei\left(-\frac{t+t_a}{\tau_T}\right) - Ei\left(-\frac{t_a}{\tau_T}\right)\right]\right\}^2\left(1 + t/t_a\right)}\,, \tag{2.8}$$

where the exponential integral is defined as

$$Ei(-x) = -\int_x^{\infty}\frac{e^{-\alpha}}{\alpha}\,d\alpha\,. \tag{2.9}$$

The qualitative interpretation of the temporal scintillation profile is illustrated in Figure 2.5:

- for $0 < t \lesssim 10\tau_S$ the observed intensity is the sum of prompt and delayed contributions;
- for $t \gg \tau_S$ the delayed component dominates and the decay tail is described by the corresponding asymptotic expression for the given scintillator medium.

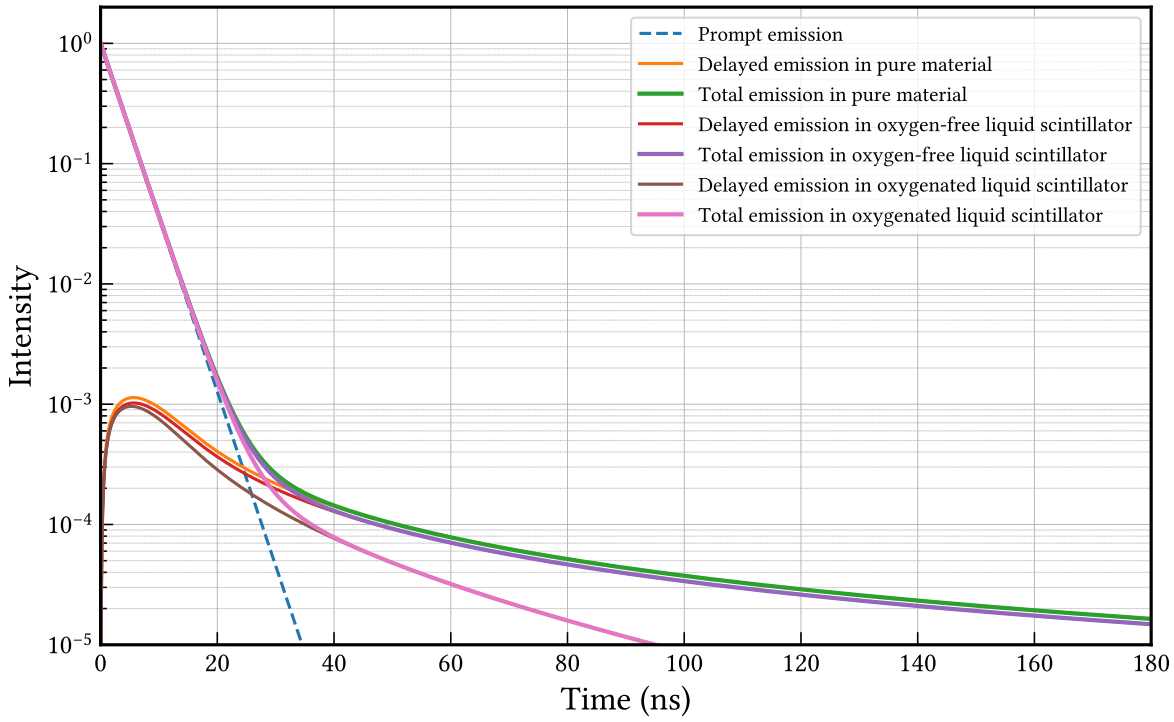

Figure 2.5: Schematic contribution of the prompt and delayed components to the total scintillation intensity for three cases: a pure scintillator, a binary liquid scintillator, and a binary liquid scintillator with dissolved oxygen [28].

The proposed description of the scintillation time profile — an exponential decay for the prompt component combined with a diffusion–kinetic model for the delayed component — was

fitted to experimental data, demonstrating that the model captures the essential features of the emission and provides physically meaningful insight into the underlying processes. A notable outcome is that the functional form of the delayed-emission decay is largely insensitive to both the solute (fluorophore) and the type of incident particle. In contrast, dissolved oxygen produces a pronounced quenching of the delayed component by shortening the effective triplet lifetime τ_T; as a result, a larger fraction of T_1 excitations relax non-radiatively before participating in triplet–triplet annihilation, which is a principal pathway to delayed fluorescence [28].

While the decay laws of the prompt and delayed components are, to first order, independent of radiation type, their *integrated* intensities depend strongly on the stopping power $\mathrm{d}E/\mathrm{d}x$ and on the charge of the incident particle, reflecting changes in the local excitation density along the track. Consequently, the relative contributions of prompt and delayed light vary between particle types [28]. This difference in temporal composition underlies pulse-shape discrimination methods, which exploit the particle-dependent balance between fast and slow scintillation components and is briefly discussed hereafter.

2.1.5 Pulse shape discrimination

The pulse-shape discrimination (PSD) technique was introduced as a means to distinguish fast-neutron interactions from γ-ray background in organic scintillators [33]. Its development was motivated by early observations by Wright [34], who determined that the scintillation decay in anthracene is slower for α-particle excitation than for electron excitation. The physical origin of this behavior was subsequently clarified by Owen [35], who showed that the observed pulse-shape differences arise from changes in the relative contributions of the prompt and delayed scintillation components. A comprehensive review of the early development of PSD is provided in [5].

An useful qualitative interpretation of the dependence of pulse shape on the stopping power $\mathrm{d}E/\mathrm{d}x$ can be obtained by assuming that ionization quenching affects primarily the prompt (fast) component, while the delayed (slow) component originates from processes that are comparatively less sensitive to the dominant "static" quenching within the dense track core [1]. Under this assumption, interactions producing high $\mathrm{d}E/\mathrm{d}x$ (e.g., recoil protons from fast neutrons) suppress the prompt light yield more strongly than interactions producing low $\mathrm{d}E/\mathrm{d}x$ (e.g., Compton electrons from γ rays), thereby increasing the relative weight of the slow tail. This particle-dependent balance between fast and slow emission components forms the basis of PSD methods used in neutron/γ discrimination (see Fig. Figure 2.6).

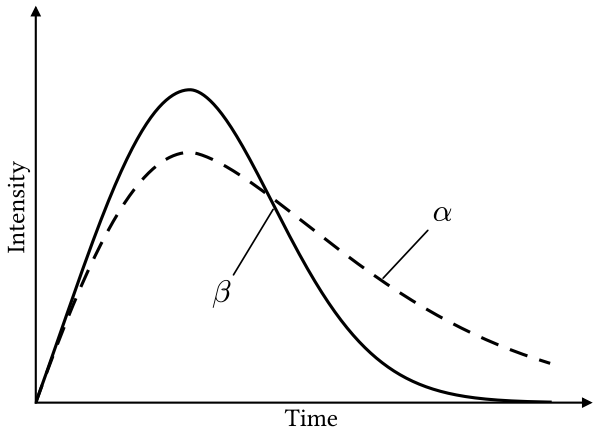

Figure 2.6: Characteristic light pulses, showing distinct shapes and durations, produced by the passage of α- and β-particles through an organic scintillator [7].

Owen [36] measured the ratio R between the relative magnitudes of the slow scintillation components produced by recoil protons and by fast electrons. Specifically, he compared the slow components L_{sp} (for recoil protons of energy E_p, up to 12 MeV) and L_{se} (for fast electrons of energy E_e), while normalizing the corresponding fast components L_p and L_e to a common reference level. Under this normalization, the ratio can be written as [1]:

$$R = \frac{L_{sp}}{L_p} \cdot \frac{L_e}{L_{se}} . \tag{2.10}$$

If the slow component L_s were independent of the stopping power $\mathrm{d}E/\mathrm{d}x$, then the slow light yield would scale approximately with the deposited energy, i.e. $L_{sp} \propto E_p$ and $L_{se} \propto E_e$. In that case [1]:

$$R = \frac{E_p}{L_p} \cdot \frac{L_e}{E_e} . \tag{2.11}$$

Since the electron scintillation efficiency $L_e/E_e = S$ is approximately constant for fast electrons, the right-hand side of Equation (2.11) can be evaluated from the measured relative scintillation response to electrons and protons of comparable energy. Owen's results suggested that, to a first approximation, the slow component is only weakly dependent on $\mathrm{d}E/\mathrm{d}x$ for electrons and protons. Subsequent studies [37, 38] refined this conclusion: although L_s is substantially less sensitive to $\mathrm{d}E/\mathrm{d}x$ than the fast component, it is not strictly independent of particle type.

It should also be emphasized that an increased *fractional* contribution of the slow component does not necessarily imply a larger *absolute* slow-light yield. For example, despite the slow component representing a larger fraction of the total emission under α excitation than under γ excitation, the slow-light yield per unit deposited energy can be lower for α particles than for γ rays.

Three general approaches have been used to implement PSD measurements:

- Prompt versus total light integration: one measures the prompt component and the total scintillation, or equivalently compares the prompt and delayed integrals, thereby forming a shape-dependent discriminator [39].

- Space-charge saturation method: the prompt component drives the final stage of the photomultiplier into space-charge saturation, producing a shape-dependent output [40].
- Zero-crossing method: a time difference is measured between the start of the scintillation pulse and the time when the pulse integral reaches a chosen fraction of its final value; this can be implemented with a zero-crossing discriminator on a double-differentiated signal [41, 42].

A fourth, more recent approach to pulse-shape discrimination was proposed by V. Jordanov [43] and implemented in the nanoPSD device [44]. The method is based on ballistic-deficit measurement using digital time-invariant pulse shaping. In this approach, the PMT signal is processed in parallel by fast and slow digital shapers, and the maximum amplitude of each shaped pulse is determined by peak-detection algorithms.

The Time-Invariant Pulse-shape Signature (TIPS) is defined as the ratio of the maximum amplitude of the slow-shaped pulse to that of the fast-shaped pulse [43]. Since scintillation pulses produced by different particle types have different temporal profiles, they yield different TIPS values and can therefore be discriminated. The nanoPSD records four spectra simultaneously: one PSD spectrum based on TIPS, the total pulse-height spectrum containing both α- and β-like events, and the separated α and β pulse-height spectra.

Pulse-shape discrimination is a standard approach for particle identification in organic scintillators because it exploits differences in the temporal dependence of the scintillation signal, rather than relying only on total light output. PSD enables efficient separation of event classes such as neutrons and γ rays, which is essential in applications including nuclear nonproliferation [45, 46, 47] and measurements in nuclear physics and astrophysics [48, 49]. The discrimination performance is governed by the intrinsic scintillation decay characteristics (i.e. the relative contributions and time constants of the prompt and delayed components), as well as by the signal processing methods. Ongoing improvements in PSD are driven both by advances in scintillator materials and by the development of discrimination algorithms [50, 51, 52, 53].

2.1.6 Ionization quenching

Ionization quenching is the reduction of scintillation yield per unit deposited energy caused by the high local density of ionizations and excitations along the charged particle track. The magnitude of the effect depends on the scintillator composition but the same qualitative behavior is observed: particles with higher linear energy transfer produce denser excitation tracks, increasing the probability of non-radiative de-excitation and bimolecular quenching processes [1]. Consequently, the scintillation response is not strictly proportional to the deposited energy. Instead, the light yield depends on the stopping power $\mathrm{d}E/\mathrm{d}x$, which itself varies with particle type and kinetic energy (see Fig. Figure 2.7).

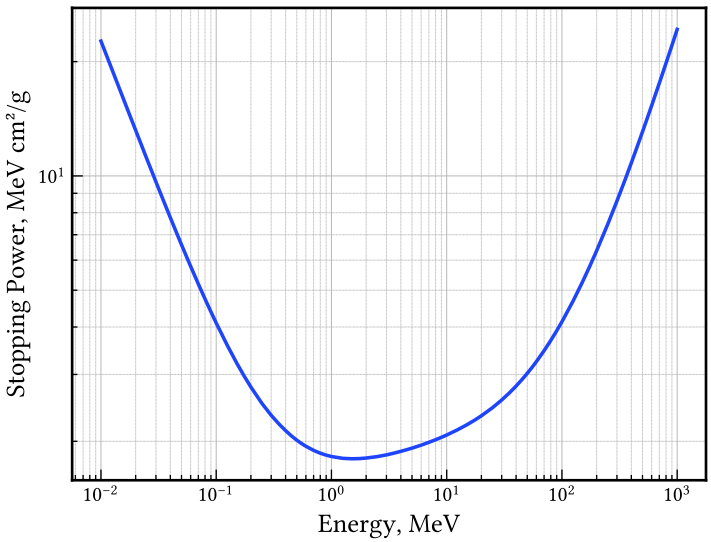

Figure 2.7: Dependence of the electron stopping power on its kinetic energy in a vinyltoluene-based plastic scintillator. The plot data was generated using ESTAR. [54].

A general phenomenological description of ionization quenching is often expressed as:

$$\frac{\mathrm{d}I}{\mathrm{d}x} = \frac{\eta_0 \cdot \frac{\mathrm{d}E}{\mathrm{d}x}}{QCF}, \quad QCF = 1 + kB\frac{\mathrm{d}E}{\mathrm{d}x} + C\left(\frac{\mathrm{d}E}{\mathrm{d}x}\right)^2 + \cdots \tag{2.12}$$

where η_0 is the absolute scintillation efficiency (ratio of total emitted photon energy to deposited energy), and the Quenching Correction Factor (QCF) is parameterized by quenching constants such as kB and C. The Birks model retains only the first-order term in the QCF [55] and is intended to describe quenching of the prompt scintillation component only [1]. The second-order term was introduced by Chou [56] and represents bimolecular quenching, i.e. non-radiative relaxation through interactions between excited molecules.

Wright subsequently proposed a phenomenological model for ionization quenching [57]:

$$\frac{\mathrm{d}I}{\mathrm{d}x} = S\,\frac{\ln\left(1 + W\frac{\mathrm{d}E}{\mathrm{d}x}\right)}{W\frac{\mathrm{d}E}{\mathrm{d}x}}. \tag{2.13}$$

where W has units identical to kB. Hong *et al.* proposed an extension of the Birks model aimed at heavy ions [58]:

$$\frac{\mathrm{d}I}{\mathrm{d}x} = \frac{S_e\left(\frac{\mathrm{d}E}{\mathrm{d}x}\right)_e + S_n\left(\frac{\mathrm{d}E}{\mathrm{d}x}\right)_n}{1 + kB_e\left(\frac{\mathrm{d}E}{\mathrm{d}x}\right)_e + kB_n\left(\frac{\mathrm{d}E}{\mathrm{d}x}\right)_n}. \tag{2.14}$$

In this model, electronic (subscript e) and nuclear (subscript n) stopping are treated separately, motivated by the expectation that these contributions affect quenching and absolute scintillation efficiency differently for heavy ions. Yoshida later extended this formulation by adding a

bimolecular-quenching term [59]:

$$\frac{\mathrm{d}I}{\mathrm{d}x} = \frac{S_e\left(\frac{\mathrm{d}E}{\mathrm{d}x}\right)_e + S_n\left(\frac{\mathrm{d}E}{\mathrm{d}x}\right)_n}{1 + kB_e\left(\frac{\mathrm{d}E}{\mathrm{d}x}\right)_e + C\left(\frac{\mathrm{d}E}{\mathrm{d}x}\right)_e^2 + kB_n\left(\frac{\mathrm{d}E}{\mathrm{d}x}\right)_n}. \tag{2.15}$$

The models above build upon the Birks framework and typically describe only the prompt scintillation component. An alternative approach due to Voltz *et al.* treats prompt and delayed scintillation components separately. For electrons, the scintillation intensity as a function of stopping power can be expressed as [25]:

$$\frac{\mathrm{d}I}{\mathrm{d}x} = \eta_S\left[\frac{1}{W_S}\frac{\mathrm{d}E}{\mathrm{d}x}\exp\left(-B_S\frac{\mathrm{d}E}{\mathrm{d}x}\right) + \alpha\,\frac{\Phi_T}{W_T}\frac{\mathrm{d}E}{\mathrm{d}x}\exp\left(-B_T\Phi_T\frac{\mathrm{d}E}{\mathrm{d}x}\right)\right]. \tag{2.16}$$

For other charged particles the expression becomes [25]:

$$\frac{\mathrm{d}I}{\mathrm{d}x} = \eta_S\left\{\frac{1-F_S}{W_S}\frac{\mathrm{d}E}{\mathrm{d}x}\exp\left[-B_S(1-F_S)\frac{\mathrm{d}E}{\mathrm{d}x}\right] + \frac{F_S}{W_S}\frac{\mathrm{d}E}{\mathrm{d}x} + \alpha\,\frac{\Phi_T}{W_T}\frac{\mathrm{d}E}{\mathrm{d}x}\exp\left(-B_T\Phi_T\frac{\mathrm{d}E}{\mathrm{d}x}\right)\right\}. \tag{2.17}$$

where W_S is the mean energy required to produce a singlet S_1 state, and W_T is defined analogously for producing a T_1 state. The parameters B_S and B_T are the quenching parameters for the prompt and delayed components, respectively, $\Phi_T \mathrm{d}E/\mathrm{d}x$ is the fraction of the energy loss activating molecules in high-density regions where triplet–triplet interactions occur, F_S is the fraction of energy carried away by energetic secondary electrons (δ-rays), and α is the number of S_1 states created per triplet-state relaxation during triplet–triplet annihilation.

Recent work compared the models of Birks, Hong *et al.*, Yoshida *et al.*, and Voltz *et al.* for describing ionization quenching of proton and carbon light-yield data in plastic and liquid scintillators [60]. It was concluded that the models of Birks and Hong did not reproduce the proton light yield over a broad energy range, whereas the Yoshida and Voltz models provided a reasonable description of the proton data. None of the models adequately reproduced the carbon-ion data, suggesting that a more sophisticated treatment of excitation-density distributions is required [60].

An alternative approach addressing ionization quenching was presented in [61], where the kinetic Blanc model [29] is employed as a more general framework than Birks-type laws. In this approach, exciton transport and quenching are derived from material properties and track structure rather than solely from an empirical quenching curve; the model was validated against proton-irradiation quenching data with good agreement over most of the measured range.

In the LSC community, Birks' equation remains the most commonly used model for correcting ionization quenching. The scintillation light yield according to Birks' equation is:

$$L(E) = \eta_0 \int_0^E \frac{\mathrm{d}E}{1 + kB\frac{\mathrm{d}E}{\mathrm{d}x}} = \eta_0 E Q(E) \tag{2.18}$$

where the integration upper limit is the initial kinetic energy of the particle and $Q(E)$ is the

ionization quenching function:

$$Q(E) = \frac{1}{E}\int_0^E \frac{\mathrm{d}E}{1 + kB\frac{\mathrm{d}E}{\mathrm{d}x}} \tag{2.19}$$

Integration of Equation (2.18) is rather straightforward, but practical implementation requires an experimentally determined value of the ionization quenching parameter kB, stopping-power data at low energies, typically below a few keV, and reliable information on the scintillator composition and density for stopping-power calculations. These issues are discussed further in the subsequent sections, where the calculation of stopping power is discussed and its implications for TDCR efficiency calculations are outlined.

2.1.7 Stopping power

Integration of Equation (2.18) requires knowledge of the stopping power $\mathrm{d}E/\mathrm{d}x$ over the relevant energy range. For low-energy electrons in particular, the combination of rapidly varying stopping power and pronounced scintillator non-linearity makes the calculation sensitive to both the chosen stopping-power formalism and to the assumed material properties of the scintillator. In addition, the numerical value of kB is often extracted by fitting procedures, so uncertainties or biases in $\mathrm{d}E/\mathrm{d}x$ can propagate directly into the determined quenching behavior and, consequently, into TDCR efficiency calculations.

The stopping power of a particle in a medium is defined as the mean rate at which it loses kinetic energy per unit path length in that medium. Microscopically, it arises from electromagnetic interactions between the particle and the electrons and nuclei of the medium: as a charged particle traverses matter, its electric field perturbs atomic electrons, transferring energy that leads to ionization and excitation, and (depending on particle type and energy) to other loss channels such as bremsstrahlung or elastic energy transfer to atoms.

Depending on particle type and energy, the stopping power is commonly decomposed into contributions:

- Collision (electronic) stopping power — energy loss due to inelastic interactions with atomic electrons (ionization/excitation).
- Radiative stopping power — energy loss through bremsstrahlung, which is present for electrons and positrons at all energies but becomes significant only at high energies, particularly in high-Z materials. In low-Z organic scintillators, it is generally negligible for the keV–MeV electron energies relevant to liquid scintillation counting.
- Nuclear stopping power — energy transfer to recoiling atoms via elastic collisions (relevant mainly for heavy ions at low energies).

Accordingly, the total stopping power is often written as:

- for electrons — $S_{tot} = S_{col} + S_{rad}$,
- for protons/ions — $S_{tot} = S_{col} + S_{nuc}$.

For heavy charged particles at sufficiently high energies, $\mathrm{d}E/\mathrm{d}x$ can be estimated using the Bethe–Bloch formalism [62]:

$$-\left\langle\frac{\mathrm{d}E}{\mathrm{d}x}\right\rangle = \frac{4\pi}{m_e c^2}\frac{nz^2}{\beta^2}\left(\frac{e^2}{4\pi\varepsilon_0}\right)^2\left[\ln\left(\frac{2m_e c^2\beta^2}{I\,(1-\beta^2)}\right) - \beta^2\right], \tag{2.20}$$

where v is the particle speed, z is the particle charge, and c is the speed of light. Furthermore, ε_0 is the vacuum permittivity, $\beta = v/c$, I is the mean excitation energy of the medium, and e and m_e are the electron charge and rest mass, respectively. The electron density of the medium is given by:

$$n = \frac{N_A Z \rho}{A M_u}, \tag{2.21}$$

where N_A is Avogadro's number, Z is the atomic number, ρ is the material density, A is the atomic mass, and M_u is the molar mass constant.

While Equation (2.20) provides the correct asymptotic behavior at intermediate and high energies, the determination of electron stopping power in the low-energy regime relevant to LSC (keV-scale electrons) requires additional corrections and dedicated formalisms. In particular, binding effects, exchange, and density-effect corrections become important, and a practical route is to use the recommendations of the International Commission on Radiation Units and Measurements (ICRU) and evaluated stopping-power tables.

ICRU Report №37 recommends the following expression for the collisional stopping power of electrons and positrons:

$$\left(\frac{\mathrm{d}E}{\mathrm{d}x}\right)^{\pm}_{col} = \frac{2\pi N_A r_e^2 m_e c^2}{\rho\,\beta^2}\,\frac{Z}{A}\left[\ln\left(\frac{E}{I}\right)^2 + \ln\left(1+\frac{\tau}{2}\right) + F^{\pm}(\tau) - \delta\right], \tag{2.22}$$

$$\tau = \frac{E}{m_e c^2}, \qquad \beta^2 = \frac{\tau(\tau+2)}{(\tau+1)^2} = 1 - \left(\frac{m_e c^2}{m_e c^2 + E}\right)^2. \tag{2.23}$$

Here $F^{-}(\tau)$ is defined for electrons:

$$F^{-}(\tau) = (1-\beta^2)\left[1 + \frac{\tau^2}{8} - (2\tau+1)\ln 2\right], \tag{2.24}$$

and $F^{+}(\tau)$ is defined for positrons:

$$F^{+}(\tau) = 2\ln 2 - \frac{\beta^2}{12}\left[23 + \frac{14}{\tau+2} + \frac{10}{(\tau+2)^2} + \frac{4}{(\tau+2)^3}\right]. \tag{2.25}$$

In practical implementations, the constant

$$2\pi N_A r_e^2 m_e c^2 = 0.153536\ \mathrm{MeV\ cm^2\ mol^{-1}} \tag{2.26}$$

is often used, where r_e is the classical electron radius and $m_e c^2$ is the electron rest energy.

Equation (2.22) depends explicitly on the material parameters Z/A and ρ. This dependence introduces a practical limitation for commercial scintillation cocktails, for which detailed chemical composition and density are not always provided. In the case of some liquid organic scintillators, approximate compositions can be obtained from the literature [11, 63]; however, the associated uncertainty should be kept in mind when interpreting fitted kB values or comparing results between cocktails.

The sensitivity of scintillation-quenching models to stopping-power input data is emphasized in [60]. Laplace *et al.* [60] reported that the choice of stopping-power database has only a minor effect for protons, as SRIM [64] and PSTAR [65] agree to within about 3%. In contrast, for carbon ions the dependence is substantially stronger: in polyvinyltoluene, SRIM [64] and MSTAR [66] predict Bragg-peak positions that differ by approximately 1.5 MeV, and no

dedicated experimental data are available to validate either prediction. Although fits to carbon light-yield measurements yielded slightly improved statistical agreement when using SRIM, the overall description remained unsatisfactory for both libraries. Consequently, Laplace *et al.* concluded that the existing data do not permit a definitive preference between the stopping-power databases for carbon ions [60].

2.2 Photomuliplier tubes

Photomultiplier tubes are vacuum electron devices designed to convert scintillation light into a measurable electrical signal. They remain the dominant photosensors in LS counting because they provide high gain, low noise, and excellent sensitivity at low light levels. A PMT typically comprises a transparent entrance window, a photocathode (transmission- or reflection-type), focusing electrodes, an electron-multiplication chain (dynode system), and an anode.

The detection process proceeds as follows. A photon enters through the window and may be absorbed in the photocathode. If the photon energy exceeds the effective work function of the photocathode material, photoemission can occur and a photoelectron is emitted into the vacuum with probability characterized by the quantum efficiency, ε_q (defined as the ratio of emitted photoelectrons to photons incident on the photocathode). The photoelectron is then accelerated by the electric field between the photocathode and the first dynode. The focusing electrodes shape this field to guide photoelectrons toward the first dynode, ideally with high collection efficiency over the full photocathode area. Upon impact on the first dynode, the primary photoelectron generates secondary electrons. These are accelerated toward subsequent dynodes by the potential differences between dynodes, forming an electron cascade whose overall amplification (gain) is the product of the secondary-emission yields at each stage. The amplified charge is finally collected at the anode and converted into an output pulse. A schematic representation of a PMT and the associated electron-multiplication process is shown in Figure 2.8.

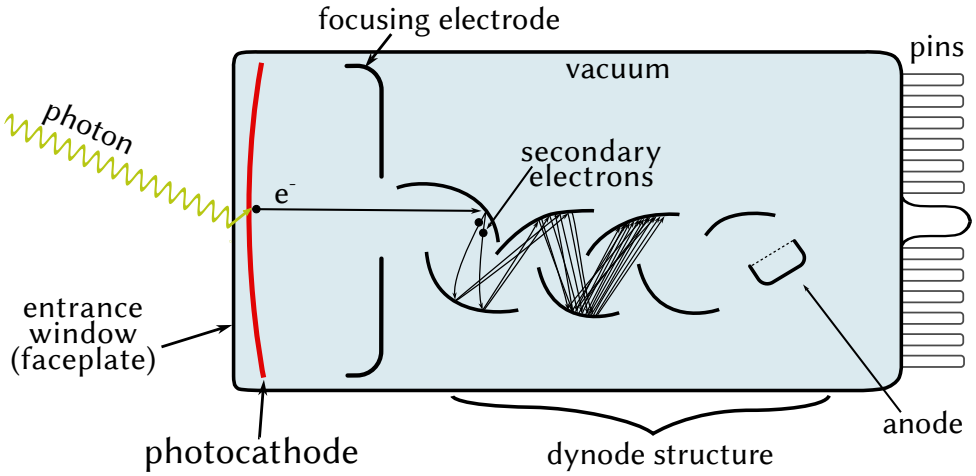

Figure 2.8: Schematic representation of the photoelectron formation process and secondary-electron multiplication in a PMT.

The entrance window is most commonly made of low-potassium borosilicate glass; fused or synthetic silica is used when high transmission in the ultraviolet is required. The photocathode composition is selected to match the application. For scintillation spectroscopy and counting,

bialkali photocathodes (Sb–K–Cs) are widely used because they provide comparatively high quantum efficiency and low dark-noise levels. Typical peak quantum efficiencies, $\varepsilon_q(\lambda)$, are on the order of 20–40% depending on photocathode type and wavelength. High-efficiency PMTs are advantageous in coincidence counting because an event must be detected by several PMTs simultaneously. Therefore, increasing the detection efficiency of each PMT increases the probability of detecting double and triple coincidences [6, 7].

PMT dynodes are typically metal electrodes (e.g., nickel, stainless steel, or Cu–Be) and they can be coated with a secondary-emissive layer (e.g., alkali-antimonides, MgO/BeO, or GaP:Cs/GaAsP) to maximize secondary-electron yield. The resulting multiplication chain defines the achievable gain. For scintillation applications with low light intensities (few detected photons per keV deposited), sufficiently high gain is required so that single-photoelectron pulses are clearly resolved.

In scintillation counting, several models measurement require non-zero single-photon sensitivity. This generally implies operation at sufficiently high PMT gain (typically $\gtrsim 10^6$) such that the single-photoelectron (SPE) peak is clearly separated from the dark-noise and electronic-noise pulse distributions. The resolution of the SPE is dominated by the multiplication factor of the first dynode. When setting discriminator thresholds in the readout electronics, the objective is to suppress electrical noise while retaining essentially all SPE pulses.

One of the most important timing characteristics of PMTs — particularly relevant for fast organic scintillators and coincidence-based methods — includes the rise time, fall time, transit time, and transit time spread (TTS). The rise time is usually defined as the interval required for the pulse to increase from 10% to 90% of its maximum amplitude and is typically 1–2 ns (Fig. Figure 2.9). The fall time is defined analogously (90% to 10%) and is typically a factor of 2–3 longer than the rise time. The full width at half maximum of the anode pulse is often 1–7 ns, but depending on the dynode structure it can be significantly larger [67]. The transit time is the delay between photon arrival at the photocathode and the appearance of the corresponding pulse at the anode. The event-to-event fluctuations of this delay define the TTS, which is typically in the range 0.3–0.5 ns. These timing characteristics depend on the applied high voltage: increasing the electric field accelerates photoelectrons and secondaries, thereby reducing the transit time.

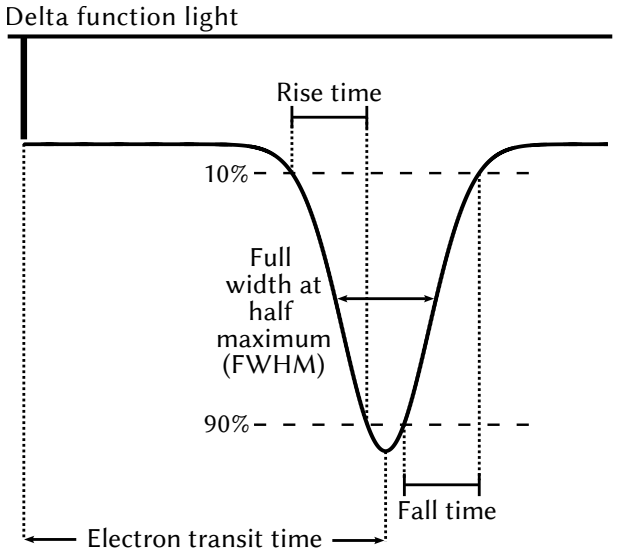

Figure 2.9: Schematic representation of the time characteristics of a PMT.

When a PMT operates in pulse-counting mode, as in scintillation measurements, spurious pulses may appear shortly after the main output pulse; these are referred to as *afterpulses*. Afterpulses can interfere with the detection of low-level signals that follow large pulses and may degrade the energy resolution in scintillation counting.

Afterpulses arise primarily from ion feedback: residual gas molecules inside the tube can be ionized during an event, creating positive ions that drift back toward the photocathode. Their impact can release secondary electrons, generating delayed pulses. The magnitude of these delayed signals depends on the ion species and on where the ions were formed, while the delay time — typically from a few hundred nanoseconds up to several microseconds — varies with the applied high voltage. Helium is a well-known contributor because it can permeate silica glass envelopes [67].

In practice, both the occurrence rate and the associated charge of afterpulses can be problematic. Although the ion production rate may be similar, operation at higher supply voltage (i.e., higher gain) increases the output charge per afterpulse. In pulse-counting measurements, afterpulses become relevant when their amplitude exceeds the discriminator threshold. To mitigate the effect of afterpulses, a dead time of at least 10 μs is often applied after each detected pulse (or after the end of the coincidence window). For the same reason, within a coincidence window only the first pulse from a given PMT is typically accepted, and subsequent pulses are rejected.An extending-type dead-time is preferred as the detection of a new pulse is only possible after a period without any pulse.

2.2.1 Origin of the photocathode response non-uniformity

The photon detection efficiency (PDE) of a PMT can be expressed as the product of the quantum efficiency (QE) and the collection efficiency (CE), i.e. the probability that an incident photon produces a photoelectron at the photocathode and that this photoelectron is subsequently collected by the first dynode. Spatial non-uniformity arises when QE and/or CE vary across the photocathode area.

The main factors affecting the photocathode *quantum efficiency* are:

PE.1 Photocathode material and fabrication: the composition and activation determine the work function and thus the attainable QE and spectral range. Quantum efficiency is strongly wavelength dependent; matching the PMT spectral response to the scintillator emission is therefore a primary practical consideration [67].

PE.2 Incidence angle and polarization: QE can vary with incident angle because reflection, absorption depth, and electron escape probability depend on the optical path and boundary conditions; polarization effects can also become relevant at larger angles [68].

PE.3 Photocathode thickness and optical stack: spatial variations in photocathode thickness can modify absorption and interference conditions, thereby affecting QE; window properties and anti-reflection coatings also contribute [68].

PE.4 Temperature: while QE is typically less temperature-sensitive than dark current, temperature can influence the effective work function and carrier transport. In practice, decreasing temperature is most clearly associated with reduced dark current [67].

The main factors affecting the PMT *collection efficiency* are:

CE.1 Electric field near the photocathode: CE depends strongly on the potential difference between the photocathode and the first dynode and on field shaping in the entrance region [67].

CE.2 Electron optics and dynode geometry: the focusing system is designed to steer photoelectrons efficiently, but trajectory deviations can occur and lead to collection losses; the dynode structure also matters, with larger effective first-dynode acceptance generally improving CE.

CE.3 Magnetic fields and orientation: external magnetic fields can deflect photoelectrons between the photocathode and first dynode, reducing CE.

CE.4 Voltage-divider design and HV stability: divider ratios, HV ripple, and loading at high anode currents can alter early-stage fields and degrade CE [67].

CE.5 Initial photoelectron energy and angle spread: photoelectrons are emitted with distributions of energies and angles; the focusing optics must capture this distribution consistently across the photocathode.

CE.6 Space-charge effects: at high instantaneous currents, space charge can distort fields in the early stages and reduce collection to the first dynode [69].

CE.7 At high gain, the last stages of the multiplication chain in the PMT might become saturated [67].

The combined influence of the effects listed above leads to a position-dependent PDE. Spatial non-uniformity of PMT response has been recognized as a limiting factor in scintillation spectroscopy since the early studies of Schardt [70] and later Godlove and Wadey [71], who also noted differences between nominally identical tubes and emphasized the role of electron optics. Subsequent work has addressed photocathode response non-uniformity across a broad range of PMT types and applications [72, 73, 74, 75, 76, 77, 78, 79, 80, 81, 82, 83]. In large-volume neutrino detectors, detailed PMT optical models incorporating spatial response variations have been developed to predict the detector energy resolution for large detector volumes [84].

2.3 Liquid scintillation spectrometers and counters

Liquid scintillation spectrometers and counters are detection systems in which one or more PMTs are optically coupled to a vial containing the scintillation sample inside a light-tight optical chamber. The chamber is typically lined with reflective material to maximize photon collection at the PMT entrance windows while simultaneously suppressing interference from ambient light. In some instruments, such as PERALS [85], optical oil is applied between the vial and the PMT window to improve optical coupling by reducing refractive-index mismatch, thereby mitigating total internal reflection losses at the vial boundary.

In LS counting — and in particular in primary activity measurements — PMTs are commonly operated at high gain in the single photon counting regime. Under these conditions, electronic noise and dark pulses can represent a non-negligible fraction of detected signals, especially at low activities. Because scintillation light is emitted approximately isotropically and the light yield is typically on the order of $\sim$ 10 photons per keV deposited by β particles [7], a decay event has a good probability to produce detectable photoelectrons in one or more PMTs. As discussed

in Section 2.1.4, scintillation emission is not instantaneous; photons are emitted over a finite time interval and the corresponding photoelectron pulses are therefore distributed in time. This motivates the use of a coincidence resolving time (coincidence window), which defines the maximum temporal separation for pulses to be attributed to the same decay event. In the context of primary activity measurements, the choice of coincidence window is not trivial [12]. Moreover, with the availability of analytical corrections for accidental coincidences [18], longer coincidence windows — previously avoided to limit random coincidences — have become practical and are increasingly used [86].

2.3.1 Applications of LS counting

Liquid scintillation counting is a versatile technique for measuring ionizing radiation, particularly for low-energy β emitters and radionuclides that are difficult to assay with detectors where there is a physical barrier between the radionuclide and the detector. Typical applications include radiation monitoring in nuclear facilities [87, 88], environmental radioactivity studies [89, 90], ^{14}C dating [91], high-energy and neutrino physics [92, 93], and radionuclide metrology [94, 95].

Several standardization approaches employ LS counting. The $4\pi\beta$–γ coincidence method [96] is applicable to nuclides that emit simultaneously both β particles and γ rays; however, it is not applicable for pure β emitters and typically requires a more complex multi-detector arrangement. The CIEMAT/NIST efficiency tracing method [97] enables standardization of a broad range of radionuclides and is implemented in commercial LS counters, but it is not purely primary, since it relies on a tracer (commonly ^{3}H) whose activity is itself established by primary methods. The TDCR method was developed to enable primary activity determination for β-emitting and electron-capture radionuclides [10]. It relies on a statistical model applied to counting rates measured with a three-PMT LS counter.

2.4 Radionuclide standardization by liquid scintillation counting

Liquid scintillation counting provides a robust basis for radionuclide standardization when the detection efficiency is close to unity. This is often the case for α emitters and for high-energy β emitters, for which the probability that a decay produces at least one detectable scintillation burst in the counter is very high [98]. For low-energy β emitters and electron-capture (EC) radionuclides, however, the detection efficiency can deviate substantially from unity and may depend on measurement conditions (cocktail composition, optical coupling, discriminator thresholds, and acquisition logic). Because the standardized activity is subsequently used to calibrate secondary instruments, its uncertainty directly propagates into downstream measurements. Therefore, metrological applications require an accurate determination of the detection efficiency and associated with a sound uncertainty budget. A widely used approach for this purpose is the *free parameter* model, which provides a statistical description of scintillation-photon production and detection in an LS counter [11].

2.4.1 The free parameter model

Following a radioactive decay, energy E can be deposited in a liquid scintillator and the expected mean number of emitted photons can be written as [11]:

$$M = \frac{\eta Q(E) E}{h\nu} \tag{2.27}$$

where η_0 is the absolute scintillation efficiency and $h\nu$ is the mean energy of the scintillation photon. The function $Q(E)$ accounts for the scintillator non-linear response — the light yield of the scintillator is not proportional to the energy deposited in the scintillator. If we assume that the photon emission follows the Poisson distribution with a mean value M, the number of photons that reach the PMT photocathode, m also follows the Poisson distribution [11]:

$$p(m, \bar{m}) = \frac{\bar{m}^m}{m!} e^{-\bar{m}} \tag{2.28}$$

$$\bar{m} = M\xi\,, \tag{2.29}$$

where $\bar{m}$ is the mean number of photons that reach the PMT and ξ is the geometric efficiency of the PMT. After the emission of m photons in a scintillation burst, that would, on average, lead to the creation of n photoelectrons from the PMT photocathode, which is given by [11]:

$$n = m\varepsilon_q \mu\,, \tag{2.30}$$

where ε_q is the quantum efficiency of the PMT and μ is the spectral matching factor between the scintillator's spectrum and the spectral response of the photocathode. The absolute efficiency of a PMT ε_{abs} is the product of ξ, ε_q and μ. Combining Equations (2.27), (2.29) and (2.30), the mean number of photoelectrons $\bar{n}$ created by a particle depositing energy E in the scintillator can be expressed as:

$$\bar{n} = M\varepsilon_{abs} = \frac{\eta \xi \varepsilon_q \mu}{h\nu} Q(E) E \tag{2.31}$$

The photoelectric process in the photocathode can be described by the binomial distribution [11]:

$$b\big(n;\, m,\, \varepsilon_q\mu\big) = \frac{m!}{n!\,(m-n)!} \left(\varepsilon_q\mu\right)^n \left(1 - \varepsilon_q\mu\right)^{m-n}, \tag{2.32}$$

which represents the probability that when m photons reach the photocathode they would produce exactly n photoelectrons. In LSC, the relevant quantity is usually the probability that a scintillation burst produces a detectable pulse, i.e. at least one detected photoelectron. This can be written as the complement of producing zero photoelectrons [11]:

$$p_e(m) = 1 - b\big(0;\, m,\, \varepsilon_q\mu\big) = 1 - \left(1 - \varepsilon_q\mu\right)^m. \tag{2.33}$$

For a detector with R number of PMTs, the m photons incident on the photocathodes can be partitioned as a set $\{m_i\}$ satisfying $m = m_1 + m_2 + \cdots + m_R$. The probability for the realization of a given partition is [11]:

$$P_d = \frac{1}{R^m} \frac{m!}{m_1!\, m_2! \cdots m_R!}\,. \tag{2.34}$$

The probabilities for different pulse types in each PMT can then be computed from Equation (2.33), and the overall counting probability P_E is obtained by summing over all admissible

photon partitions $\{m_i\}$. In the special case of a single PMT ($R = 1$), $P_x = p_e(m)$ and $P_d = 1$, so the probability to detect a scintillation event for a mean number of $\bar{m}$ photons reaching the photocathode is [11]:

$$\begin{aligned} P_E &= \sum_{m=0}^{\infty} p(m,\bar{m})\left[1-\left(1-\varepsilon_q\mu\right)^m\right] \\ &= 1-\sum_{m=0}^{\infty}\frac{\bar{m}^m}{m!}e^{-\bar{m}}\left(1-\varepsilon_q\mu\right)^m \\ &= 1-e^{-\bar{m}}\sum_{m=0}^{\infty}\frac{\left[\bar{m}\left(1-\varepsilon_q\mu\right)\right]^m}{m!} \\ &= 1-e^{-\bar{m}}e^{\left(\bar{m}\left(1-\varepsilon_q\mu\right)\right)} \\ &= 1-e^{-\bar{m}\varepsilon_q\mu} = 1-e^{-\bar{n}}. \end{aligned} \tag{2.35}$$

Thus, the cascade of three random processes — Poisson emission Equation (2.28), binomial photoemission Equation (2.32), and multinomial photon sharing between PMTs Equation (2.34) — can be reduced to an effective Poisson description for the mean number of photoelectrons $p(n,\bar{n})$ [11]. For common pulse types and coincidence conditions, the resulting counting probabilities, expressed via the non-detection probability p_0, are summarized in Table 2.1 [11].

Table 2.1: Probability of counting $P(E,\lambda)$ for various types of pulses produced by a monoenergetic particle in LS detector with R PMTs of identical or non-identical response. The non-detection probability is $p_0 = e^{-\bar{n}/R}$. The kind of signals are: U — no coincidence, D — double coincidence, D_3 — the logical sum of double coincidences and T — triple coincidence.

R	Signal mode	Signal	Probability of counting $P(E,\lambda)$
			Identical PMTs, $p_A = p_B = p_C = p_0$
1	A	U	$1-p_0$
2	$A;B$	U	$1-p_0$
	AB	D	$(1-p_0)^2$
3	$A;B;C$	U	$1-p_0$
	$AB;BC;AC$	D	$(1-p_0)^2$
	ABC	T	$(1-p_0)^3$
			Non-identical PMTs, $p_A \neq p_B \neq p_C$
1	A	U	$1-p_A$
2	$A;B$	U	$(1-p_A);\ (1-p_B)$
	AB	D	$(1-p_A)(1-p_B)$
3	$A;B;C$	U	$(1-p_A);\ (1-p_B);\ (1-p_C)$
	$AB;BC;AC$	D	$(1-p_A)(1-p_B);\ (1-p_A)(1-p_C);\ (1-p_B)(1-p_C)$
	$AB+BC+AC$	D_3	$(1-p_A)(1-p_B)+(1-p_A)(1-p_C)+$ $(1-p_B)(1-p_C)$-$2(1-p_A)(1-p_B)(1-p_C)$
	ABC	T	$(1-p_A)(1-p_B)(1-p_C)$

The performance of an LS counter can be expressed through the relationship between the

energy deposited in the scintillator, E (equal to the particle's initial energy only under full energy containment), and the mean number of scintillation photons $\bar{m}$ (or detected photoelectrons $\bar{n}$) produced. This parameter is widely known as a figure of merit (FOM). The term *free parameter* λ, coined in [99] and adopted here, is defined as the mean number of photoelectrons produced at the photocathode per unit of energy deposited in the scintillator taking into account the ionization quenching:

$$\lambda = \frac{\bar{n}}{EQ(E)} = \frac{\eta \xi \varepsilon_q \mu}{h\nu} \tag{2.36}$$

If the detection probability of a single photoelectron is non-zero, the non-detection probability for R identical PMTs is $p_0 = e^{-\bar{n}/R}$; therefore, the corresponding counting probability follows directly as $P = 1 - p_0$. In practice, achieving non-zero single-photoelectron detection probability requires setting discriminator thresholds just below the single-photoelectron peak. The counting probability of an LS counter including R identical PMTs is given by [11]:

$$P = 1 - e^{\frac{\bar{n}}{R}} \tag{2.37}$$

where the mean number of photoelectrons produced in all PMTs is:

$$\bar{n} = EQ(E)\lambda \tag{2.38}$$

The counting probability P depends on the energy E and the free parameter λ. For high-energy particles, the deposited energy can differ from the initial kinetic energy because a fraction of particles (or secondaries) may escape the scintillator volume ("wall effects"). Such effects can be corrected using Monte Carlo simulation [99, 100]. A further simplifying assumption of the free-parameter model is that the optical collection (and thus ξ) is independent of the decay position within the sample volume. In practice, the light collection can exhibit position dependence, particularly for low-energy depositions, and this can lead to measurable efficiency variations [101].

2.4.2 Calculation of counting efficiency

The counting efficiency for an LS counter, φ, is a function of the FOM and depends on the decay mode of the radionuclide. For pure β emitters, φ is obtained by weighting the pulse counting probability $P(E, \lambda)$ (see Table 2.1) by the β spectrum $S(E)$ and integrating over the full decay-energy range [11]:

$$\varphi(\lambda) = \int_0^{E_{max}} S(E)\, P(E, \lambda) \mathrm{d}E\,, \tag{2.39}$$

where E_{max} is the maximum energy of the β spectrum.

For electron capture, the electron vacancy is followed by atomic re-arrangements, leading to the emission of photons and Auger electrons. In this case, the counting efficiency is expressed as a discrete sum over emitted radiations with energies E_j and intensities $I(E_j)$ [11]:

$$\varphi(\lambda) = \sum_{j=0}^{k} I(E_j)\, P(E_j, \lambda) \tag{2.40}$$

2.4.3 Calculation of energy spectra

The efficiency calculation requires the calculation of the energy spectrum that is effectively deposited in the liquid scintillator. This spectrum is not necessarily identical to the theoretical spectrum of particles emitted in the nuclear decay. Therefore, it is useful to distinguish between two steps. First, the theoretical β spectrum is calculated from nuclear decay theory and decay data. Second, this theoretical spectrum is transferred to the deposited energy spectrum in the scintillator by accounting for particle transport, photon interactions, finite sample geometry, and possible energy escape.

For radionuclides undergoing β^- or β^+ decay, the starting point is the theoretical β-particle spectrum. In the Femri theory, the probability of emitting an electron or positron with total energy $W = 1 + E/m_0c^2$ in the interval $(W, W + \mathrm{d}W)$ can be written as [11]:

$$N(W), \mathrm{d}W = \frac{g^2}{2\pi^3}\sqrt{W^2-1}, W, (W_0 - W)^2 F(Z, W)(1 + \delta_R(W, Z))C(W), \mathrm{d}W, \tag{2.41}$$

where g is the weak-interaction coupling constant, W_0 is the maximum energy, $F(Z, W)$ is the Fermi function, $\delta_R(W, Z)$ accounts for radiative corrections, Z is the atomic number of the daughter nucleus, and $C(W)$ is the shape-factor function. After normalization, this expression gives the theoretical emitted β spectrum, denoted here as $S_\beta(E_0)$, where E_0 is the kinetic energy of the emitted particle.

Several codes are available for the calculation of theoretical β spectra, including EFFY [102] and SPEBETA [103]. A more comprehensive implementation is provided by the BetaShape code of X. Mougeot [104], where atomic effects are taken into account. BetaShape spectra are available through the DDEP resources [105]. High-precision analytical descriptions of allowed β spectra are reviewed in [106]. The influence of spectral-shape assumptions on TDCR efficiency calculations has been studied in detail by Kossert and Mougeot [107].

The spectrum entering the liquid-scintillation efficiency calculation is the spectrum of deposited energy, here denoted by $S(E)$. It is normalized as [11]:

$$\int_0^{E_{\max}} S(E), \mathrm{d}E = 1. \tag{2.42}$$

For many pure β emitters, especially at low energies, the emitted electron is assumed to deposit its full kinetic energy in the scintillator. In this approximation, the deposited-energy spectrum is equal to the theoretical emitted spectrum:

$$S(E) \simeq S_\beta(E). \tag{2.43}$$

This approximation is commonly used when the electron range is small compared with the sample dimensions and when wall losses are negligible.

The best practice is to convert the theoretical β-spectrum into the corresponding deposited energy spectrum. This conversion describes the probability that a particle emitted with kinetic energy E_0 deposits an energy E in the scintillator. This probability distribution is usually obtained by Monte Carlo transport calculations rather than by an analytical expression. For high-energy β emitters, such simulations can be used to estimate wall effects and incomplete energy deposition; the spectrum distortion can be non-negligible, but its effect on the detection efficiency is often small because the overall detection efficiency is already close to unity [108].

Following an electron-capture process, a vacancy is created in the atomic shell of the daughter

atom. Subsequent relaxation leads to emission of Auger electrons and characteristic X rays; emitted X and γ rays may also generate secondary electrons in the scintillator via photon interactions. Consequently, calculating the detection efficiency of EC radionuclides requires replacing the continuous β spectrum with an inventory of emitted Auger electrons and of secondary electrons produced by photon transport and interaction. In practice, Monte Carlo procedures are typically used to account for the contribution of X- and γ-ray interactions in the finite sample geometry. An overview of models used to compute counting efficiency for EC radionuclides is given in [11], and recent efforts toward higher-precision EC decay modelling are discussed in [109].

Except for pure β emitters, many decays are accompanied by photon emission. Low-energy X rays (typically a few keV) often deposit a large part of their energy within the scintillator [11]. However, because the scintillator response is non-linear, the partition of photon energy among secondary electrons matters. For example, if a photon transfers its full energy E to a single electron, the light-yield contribution scales as $EQ(E)$, which can differ from the case in which the same energy is shared between two electrons contributing $E_1Q(E_1) + E_2Q(E_2)$ with $E = E_1 + E_2$. For higher energy photons, photon escape and Compton scattering becomes more probable, the deposited-energy fraction decreases, and the probability of photon escaping without interaction increases.

The deposited energy distribution and photon interaction probabilities in the scintillation cocktail can be computed using Monte Carlo transport code. The dimensions of the sample must be included as they affect the absorption probability and escape fraction for photons. Finally, photon-transport simulations should also include interactions in the immediate surroundings of the sample, since backscattered photons or electrons can contribute to the detected signal [11].

2.4.4 The Triple-to-Double Coincidence Ratio method

The Triple-to-Double Coincidence Ratio (TDCR) method is a primary liquid scintillation technique based on the free-parameter model and a dedicated three-PMT counter. By exploiting the relationship between the measured coincidence counting rates and the corresponding detection efficiencies, the method enables activity determination without the need for calibration against an external radioactive standard. A historical overview and practical implementations of TDCR counting are discussed in [94]. Typical TDCR counter design have been reported, for example, by Cassette and Vatin [110]. The correct application of the TDCR method also requires dedicated acquisition electronics capable of applying a well-defined coincidence resolving time, recording the relevant coincidence channels, and imposing a the dead time. In most TDCR systems, an extendable dead time is applied after each accepted event. During this interval, additional pulses are rejected and, if they occur before the end of the interval, the dead time is extended.

For precise activity determination, it is not sufficient only to define the dead-time base duration. This is usually achieved by recording both the real time and the live time of the acquisition, so that the counting rates can be calculated for the live measuring time. The best method for recording the live-time is in using a live-time clock: short pulses (a few ns duration) are generated from a reference oscillator and these pulses are sampled by the dead-time signal. The number of surviving pulses gives the live-time of the measurement, without requiring cumbersome calculations, as this is the case when using fixed dead-time. Accurate determination of the live time is essential, because this directly affect the measured double- and triple-coincidence rates used in the TDCR efficiency calculation. Even small errors in the

dead-time correction can therefore propagate into the calculated activity, especially at higher counting rates.

Widely used implementations of the acquisition electronics include the MAC3 module [111], while later developments include the PTB 4KAM [112] which is an implementation of the MAC3 logic in a FPGA, compact systems such as nanoTDCR [113], and digital approaches based on CAEN digitizers [114]. In all cases, the minimum requirement is the ability to record the three double-coincidence counting rates (AB, BC, AC) and the triple-coincidence counting rate T for the application of the TDCR method.

For a three-PMT system ($R = 3$), the coincidence efficiencies can be calculated by combining the appropriate counting probability $P(E, \lambda)$ (see Table 2.1) with the deposited energy spectrum $S(E)$ through Equation (2.39). Assuming identical PMTs, the efficiencies for the double-coincidence channel and for triple coincidences are given by [11]:

$$\varphi_2 = \int_0^{E_{max}} S(E) \left(1 - e^{-\bar{n}/3}\right)^2 \mathrm{d}E = \int_0^{E_{max}} S(E) \left(1 - e^{-\lambda E Q(E)/3}\right)^2 \mathrm{d}E\,, \tag{2.44}$$

$$\varphi_T = \int_0^{E_{max}} S(E) \left(1 - e^{-\bar{n}/3}\right)^3 \mathrm{d}E = \int_0^{E_{max}} S(E) \left(1 - e^{-\lambda E Q(E)/3}\right)^3 \mathrm{d}E\,, \tag{2.45}$$

where E_{max} is the maximum charged particle energy, $Q(E)$ is the ionization-quenching function (Equation (2.19)), and λ is the free parameter.

For activity determination it is convenient to use the logical sum of the double coincidences, whose efficiency is [11]:

$$\varphi_D = \int_0^{E_{max}} S(E) \left[3\left(1 - e^{-\lambda E Q(E)/3}\right)^2 - 2\left(1 - e^{-\lambda E Q(E)/3}\right)^3\right] \mathrm{d}E\,. \tag{2.46}$$

The logical sum of the double coincidences is defined as [11]:

$$D = AB \vee BC \vee AC\,, \tag{2.47}$$

and can be expressed in terms of the measured double- and triple-coincidence counting rates as [11]:

$$D = AB + BC + AC - 2\,T\,. \tag{2.48}$$

For identical PMTs, the TDCR observable is the ratio T/D, which converges (for a sufficient number of recorded pulses) toward the ratio of efficiencies φ_T/φ_D which is the ratio of probabilities of detection. This ratio can be written as [11]:

$$\frac{\varphi_T}{\varphi_D} = \frac{\int_0^{E_{max}} S(E) \left(1 - e^{-\lambda E Q(E)/3}\right)^3 \mathrm{d}E}{\int_0^{E_{max}} S(E) \left[3\left(1 - e^{-\lambda E Q(E)/3}\right)^2 - 2\left(1 - e^{-\lambda E Q(E)/3}\right)^3\right] \mathrm{d}E}\,. \tag{2.49}$$

Thus, the experimentally determined ratio T/D provides an estimate of φ_T/φ_D, while the right-hand side can be evaluated once $S(E)$ is specified and a value for the ionization-quenching parameter kB is assumed. Solving Equation (2.49) yields the free parameter λ, which can then be used to calculate the coincidence efficiencies (e.g. φ_D) required for activity determination.

In practical TDCR counters, the assumption of identical PMTs is not strictly satisfied. To account for inter-channel differences, three independent efficiency-ratio equations are solved

using the three measured coincidence ratios T/AB, T/BC, and T/AC [11]:

$$\frac{\varphi_T}{\varphi_{AB}} = \frac{\int_0^{E_{\max}} S(E)\left(1-e^{-\lambda_A EQ(E)}\right)\left(1-e^{-\lambda_B EQ(E)}\right)\left(1-e^{-\lambda_C EQ(E)}\right)\mathrm{d}E}{\int_0^{E_{\max}} S(E)\left(1-e^{-\lambda_A EQ(E)}\right)\left(1-e^{-\lambda_B EQ(E)}\right)\mathrm{d}E},$$

$$\frac{\varphi_T}{\varphi_{BC}} = \frac{\int_0^{E_{\max}} S(E)\left(1-e^{-\lambda_A EQ(E)}\right)\left(1-e^{-\lambda_B EQ(E)}\right)\left(1-e^{-\lambda_C EQ(E)}\right)\mathrm{d}E}{\int_0^{E_{\max}} S(E)\left(1-e^{-\lambda_B EQ(E)}\right)\left(1-e^{-\lambda_C EQ(E)}\right)\mathrm{d}E}, \tag{2.50}$$

$$\frac{\varphi_T}{\varphi_{AC}} = \frac{\int_0^{E_{\max}} S(E)\left(1-e^{-\lambda_A EQ(E)}\right)\left(1-e^{-\lambda_B EQ(E)}\right)\left(1-e^{-\lambda_C EQ(E)}\right)\mathrm{d}E}{\int_0^{E_{\max}} S(E)\left(1-e^{-\lambda_A EQ(E)}\right)\left(1-e^{-\lambda_C EQ(E)}\right)\mathrm{d}E},$$

where λ_A, λ_B and λ_C are the figures of merit of the individual PMT channels and $\lambda = \lambda_A + \lambda_B + \lambda_C$. For sufficiently large counting statistics, the experimental ratios converge toward the corresponding efficiency ratios, and the system Equation (2.50) can be solved numerically. A common approach is to determine $(\lambda_A, \lambda_B, \lambda_C)$ by minimizing [11]:

$$\Delta = \left(\frac{\Phi_T}{\Phi_{AB}} - \frac{T}{AB}\right)^2 + \left(\frac{\Phi_T}{\Phi_{BC}} - \frac{T}{BC}\right)^2 + \left(\frac{\Phi_T}{\Phi_{AC}} - \frac{T}{AC}\right)^2, \tag{2.51}$$

for example using the Downhill Simplex algorithm [115].

Once the figure-of-merit parameters are determined for a given kB value, the coincidence efficiencies can be computed (e.g. φ_D), and the activity is typically obtained from the logical sum of the double coincidences as

$$A = \frac{D}{\varphi_D(kB, \lambda_A, \lambda_B, \lambda_C)}. \tag{2.52}$$

For pure β emitters, the minimization problem associated with Equation (2.51) generally yields a single physically relevant solution. For electron-capture radionuclides or β–γ radionuclides, multiple solutions can occur, and the counting efficiency is therefore varied experimentally to identify the correct branch of the efficiency curve corresponding to the measured TDCR value.

Finally, it should be emphasized that the TDCR efficiency calculation depends on the choice of the ionization-quenching parameter kB, which is the main adjustable parameter in the standard implementation of the model. For high-energy β emitters (typically above a few hundred keV), the detection efficiency is close to unity and the influence of kB is small. In contrast, for low-energy β emitters such as ^{3}H, the efficiency is strongly dependent on kB (Fig. Figure 2.10), making a robust kB determination essential for accurate standardization. Consequently, reliable TDCR measurements require not only an appropriate counter design, but also well-controlled vials, acquisition logic, and data-analysis procedures.

2.4.5 Practical considerations of the TDCR method

The practical implementation of the TDCR method requires careful control of both the LS sample (in particular the vial, cocktail stability and optical coupling) and the detection system

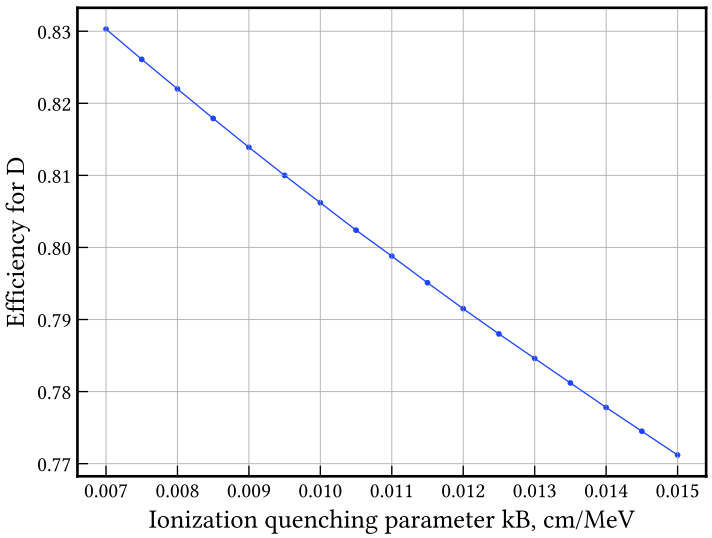

Figure 2.10: Dependence the detection efficiency for ^{3}H in toluene-base cocktail as a function of the kB parameter while other parameters are the kept the same.

(PMTs, coincidence logic, and dead-time handling), as these factors directly influence the counting statistics and the validity of the assumptions underlying the efficiency model.

Liquid scintillation vials

Liquid scintillation vials are designed to safely enclose the radioactive sample and the scintillation cocktail while providing stable optical conditions during measurement. The most widely used vials are either plastic (polyethylene or PTFE-coated polyethylene to reduce absorption in the walls) or glass (standard or low-potassium borosilicate) with a nominal volume of 20 mL. Plastic vials typically provide higher apparent light-collection efficiency than clear glass because their diffusive walls reduce total internal reflection and promote more uniform photon escape toward the optical chamber [116]. This advantage is partly offset by increased light absorption in plastic and by diffusion of cocktail components into the vial walls, which may affect long-term stability.

Glass vials offer superior chemical compatibility and lower permeability, but due to the refractive-index mismatch between glass and air, a fraction of the scintillation light can be trapped by total internal reflection. This reduces the detected light yield and, importantly, can introduce position dependence: light emitted closer to the vial wall may be more strongly affected. Such effects conflict with the fundamental assumption that the number of photons reaching each PMT photocathode is Poisson-distributed with a position-independent same mean over the sample volume. To mitigate total internal reflection in glass vials, the outer surface can be made diffusive (e.g. by chemical or mechanical etching) or, more simply, by wrapping the vial with diffusive adhesive tape [11].

Liquid scintillation counters

For low-energy β emitters, the scintillation light yield per decay is small, and reliable counting therefore requires optimized optical transport and sensitive photodetectors. Photomultiplier tubes remain the preferred choice because they offer high gain, low noise, and quantum efficiencies typically in the range 20–40% [67]. In TDCR counting, the PMTs must exhibit non-

zero sensitivity to single photons; in practice, this requires that the single-photoelectron peak be sufficiently separated from electronic noise so that discriminator thresholds can be set to reject noise while retaining essentially all single-photoelectron pulses. This is facilitated by PMTs with high gain and a favorable peak-to-valley ratio in the single-photoelectron spectrum [117].

A further stringent requirement is imposed on the acquisition electronics. Scintillation light pulses are typically only a few nanoseconds long, and the readout must implement coincidence logic with a well-defined coincidence resolving time. The selection of an appropriate coincidence resolving time is non-trivial and has been examined in several recent studies [18, 118, 119]; it is also discussed in Chapter 8. In addition, the electronics must reliably handle noise and correlated late pulses (e.g. afterpulses) in a way consistent with the chosen counting logic.

In radionuclide standardization by LS counting, it is common practice to apply a dead-time after each detected event in order to suppress spurious coincidences arising from thermal emission, afterpulses, and delayed scintillation. The dead-time base duration is typically a few microseconds. Accurate estimation of the real dead time of the measurement is particularly important for decay chains containing short-lived daughters. For example, in the ^{222}Rn decay chain, a significant fraction of ^{214}Po decays (half-life 164 μs) may occur during the dead-time following the decay of its parent, effectively reducing the detection efficiency unless corrected. A comparison of two common implementations—common dead time (CDT), where any pulse triggers dead time in all channels, and individual dead times (IDT), where dead time is applied only to the channel that fired—showed excellent agreement between the two logics based on experimental data and Monte Carlo simulations [120].

The PMTs are typically arranged symmetrically around the vial inside a reflective optical chamber. The consistency of the acquisition logic can be verified using the balance relations [94]:

$$A + B + C = T + D + S\,, \tag{2.53}$$

$$AB + BC + AC = 2T + D\,, \tag{2.54}$$

where A, B, and C are the single-channel counting rates, AB, BC, and AC are the double-coincidence counting rates, T is the triple-coincidence counting rate, D is the logical sum of the doubles, and S is the logical sum of the non-coincident singles. To evaluate these relations and to apply the TDCR method, the acquisition system must be able to record A, B, C, S, AB, BC, AC, D, and T. Agreement with Equation (2.54) provides a useful diagnostic that the coincidence logic and channel bookkeeping are implemented correctly [94].

Efficiency calculation code

Applying the TDCR model in practice requires numerical integration of Equation (2.50) together with Equation (2.19), calculation of electron stopping power, and minimization of Equation (2.51). A dedicated computer program developed by P. Cassette has been widely used for this purpose. In this work, the *TDCR18* code was used to determine the figure-of-merit parameters and the detection efficiencies for β-emitting radionuclides measured with a TDCR counter. The main features of the program include:

- scintillation emission following Poisson statistics, consistent with Equation (2.35);
- scintillator non-linearity described by Birks' formula Equation (2.19);
- electron stopping power computed using ICRU Report №37 (Equation (2.22)) above 100 eV,

with linear extrapolation below 100 eV; alternatively, stopping-power estimates by Tan and Xia [121] may be used for relevant scintillators;

- β spectra computed internally using SPEBETA [103] or imported as an external normalized spectrum.

The program requires the radionuclide atomic data, the scintillator density and Z/A ratio, and the range of kB values for which the calculation is performed. A particularly useful option is the use of the three experimental ratios (T/AB, T/BC, T/AC), which accounts for channel asymmetry. The outputs include the detection efficiency of the logical sum of the doubles, ε_D, the triple-coincidence efficiency, ε_T, and estimates of the relative PMT quantum efficiencies. In addition, many calculation codes were developed in National Metrology institutes, like the MICELLE code at CIEMAT and PTB [122], and others codes using Mathematica, C++ and Root and in-house Python scripts for TDCR applications and kB variation in SU [123]. A Python-based TDCR efficiency calculation tool is now maintained by the Bureau International des Poids et Mesures (BIPM) [124].

Efficiency variation method

The efficiency variation method is the standard metrological approach for determining kB in TDCR-based standardization, particularly for low-energy β emitters such as ^{3}H, where the calculated efficiency is strongly dependent on kB. For higher-energy emitters, the efficiency is closer to unity and the accurate activity calculation is not strongly dependent on the kB parameter. Efficiency variation techniques also provide a practical means of resolving ambiguities that can arise when a single TDCR value corresponds to more than one possible counting efficiency, as may occur for certain electron capture or β-γ radionuclides. By deliberately changing the detection efficiency and observing the corresponding evolution of the TDCR value, it becomes possible to identify the relevant region of the efficiency curve associated with the experimental measurement.

For a correctly modelled system, the activity estimate should be invariant under changes in detection efficiency. This principle motivates the *efficiency variation* approach: the counting efficiency is deliberately reduced in a controlled manner and the activity is recalculated for a range of kB values. The kB is determined as the value that minimizes the variation of the calculated activity across the set of measurements.

In practice, efficiency variation is commonly achieved by: defocusing the PMTs, introducing chemical quenchers into the cocktail, or placing coaxial gray filters over the vial. Because a properly designed counter operates near maximum efficiency under nominal conditions, these methods act primarily in one direction, i.e. they decrease the efficiency. Comparative studies have shown good overall agreement between these approaches [98], although differences between chemical quenching and gray-filter methods have also been reported [119]; the applicability of PMT defocusing is discussed in Section 3.1.10.

Accidental coincidence correction

In TDCR/LSC coincidence counting, *accidental (random) coincidences* are events where pulses from unrelated origins (different decays, background, PMT dark noise, or electronics) fall within the coincidence resolving time and are therefore registered as a coincidence. For two uncorrelated channels with rates N_1 and N_2 and resolving time (τ), the basic accidental rate is ($N_a = 2\tau N_1\, N_2$) [18].

In [18], two complementary correction approaches were described. The *experimental* (list-mode) correction method uses the time-delay distribution between the first ("primary") pulses in the PMT channels. The measured distribution is treated as a sum of a true-coincidence component concentrated at short delays and an accidental component that dominates at long delays. By fitting the tail of the delay distribution in a region where true coincidences are negligible (e.g., 2000–2500 ns), one estimates the accidental background level and integrates it over the resolving time to obtain the accidental contribution for each coincidence channel.

In the implementation of the *analytical* correction, first the "pure" counting rates are reconstructed by removing overlaps between coincidence channels: for a three-PMT TDCR system this involves estimating the pure singles (P_A, P_B, P_C) and pure coincidences (P_{AB}, P_{BC}, P_{AC}) from the measured channels. The accidental rate is then computed by summing contributions of two kinds [18]:

- type-1: if an uncorrelated P_C happens and, within τ, an uncorrelated P_A happens, then the electronics sees A and C within one coincidence window and registers an AC coincidence
- type-2: they occur when an event of the channel that is corrected (e.g. P_{AB} when correcting the AB channel) is recorded inside a coincidence window that was opened by some other uncorrelated channel. For example P_C starts the window and then a P_{AB} event arrives; the P_{AB} contributes to the measured AB rate, but it is "accidental" because the window was started by an unrelated decay.

For the analytical method, the required inputs are the single/double/triple counting rates, the resolving time (τ), and the detector dead-time logic. The experimental method additionally requires list-mode timing information (typically via a fast digitizer/FPGA acquisition) to build and fit the time-delay distributions. The importance of this correction has been well acknowledged by the LS metrology community and its application is becoming a standard practice [118, 86].

2.5 The Compton coincidence method

Compton-coincidence spectrometers were developed to investigate scintillator non-linearity by measuring the light output produced by Compton electrons of known energy [13, 125]. In such measurements, monoenergetic photons interact in the scintillator and produce recoil electrons by Compton scattering. The main motivation of this approach is to determine the scintillator response as a function of electron energy directly from experiment, rather than relying only on semi-empirical descriptions such as Birks model. The measured response can then be fitted by this model in order to determine quenching parameter. Compton-coincidence techniques have been widely applied to inorganic scintillators [125, 126, 127, 128], and analogous measurements have also been performed for liquid scintillators [13, 14].

The central concept is to expose the scintillator to a collimated monoenergetic γ-ray beam and to detect, in coincidence, both the scintillation signal and the scattered γ ray, as shown in Figure 2.12. For low-Z organic media and for the photon energies typically employed, Compton scattering is the dominant interaction. If the energy of the incident photon is E_γ and the scattered photon is emitted at an angle θ, its energy is given by the Compton relation:

$$E'_\gamma = \frac{E_\gamma}{1 + \frac{E_\gamma}{m_e c^2}(1 - \cos\theta)}, \tag{2.55}$$

where $m_e c^2$ is the electron rest energy. The kinetic energy of the Compton electron is therefore:

$$E_e = E_\gamma - E'_\gamma. \tag{2.56}$$

By measuring the energy of the scattered photon with a γ detector, the energy deposited by the Compton electron in the scintillation cocktail can be calculated.

The choice of the γ-ray energy is important because the expected non-linearity of the liquid scintillator response is most pronounced at low electron energies, particularly below about 20 keV. Therefore, low-energy monoenergetic γ-ray sources are required. In this work, ^{241}Am is used because its 59.54 keV γ ray produces Compton electrons in the 3–6 keV region for scattering angles around 90°.

The angular distribution of Compton scattering is described by the Klein–Nishina differential cross section:

$$\frac{d\sigma}{d\Omega} = \frac{r_e^2}{2}\left(\frac{E'_\gamma}{E_\gamma}\right)^2\left[\frac{E'_\gamma}{E_\gamma} + \frac{E_\gamma}{E'_\gamma} - \sin^2\theta\right], \tag{2.57}$$

where r_e is the classical electron radius. The angular dependence calculated from Equation (2.57) is shown in Figure 2.11. For the 59.54 keV photons emitted by ^{241}Am, the scattering probability at intermediate and large angles is still appreciable. This contrasts with higher-energy γ rays, for which Compton scattering becomes increasingly forward oriented. The Compton-TDCR geometry therefore takes advantage of this property by detecting photons scattered near 90°. In this configuration, the corresponding Compton electrons have sufficiently low energy to measure in the non-linear response region, while still producing enough scintillation light to be detected by the TDCR channel.

Selecting a narrow region of interest (ROI) in the scattered-γ spectrum defines a narrow interval of Compton-electron energies. This provides an approximately monoenergetic electron probe, whose energy can be changed by the ROI definition, enabling a direct mapping of scintillation response as a function of deposited energy.

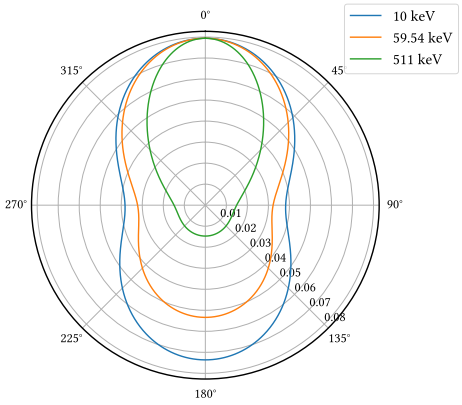

Figure 2.11: Klein–Nishina differential cross section in b sr^{-1} as a function of the scattering angle for selected incident γ-ray energies. For the 59.54 keV photons emitted by ^{241}Am, scattering at intermediate and large angles remains significant compared with higher-energy photons, for which the angular distribution is more strongly forward directed.

Early Compton-scattering spectrometers for liquid scintillators employed a single PMT to record the scintillation pulse-height spectrum in coincidence with the γ detector. Subsequently, a TDCR counter was introduced as a scintillation channel [15]. More recently, compact Compton-TDCR system has been used to study both light-yield non-linearity and timing properties of commercial liquid scintillators, as well as plastic and inorganic scintillators [16]. A key advantage of a TDCR-based scintillation channel is that it allows the mean number of detected

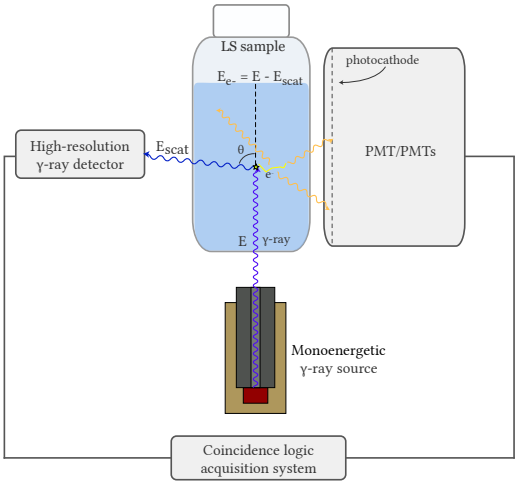

Figure 2.12: Scheme of a Compton-coincidence system, in which the energy deposited by the electron in the scintillation cocktail is determined from the measured energy of the scattered γ ray.

photoelectrons to be determined directly for a given Compton electron energy, provided that the PMTs are operated with single-photon sensitivity.

If the thresholds of all PMTs are adjusted to allow single photon sensitivity, the detection probability of a light pulse emitted after the absorption of energy in the scintillator can be derived from the calculation of the non-detection probability. For an energy deposition E producing, on average, $\bar{m}$ scintillation photons, the detection probability in PMT X is [15]:

$$p_X = 1 - e^{\left(-\frac{\varepsilon_X \bar{m}}{3}\right)}, \qquad X = A,\ B,\ C, \tag{2.58}$$

where ε_X denotes the quantum efficiency of a given PMT X, and $\bar{n}_X = \varepsilon_X \bar{m}$ is the corresponding mean number of detected photoelectrons. Assuming no correlation between the PMTs, the double- and triple-coincidence efficiencies are then [15]:

$$p_{XY} = \left(1 - e^{\left(-\frac{\varepsilon_X \bar{m}}{3}\right)}\right)\left(1 - e^{\left(-\frac{\varepsilon_Y \bar{m}}{3}\right)}\right), \qquad XY = (AB,\ BC,\ AC), \tag{2.59}$$

$$p_T = \prod_{X=A,B,C}\left(1 - e^{\left(-\frac{\varepsilon_X \bar{m}}{3}\right)}\right). \tag{2.60}$$

For sufficiently large counting statistics, the measured ratios of coincidence counting rates approach the corresponding efficiency ratios. In particular, for a given double coincidence XY, the ratio T/XY estimates the single-channel detection probability of the remaining PMT Z (with $Z = C$ for $XY = AB$, $Z = B$ for $XY = AC$, and $Z = A$ for $XY = BC$). Hence, the mean number of detected photoelectrons in channel Z can be written as [15]

$$\bar{n}_Z = -3\ln\left(1 - \frac{p_T}{p_{XY}}\right) \approx -3\ln\left(1 - \frac{T}{XY}\right), \qquad Z \in \{A, B, C\}. \tag{2.61}$$

This approach implicitly assumes that, independent of where the Compton interaction occurs within the vial, the optical transport leads to identical photon sharing among the PMTs. In clear glass vials, this assumption may be compromised by total internal reflection and position-dependent light-collection effects. The assumption is better fulfilled when diffusive vials are used, when the vial walls are wrapped with diffusive material.

The method is most informative when the system is not saturated (i.e. when coincidence efficiencies are well below unity). This condition is typically fulfilled in the low-energy regime,

which is particularly valuable because scintillator non-linearity is most pronounced there. In this context, Cassette and Do [15] proposed using the Compton-TDCR approach to determine the scintillator non-linearity as a function of deposited energy and to incorporate this experimentally derived response into TDCR analyses. This replaces the Birks equation by a purely parametric description and eliminates the need of adjusting the kB arameter, which is a major source of uncertainty for low-energy radionuclides. Building on this concept, Bignell *et al.* [17] proposed the *Zero Model by Using Coincidence Scintillation (ZoMBieS)* method.

The Compton spectrometer efficiency tracing (CSET) method uses the same setup. Events in a ROI in the γ spectrum are recorded in coincidence with the LS double coincidences, and the Compton electron energy is derived from the spectrum of the scattered Compton photons. The intrinsic figure of merit is solved for that specific source, then the external source is removed, and the detection efficiency for the relevant radionuclide is calculated from this FOM. The method is less dependent on the kB value than TDCR method because the Birks formula is applied twice, and it requires no radioactive standard . The CSET method is similar in principle to the CIEMAT/NIST method but offers several advantages: the characterization is done with the source itself rather than a separate tracer, no radioactive standard is needed, and moderate changes in the external γ-source geometry do not affect the result [15].

The *Zero Model by Using Coincidence Scintillation* method is an absolute activity measurement technique that avoids assuming a specific scintillation-response or PMT-efficiency model (hence the term "zero model"). It is based on a Compton-coincidence configuration in which a TDCR counter is operated in coincidence with an γ detector to measure the energy of monoenergetic Compton-electron energy deposits in the scintillator. For a given energy, the ratio of the triple-coincidence rate T to a selected double-coincidence rate XY approaches the detection probability of the remaining PMT Z, i.e. $T/XY \rightarrow \varepsilon_Z$, thereby providing an experimental estimate of the single-channel detection efficiency as a function of deposited energy. Repeating this procedure over multiple γ energy ROIs yields an efficiency–versus–electron energy curve spanning the measurable Compton electron range. The resulting efficiency curve is then parameterized (using an 'arbitrary' function) and integrated over the β-spectrum of the radionuclide of interest to obtain the corresponding detection efficiency. The activity is finally determined directly from the measured count rate and the calculated efficiency, without introducing a dedicated light-yield (e.g. Birks) model or assuming a Poisson distribution of the photoelectrons.

3 Studies of PMTs photocathode response non-uniformity

The influence of photon detection efficiency (PDE) non-uniformity on the TDCR method is connected with several assumptions underlying the TDCR efficiency calculation. The TDCR method presupposes that the scintillator emits photons following a Poisson distribution, that single-photon detection occurs with non-zero probability, and that the scintillation light yield as a function of deposited energy follows Birks' law, characterized by the non-linearity constant kB [11].These assumptions inherently depend on additional, often implicit, conditions: the photodetectors exhibit uniform sensitivity across their active surfaces; the likelihood of detecting individual photons is identical at every point of the photocathode; and the non-linearity model applies solely to the prompt component of the scintillation emission [1]. To assess the validity of the first two implicit conditions, we conducted an investigation of the spatial response uniformity of some PMT photocathodes used in TDCR systems.

In our previous work at the MIL laboratory, measurements with a plastic scintillator revealed a position dependence of the energy resolution [129]. This finding motivated the development of a manually operated scanning system, which was used to map the photocathode response of the Hamamatsu R7600U-200 and H11934-203 PMTs [130]. Although the manual operation limited the number of measurement points, the study demonstrated that the PDE can vary substantially with the position on the photocathode and that the response pattern depends on the dynode structure. Furthermore, the impact of photocathode non-uniformity on the energy resolution of plastic scintillators was investigated more systematically, and a position-dependent effect on pulse-shape discrimination was also observed. These results were the motivation for developing an automated scanning system capable of mapping the full PMT window. The next section describes this system and presents the corresponding results for PMTs used in TDCR counters for primary activity measurements.

3.1 Automatic system for scanning the photocathode non-uniformity

The setup used to map the photocathode spatial response is shown schematically in Figure 3.1. It includes a custom-built LED pulser (see Figure 3.2) a holder for calibrated neutral-density (ND) filters (Thorlabs NDK01), used to adjust the light intensity, and a fiber collimator coupled to a 200 μm-core multimode optical fiber. The scanning stage is a custom motorized assembly that translates the fiber across the PMT window. Motion is provided by a x-y mechanics driven by stepper motots and controlled by a commercial microcontroller board (Arduino Uno with a CNC shield). The minimum step is effectively limited by the fiber diameter, and the usable scan area is $3.6 \times 3.2\,\mathrm{cm}^2$.

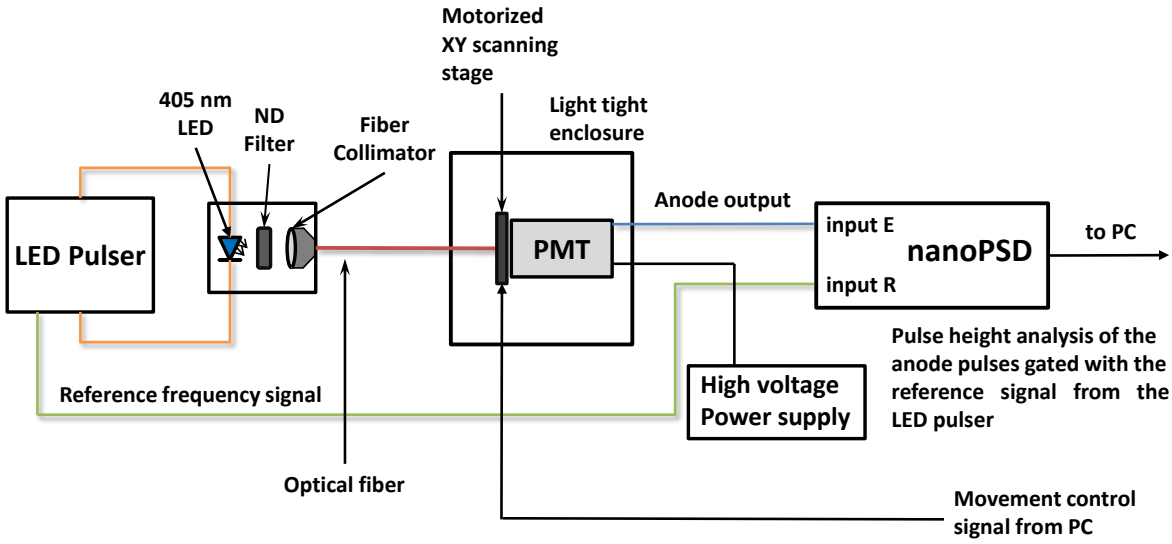

Figure 3.1: Schematic of the experimental setup employed to characterize the spatial non-uniformity of the PMT photocathode response [131].

The fiber collimator directs the LED light into one end of the optical fiber, while the opposite end is positioned at about 1 mm off the PMT window. The wavelength of the LED in the pulser (Figure 3.2) is 405 nm. The LED is driven by a fast-switching signal with a frequency of 2.6 kHz, which can be controlled by a variable-frequency oscillator. The transistor driving the LED operates in avalanche mode, allowing a switching time constant of approximately 0.25 ns. The coincidence counting capability of the nanoPSD device [44] is used to analyze the PMT anode signal in coincidence with the reference frequency signal generated by the LED pulser. The acquisition time for each measurement point in all scans is set to 30 seconds.

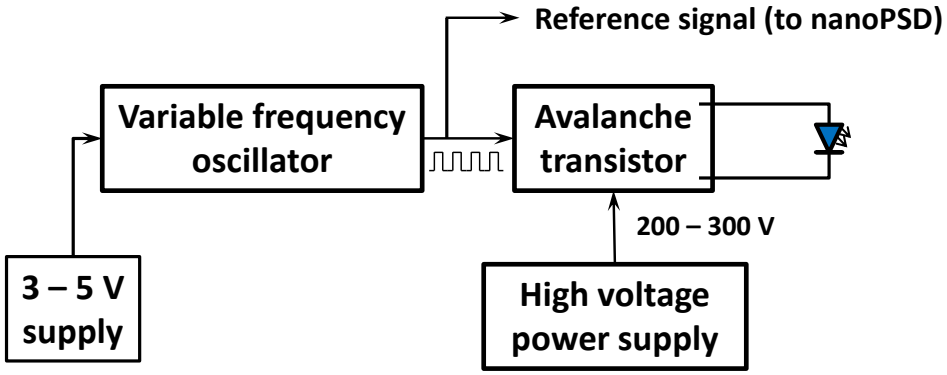

Figure 3.2: Schematic of the custom-built LED pulser used in the experimental setup [131].

The distribution of the light pulses from the generator (see Figure 3.3), as recorded by the photomultiplier tube, exhibits a Gaussian-shaped peak. The variation of the photocathode response with respect to the position of the light spot was evaluated using the centroid position obtained from fitting the light pulses peak, since the centroid position is proportional to the number of photoelectrons produced in the PMT per event. For each spectrum, the standard deviation was also determined and taken as an estimate of the uncertainty of the PMT response.

A photo inside the light tight box with a PMT and the scanning stage is shown in Figure 3.4. In addition to scanning the photocathode response, a TOPDON TC001 thermal camera [132]

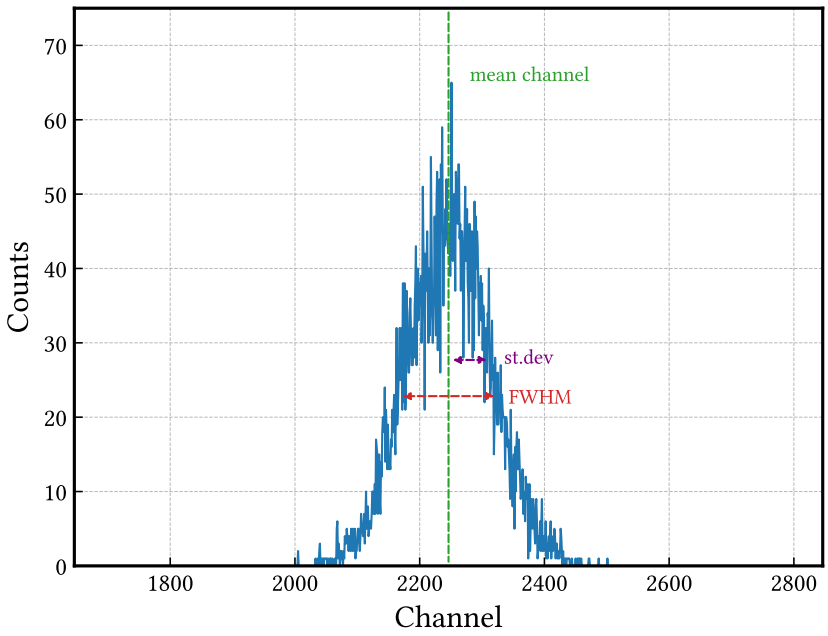

Figure 3.3: Experimental spectrum from the Hamamatsu R7600U-200 PMT, with the mean channel and standard deviation used to determine the PMT response and its uncertainty.

was employed to monitor the heat distribution generated by the PMT during operation. This device offers a resolution of 256 × 192 pixels, operates over a temperature range of -20 °C to 550 °C, and can detect surface temperature variations as small as 0.1 °C. Real-time visualization and data acquisition were performed via USB connection to a computer or through a dedicated mobile application.

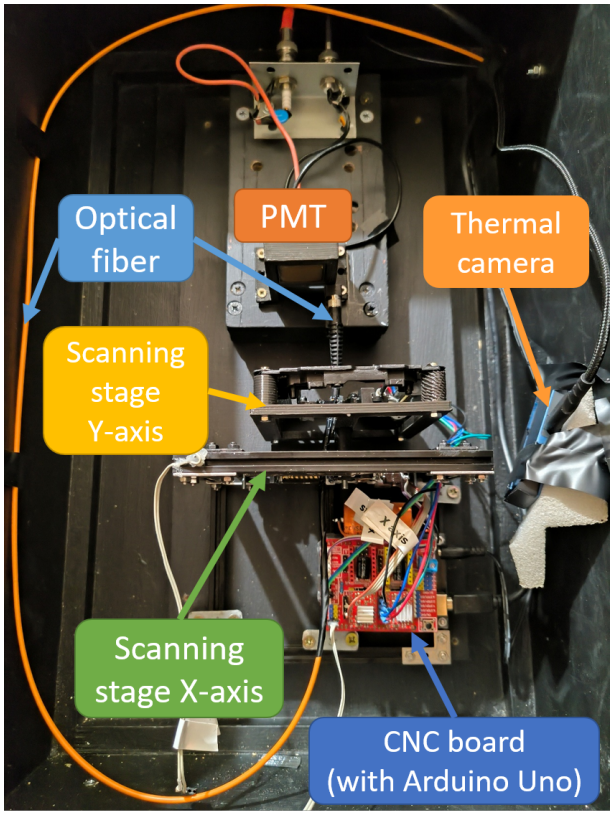

Figure 3.4: Photo of the scanning system with the PMT mounted in a holder and ready for scanning.

The spectra acquisition performed with the nanoPSD software and the motion control of the scanning system were coordinated by a custom script developed by P. Cassette. The script automated the measurement sequence by moving the scanning stage to predefined positions and triggering the corresponding spectrum acquisition at each point. A Python script was developed for the purposes of the thesis to batch process all nanoPSD spectra, compile the results into tabular form, and generate the corresponding figures.

During scanning, each PMT was securely positioned in a dedicated holder. For circular PMTs exceeding the available scanning area, the scan was conducted in four quadrants. After completing one quadrant, the PMT was rotated by 90°, and the process was repeated until all four quadrants were scanned. The boundaries of each quadrant were manually marked at their outer midpoints. However, this method introduces a limitation: the imperfections stemming from manual PMT repositioning after each rotation and marker placement accumulate, resulted in minor misalignments between the quadrants. These misalignments induce as artifacts along the central axes in the final composite image of the PMT.

3.1.1 Testing the scanning system

To evaluate the performance of the scanning system, an extended series of measurements was conducted at a fixed point on the photocathode of the Hamamatsu H11934 photomultiplier tube. Only during the testing of the system, each measurement lasted for five minutes. The parameters of the peak in the spectrum of the LED light-pulse generator (see Figure 3.3) were used to assess the temporal stability of the system. Figure 3.5 illustrate the time evolution of the LED peak centroid, the full width at half maximum (FWHM) of the peak, and the counting rate (s^{-1}), estimated as the peak area divided by the measurement duration.

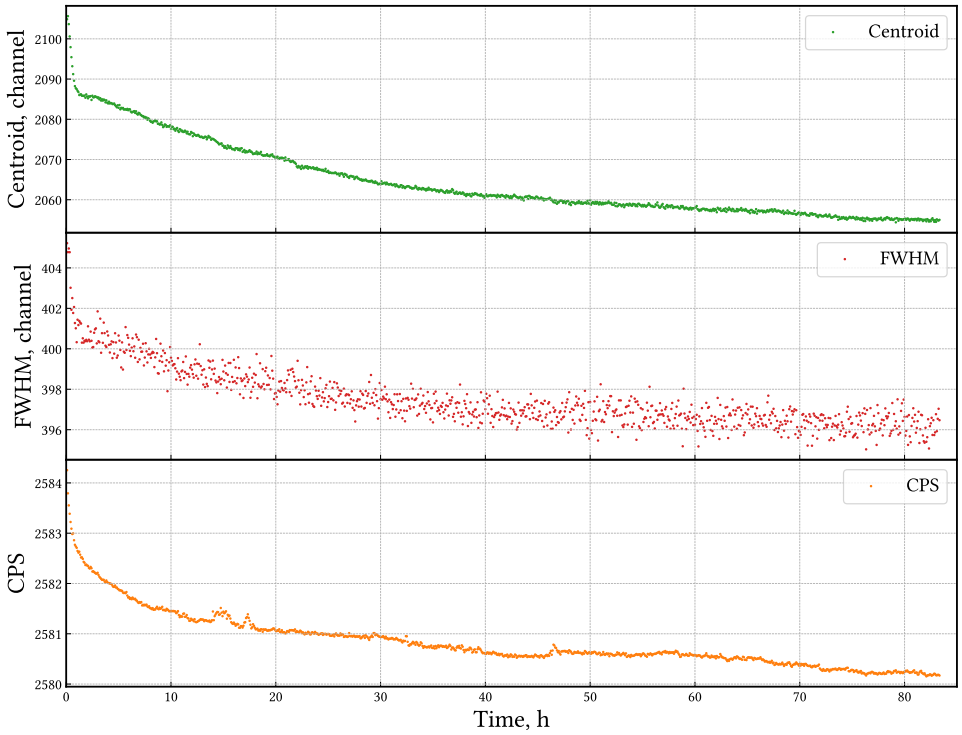

Figure 3.5: Time variation of the centroid, FWHM and the counting rate of the peak at a single point on the photocathode of a Hamamatsu H11934 PMT.

From the results presented in Figure 3.5, it can be seen that during the first few hours, the position of the peak centroid varies significantly. However, between the 40^{th} and 80^{th} hour, the variation is only about five channels. Despite the observed drift in the centroid position, this effect would not lead to a noticeable shift in the data when studying the non-uniformity of the photocathode response, since the measurement time at a single point on the photocathode is short.

Furthermore, the variations in the position of the LED peak centroid observed during scanning of the photocathode are considerably larger than the change of the centroid during the operation of the system. To ensure that the operating characteristics of the system remain stable between consecutive scans, the LED pulse generator was left running continuously.

From the variations in the FWHM of the peak and in the counting rate shown in Figure 3.5, we observed that, after the first few hours, the fluctuations in these parameters become smaller and remain nearly constant until the end of the measurement series.

The tests presented above indicate that the scanning system for studying the non-uniformity of the PMT photocathode response exhibits good temporal stability after the initial transient period. This stability supports reliable mapping of PMT photocathode non-uniformity and minimizes the risk of systematic bias in the measured response.

3.1.2 PMTs included in the study

Two of the scanned PMTs — the Hamamatsu R7600U-200 and Hamamatsu H11934-203 are compact, square PMTs featuring a borosilicate glass window, an ultra-bialkali photocathode, and a metal-channel dynode structure. The entrance windows of these PMTs are shown in Figures 3.6 (a) and 3.6 (b). A schematic cross-section of this PMT type is presented in Figure 3.6 (c), and the coordinate system used for the scans is shown in Figure 3.6 (d).

The other PMTs are circular, featuring bialkali photocathodes and linear-focused dynode structures. These include the Hamamatsu R9779 [133], the Hamamatsu R331-05 [134] — which has a frosted concave-convex borosilicate window — and the Philips XP2020Q [135], which has a fused silica window allowing transmission down to 160 nm. The high voltage applied to each PMT was either optimized for single-photon detection or set to the manufacturer's maximum recommended level: +850 V for the Hamamatsu R7600U-200, +1000 V for the Hamamatsu H11934-203, -1700 V for the Hamamatsu R9779, +1500 V for the Hamamatsu R331-05, and +2000 V for the Philips XP2020Q.

3.1.3 Automatic scan of the Hamamatsu R7600U-200

The automatic scan of the Hamamatsu R7600U shown in Figure 3.7 is an extension to the manual scan shown in [130] bringing a full scan of the photocathode response.

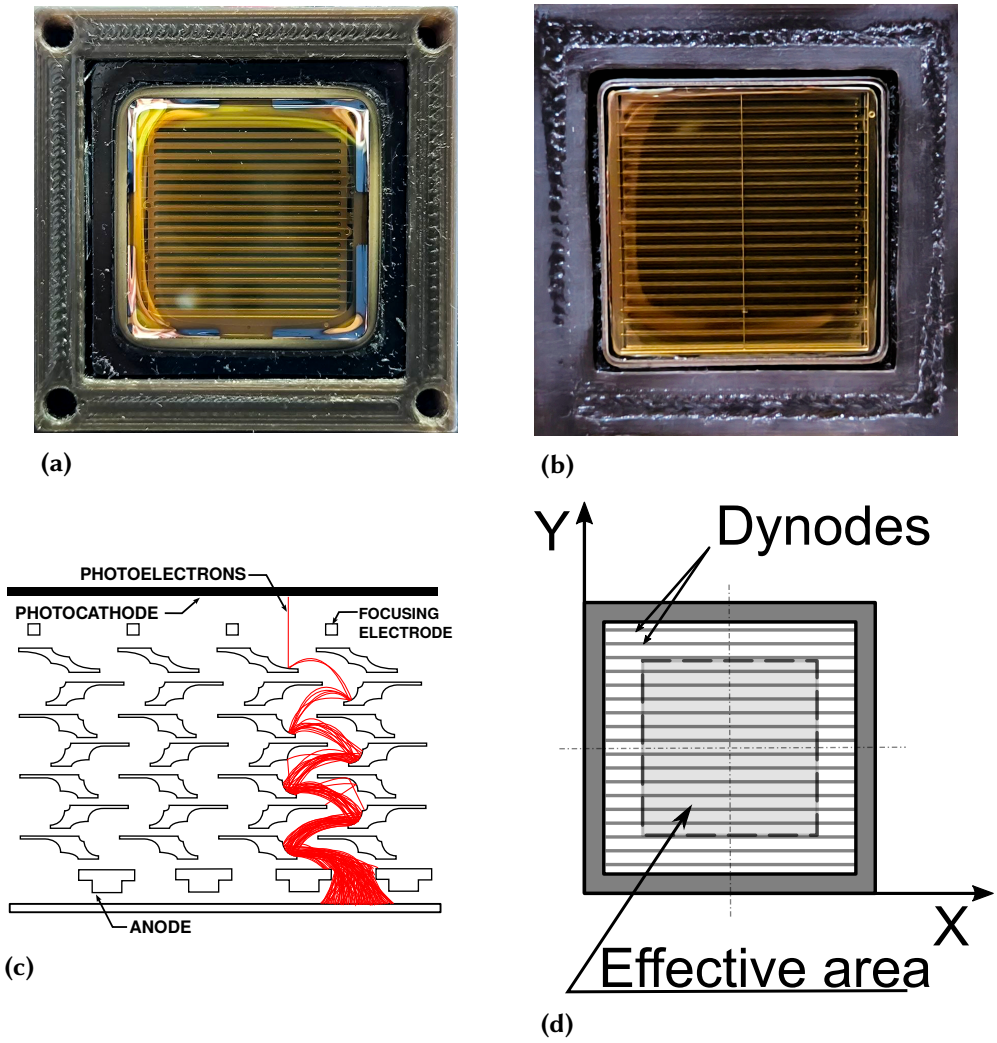

Figure 3.6: (a) Photograph of the entrance window of the Hamamatsu R7600U-200; (b) Photograph of the entrance window of the Hamamatsu H11934-203; (c) Cross-section of a metal-channel dynode structure [67]; (d) Coordinate system used for scanning the photocathode of the PMT [130].

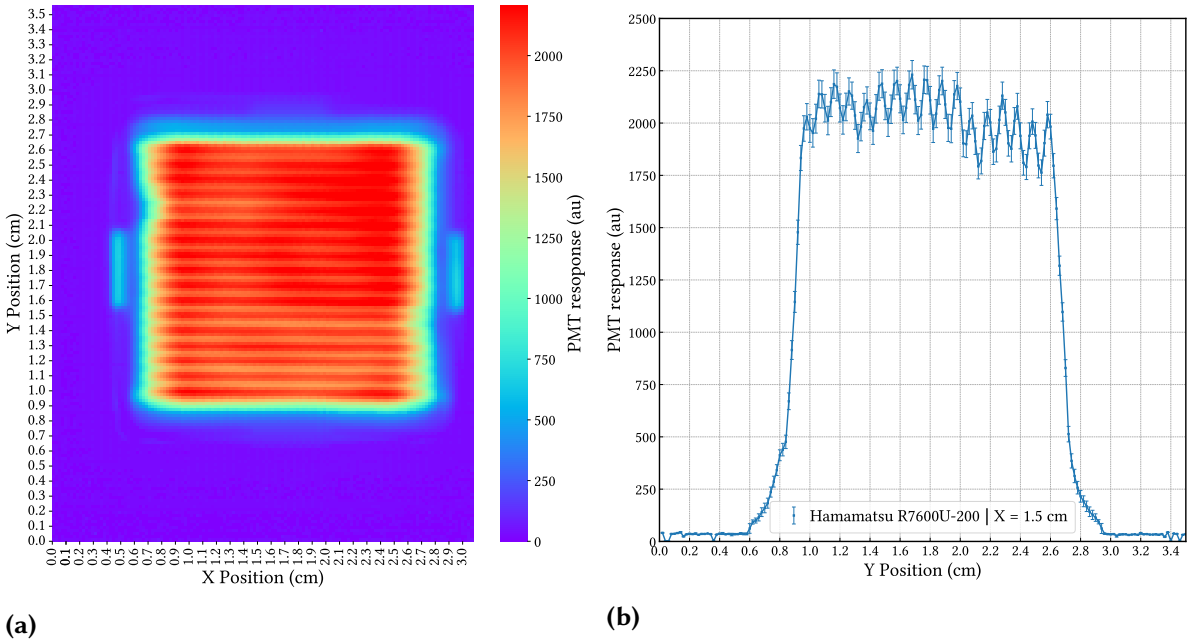

Figure 3.7: Photocathode response map of the Hamamatsu R7600U-200 PMT (a), and a cross-sectional profile along the Y-axis at X = 1.5 cm (b) [131].

The presented scan confirms the findings in [130] that the structural non-homogeneity spans across the whole PMT window and is probably due to the first dynodes. A brighter spot with higher quantum efficiency is present on the top right corner and could be due to a difference in the thickness of the photocathode layer. The cross-sectional profile shown in Figure 3.7 (b) reveals the influence of the dynode structure, manifested as peaks and valleys in the PMT response, with amplitudes of approximately 15% between the minimum and maximum values. The photocathode's effective area, specified by the manufacturer as $1.8 \times 1.8\,\mathrm{cm}^2$, spans from 0.8 to 2.6 cm along the X axis and from 0.9 to 2.6 cm along the Y axis. Given that the total window size of the PMT is $2.57 \times 2.57\,\mathrm{cm}^2$, the effective photocathode area comprises only about 49% of the window area.

The regions outside the effective area exhibit significantly reduced sensitivity to incident photons, which leads to degraded resolution in scintillation spectrometry [72, 129, 130] and a loss in counting statistics. This effect is particularly critical in applications that rely on high single-photon detection efficiency, such as TDCR counting.

3.1.4 Automatic scan of the Hamamatsu H11934-203

Building on and extending the studies reported in [130], the Hamamatsu H11934-203 PMT — previously characterized with the manual scanning system — was also mapped using the automated setup. The resulting scan are shown in Figure 3.8.

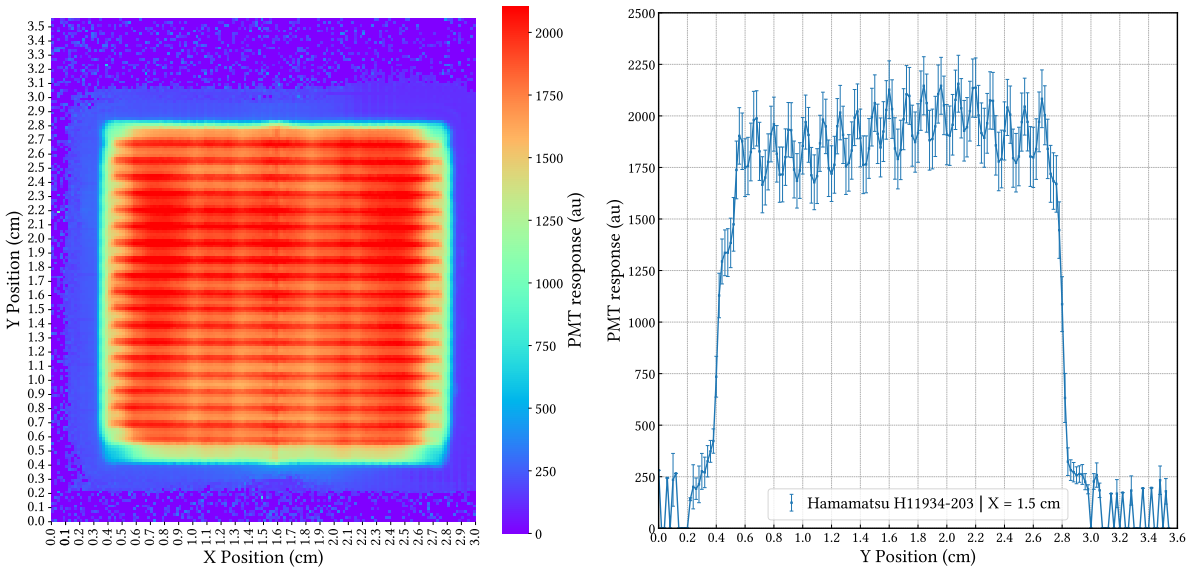

Figure 3.8: Photocathode response map of the Hamamatsu H11934-203 PMT (a), and a cross-sectional profile along the Y-axis at X = 1.5 cm (b) [131].

Based on the scan, the effective area of the H11934 PMT was found to be approximately $2.3 \times 2.3\,\mathrm{cm}^2$, consistent with the specifications provided by the manufacturer. This represents a substantial increase in the span of the effective area — up to about 78% of the total window area ($2.6 \times 2.6\,\mathrm{cm}^2$) — compared to the R7600U PMT. However, the dynode configuration appears to influence the uniformity of the detector's response, as evidenced by the pattern observed in Figure 3.8 (a) and the distinct peaks and valleys in Figure 3.8 (b), which exhibit variations of

approximately 13%. Moreover, a broader non-uniformity across the photocathode surface is apparent, with certain regions demonstrating noticeably higher sensitivity.

The compact Hamamatsu PMTs enable more portable TDCR counter design but the periodic efficiency pattern makes them not optimal considering the assumptions used in the TDCR model.

3.1.5 Automatic scan of the Hamamatsu R9779

To the best of our knowledge, the Hamamatsu R9779 PMTs are not used in TDCR counters. The interest in scanning the response of this PMT stem from the fact that they are used in liquid scintillation detector in the Metrology of Ionizing Radiation laboratory in the Faculty of Physics, Sofia University. Figure 3.9 presents the results from scanning the response of this PMT.

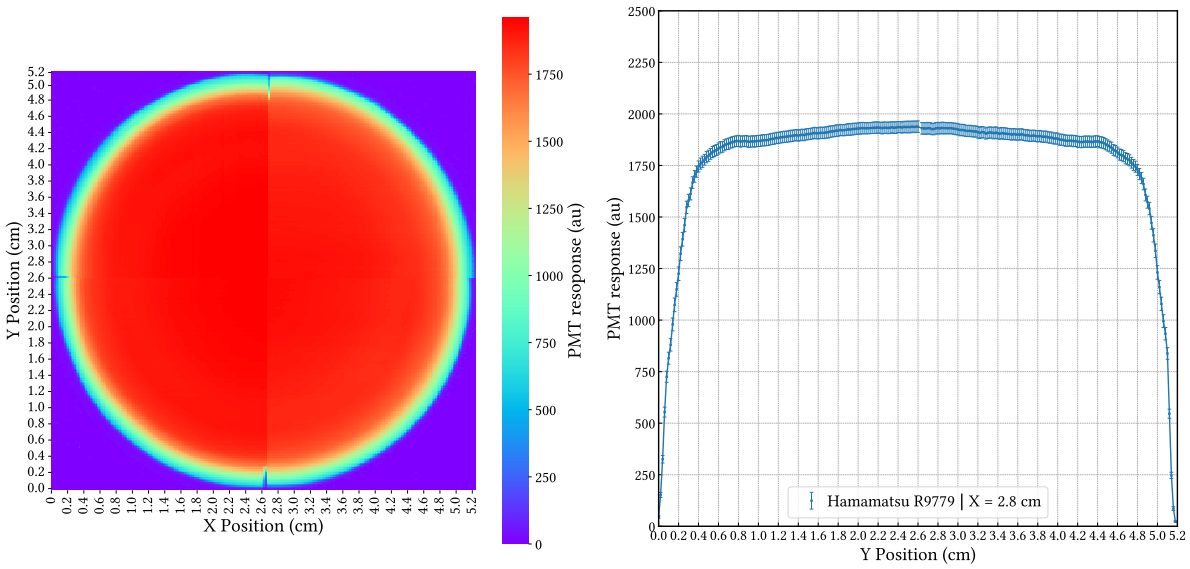

Figure 3.9: Photocathode response map of the Hamamatsu R9779 PMT (a), and a cross-sectional profile along the Y-axis at X = 2.8 cm (b) [131].

The photocathode scan shows no non-homogeneities attributable to the dynode structure of this PMT. The same observation applies to the other scanned PMTs employing a linear-focused dynode configuration. The only non-uniformity of the response appears at the periphery of the PMT window, outside the effective area specified by the manufacturer (∅ 4.6 cm, see Figure 3.9 (b)). Nevertheless, this peripheral non-uniformity could still influence measurements in which single-photon counting is required.

The “ineffective” points at the midpoints where alignment markers were located and a discontinuity visible along the boundaries where the quadrants are joined are an unavoidable artefact inherent to scanning the PMT response in four separate segments with our system. These considerations apply to all circular PMTs scanned with this method; however, they do not impede the determination of each PMT’s effective area nor the characterisation of its response outside this region.

Although this PMT features a very homogeneous response over its effective area, it was

not suitable for single electron counting due to excessive noise and therefore was not used for constructing a TDCR counter.

3.1.6 Automatic scan of the Hamamatsu R331-05

The response of the Hamamatsu R331-05 PMTs was characterized as part of the photocathode response study performed in this work as possible candidate for a TDCR counter.

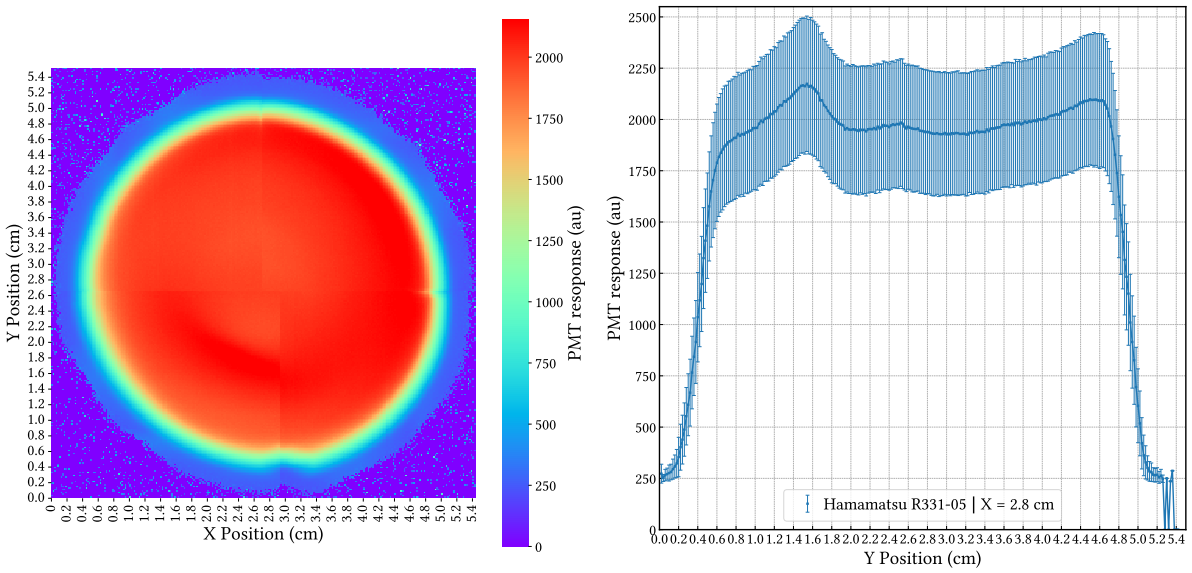

Figure 3.10: Photocathode response map of the Hamamatsu R331-05 PMT (a), and a cross-sectional profile along the Y-axis at X = 2.8 cm (b) [131].

In the lower portion of the scan shown in Figure 3.10 (a) at $X = 3.0$ cm, the darker region intruding slightly into the effective area is caused by the quadrant-boundary marker rather than by any intrinsic feature of the PMT. The response of the R331-05 PMT appears largely homogeneous; however, the region of reduced efficiency near the edge of the photocathode is nearly twice as wide as that observed for the R9779 (see Figure 3.9 (a) in comparison to Figure 3.10 (b)). The larger uncertainties estimates of the PMT response originate from the diffusive window of this PMT. Given its homogeneous response, large effective area and high gain, this PMT has proven to be suitable for the Compton-TDCR counter shown in Section 5.1. For both the Hamamatsu R9779 and R331-05 tubes, knowledge of the extent of this ineffective peripheral region enables mitigation by masking the outer perimeter of the PMT window.

3.1.7 Automatic scan of the Philips XP2020Q

The final PMT investigated was a Philips XP2020Q, an older model manufactured in the early 1990s. Its measured response is shown in Figure 3.11.

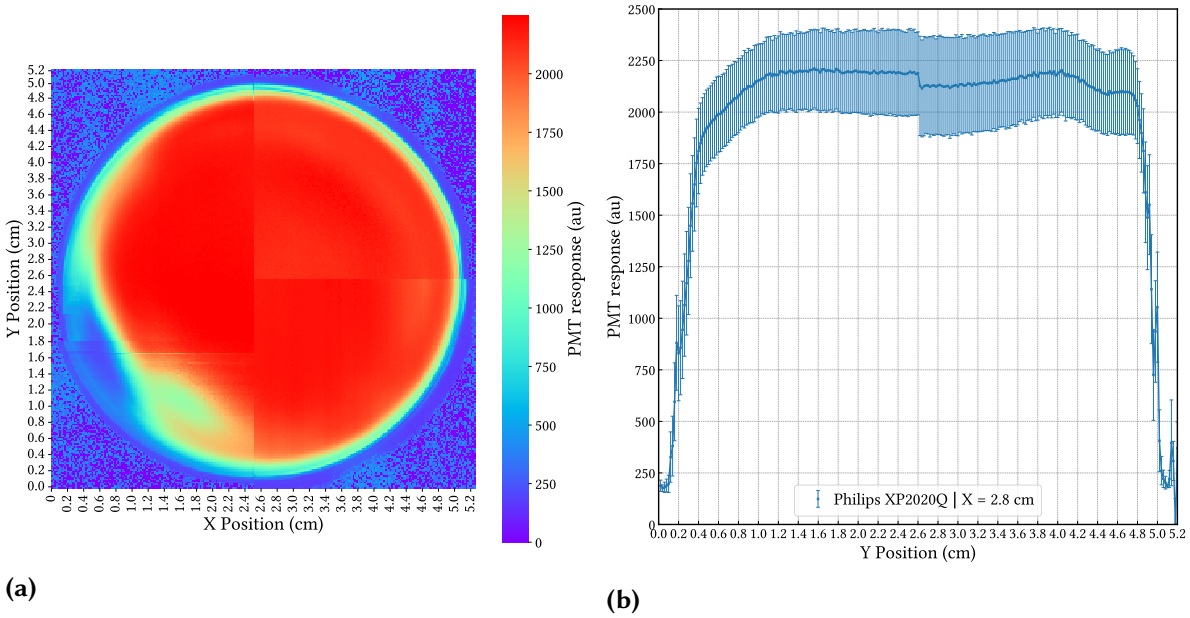

Figure 3.11: Photocathode response map of the Philips XP2020Q PMT (a), and a cross-sectional profile along the Y-axis at X = 2.8 cm (b) [131].

The scan results reveal a pronounced non-uniformity in the response of this PMT, consistent with the findings reported in [136]. No visible damage was observed on the photocathode window during visual inspection. Thus, the reduced sensitivity in the lower-left region of the photocathode, manifested as an effective "blind spot", does not appear to originate from macroscopic damage.

The cross-section at X=2.8 cm, shown in Figure 3.11 (b), indicates that the response is uniform within the interval Y=0.3 to 4.2 cm. A small discontinuity at Y=2.6 cm, corresponding to the boundary between two scanned quadrants, is attributed to a scanning artefact.

From the cross-section taken along the diameter of the PMT Figure 3.11 (b), the distance between the points at which the response falls to 90% of its maximum value is measured to be 4.3 cm. Although the manufacturer specifies a useful diameter exceeding 4.4 cm, both the present results and earlier studies [136] indicate a slightly smaller effective diameter.

Despite their age, XP2020Q PMTs remain in operation [31], including in certain systems used for primary activity standardization [137]. However, the pronounced non-uniformity observed in this study suggests that these tubes may no longer represent an optimal choice for modern scintillation detector applications.

3.1.8 Automatic scan of defocused Philips XP2020Q

An investigation of the photocathode response under non-optimal operating conditions was carried out. Defocusing of PMTs is commonly employed in TDCR measurements as a means of adjusting the detection efficiency [137]. However, the possibility that defocusing may induce spatially non-uniform variations in photodetector sensitivity is often overlooked, even though it violates key assumptions of the TDCR model. The defocusing of the XP2020Q tube was achieved by reducing the potential difference between the focusing electrode and the photocathode. The resulting PMT response after defocusing is presented in Figure 3.12.

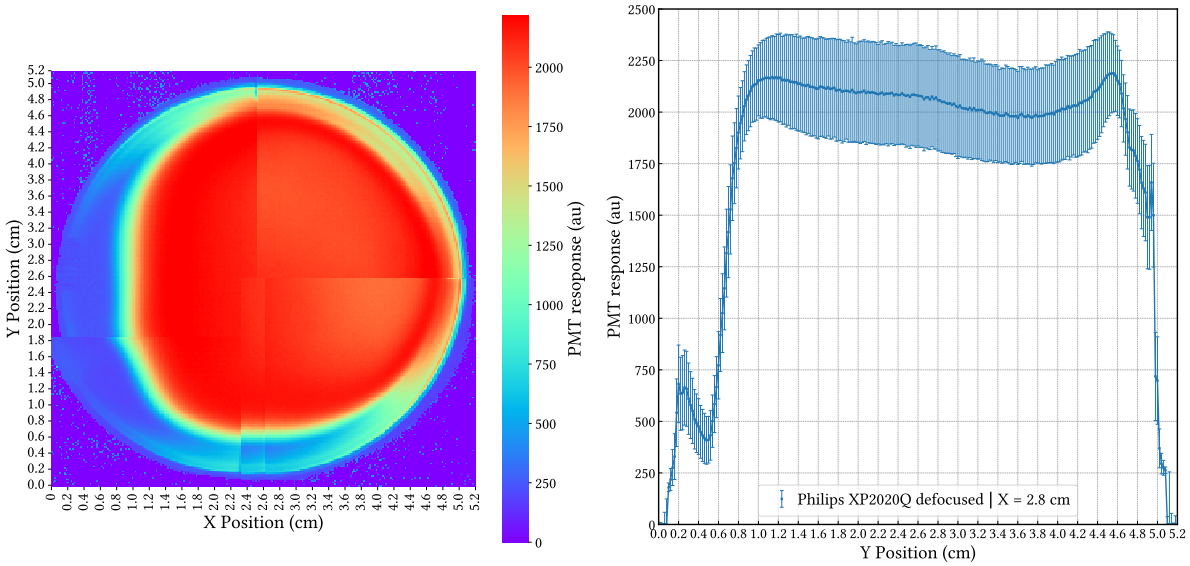

Figure 3.12: Photocathode response map of the defocused Philips XP2020Q PMT (a), and a cross-sectional profile along the Y-axis at X = 2.8 cm (b) [131].

Figure 3.12 (a) shows that, following defocusing, the previously observed low-response region Figure 3.11 (a) expands significantly, occupying a much larger portion of the photocathode surface. Based on the cross-section shown in Figure 3.12 (b), the diameter of the effective region is reduced to approximately 3.8 cm. Furthermore, the ineffective area is clearly asymmetric with respect to the center of the PMT window, implying that the tube's light-detection efficiency becomes strongly dependent on the emission position.

To further illustrate the impact of defocusing on the PMT response, Figure 3.13 presents a comparison of cross-sections taken at Y=1.0 cm from Figure 3.11 (b) and Figure 3.12 (b).

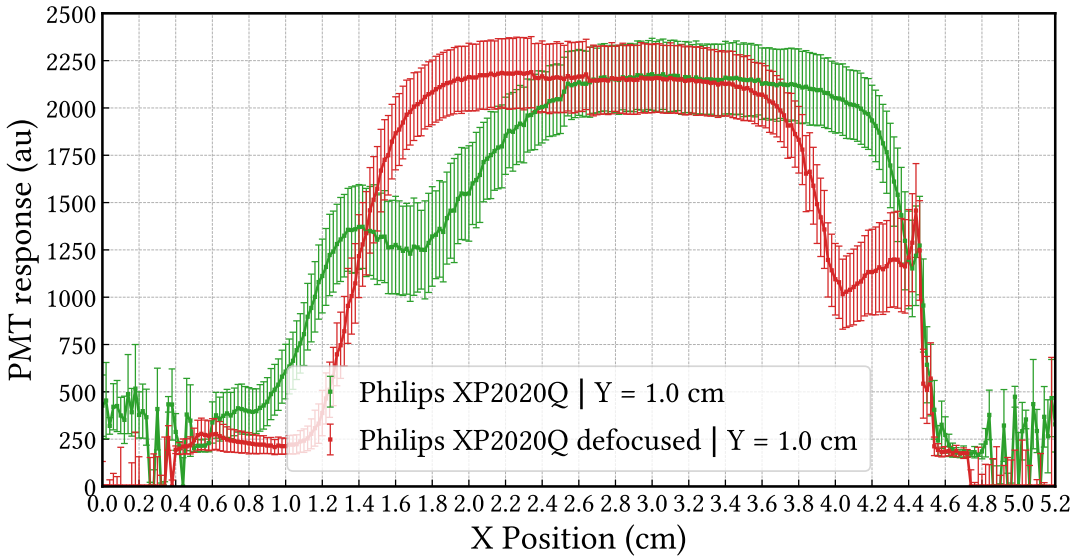

Figure 3.13: Comparison of X-axis cross-sections at Y=1.0 cm for the XP2020Q operated under nominal conditions (green) and in a defocused state (red) [131].

The results presented in Figure 3.13 indicate that defocusing leads to a reduction in the

response at both edges of the PMT. It should be noted that this cross-section passes through the low-response region already present under nominal operating conditions. The difference in the extent of the effective area before and after defocusing is particularly pronounced for Y>2.4 cm. Moreover, the relative change in the area over which the response exceeds the values of 1500 a.u. (see Figures 3.11 (a) and 3.12 (a)) was approximately 13%.

3.1.9 Heating of PMTs and its possible effects on detection efficiency stability

The response-mapping experiments also provided an opportunity to investigate the temperature distribution of PMT during operation. This assessment was performed using the TOPDON thermal camera described at the beginning of Section 3.1.

Prior to acquiring the thermal images, the PMTs were kept powered off for more than 12 h to ensure thermal equilibrium with the ambient room temperature (≈ 23 °C). After applying the high voltage, the PMTs warmed up and reached a steady operating temperature after approximately 3–4 h for the devices investigated in this study.

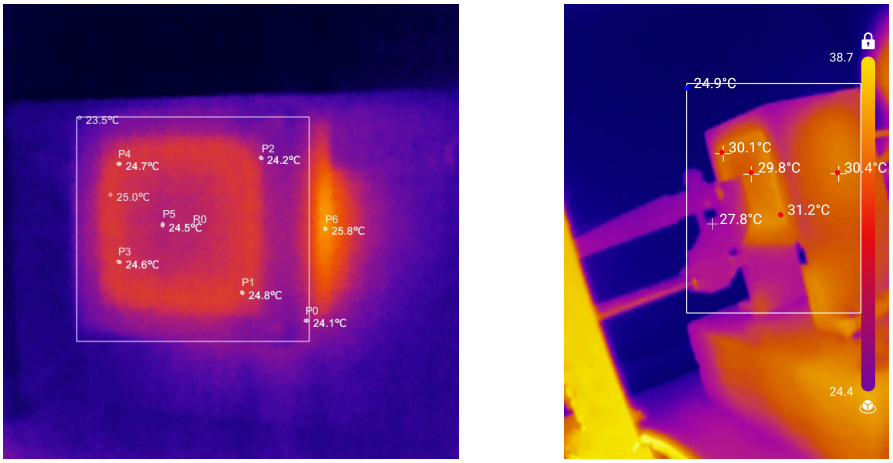

(a) **(b)**

Figure 3.14: Thermal images of the PMTs: (a) front view of the Hamamatsu R7600U-200 taken 3 hours after applying +850 V, and (b) side view of the Hamamatsu H11934-203 taken 1 hour after applying +1000 V [131].

Figure 3.14 shows that the R7600U PMT operates at a temperature approximately 1–2 °C higher than that of its surrounding plastic holder. The hottest point (P6) on the tube corresponds to the location where the photomultiplier is connected to its voltage divider. For the H11934 PMT, the measurements indicate that, only one hour after applying high voltage, the photocathode temperature exceeds that of the system enclosure by more than 4 °C. Although the compact design of these PMTs offers clear advantages, it also presents challenges for TDCR counter implementations, particularly with regard to ensuring adequate thermal management. Other studies have shown that custom-built PMT voltage dividers can substantially mitigate photocathode heating in TDCR applications [138].

For conventional and larger PMTs—where the voltage dividers are positioned farther from the photocathode - the heat generated by the divider does not propagate to the photocathode. Consequently, it is unlikely to contribute to any temperature increase in the liquid scintillator sample being measured.

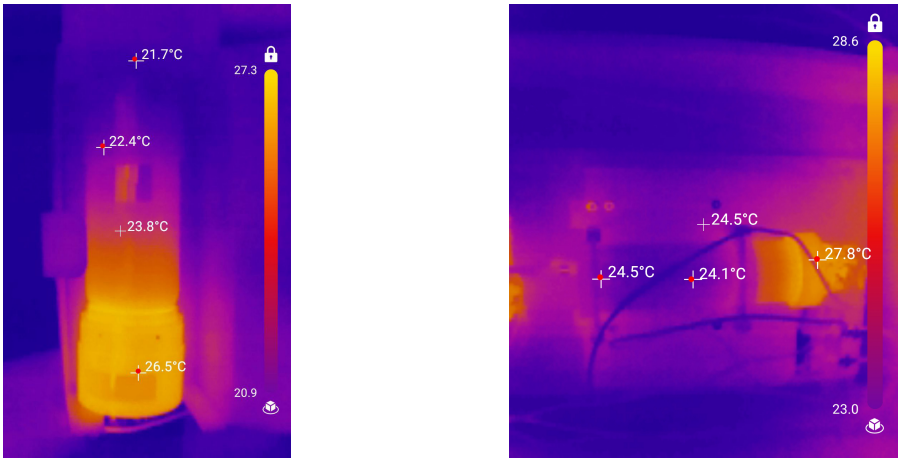

(a) (b)

Figure 3.15: Thermal images of (a) the Hamamatsu R331-05 PMT after 50 hours of operation at +1500 V, and (b) the Philips XP2020Q PMT after 50 hours of operation at +2000 V [131].

For both PMTs presented in Figure 3.15, the hottest regions correspond to the voltage dividers, while the areas surrounding the photocathodes remain at approximately room temperature. The placement of the divider in these PMTs also facilitates more effective thermal management, as it can be cooled more easily and isolated from the rest of the detector assembly.

3.1.10 Effect of photocathode non-uniformity on TDCR detection efficiency

The TDCR model relies on the assumption that the number of emitted photons follows a Poisson distribution and that the photomultiplier tubes are capable of registering individual photons with uniform sensitivity across the photocathode. When the photocathode response is non-uniform, this assumption is no longer valid. In such cases, the photon-detection process is more accurately described by a compound Poisson distribution, in which the mean number of photoelectrons becomes a random variable dependent on the spatial location at which the photons are detected.

As suggested by P. Cassette, for large numbers of photons, the impact of this non-uniformity is negligible due to the effective averaging over the entire photocathode surface. However, for events involving only a small number of photons, the spatial variations in photocathode sensitivity introduce additional variance into the detection process. This effect is described in Chapter 4 and has been published in [139]. Although the magnitude of the extra variance is relatively small [139], it should nevertheless be taken into account when measuring low-energy pure β-emitters such as ^{3}H and ^{63}Ni, as well as pure electron-capture radionuclides such as ^{55}Fe.

In light of these findings, several implications arise for TDCR counting systems employing the PMTs investigated in this study:

1. Optical chamber design: It is advisable to design the optical chamber such that the ineffective regions of the PMTs are covered or excluded from the field of view, as these areas effectively act as photon sinks and do not contribute to the detection process.

2. Uncertainty estimation: Owing to the observed spatial variation in PMT response, the standard deviation of the count rate should be used when estimating measurement

uncertainties, rather than the standard deviation of the mean as previously suggested in [139].

3. Thermal management in compact PMTs: For TDCR counters featuring compact PMTs, dedicated thermal-management strategies should be implemented to dissipate the heat generated during operation and prevent temperature-induced instabilities in the LS cocktail.

4. Considerations regarding efficiency variation techniques: Defocusing is sometimes employed in TDCR measurements as a means of varying the detection efficiency in order to determine the *kB* parameter for the scintillator nonlinearity model. However, as shown in Figure 3.12, defocusing reduces the effective detection area of the photocathode. This constitutes a change in detection geometry, meaning that measurement conditions are no longer strictly comparable. Since the validity of the nonlinearity model requires that the inferred activity be independent of the global detection efficiency — provided that all other conditions remain unchanged — defocusing introduces a systematic change that is inconsistent with this assumption.

   For this reason, defocusing is unlikely to be an optimal technique for efficiency variation. The use of neutral-density (grey) filters represents a more robust alternative, as it allows the detection efficiency to be modified while preserving the measurement geometry and other experimental conditions. Chemical quenching is sometimes used for the same purpose, but it may also alter the physical processes governing scintillation light production — particularly by changing the relative contributions of prompt and delayed components — and therefore modify the global measurement conditions.

Beyond TDCR counting, PMT response non-uniformity is also important in scintillation spectrometry, where the measured pulse-height distribution is used to determine the deposited energy and where energy resolution is often a key performance parameter. If the photocathode response is spatially non-uniform, scintillation photons produced at different positions or reaching different regions of the photocathode may contribute differently to the detected signal. This can broaden the measured energy distribution and degrade the energy resolution, even when the intrinsic scintillator response remains unchanged.

Such effects are particularly relevant when studying the intrinsic energy resolution or non-proportionality of scintillators, since variations caused by the photocathode non-uniform response may be incorrectly attributed to the scintillator itself. Therefore, PMT selection, optical coupling, reflector geometry, and sample positioning must be carefully controlled in precision scintillation spectrometry measurements.

The following chapter presents the practical studies on how the optical effect — photocathode response non-uniformity and the vial walls (clear or diffusive) affects the uncertainty of TDCR measurements.

4 Optical effects and their impact on TDCR measurement uncertainty

The purpose of the study was to assess whether spatial variations in the photon detection response of the PMTs could influence the assumptions used in liquid scintillation coincidence counting. The study presented in this chapter was initiated following a proposal by P. Cassette, who suggested both the scientific objective and the experimental approach used to investigate the possible effect of the spatial response non-uniformity of PMT photocathodes and the LS vials on TDCR systems.

Assuming that scintillation light production follows a Poisson distribution, the distribution of photons among the different detection channels can be described by a multinomial process, while the generation of photoelectrons at the photocathode adheres to a binomial distribution. As shown in [11], the combined effect of this cascade of stochastic processes can be reduced to an equivalent Poisson distribution.

When an ionizing particle deposits an energy E in the liquid scintillator, a number of scintillation photons is produced. If the mean number of emitted photons is denoted by m, and if photon production is assumed to follow Poisson statistics, the probability of emitting x photons is given by [139]:

$$P(x|m) = \frac{m^x e^{-m}}{x!} \tag{4.1}$$

In a liquid scintillation counter, the counted quantities are the pulses generated by photoelectrons within the PMTs. The mean number of detectable photoelectrons, n, corresponds to the average number of emitted photons multiplied by their probability of detection [139]:

$$n(E) = m(E) \cdot \varepsilon_{abs} p \tag{4.2}$$

This detection probability is governed by several factors, including the source–detector geometry, the quantum efficiency of the photocathodes, and the probability that photoelectrons produced at the photocathode are subsequently detected. In Equation (4.2), ε_{abs} denotes the absolute efficiency of the PMT, while p represents the probability that a photoelectron emitted from the photocathode ultimately produces an electrical pulse. The value of ε_{abs} depends on the photocathode material and on the wavelength of the scintillation photons, whereas p, which in a well-adjusted PMTs is considered equal to one, is determined by the electrostatic field configuration within the PMT and can be modified by defocusing or perturbed by the presence of an external magnetic field.

In a three-PMT counter with 120°symmetry and identical photodetectors, the detection efficiency for a single PMT, for a given energy deposit E, can be expressed as the complement of the non-detection probability — that is, the probability of registering zero pulses when an average of m photons is expected [139]:

$$\varepsilon_1 = 1 - P(0|n) = 1 - e^{\frac{n}{3}} \tag{4.3}$$

Here, n is defined by Equation (4.2) and, for a single PMT, corresponds to one third of that value. Assuming that the detection processes in the individual PMTs are statistically independent, the detection efficiency for double coincidences between two PMTs is given by [139]:

$$\varepsilon_2 = (1 - P(0|n))^2 = (1 - e^{\frac{n}{3}})^2 \tag{4.4}$$

An analogous expression can be obtained for the detection efficiency corresponding to triple coincidences [139]:

$$\varepsilon_3 = (1 - P(0|n))^3 = (1 - e^{\frac{n}{3}})^3 \tag{4.5}$$

The detection efficiency associated with the logical sum of the double-coincidence channels (D) is given by:

$$\varepsilon_D = 3\varepsilon_2 - 2\varepsilon_3 = 3\left(1 - e^{\frac{n}{3}}\right)^2 - 2\left(1 - e^{\frac{n}{3}}\right)^3 \tag{4.6}$$

For simplicity, the three PMTs are assumed to possess identical characteristics; however, the expressions in Equations (4.4) to (4.6) can be readily generalized to the case of PMTs with differing quantum efficiencies.

Within the classical free-parameter model, n is treated as a constant that characterizes the intrinsic efficiency of the liquid scintillation photodetector for a given counter, scintillation source, and absorbed energy E. Since n is assumed to be constant for a fixed energy deposit, it is considered to have no associated variance and does not contribute to the uncertainty.

In practice, however, n may exhibit variability arising from the following effects [139]:

- When optically non-diffusive glass vials are used in liquid scintillation counting, same light emission is produced from the whole volume of the LS cocktail; however, the probability of detecting the emitted photons depends on the position at which the scintillation event occurs. The photons must propagate toward the photodetectors while traversing several refractive index discontinuities — from the cocktail (≈ 1.5), to air (≈ 1), and then to the PMT window (≈ 1.5). Light originating near the vial walls is subject to attenuation due to internal reflection effects. This behavior becomes particularly significant when the energy of the emitted electrons is low, resulting in a quasi-pointlike light source for each disintegration event.

- The quantum efficiency of PMT photocathodes is not uniform across the entire active surface, and the probability that an emitted photoelectron reaches the first dynode depends on the local electric field in the vicinity of the focusing electrode. As a result, this probability is generally not constant over the photocathode area. Consequently, both the emission and detection of photoelectrons are influenced by the spatial location at which the scintillation photons are produced and subsequently detected.

For a given deposited energy in the scintillator, n should be regarded as a random variable rather than a fixed constant. Under these conditions, the statistical distribution of the number of photoelectrons is more accurately described by a compound Poisson distribution, which retains the structure of a Poisson law but with a mean value that itself follows a probability distribution. The parameter n is therefore characterised by a probability density function (pdf), which may be evaluated using a Monte Carlo model that simulates the optical behavior of the source–detector system.

To obtain an intuitive assessment of the significance of these effects, a simplified treatment may be applied in which the previously derived expressions are extended to incorporate both the mean value of n, denoted $\hat{n}$, and its associated variance u_n^2. Equation (4.6) remains applicable for the calculation of the double-coincidence detection efficiency, provided that n is replaced

by its mean value. However, the presence of a non-zero variance implies that an intrinsic uncertainty is introduced into the calculated detection efficiency.

By evaluating the standard deviation of ε_2 from Equation (4.4) and applying the law of propagation of variances, one obtains [139]:

$$u_{\varepsilon_2} = \frac{\partial \varepsilon_2}{\partial n} u_n = \frac{2}{3} e^{-\frac{2n}{3}} \left(e^{\frac{n}{3}} - 1 \right) u_n \tag{4.7}$$

Corresponding formulations can likewise be obtained for u_{ε_3} and u_{ε_D} [139]:

$$u_{\varepsilon_3} = \frac{\partial \varepsilon_3}{\partial n} u_n = e^{-n} \left(e^{\frac{n}{3}} - 1 \right)^2 u_n \tag{4.8}$$

$$u_{\varepsilon_D} = \frac{\partial \varepsilon_D}{\partial n} u_n = 2e^{-n} \left(e^{\frac{n}{3}} - 1 \right) u_n \tag{4.9}$$

The corresponding relative standard deviation of ε_D is given by [139]:

$$\frac{u_{\varepsilon_D}}{\varepsilon_D} = \frac{2e^{-n} \left(e^{\frac{n}{3}} - 1 \right)}{3\left(1 - e^{\frac{n}{3}} \right)^2 - 2\left(1 - e^{\frac{n}{3}} \right)^3} u_n \tag{4.10}$$

The sensitivity factor associated with the uncertainty of the mean of the compound Poisson distribution, f, is defined as [139]:

$$f = \frac{2e^{-n} \left(e^{\frac{n}{3}} - 1 \right)}{3\left(1 - e^{\frac{n}{3}} \right)^2 - 2\left(1 - e^{\frac{n}{3}} \right)^3} u_n \tag{4.11}$$

Equation (4.10) then becomes [139]:

$$\frac{u_{\varepsilon_D}}{\varepsilon_D} = f \cdot u_n \tag{4.12}$$

The sensitivity factor f provides a quantitative measure of the extent to which the uncertainty in the mean number of photoelectrons contributes to the relative uncertainty of the detection efficiency. The dependence of f on n, as given by Equation (4.11), is shown in Figure 4.1 together with the detection efficiencies for double, triple, and logical-sum of double coincidences.

For large mean numbers of photoelectrons, the value of f becomes small, and the resulting relative standard deviation, defined in Equation (4.12), is negligible. However, this is no longer true when the mean number of photoelectrons is low. In measurements involving low-energy radionuclides such as ^{3}H or ^{55}Fe, or when the detection efficiency is intentionally reduced — for example, to determine the optimal value of the Birks parameter — the expected mean number of photoelectrons may fall below five. Under such conditions, the standard deviation of the counting efficiency must be explicitly taken into account.

The increase in standard uncertainty arising from photocathode non-uniformity or from optical effects within the source affects not only the calculated detection efficiency but also contributes intrinsically to the detection process itself. Consequently, it should have an observable influence on the experimental counting statistics. Since the measured counting rate corresponds to the product of the activity and the detection efficiency, the standard deviation of the experimental counting rate is given by the quadratic combination of the standard deviation associated with the radioactive decay process and that associated with the detection efficiency.

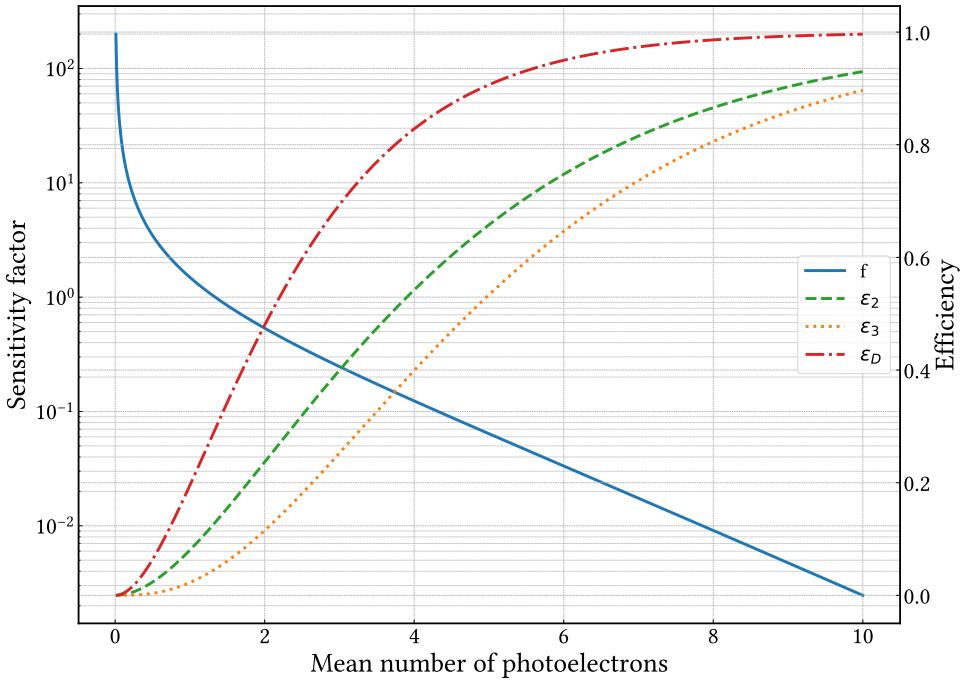

Figure 4.1: Sensitivity factor and the detection efficiencies in double and triple coincidences as a function of the mean number of photoelectrons for a monoenergetic source.

The former is typically assumed to follow Poisson statistics — although in practice it is slightly sub-Poissonian due to counter dead time, which reduces the variance relative to a pure Poisson process. Therefore, if the uncertainty associated with optical effects is non-negligible, it should manifest as an increase in the experimentally determined standard deviation of repeated measurements compared with the Poisson expectation under identical conditions.

4.1 Experimental study of the influence of the vial on detection efficiency

As discussed earlier, differences in refractive index between the LS cocktail, the glass vial, and the surrounding air give rise to internal reflection phenomena within the vial. The refractive index of the LS cocktail is approximately 1.5, which is close to that of glass. At the interface between the exterior surface of the vial and air, total internal reflection may occur, with a critical angle of about 42°. Consequently, scintillation light produced near the vial wall reaches the PMTs with a lower intensity than light originating at the centre of the vial. For a given energy deposited by the ionizing radiation following radionuclide decay, the total detectable light emission is therefore not uniform throughout the entire scintillation volume. This effect can be mitigated by employing optically diffusive vials, which reduce the probability of internal reflection [139].

In TDCR measurements, the influence of this phenomenon is less significant for high-energy radionuclides for two reasons: the interaction region is spatially more extended due to the longer electron path length, and the larger number of emitted photons increases the likelihood that some will reach the PMTs, even if internal reflection reduces the overall detected light yield.

The internal reflections occurring in non-diffusive glass vials result not only in a reduction of

the global detection efficiency but also in an increase in its variance. This behavior must therefore be verified experimentally through repeated measurements. Since the effect is expected to be more pronounced for low-energy radionuclides, measurements were performed using ^{3}H and ^{55}Fe LS sources contained in both non-diffusive and optically diffusive glass vials. Optical diffusion was achieved by wrapping the vials with diffusive adhesive tape, allowing direct comparison while keeping the LS source identical.

The ^{3}H and ^{55}Fe LS sources were prepared using Ultima Gold cocktail and measured with the LNHB mini- and micro-TDCR counters [140], equipped respectively with R7600U-200 and H11934-203 PMTs and operated with the nanoTDCR acquisition system [141]. Coincidence resolving times of 40 ns and 200 ns were applied and extending-type dead time of 50 µs. Each measurement was performed for 1000 s and repeated 24 times under identical conditions. The data sets were examined to confirm the absence of systematic trends in the counting rate, ensuring that the observed dispersion was attributable solely to statistical fluctuations rather than potential instabilities in the counter or scintillation cocktail.

The results for ^{3}H at 40 ns and 200 ns resolving times are summarised in Table 4.1 and compared with expectations based on Poisson statistics, for which the standard deviation of the count number equals the square root of its mean. Equivalent measurements were carried out for ^{55}Fe under the same experimental conditions, with results presented in Table 4.2.

Table 4.1: TDCR values, counting rates, and corresponding relative standard deviations obtained for a ^{3}H liquid scintillation source measured with clear and diffusive glass vials at coincidence resolving times of 40 ns and 200 ns, together with the expected Poisson uncertainties [139].

RT (ns)	Vial type	TDCR	D (s^{-1})	$\frac{u_D}{D}$	$\frac{u_D}{D_{\text{Poisson}}}$	T (s^{-1})	$\frac{u_T}{T}$	$\frac{u_T}{T_{\text{Poisson}}}$
40	Clear	0.5794	3659.6	0.09%	0.05%	2120.2	0.10%	0.07%
40	Diffusive	0.5914	3709.0	0.05%	0.05%	1860.9	0.08%	0.07%
200	Clear	0.5899	3733.8	0.09%	0.05%	2202.6	0.10%	0.07%
200	Diffusive	0.6019	3783.0	0.04%	0.05%	2276.8	0.07%	0.07%

Table 4.2: TDCR values, counting rates, and associated relative standard deviations obtained for a ^{55}Fe liquid scintillation source measured with clear and diffusive glass vials at coincidence resolving times of 40 ns and 200 ns, together with the expected Poisson uncertainties [139].

RT (ns)	Vial type	TDCR	D (s^{-1})	$\frac{u_D}{D}$	$\frac{u_D}{D_{\text{Poisson}}}$	T (s^{-1})	$\frac{u_T}{T}$	$\frac{u_T}{T_{\text{Poisson}}}$
40	Clear	0.3809	2423.0	0.08%	0.06%	922.9	0.16%	0.10%
40	Diffusive	0.3973	2507.8	0.07%	0.06%	997.2	0.10%	0.10%
200	Clear	0.4215	2600.1	0.08%	0.06%	1096.0	0.16%	0.10%
200	Diffusive	0.4395	2681.6	0.08%	0.06%	1178.6	0.10%	0.09%

The results demonstrate that the use of diffusive vials leads to an increase in both TDCR and detection efficiency — and therefore in counting rates — while simultaneously reducing counting-rate fluctuations. No significant excess variance beyond Poisson expectations is observed for diffusive vials. In contrast, clear glass vials exhibit additional standard deviation for both ^{3}H and ^{55}Fe measurements.

As anticipated, increasing the coincidence resolving time results in higher TDCR values and increased counting rates, but it does not significantly affect the excess standard deviation observed for clear vials.

4.2 Impact of PMT response non-uniformity on TDCR measurements

The photocathode response at each position, illustrated by the example in Figure 3.7, was approximately Gaussian. Therefore, each peak was fitted with a Gaussian function to determine its centroid and standard deviation. The mean number of photoelectrons was then obtained from the measured standard deviation, assuming Poisson statistics for the detected photoelectrons.

This procedure allowed the PMT response to be expressed as the number of photoelectrons generated for each light-source position on the photocathode. The validity of the Poisson assumption was checked using calibrated optical filters placed in front of the light source. As shown in Figure 4.2, the mean number of photoelectrons changed linearly with the filter transmission, with a slope consistent with unity, confirming that the detected photoelectrons follow Poisson statistics under these experimental conditions [139].

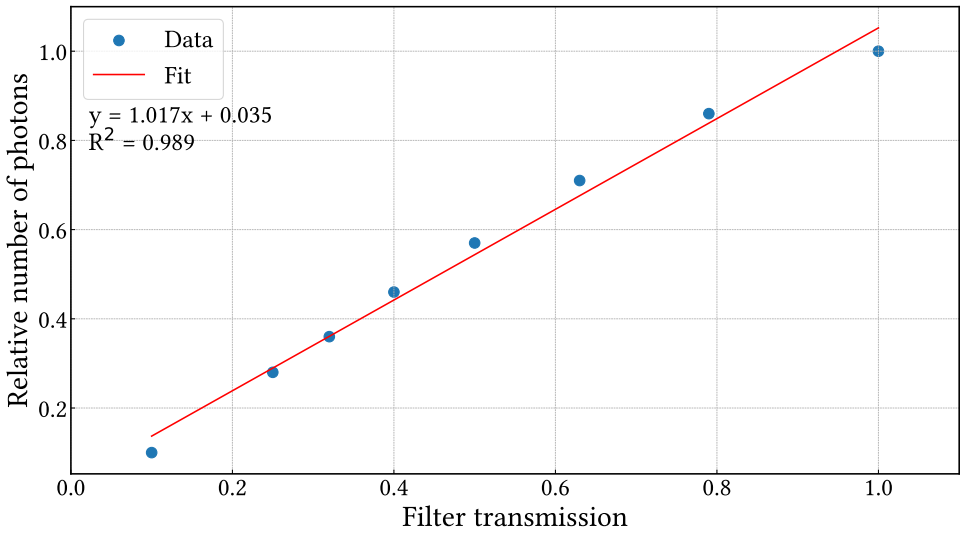

Figure 4.2: Variation of the relative number of detected photoelectrons with the transmission of the optical filters placed in front of the light source.

The mean number of photoelectrons detected at each position of the light source, expressed in (x,y) coordinates, provides a spatial representation of the PMT's detection efficiency. These values are stored in a matrix that characterizes the spatial response of the photocathode for each PMT.

From these data, the relative standard deviation of the mean detection efficiency can also be evaluated for each point on the effective part of the photocathode. For Hamamatsu R7600U-200, a relative standard deviation of the average number of photoelectrons of 0.26% was obtained and 0.64% for the H11934-203 [139].

For the measurements of ^{55}Fe, it is assumed that the majority of the deposited energy originates from K-shell electron-capture processes, which produce either characteristic X-rays or Auger electrons. Because L-shell rearrangement releases considerably less energy, the light output of the scintillation cocktail can be regarded as arising almost entirely from energy deposits of approximately 6 keV, resulting in a narrow distribution. Under these conditions, the influence of PMT photocathode non-uniformity can be approximated using the monoenergetic approach presented in equations Equations (4.8) and (4.9) [139].

The liquid scintillation sources were prepared with Ultima Gold cocktail and placed in an optically diffusive vial. Measurements were carried out using the LNHB miniTDCR system equipped with R7600U-200 photomultipliers, operating with a 40 ns coincidence window; the detection efficiency was intentionally decreased by inserting a neutral-density (grey) filter. Table 4.3 compares the experimental results with the predictions obtained from the analytical monoenergetic model.

Table 4.3: Comparison between experimentally measured relative standard deviations of the double- and triple-coincidence detection efficiencies for a ^{55}Fe liquid scintillation source and the values predicted by the analytical model [139].

Measurement conditions	**TDCR**	$\mathbf{u_{\varepsilon_D}/\varepsilon_D}$ **exper.**	$\mathbf{u_{\varepsilon_D}/\varepsilon_D}$ **predicted**	$\mathbf{u_{\varepsilon_T}/\varepsilon_T}$ **exper.**	$\mathbf{u_{\varepsilon_T}/\varepsilon_T}$ **predicted**
No filter	0.4370	0.053%	0.047%	0.12%	0.12%
Grey filter	0.1221	0.076%	0.12%	0.24%	0.20%

The average number of photoelectrons was determined from the measured TDCR values by applying equations Equations (4.5) and (4.6), assuming that the dominant contribution to the scintillation signal corresponds to K-shell electron capture in ^{55}Fe. Using this estimate, the relative uncertainties associated with the double- and triple-coincidence detection efficiencies were then computed using Equation (4.12).

The findings indicate that the influence of spatial non-uniformity of the photocathode on the variability of the double- and triple-coincidence counting efficiency is modest but not entirely negligible, with a more pronounced effect observed for triple coincidences. In addition, the analytical model appears to slightly overpredict the contribution of this effect in the case of double coincidences.

Applying the analytical model to estimate the uncertainty of the detection efficiency in a TDCR system becomes challenging when optical effects must be considered for radionuclides emitting a spectrum of energies. For this reason, a Monte Carlo method was adopted to account for the impact of photocathode non-uniformity. In the case of the R7600U-200 photomultipliers, the experimentally determined spatial response of the photocathode — represented by the matrix introduced earlier and normalized to unity — was used as input. This spatial map was incorporated into the TDCR computation by modifying the figure of merit with a factor λ, drawn randomly from the normalized matrix and treated as a centred random variable. The factor λ is introduced in the expressions for the detection efficiencies of each PMT similar to Equation (4.2) [139].

For a fixed set of measurement conditions (radionuclide, TDCR value, Birks coefficient kB and so on), the figure of merit, expressed as the number of photoelectrons per keV, is first evaluated. A Monte Carlo simulation is then performed in which, at each iteration, a random value of λ is generated, the figure of merit is scaled by this factor, and the corresponding double- and triple-coincidence efficiencies ε_D and ε_T are computed. This procedure is repeated 10^5 times. The resulting mean values and standard deviations of ε_D and ε_T are then determined. It is confirmed that the mean efficiencies agree with those obtained from experimental TDCR measurements (equivalent to setting $\lambda = 1$), while the standard deviations provide estimates of the additional uncertainty arising from photocathode non-uniformity.

Experimental measurements were performed using the miniTDCR system at Sofia University, equipped with R7600U-200 tubes and operated with the nanoTDCR acquisition electronics.

Example results for a ^{3}H liquid scintillation source in a diffusive glass vial, employing a toluene–PPO scintillator, are presented in Table 4.4. The calculations use a Birks parameter of kB =0.01 cm/MeV and include the experimentally observed relative standard deviations of the double- and triple-coincidence counting rates, alongside the Poisson expectations. For simplicity, the PMTs are assumed to have equivalent detection efficiencies.

Table 4.4: Comparison between experimentally measured relative standard deviations of the double- and triple-coincidence detection efficiencies for a ^{3}H liquid scintillation source and the values predicted by the Monte Carlo model [139].

Filter transmission	**TDCR**	$\mathbf{u_{\varepsilon_D}/\varepsilon_D}$ **exper.**	$\mathbf{u_{\varepsilon_D}/\varepsilon_D}$ **predicted**	$\mathbf{u_{\varepsilon_T}/\varepsilon_T}$ **exper.**	$\mathbf{u_{\varepsilon_T}/\varepsilon_T}$ **predicted**
100%	0.6292	0.07%	0.05%	0.11%	0.08%
60%	0.3094	0.09%	0.11%	0.14%	0.18%
50%	0.2630	0.11%	0.13%	0.25%	0.21%

A slight increase in the relative standard deviation of the double-coincidence counting rates is observed, with a more pronounced effect for triple coincidences, particularly when the detection efficiency is low.

4.3 Influence of photocathode response non-uniformity on the uncertainty budget in TDCR measurements

Counting statistics are routinely included in the uncertainty budget of TDCR measurements. According to the GUM, they may be evaluated either by a type A or a type B approach. In a type A evaluation, repeated measurements are used and the uncertainty is obtained from the standard deviation of the mean count rate. In a type B evaluation, the uncertainty is based on an assumed statistical model, most commonly Poisson statistics, for which the standard uncertainty is taken as the square root of the number of recorded events.

For TDCR measurements, the type A approach is generally preferable because it does not require an assumed distribution and can reveal uncontrolled variations during repeated acquisitions. However, the standard deviation of the mean decreases as the number of repetitions increases and may therefore no longer represent the intrinsic fluctuations of the counting process.

This is important when optical effects are studied, since variations in detection efficiency can lead to corresponding fluctuations in the double- and triple-coincidence count rates. These fluctuations should be included in the uncertainty budget. Using only the standard deviation of the mean may underestimate their contribution unless an additional term, obtained for example from Monte Carlo simulation or an analytical model, is added in quadrature.

A more direct approach is therefore to use the experimental standard deviation of the count rates themselves rather than the standard deviation of the mean. This preserves the observed variability of the measurements and includes both intrinsic efficiency fluctuations and possible uncontrolled changes during acquisition.

5 Development of a Compton-TDCR spectrometer

Based on the results presented in Chapter 3 and their implications for TDCR counting (see Chapter 4), the practical impact of PMT photocathode non-uniformity in the TDCR method can, at present, be considered understood. In particular, the response mapping enables informed PMT selection, supports the use of diffusive vials, and provides a basis for identifying operating conditions (e.g. defocusing) under which non-uniformity may become significant.

With the recent development of analytical correction methods for accidental coincidences [18], the use of longer coincidence windows in TDCR counting has become increasingly acceptable [86]. Nevertheless, extending the coincidence window should be approached with caution. The standard TDCR efficiency model typically represents scintillator non-linearity via Birks ionization quenching, which parameterizes the light yield as a function of deposited energy but does not account for the delayed scintillation, so that the determined quenching parameter (e.g. kB) may become a quantity that depends on the acquisition settings rather than a purely cocktail intrinsic parameter.

In principle, this limitation can be addressed in several ways. One option is to use scintillation cocktails with minimal delayed fluorescence; however, this is not generally compatible with current material-development trends, where more pronounced delayed component is often desirable because it improves pulse-shape discrimination and easier light pulse digitization [142]. A second option is to replace the Birks description with a more comprehensive model that explicitly separates prompt and delayed light. Such an approach would introduce additional parameters, which are typically not known *a priori* and could complicate both the TDCR efficiency model.

A practical alternative is to avoid assuming a parametric light-yield model altogether and instead determine the scintillator response experimentally. This is the premise of the Compton-TDCR approach: a monoenergetic γ-ray beam irradiates the scintillator, and events are selected in coincidence with a γ detector so that the energy of the Compton-scattered photon, and thus the corresponding Compton-electron energy deposited in the scintillator, is known from kinematics. The TDCR channel then provides the mean photoelectron yield for electrons of that selected energy. Repeating the measurement over multiple γ-energy ROIs yields an empirical response curve, which can be introduced directly into TDCR efficiency calculations, thereby reducing reliance on an assumed quenching parameterization. The basic principles of this method were proposed by Cassette and Do [15], building on earlier Compton-coincidence measurements by Péron and Cassette [13]. Short description of the method is given in Section 2.5.

The motivation for developing the Compton–TDCR spectrometer was to establish a measurement system with optimized and well-characterized components, capable of performing metrologically robust determinations of liquid-scintillator light yield. In particular, the aim was to enable measurements with a well-defined uncertainty for both the Compton-electron energy deposited in the scintillator and the corresponding mean number of detected photoelectrons measured by the TDCR channel.

5.1 Design of the Compton-TDCR

A Compton scintillation spectrometer has two main parts - scintillation detector and a gamma-ray detector and the acquisition electronics that binds the two systems to work in coincidence. The two channels are linked by the electronics so that only time correlated events are selected. This section describes the Compton–TDCR spectrometer assembled as part of the work in this thesis. The instrument is installed in the MIL laboratory at the Faculty of Physics, Sofia University, and is hereafter referred to as CTDCR-SU.

5.1.1 The TDCR channel

The TDCR counter of CTDCR-SU is equipped with three Hamamatsu R331-05 PMTs [134]. These are cylindrical linear-focused PMTs and are already established in the field of TDCR counting [143, 144, 145]. The PMTs feature large photocathode with a diameter of 4.6 cm, high gain and very good resolution of the single electron peak. The PMT's window is convex and diffusive. The photocathode response of these PMTs was studied and is shown in Section 3.1.6, observing large homogeneous area with sharp decrease towards the edge of the window [131]. The voltage dividers used in the counter are the Hamamatsu E5859-03 [146] which supply positive high voltage and grounded photocathode [147]. In Section 3.1.9, it was shown that there is a negligible transfer of heat from high-voltage dividers of the PMTs to the photocathode region under working conditions [131]. Therefore, it was expected and then checked by thermal imaging that there was negligible warming of the LS vials when measured in the TDCR. A four-channel CAEN DT1470ET power supply with individual voltage control in each channel was utilized in the counter [148]. The voltage supplied to each PMT was +1800 V in all measurements presented in this thesis.

The optical chamber was developed to be used with standard 20 mL vials (see Figure 5.1 (a)). The design of its internal walls was optimized and they were covered with 3M reflective foil [149] for the best possible light collection. The optical chamber and its outer light-opaque shell were 3D-printed from PLA. The outer shell of the optical chamber is painted with conductive paint and the PMTs are shielded in metal tubes. The assembled TDCR channel is presented in Figure 5.1 (b). The TDCR counter is placed in a metal housing acting as a second shield against electromagnetic interference.

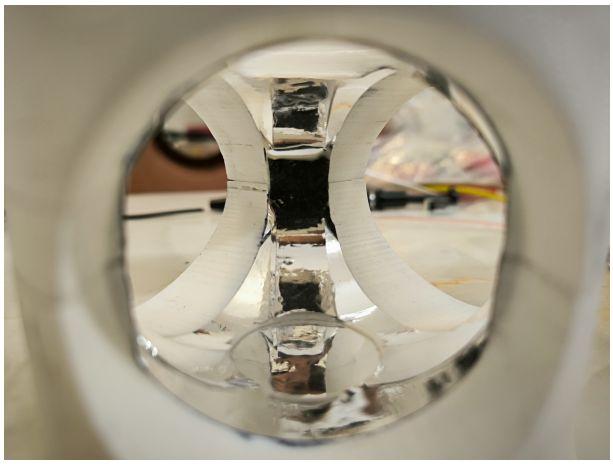

(a)

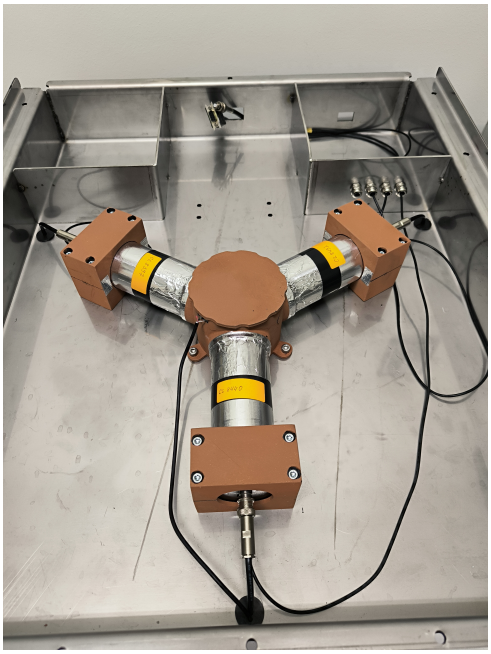

(b)

Figure 5.1: (a) PMT's view of the optical chamber.(b) The assembled TDCR channel. On the right is a compartment for the acquisition electronics [150].

The TDCR channel can perform simultaneous measurements with two acquisition electronics modules. This is possible via a CAEN Fast Amplifier (model N978) [151] which has four input channels and two outputs per each input channel. The amplifier was operated at gain 1. The signals from the three PMTs are fed to three of the input channels of the amplifier and the two outputs of each channel is connected to either:

- a nanoTDCR+ (TD9020) analyzer [152]
- a CAEN DT5751 Digitizer [153]

The nanoTDCR+ is a Field-Programmable Gate Array (FPGA) based analyzer making it flexible as its functionality can be change by simply programming an FPGA design. The nanoTDCR+ is developed by V. Jordanov (Yantel LLC [152]). The nanoTDCR has been tested for TDCR counting [120] and it has been successfully used in ^{3}H intercomparison organized by BIPM [154]. In the CTDCR-SU counter we used a special modification of the nanoTDCR+ device.

This device has three analog inputs A, B and C accepting anode signals from the three PMTs. The anode signal of every PMT is amplified by a fast amplifier whose output is split in two. One signal branch is routed to a multiplexer that feeds a multichannel analyzer (MCA). The second branch is sent to a comparator, whose threshold is digitally set by the labZY-TDCR software. The comparator outputs are then used as inputs to the TDCR counters. In pulse-height analyzer (PHA) mode, the MCA records a pulse-height spectrum of the PMT signals (triggered by the TDCR comparators). The single-photoelectron peak in this spectrum is then used to set each PMT threshold slightly below that peak, ensuring single-photon sensitivity while rejecting noise. The nanoTDCR+ also have one digital input R accepting TTL or CMOS logic signals. In this version of the device the S and T digital outputs can be set as inputs also. A key feature of the nanoTDCR is that it generates the coincidence windows and applies extending

dead time independently for each PMT channel. In a single measurement run, the instrument simultaneously processes two extending dead time settings (Extension 1 and Extension 2) and two coincidence windows (Window N and Window M), effectively performing four TDCR measurements in parallel. For each run, the nanoTDCR reports the four sets of coincidence counting rates AB, BC, AC, D, and T.

The CAEN DT5751 is a four channel desktop digitizer with a 1 GS/s sampling rate and 10 bits resolution. The DT5751 digitizer is FPGA-based; its acquisition and buffering logic are implemented in FPGA firmware. Key advantage of digitizers is the possibility to record the timestamp, energy and waveform of each signal coming from the PMT. The experimental data is stored in a list-mode format on a computer storage and it can be analyzed offline which allows the comparison of different analysis algorithms on the same set of data. The software for the analysis used in this thesis was developed previously in [155]. The digitizer has been used only for TDCR measurements in this thesis as it was not capable for handling the signal of the gamma channel of the Compton-TDCR system.

Benchmarking of the TDCR channel of the CTDCR-SU detector against three established TDCR systems in the MIL Laboratory is presented in Chapter 6. In brief, the newly developed TDCR counter yields activity estimates coherent with those obtained from the other systems for the investigated radionuclides and exhibits the highest detection efficiency among the compared counters. This high efficiency is particularly advantageous for Compton-TDCR measurements, as it provides sufficient coincidence statistics even for very low-energy electrons, where the scintillation light output is minimal.

5.1.2 The gamma channel

The choice of the γ-ray source for the Compton–TDCR spectrometer is dictated by the energy region in which the scintillation response of liquid scintillators is expected to be most non-linear. Since this non-linearity is particularly pronounced for low-energy electrons, especially below about 20 keV, a low-energy monoenergetic γ source is required in order to produce Compton electrons in this range. In the present system, an ^{241}Am source is used, and the scattered γ rays detected after Compton interaction in the scintillator are expected mainly in the 50–60 keV range. Therefore, the γ-ray channel requires a detector with good detection efficiency and sufficient energy resolution in this low-energy region, since the Compton-electron energy is derived directly from the measured scattered photon energy.

For this purpose, the γ-ray detecting part of the Compton-TDCR system was based on a planar n-type HPGe (nHPGe) detector, shown in Figure 5.2 (a). The germanium crystal is 5 mm thick and 10 mm in diameter and is positioned approximately 7 mm behind a 250 μm-thick beryllium window. An X-ray image of the detector, shown in Figure 5.2 (b), was acquired to determine the position of the germanium crystal inside the cryostat. This geometrical information was subsequently used in the Monte Carlo simulation of the experiment.

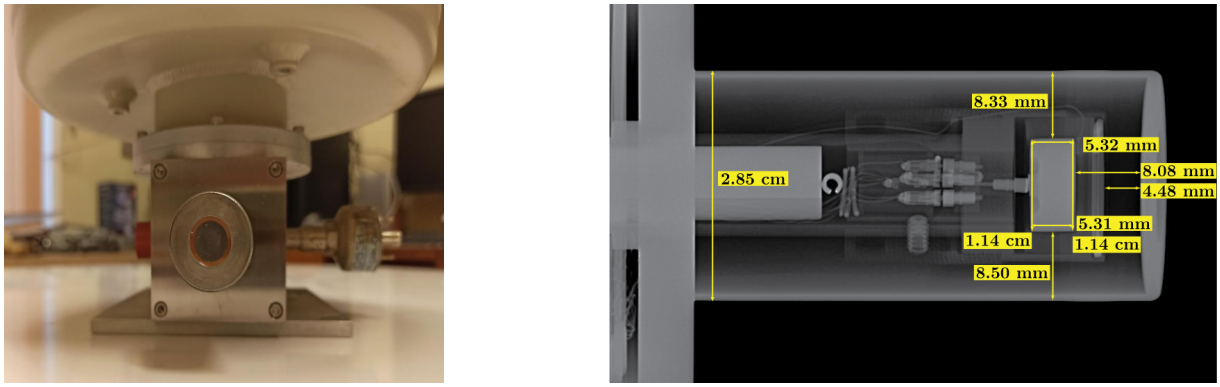

(a) **(b)**

Figure 5.2: (a) Frontal photo of the nHPGe detector with its beryllium window. (b) X-ray image of the germanium crystal and the surrounding cryostat of the nHPGe detector [150].

This nHPGe detector is equipped with a transistor-reset charge-sensitive preamplifier custom built by V. Jordanov. For a transistor reset preamplifier, the detector current pulse is integrated on the feedback capacitor, producing a step-like increase of the preamplifier output; the step amplitude is proportional to the collected charge (and therefore to the deposited energy). Successive events therefore appear as a staircase on the output baseline. As the output approaches the maximum dynamic range (approximately 4 V for our detector), an electronic reset is triggered: a transistor briefly discharges the feedback capacitor and restores the baseline, after which normal integration resumes. During the reset interval the preamplifier is momentarily insensitive, so acquisition electronics apply an inhibit to avoid recording reset-related transients (amplitude of $\approx$ 4 V). To handle both the output and the inhibit signals from the preamplifier, a nanoMCA-II MCA was utilized [156]. The output of the preamplifier was connected to input A and the inhibit signal to input C of the nanoMCA-II. The nanoMCA-II integrates a programmable amplifier, pulse shaper and multichannel analyzer based on Digital Pulse Processing (DPP), which allows the shaping parameters to be configured in software. In order to achieve the best energy resolution with the nHPGe detector, the shaping parameters of the nanoMCA-II were optimized.

The transistor-reset preamplifier operates as a charge-sensitive stage: each detected event produces a step-like increase at the preamplifier output, with step height proportional to the collected charge. The role of the nanoMCA-II is to convert this step response into a well-defined pulse whose amplitude can be measured accurately. This is accomplished with a digital trapezoidal shaper. In this representation, the slow shaper rise time determines the effective integration time (and therefore the balance between electronic noise filtering and pile-up susceptibility), while the flat top provides a plateau over which the pulse-height measurement is less sensitive to variations in charge-collection time (i.e. it mitigates ballistic deficit). Consequently, these two parameters have the strongest influence on the achievable energy resolution.

A systematic optimization was performed by H. Stoycheva in [157], by using the 59.54 keV γ line of ^{241}Am, by scanning the slow-shaper rise time and flat-top settings and evaluating the resulting FWHM. The study of the FWHM for different values of the rise time and the flat-top is shown in Figure 5.3. The optimal values were found to be 3.2 μs (rise time) and 0.16 μs (flat top). With these settings, the measured relative energy resolution at 59.54 keV was 0.62% (FWHM = 370 eV).

This optimization is critical for the Compton–TDCR spectrometer, since the Compton-

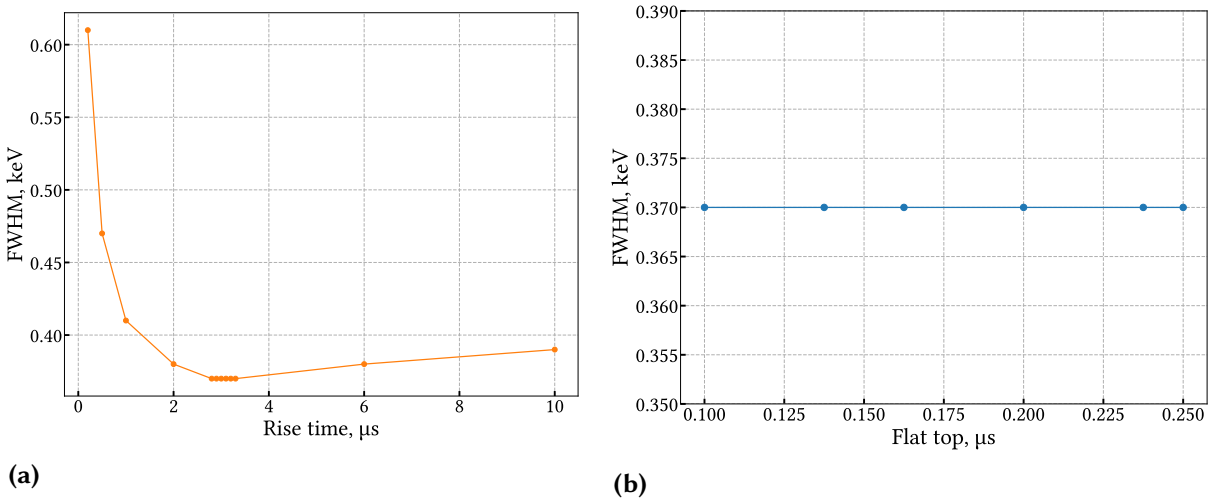

Figure 5.3: Study of the influence of the settings of (a) rise time and (b) flat-top of slow shaper of nanoMCA-II on the FWHM of the 60 keV line of ^{241}Am point source [157].

electron energy is derived from the scattered γ-ray energy measured with the nHPGe detector; therefore improved HPGe resolution reduces the uncertainty of the measured Compton electron energy.

An ^{241}Am point source was also used to characterize the position-dependent full-energy peak efficiency of the nHPGe detector for the 59.54 keV γ line. The source was placed at different positions within the volume normally occupied by the liquid-scintillation vial inside the TDCR optical chamber. In this way, the measurement reproduced the relevant geometrical conditions of the Compton-TDCR setup and provided an experimental map of the γ-detection efficiency as a function of position.

The resulting efficiency map is shown in Figure 5.4. It provides useful information on the spatial dependence of the nHPGe detection probability in the actual detector geometry. This information is important for MC simulations of the system, where it can be used to validate the geometrical model and to account for the position-dependent detection efficiency of photons reaching the nHPGe detector.The efficiency map also indicates that Compton-scattering events occurring closer to the nHPGe detector would be detected with higher efficiency, which could introduce an asymmetry. However, such effects cannot be distinguished with certainty from the Compton-TDCR measurements alone.

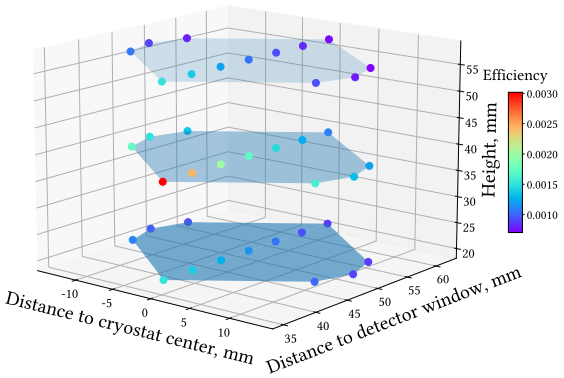

Figure 5.4: Position-dependent full-energy peak efficiency map of the nHPGe detector for the 59.54 keV γ line of an ^{241}Am point source. The source positions correspond to points within the volume normally occupied by the liquid-scintillation vial in the TDCR optical chamber [157].

5.1.3 Assembly of the Compton-TDCR

The mechanical platform that integrates the TDCR and gamma channels of the Compton–TDCR system was designed to shield the electronics and optical chamber from electromagnetic interference and ambient light, while minimizing attenuation of both the primary and scattered γ rays. Both the TDCR counter and the γ detector are mounted in a stainless-steel housing, which provides mechanical support and electrical shielding. A circular opening of 30 mm diameter is provided beneath the optical chamber in order to avoid attenuating the primary γ-ray beam from the excitation source. This opening is light-sealed with a 0.3 mm aluminium foil, which blocks ambient light while introducing only minor attenuation of the excitation photons.

The platform improves the detection efficiency for Compton scattered photons primarily through geometric optimization and minimization of intervening material. First, the optical chamber wall and the light-tight outer shell (3D-printed in black PLA) are locally thinned on the bottom side and on the side facing the nHPGe window, thereby reducing the material traversed by both the primary and scattered photons and limiting absorption and additional scattering before they enter the scintillator volume or the nHPGe detector. Second, the distance between the nHPGe window and the LS vial wall was set to a minimum value of 35 mm, increasing the solid angle subtended by the germanium crystal and therefore the probability that a photon scattered in the scintillator reaches the detector. Third, in order to detect gamma rays that are scattered predominantly at 90°, the height of the meniscus of 10 mL of liquid in the vial corresponds to the center of the germanium crystal along the vertical axis. The assembled TDCR counter and the gamma channel of the CTDCR-SU system are shown in Figure 5.5 (a), and an exploded view is provided in Figure 5.5 (b).

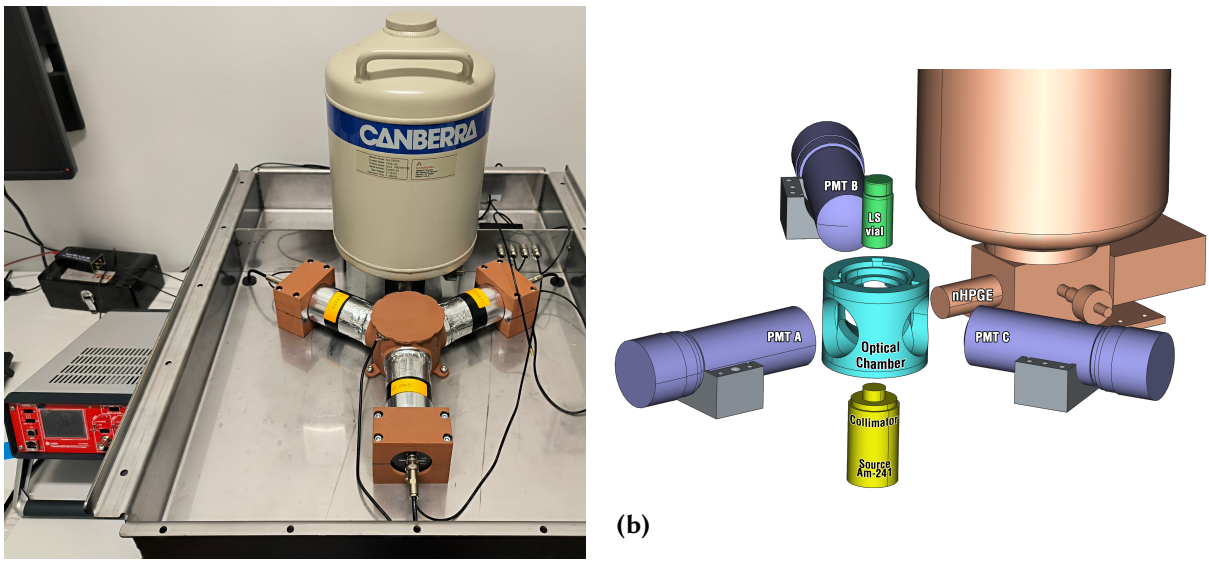

(a) (b)

Figure 5.5: (a) The assembled state of the CTDCR-SU (b) Exploded view showing the main parts of the CTDCR-SU detector [150].

5.1.4 Compton coincidence acquisition setup

The acquisition electronics of the CTDCR-SU system was developed by V. Jordanov with some modification of the nanoTDCR and the nanoMCA-II implemented specifically for the purposes of this experiment. Figure 5.6 shows a dedicated acquisition scheme for energy-selective gating of Compton electrons. It supports coincidence measurements between the TDCR channel and the nHPGe detector, while still allowing conventional TDCR operation without any hardware reconfiguration.

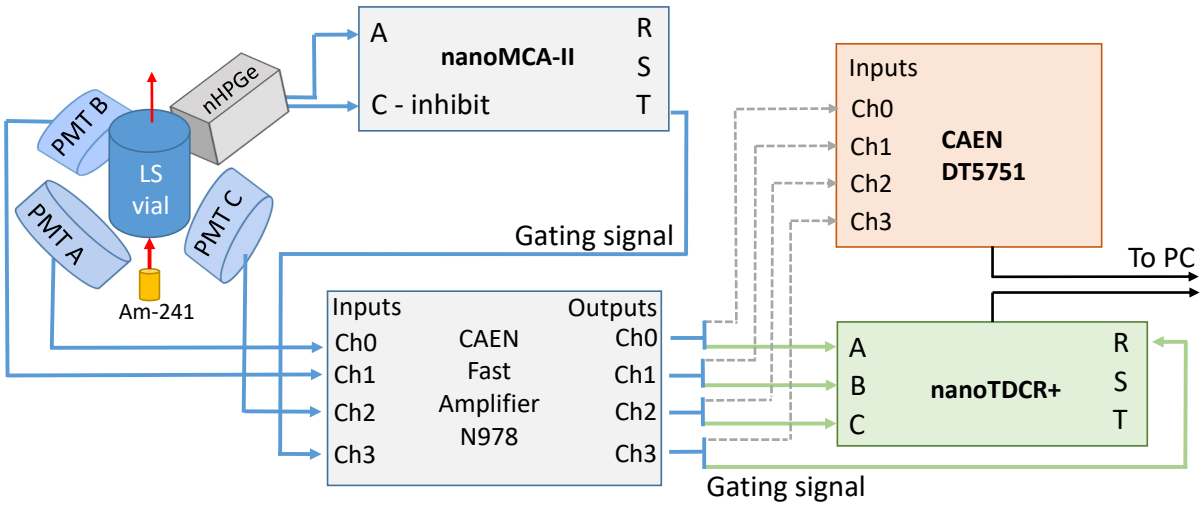

Figure 5.6: Scheme of the Compton-TDCR acquisition system [150].

When a γ-ray event is recorded within a predefined ROI in the spectrum, the nanoMCA-II can generate a gating logic pulse at its terminal *T* (see Figure 5.7). In the *labZY-MCA* software, the *T* output was configured in *PUSH-PULL* mode and assigned the function *ROI-TSCA 8 ns*, which produces an 8 ns-wide logic pulse for events accepted in the selected ROI. The ROI used for gating is defined by placing the spectrum cursor within the desired interval and enabling the *ROI-SCA* option in the Trace Viewer, which displays the corresponding start and end channels. The timing of the gating pulse is derived from the shaped signal using constant-fraction peak detection, referenced to the falling edge of the trapezoidal pulse.

The gating pulses from the nanoMCA-II were fed to the *R* input of the nanoTDCR+. Each gating pulse opens a coincidence window of width 40 ns (set in the *labZY-TDCR* software). A valid Compton coincidence event is registered when TDCR coincidence (double or triple) occur within this window and the TDCR counters are incremented. Specifically, the nanoTDCR+ uses the internal sources *TDCR S1* and *TDCR S2*, where *TDCR S1* corresponds to the first-arriving discriminator pulse on inputs *A*, *B*, or *C* and is associated with Extension 1 of the extending dead-time logic. During the Compton–TDCR measurements, Extensions 1 and 2 were set equal and both were configured to 40 μs.

Because the TDCR discriminator pulses are generated much earlier than the corresponding γ-gating logic (owing to the shaping and timing in the nHPGe channel and the time needed for the pulse to travel to the nanoTDCR+), the nanoTDCR+ delay functionality was used to delay *TDCR S1* and *TDCR S2* so that the TDCR pulses arrive after the coincidence window has been opened by the nHPGe gate. The applied delay was 3.904 μs, ensuring temporal alignment between the delayed TDCR logic pulses and the ROI-based gating window.

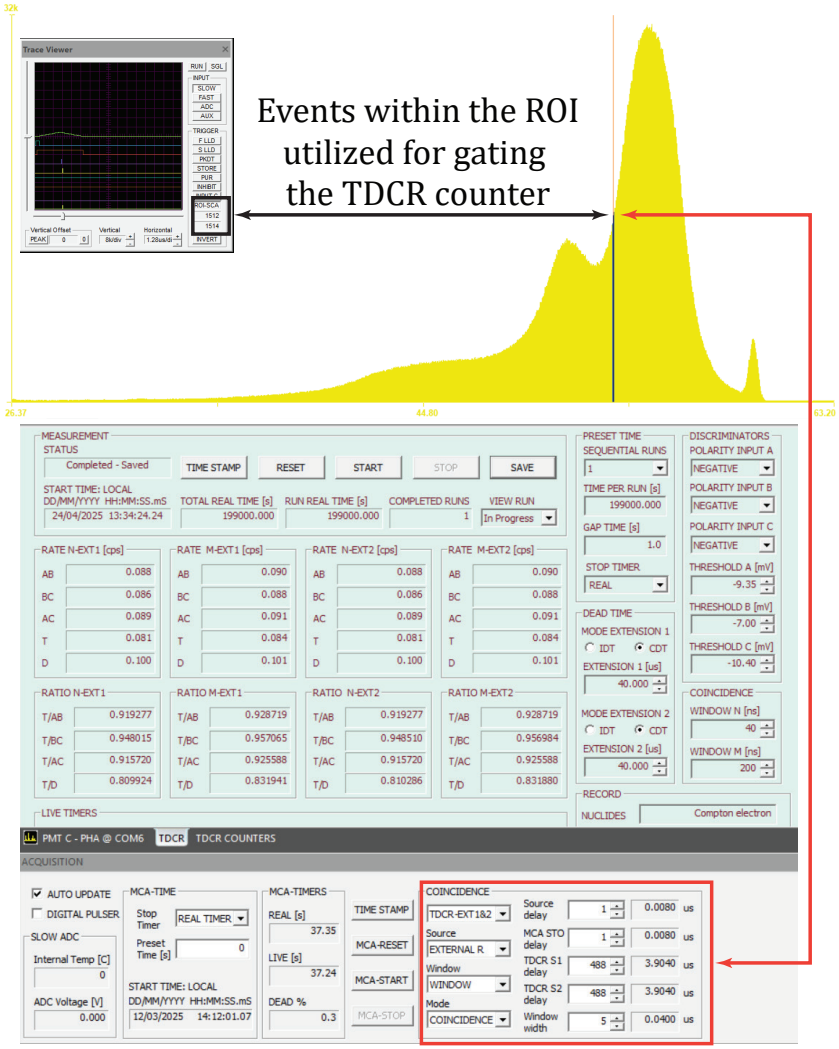

Figure 5.7: Compton spectrum of the ^{241}Am source obtained with the nHPGE detector with a single energy set-up to gate the TDCR channel [150].

In the Compton-coincidence measurements, the CAEN DT5751 digitizer was not used, although it remained connected for conventional LSC operation of the TDCR counter. The principal limitation is that the nHPGe detector is equipped with a transistor-reset charge-sensitive preamplifier; its output is a staircase-like waveform with reset transients, which is not compatible with the DT5751 acquisition and triggering scheme in the present configuration. Even if a resistive feedback HPGe was used, the digitizer might not be suitable option due to the long pulses from the HPGe detector and the energy resolution acquirable with a nanoMCA-II is expected to provide superior energy resolution compared with digitizer owing to its advanced DPP algorithm [158].

In an ideal implementation, the digitizer would acquire both the TDCR and γ channels and write a list-mode file containing the timestamps of pulses in each channel and the energy of each γ-ray event. In offline analysis, one would select a γ-ray energy ROI and, for each γ-event in that ROI, open a coincidence window of width τ; TDCR pulses with timestamps falling within that window would be counted as Compton-coincidence events. This approach would allow the ROI and coincidence conditions to be adjusted a posteriori, eliminating the need for separate acquisitions for different ROIs. In that case, the Compton-electron energy dependence could be extracted from a single long acquisition, rather than repeating measurements for multiple

ROIs. A system following this concept was demonstrated in [16], where a CdTe detector was used for the γ channel but with a much lower energy resolution than our detector.

In the present setup, feeding the logic pulses from the T output of the nanoMCA-II into the digitizer and applying them as an offline gate would not provide a meaningful advantage: the energy selection would still be fixed by the ROI-defined logic generated by the nanoMCA-II, and the digitizer would not add additional spectral or timing information beyond what is already available.

After completing the initial liquid-scintillator study and validating correct operation of the Compton–TDCR system, the setup was upgraded to reduce the total measurement time by enabling multi-ROI Compton-coincidence acquisitions. The upgrade was proposed and implemented by V. Jordanov and required new FPGA, firmware, and software versions for both the nanoMCA-II and the nanoTDCR+.

The hardware modifications were minimal: the T, S and R outputs of the nanoMCA-II were connected to the corresponding T, S and R inputs of the nanoTDCR+ (see Figure 5.8). The nanoMCA-II FPGA was updated to define eight non-overlapping ROIs that operate simultaneously. When the HPGe pulse amplitude falls within any ROI, a coincidence logic pulse is generated; in addition to the timing signal, an address identifying the firing ROI is added to the logic output. This ROI-address information is passed to the nanoTDCR+, which stores the corresponding double- and triple-coincidence counting rates in separate sequential "runs" associated with the ROI index with each 'run' being is a separate TDCR measurement itself. In this way, a single acquisition produces eight simultaneous Compton-coincidence datasets, corresponding to eight distinct Compton-electron energies, each with the full set of coincidence TDCRs.

Implementation of the eight-ROI mode required several timing adjustments. The logic-pulse width generated by the nanoMCA-II was increased to 40 ns, the delays applied to *TDCR S1* and *TDCR S2* were increased to 3.984 μs, and the coincidence window opened by the gating signal was extended to 96 ns. In the *labZY-MCA* software, a dedicated ROI tab was introduced (see Figure 5.10) to define the multi-ROI configuration: the user specifies the start channel of the ROI corresponding to the highest Compton-electron energy, the ROI width, and the channel gap between adjacent ROIs. The software then generates eight equally spaced ROIs of identical width from left to right in the spectrum, corresponding to progressively decreasing Compton-electron energies.

A mechanical upgrade to the system included a dedicated guide for positioning the Compton excitation source (see Figure 5.9). The guide was designed and 3D-printed in PLA to ensure that the ^{241}Am source is precisely centered beneath the LS vial and that its placement is reproducible between measurements. Figure 5.9 (a) shows the guide components: one part is mounted on the underside of the Compton–TDCR metal enclosure, while the second part is fixed to the excitation-source container. The two parts form a keyed interface that allows engagement in a single orientation, thereby ensuring consistent source alignment with respect to the vial.

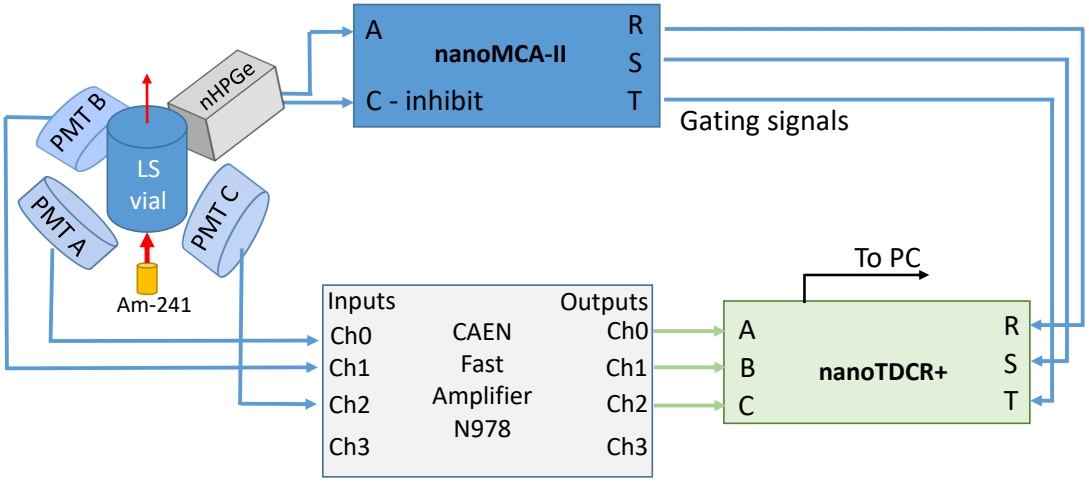

Figure 5.8: Scheme of the upgraded Compton-TDCR acquisition system for 8 simultaneous ROIs in the gamma spectrum.

(a) **(b)**

Figure 5.9: (a) Parts of the 3D-printed source guide. (b) The source guide installed below the TDCR counter with the collimator and source in it [150].

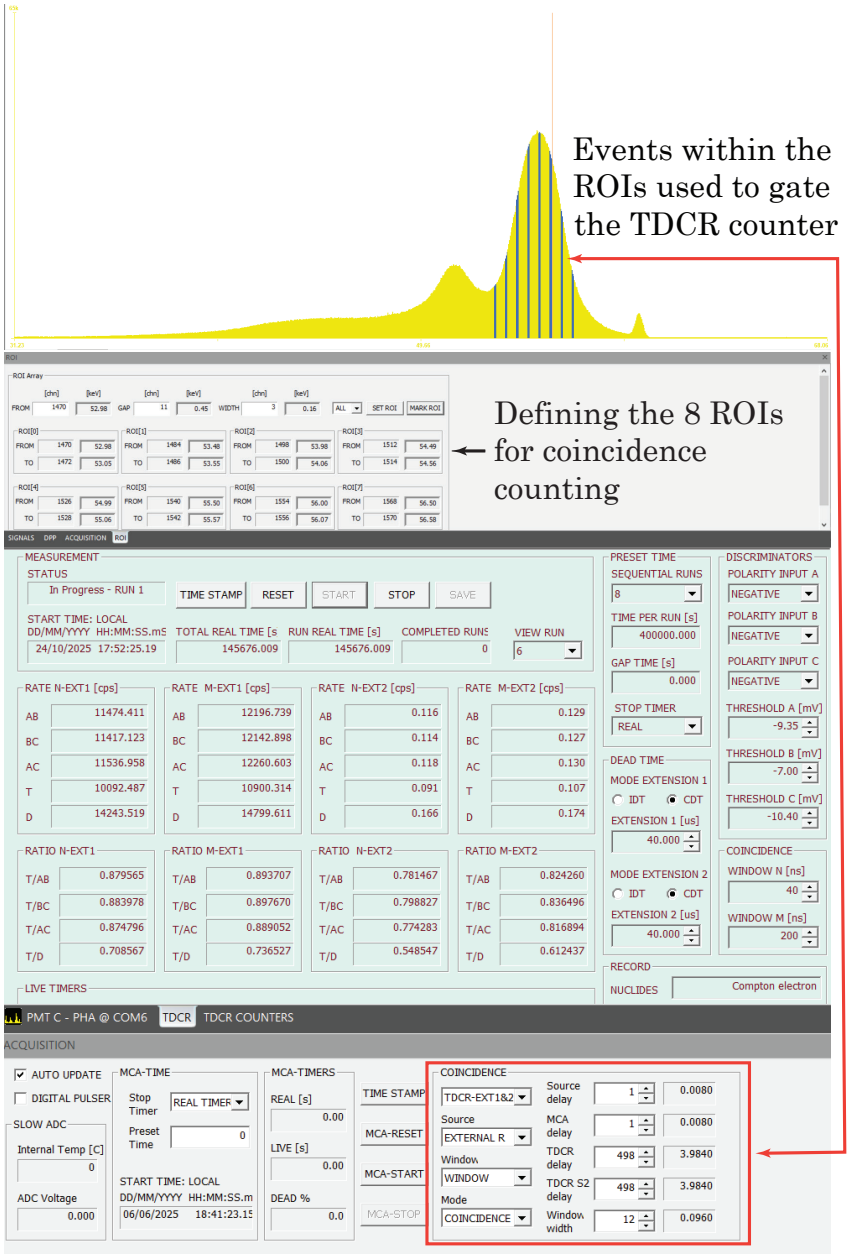

Figure 5.10: Compton spectrum of the ^{241}Am source with the 8 ROIs for gating the TDCR channel.

5.1.5 The ^{241}Am source and collimator

As already mentioned, the Compton coincidence measurements were performed with a ^{241}Am sealed source produced by Amersham. The activity of the source as of April 2025 was 341 MBq with $9.9 \cdot 10^7$ photons/s under 4πsr certified emission rate of the 59.54 keV gamma line. According to the manufacturer, the active component of the source is a ceramic containing americium oxide. Such sources are known to emit neutrons through the (α, n) reaction with oxygen [159]. The approximate neutron emission rate of the source was determined by comparison with a reference Am–Be neutron source, yielding an estimated value of about 625 neutrons/second over 4πsr. The neutron emission rate is sufficiently low that the probability of a simultaneous detection of a Compton-scattered photon in the gamma channel and a neutron interaction within the cocktail is negligibly small, based on our estimation.

Accurate determination of the initial kinetic energy of Compton electrons requires the absence of high-energy gamma-ray emissions from the source. The presence of such gamma-rays could lead to Compton scattering within the scintillation cocktail and their subsequent detection within the corresponding ROI of the HPGe detector, thereby preventing reliable identification of the Compton electron's initial kinetic energy based on scattering kinematics. To confirm that no significant gamma-ray emissions above 59.54 keV are present, the source was measured using a p-type HPGe detector. The results showed that the intensity of the 59.54 keV line is at least 10^4 times greater than that of the most intense higher-energy gamma lines, rendering their potential influence negligible.

The source is enclosed in a cylindrical brass container equipped with a cylindrical lead collimator, as illustrated in Figure 5.11 (a). A 0.2 mm thick copper foil was placed on top of the collimator to filter out the low-energy gamma and X-ray emissions from the ^{241}Am source.

Figure 5.11 (a) shows a simplified representation of the experimental setup that was implemented in the MC simulation to study the source collimation and the resulting Compton spectrum in the nHPGe detector. The source was positioned at a distance that ensures the unscattered gamma-ray beam remains fully confined within the vial walls along the entire height of the vial, as illustrated in Figure 5.11 (b).

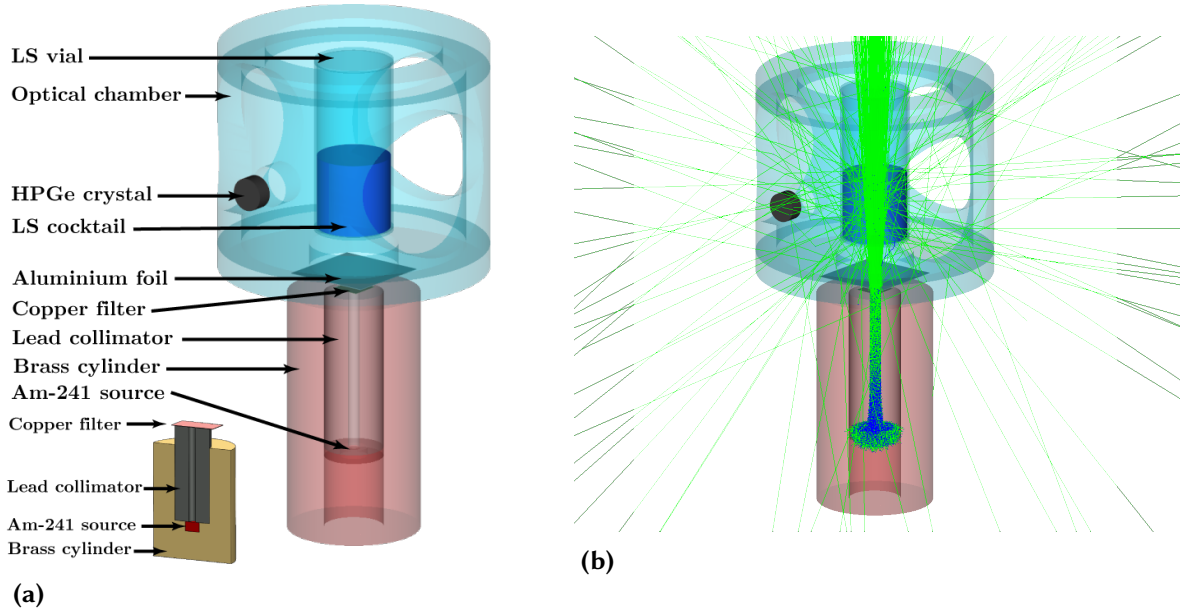

Figure 5.11: (a) Simplified geometry of the experimental setup used in the MC simulation. The inset shows a cross-sectional view of the collimator and the source. (b) Simulated trajectories of gamma-rays (green) and electrons (blue) [150]. Courtesy to S. Ivanov.

The ^{241}Am source collimator as well as the MC GEANT4 simulations of the experiment were made by Simeon Ivanov and the author is much obliged to him.

5.2 Monte Carlo simulation of the Compton scattered gamma-ray spectrum

The experimentally measured spectrum of Compton-scattered photons shown in Figure 5.7 needed careful analysis as the origin of the peak to the left of the peak of the Compton scattered

γ rays was unknown. To ensure a correct interpretation prior to further liquid-scintillator characterization, the origin of this spectral form was investigated in more detail. Monte Carlo simulations based on the GEANT4 toolkit were performed by S. Ivanov to gain more insight in the expected spectrum of Compton-scattered γ rays. Simplified geometry of the experiment that was used in the simulation is presented in Figure 5.11 (a). Figure 5.12 (a) presents the experimental and MC simulated spectra, while Figure 5.12 (b) presents the simulated Compton spectrum resolved by the number of Compton interactions of the 59.54 keV γ rays within the liquid scintillator.

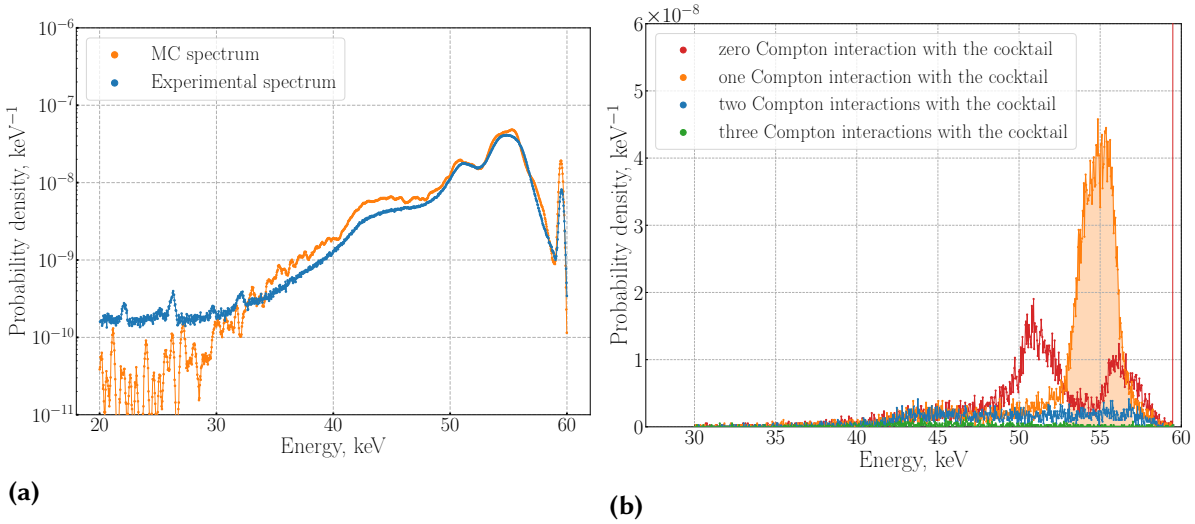

Figure 5.12: (a) Probability density distribution of the energy deposited in the HPGe detector per 59.54 keV photon emitted by the source. (b) Simulated probability density spectrum showing the number of Compton interactions a photon undergoes in the LS cocktail before detection by the nHPGe detector. The shaded region indicates the range of gamma-ray energies selected for Compton coincidence counting [150]. Courtesy to S. Ivanov.

The results shown in Figure 5.12 (a) demonstrate good agreement between the experimental detection probability and the values obtained from the MC simulation. To enable a direct comparison between the simulated and experimental spectra, the MC spectrum was broadened to include the finite energy resolution of the detector. The applied broadening was based on the experimentally measured dependence of the FWHM on energy shown in Figure 5.13.

Since the experimental FWHM values were available only at discrete energies, their energy dependence was fitted with a linear function, shown in Figure 5.13. The fit was used to assign an energy-dependent Gaussian detector response to each simulated deposited energy, after converting the corresponding FWHM value to a standard deviation. For each simulated event, a detected energy was randomly sampled from the Gaussian detector response, and the resulting energies were rebinned to obtain the broadened MC spectrum. This procedure accounts for the finite energy resolution of the detector and provides an equivalent basis for comparison with the experimentally measured spectrum.

The discrepancy observed below 50 keV most likely arises from imperfections in the model of the vial's aluminium cap used in the simulation. The excess of events in the MC spectrum at the 60 keV peak is probably due to an incomplete description of the HPGe detector and the surrounding metallic components in the simulation resulting in more photons undergoing Rayleigh scattering rather than interacting by photoelectric effect or Compton scattering. The origin of the peak at 51 keV in both the experimental and the MC spectra has been understood

from Figure 5.12 (b), where the photons have been classified by the number of Compton interactions before being detected in the nHGPe in the MC simulation.

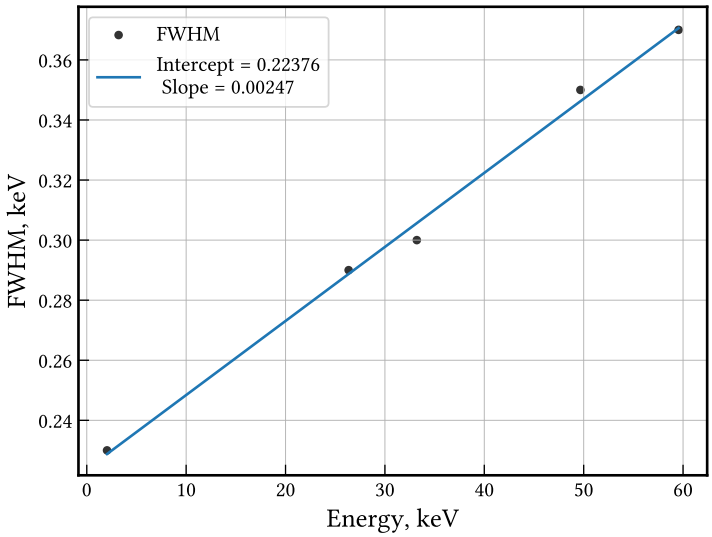

Figure 5.13: Liner fit of the FWHM estimated for the 26.35 keV, 33.21 keV and 59.54 keV gamma lines of ^{241}Am and the 11.87 keV and 59.54 keV germanium Kα escape peaks. The experimental points are obtained during the energy calibration of the nHPGe detector with an ^{241}Am point source. FWHM study is from [157].

Figure 5.12 (b) presents the MC spectrum of photons undergoing zero, one, or multiple Compton interactions within the cocktail before being detected by the nHPGe detector. Events classified as zero Compton interactions correspond to photons that do not scatter in the cocktail and therefore cannot produce a Compton electron in the scintillator volume. Instead, they are most plausibly scattered in surrounding materials, such as the vial glass (giving rise to the peak at 56 keV) or the aluminium cap (peak at 51 keV). These components are irrelevant for the Compton–TDCR dataset, because they are not accompanied by scintillation light from a Compton electron in the cocktail and therefore do not contribute to coincidences with the TDCR channel except for a chance of random γ-TDCR coincidence.

The 53–56 keV interval (highlighted in Figure 5.12 (b)) is intended to select predominantly single-scatter events in the cocktail, for which the scattered-photon energy provides a well-defined estimate of the corresponding Compton-electron energy. In this region, the MC results show that single-scatter events dominate, while the contribution from multiple Compton interactions remains small: the ratio of double to single Compton interactions is 0.05. Since multiple-scatter events break the one-to-one relationship between the nHPGe energy and the Compton-electron energy, their limited contribution indicates that the energy selection is only weakly affected and that any associated bias is expected to be negligible. In future upgrades, the multiple-scatter fraction could be reduced by decreasing the collimator diameter, at the expense of a lower coincidence counting rate.

Taken together, this analysis demonstrates that Compton–TDCR measurements targeting Compton-electron energies in the 3–6 keV range can be performed without significant bias from multiple-Compton-scattering events. The Compton–TDCR system was therefore considered suitable for systematic measurements of liquid-scintillator response in this low energy region.

5.3 Compton-TDCR experiments for estimating liquid scintillators non-linearity

With the first major goal of the thesis completed - designing, setting up and MC validating of the CTDCR-SU system it was then time to step to the second major goal: the study of

liquid-scintillator response using the newly developed Compton-TDCR spectrometer. Such measurements are particularly important at low electron energies, where organic scintillators exhibit their strongest non-proportionality. This low-energy response has an impact on TDCR efficiency calculations and on the uncertainty of activity standardization for low-energy β-emitting and electron-capture radionuclides.

To study the light response of a given liquid scintillator, a sample with LS of at least 10 mL is prepared in a glass or plastic vial and placed in the optical chamber of the CTDCR-SU system. The collimated ^{241}Am source is positioned beneath the counter, as shown in Figure 5.5 (b). The TDCR channel is gated by the γ channel: when an event is recorded within a selected ROI in the Compton scattered photon spectrum, a gating signal is sent to the nanoTDCR+ module (see Section 5.1.4). In this way, TDCR events are accepted only when they are temporally correlated with a scattered photon of selected energy.

For a single Compton-scattering event, the energy deposited by the Compton electron is determined by the difference between the incident γ-ray energy and the energy of the scattered photon measured by the nHPGe detector. Thus, selecting a narrow ROI in the scattered photon spectrum also selects a corresponding range of Compton electron energies. Since the range of these low-energy electrons is small compared with the scintillator volume, their kinetic energy can be assumed to be fully deposited in the liquid scintillator.

The light response is therefore expressed as the mean number of detected photoelectrons produced in the TDCR channel by a Compton electron of energy E. Converting the number of detected photoelectrons to the absolute number of scintillation photons produced in the liquid would require additional estimates for losses due to total internal reflection, the optical collection efficiency, and the quantum efficiencies of the individual PMTs. The photon losses and the quantum efficiency of each PMT are generally difficult to determine. For this reason, the present study uses the mean number of detected photoelectrons as an experimental measure of the scintillator response, since this quantity is directly obtained from the TDCR coincidence ratios and characterizes the response of the complete CTDCR-SU detection system.

In this thesis, the average number of photoelectrons registered in each PMT at energy E is determined according to Equation (5.1) [15]:

$$\bar{n}_Z(E) = -3\ln\left(1 - \frac{T(E)}{XY(E)}\right),\ XY = (AB, BC, AC),\ Z \neq X \text{ or } Y \tag{5.1}$$

where A, B, and C denote the three PMTs, AB, BC, and AC represent the coincidence counting rates between pairs of PMTs, and T is the triple coincidence counting rate of the TDCR channel in coincidence with gamma-channel events at a specific energy E (refer to Section 2.5 for details on the derivation of Equation (5.1)). The total mean number of detected photoelectrons is obtained by summing the contributions from all three PMTs:

$$\bar{n} = \sum_{i}^{A,B,C} \bar{n}_i\,, \tag{5.2}$$

where $\bar{n}(E)$ here is kB independent estimate. The experimentally measured light response of the studied scintillator, can be used directly in the TDCR method but it is also interesting to investigate if Birks model is applicable to describing the expected non-linearity of the light output. Therefore, the mean number of photoelectrons as a function of the deposited energy was fitted to Birks' semi-empirical ionization quenching model [1]:

$$L(E) = \int_0^E \frac{\mathrm{d}E'}{1 + kB\,\frac{\mathrm{d}E'}{\mathrm{d}x}} \tag{5.3}$$

where $\mathrm{d}E'/\mathrm{d}x$ corresponds to the stopping power of an electron of energy E', and kB denotes the ionization quenching constant.

The average number of detected photoelectrons is given by:

$$\bar{n}(E) = S \cdot L(E) \tag{5.4}$$

where S represents the mean number of photoelectrons detected per keV of energy deposited within the scintillator in the absence of ionization quenching. The value of this parameter is governed by the scintillator's intrinsic light yield, the PMT photocathode efficiency, and the experimental geometry.

The fitting procedure provides estimates of the ionization-quenching parameter kB (in cmMeV^{-1}) and S (in keV^{-1}). An independent estimate of kB can also be obtained using the efficiency-variation method (see Section 2.4.5). This method was applied to all liquid scintillators studied in this thesis as part of the benchmarking of the TDCR channel of the CTDCR-SU system (see Chapter 6), thereby providing a basis for comparison between the kB values obtained from Compton-TDCR measurements and from conventional TDCR efficiency variation.

Since the efficiency variation method requires a radionuclide to be present in the measured liquid-scintillator sample, the same samples were also used in the Compton-TDCR measurements. The presence of the radionuclide does not contribute to the Compton-TDCR coincidence signal. Its decay events produce scintillation pulses in the TDCR channel, but they are not accompanied by time correlated photons in the selected ROI of the γ-ray detector. Therefore, they can only contribute through random coincidences, i.e. when an uncorrelated radionuclide-induced TDCR pulse occurs within the coincidence window started by an unrelated nHPGe logic pulse.

The magnitude of this random contribution was evaluated experimentally by applying an additional delay of more than 2 μs to the TDCR $S2$ signal (first arriving pulse from either PMT A or B or C; see Section 5.1.4). In this configuration, true Compton-TDCR coincidences are suppressed, and only random coincidences with the logical pulse from the nHPGe detector are expected. The counting rate measured under these conditions was considered negligible compared to the coincidence counting rate obtained for the lowest energy of the Compton electron. The contribution of radionuclide-induced random coincidences was therefore considered negligible for the determination of the Compton electron light response.

Data analysis

The electron stopping power in Equation (5.3) between 100 eV and the initial Compton electron energy was calculated using the ICRU 37 formula [160] (see Section 2.1.7 for more details), with a linear extrapolation applied below 100 eV. The integration of Equation (5.3) employed the *quad* function from the *scipy.integrate* package [161], using the scintillator's mean ionization potential as the lower limit. The *quad* integration produced results identical to those from the *Romberg* and *Simpson's rule* methods, though the latter were omitted due to their lower computational efficiency.

The fitting procedure employs orthogonal distance regression (ODR), implemented in the *scipy.odr* package, which provides an interface to the ODRPACK library [162]. ODRPACK performs a trust-region Levenberg–Marquardt minimization. The motivation for using ODR is

that the fitting procedure takes as weights the estimated uncertainties for both the deposited energy and the mean number of photoelectrons. The fit is considered to converge when the relative change in the residual sum of squares (RSS) becomes sufficiently small, indicating that the weighted sum of squared observation errors meets the convergence criterion (Sum of Squares Tolerance $< 10^{-12}$) [162].

In this thesis, the uncertainty assigned to the selected Compton electron energy is treated as a critical parameter in the investigation of the non-proportional response of liquid scintillators. The Compton-electron energy is inferred from the energy of the scattered photon measured by the nHPGe detector. The dominant contributions to the uncertainty of the Compton electron energy considered here are the finite energy resolution of the nHPGe detector and the width of the ROI used to select the scattered-photon events.

In a Compton-TDCR measurements reported by Sabot *et al.* [16], events selected within a single channel of a CdTe detector, corresponding to an energy interval of approximately 270 eV, were considered sufficiently narrow to approximate the associated Compton electrons as monoenergetic. However, an explicit uncertainty budget for the selected Compton-electron energy was not reported. For the aim of this thesis, the uncertainty of the Compton electron energy was evaluated and assigned to each measured light-response point.

The energy-resolution study reported in [157] gave a a standard deviation $\sigma_{\mathrm{ph}} = 157$ eV (FWHM/2.35) for the 59.54 keV photopeak of a point-like ^{241}Am source measured with the nHPGe detector. For the Compton–TDCR measurements, the TDCR channel was gated using an ROI spanning three MCA channels in the Compton-scattered photon spectrum, with a total width of $w_{\mathrm{ROI}} = 120$ eV. The uncertainty associated with the finite ROI width was modelled by a rectangular probability distribution, giving a standard uncertainty of $w_{\mathrm{ROI}}/\sqrt{12}$. The combined standard uncertainty of the Compton electron energy is therefore [150]:

$$\sigma_E = \sqrt{(w_{\mathrm{ROI}}/12)^2 + \sigma_{ph}^2} = 161\,\mathrm{eV}, \tag{5.5}$$

In this thesis, the statistical uncertainty of the triple-coincidence counts was considered to be the dominant contribution to the uncertainty of the mean number of photoelectrons detected by an individual PMT. For PMT A, the standard uncertainty of the mean number of detected photoelectrons, given in Equation (5.1), can be expressed as

$$\sigma_{\bar{n}_A} = \frac{\frac{C_T}{C_{BC}}}{\sqrt{C_T}\left(1 - \frac{C_T}{C_{BC}}\right)}, \tag{5.6}$$

where C_T and C_{BC} are the counts for the triple and BC coincidences. The uncertainty of the photoelectron number for PMTs B and C can obtained in a similar manner. Applying the uncertainty propagation formula to Equation (5.2), the uncertainty of the total mean number of detected photoelectrons can be expressed as:

$$\sigma_{\bar{n}} = \sqrt{\sigma_{\bar{n}_A}^2 + \sigma_{\bar{n}_B}^2 + \sigma_{\bar{n}_C}^2}. \tag{5.7}$$

5.3.1 Compton-TDCR results

The first Compton-coincidence measurements with the CTDCR-SU system were performed to study the non-linear light response of a toluene+PPO liquid scintillator. These measurements used the acquisition configuration shown in Figure 5.6, which allowed one Compton-electron energy to be measured per run. The scintillation sample was the ^{3}H-Wallac source, also used

in the efficiency variation measurements (see Section 6.1); the vial walls were wrapped with diffusive tape to improve light-collection uniformity.

For each selected γ-ray ROI, the corresponding Compton electron energy was determined from the measured Compton scattered photon energy, and the TDCR coincidence ratios were used to calculate the mean number of detected photoelectrons. Repeating this procedure for several ROI positions provided the experimental light-response curve of the scintillator in the range between 3 and 6 keV. The resulting response of the toluene+PPO scintillator, obtained with a resolving time of 40 ns, is shown in Figure 5.14.

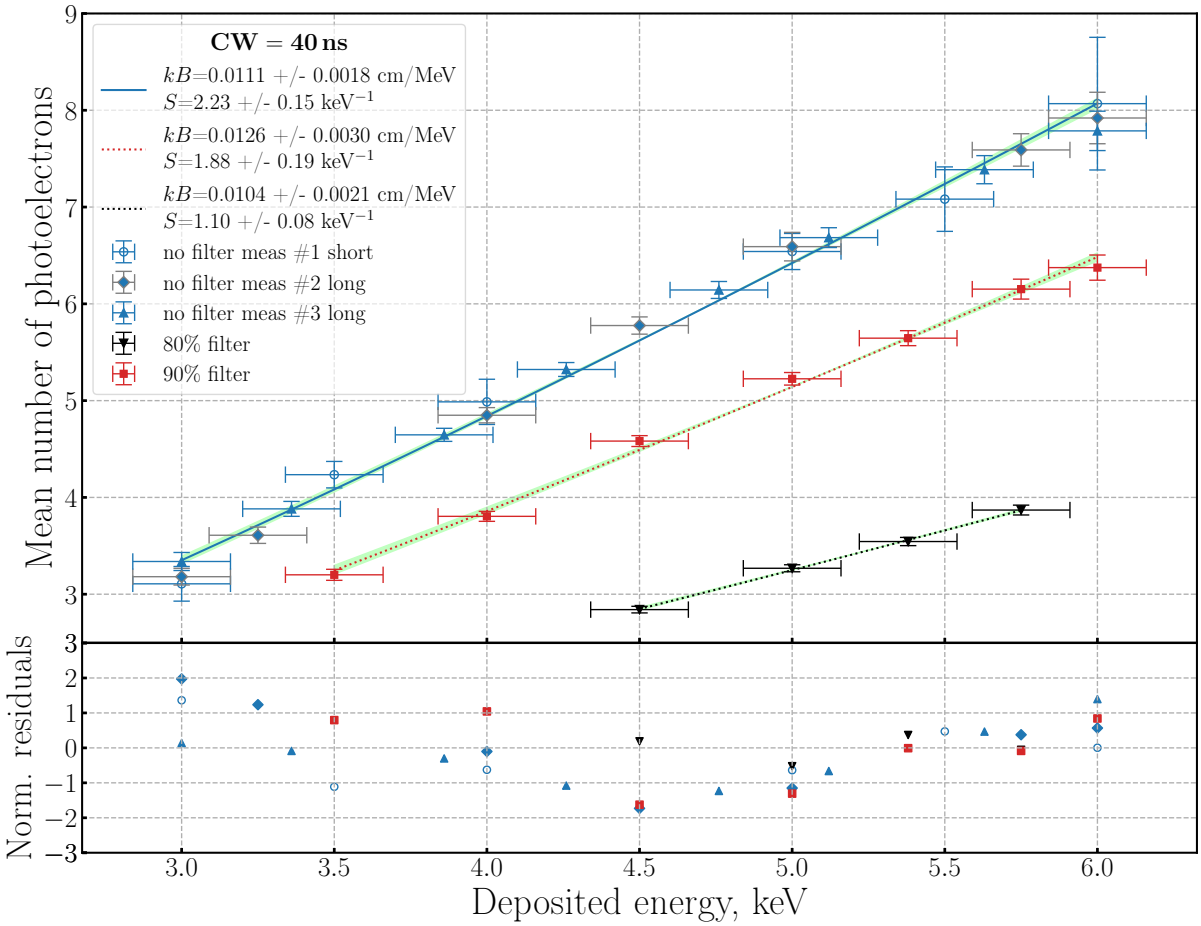

Figure 5.14: Dependence of the mean number of photoelectrons on the deposited energy in the scintillator for measurements acquired with a 40 ns coincidence window (CW). Markers in blue show the measurement of the source performed without filter, the markers in red show measurement performed with 90% grey fileter and the markers in black show measurements performed with 80% grey filter. Highlighted in green is the 1σ confidence interval. The error bars represent the estimated standard uncertainties. The values of the parameters determined by the fit (S, kB) are shown in the legend with their estimated uncertainty as returned from the fitting function. [150].

The Birks' formula was fitted to measurements obtained both without a grey filter and with filters of varying transmission. All measurements, with the exception of the data labelled "short", were acquired over a two-day period. The mean number of detected photoelectrons per keV energy deposited in the scintillator S depend on the light yield, the measurement geometry and the quantum efficiency of the PMTs. The ionization quenching parameter kB should depend only on the liquid scintillation cocktail and should remain constant under different

measurement conditions. It was, then, interesting to measure the same sample under different detection efficiencies. This was accomplished by placing optical gray filters around the vial containing the liquid scintillator. This way, the properties of the cocktail remain unchanged and only a decrease in the number of detected photoelectrons is expected. The values of the *kB* and *S* parameters together with the uncertainties estimated from the fitting procedure are indicated in the legend of Figure 5.14. The fitted *kB* values differ slightly between the three curves, but no systematic dependence on the used filters is observed. Moreover, the values remain consistent within the corresponding fit uncertainties. This behaviour suggests that the fitted ionization quenching parameter is not affected by the reduction of the detected light as should be expected.

In contrast, the detected number photoelectron per unit deposited energy, is expected to depend on the optical transmission of the filters. Since the filters used in this study were not calibrated, the absolute reduction of *S* could not be quantified. The values of *S* obtained from the fit, however, show the expected trend, decreasing as the filter transmission is reduced. This suggests that Compton–TDCR measurements could also be used to estimate the transmission of optical filters by comparing the value of the fitted parameter *S* obtained with a filter to the corresponding value obtained without a filter under identical experimental conditions.

For the measurements performed without optical filtering, the *kB* value obtained from the Compton-TDCR fit is in good agreement with the value determined by the efficiency variation technique (*kB* =0.122(4) cm/MeV, see Section 6.1) using the same detector and liquid scintillator cocktail. In addition, the *kB* value reported in Section 6.2, obtained for the same scintillator but using a different radionuclide (^{14}C, *kB* =0.110(4) cm/MeV), is also consistent within its uncertainty with the value obtained from the Compton-TDCR measurements. This agreement shows that the *kB* value obtained from Compton-TDCR measurements is consistent with the values independently determined by the TDCR efficiency variation method.

To examine the influence of the coincidence resolving time on the scintillator response, the data were evaluated using both 40 ns and 200 ns coincidence windows. Owing to the functionality of the nanoTDCR+, these two resolving times were applied to the same acquisitions and therefore to the same set of pulses. The scintillator response results obtained with the 200 ns coincidence window are shown in Figure 5.15.

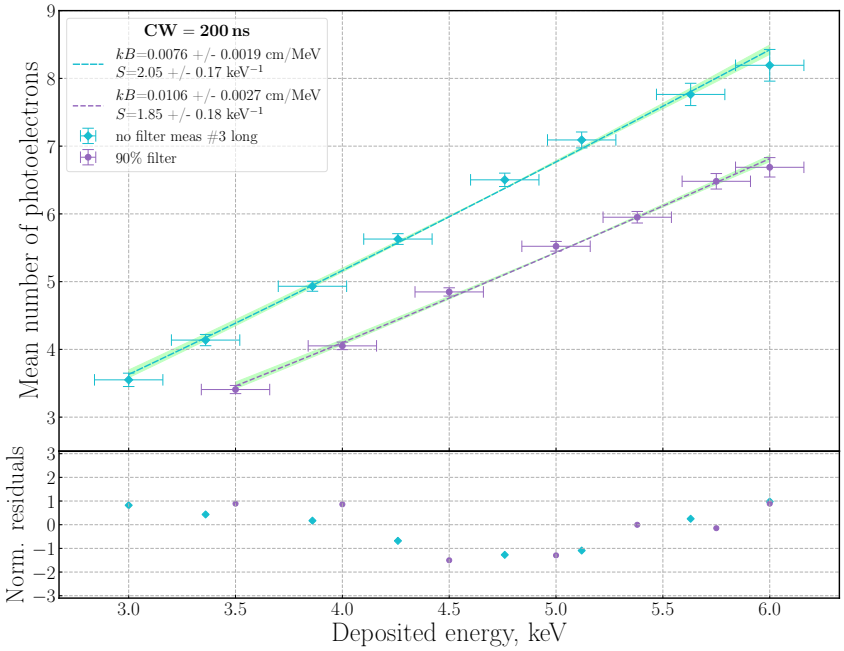

Figure 5.15: Dependence of the mean number of photoelectrons on the deposited energy in the scintillator for data evaluated with a 200 ns coincidence window (CW) [150].

For ease of comparison, the fitted response curves obtained using 40 ns and 200 ns coincidence windows are plotted together in Figure 5.16. The figure illustrates how the measured light response curve changes by changing the coincidence window.

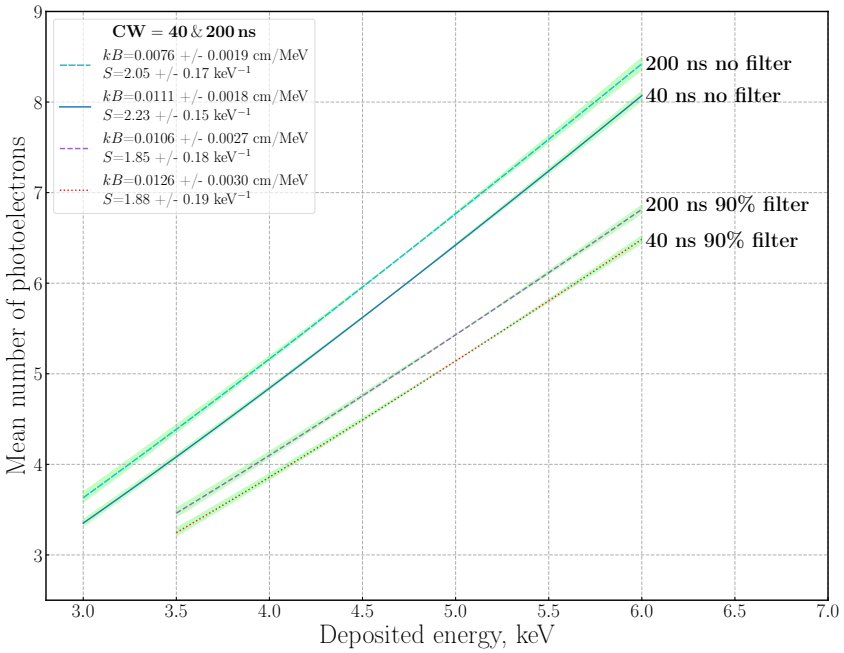

Figure 5.16: Fitted curves of the experimental data evaluated with 40 ns and 200 ns coincidence windows (CW), obtained both without a filter and with a 90% transmission filter [150].

The results obtained with the 200 ns coincidence window yield systematically lower *kB* values than those obtained with the 40 ns window. A similar decrease was also observed when

the efficiency variation method was applied using the same two resolving times. This behaviour should not be interpreted as a physical dependence of the Birks parameter on the coincidence window.

The observed decrease of the fitted *kB* value indicates that the 200 ns coincidence window is not suitable for estimating *kB* for the Birks' model. A longer coincidence window allows a larger fraction of delayed scintillation photons to contribute to the TDCR coincidences, including contributions from delayed fluorescence. Since Birks' formula describes the non-linearity of the prompt scintillation yield and does not include the kinetics or intensity of delayed fluorescence, fitting the 200 ns data with this model seems to be an acquisition dependent parameter.

The same experimental data shown in Figure 5.14 were also analysed using a fixed *kB* parameter. First, Birks' formula was fitted to the measurements performed without an optical filter, with both *kB* and *S* treated as free parameters. The *kB* value obtained from this fit was then fixed and used in the fit of the measurements performed with grey filters, for which only the *S* parameter was varied. This procedure tests whether the data obtained with filters can be described using the same ionization quenching parameter, while accounting for the reduced detected light output through a change in the mean photoelectron yield.

The result of is shown in Figure 5.17. The fitted curves for the data obtained with filters reproduce the experimental points within the estimated uncertainties, indicating that the reduction in detected photoelectron yield caused by the grey filters can be described primarily by a decrease of (S), without requiring a different value of *kB* .

Figure 5.17 presents the same experimental data shown in Figure 5.14. The Birks' formula was first fitted to the measurements obtained without a filter, after which the resulting *kB* value was fixed and subsequently applied to fit the experimental data acquired with the grey filters.

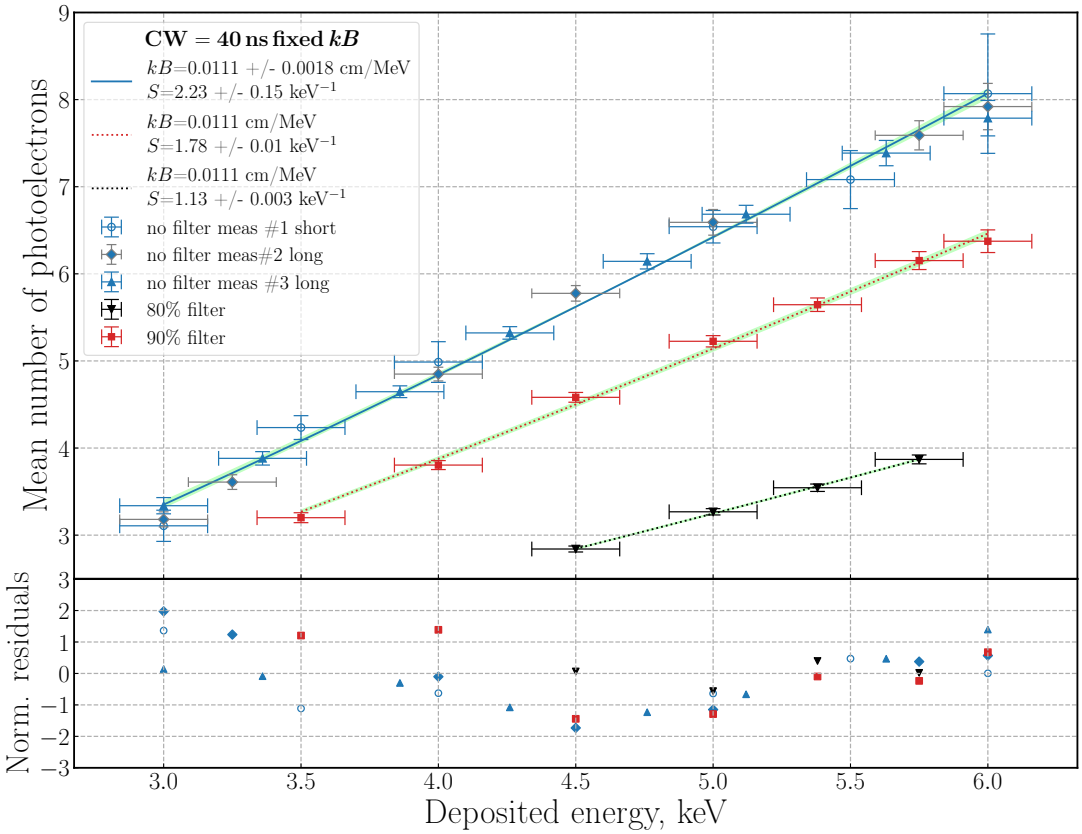

Figure 5.17: Dependence of the mean number of photoelectrons on the energy deposited in the scintillator. The *kB* parameter was fixed for the fits of the data obtained with grey filters, and the shown uncertainties were obtained from the fitting procedure [150].

The ability to obtain a satisfactory fit to the experimental data while keeping the *kB* parameter fixed suggests that the estimated uncertainties are reasonable. It should be noted that the correlation coefficient between the *kB* and *S* parameter is approximately 0.99. This may means that the estimated mean number of photoelectrons adjusts to compensate for the difference between the fixed *kB* value and the value obtained from the fits shown in Figure 5.14.

After the initial Compton–TDCR measurements, the CTDCR-SU system was upgraded to enable multichannel Compton-coincidence acquisition, as described in Section 5.1.4. In the upgraded setup, eight non-overlapping ROIs in the scattered photon spectrum can be selected simultaneously, allowing the scintillator response at eight Compton electron energies to be measured within a single acquisition. This represents a significant improvement over the initial configuration, where only one selected Compton electron energy could be measured per run.

Following the upgrade, Compton-coincidence measurements were repeated using the same ^{3}H-Wallac source in order to verify that the upgraded acquisition logic and multi-ROI event gating did not introduce a systematic change in the measured light response. The objective of this measurement was therefore not only to obtain a new estimate of the *kB* and *S* parameters, but also to confirm consistency with the results obtained before the upgrade and with the independent *kB* value determined by the TDCR efficiency variation method. The scintillator non-linearity results obtained before and after the upgrade are shown in Figure 5.18.

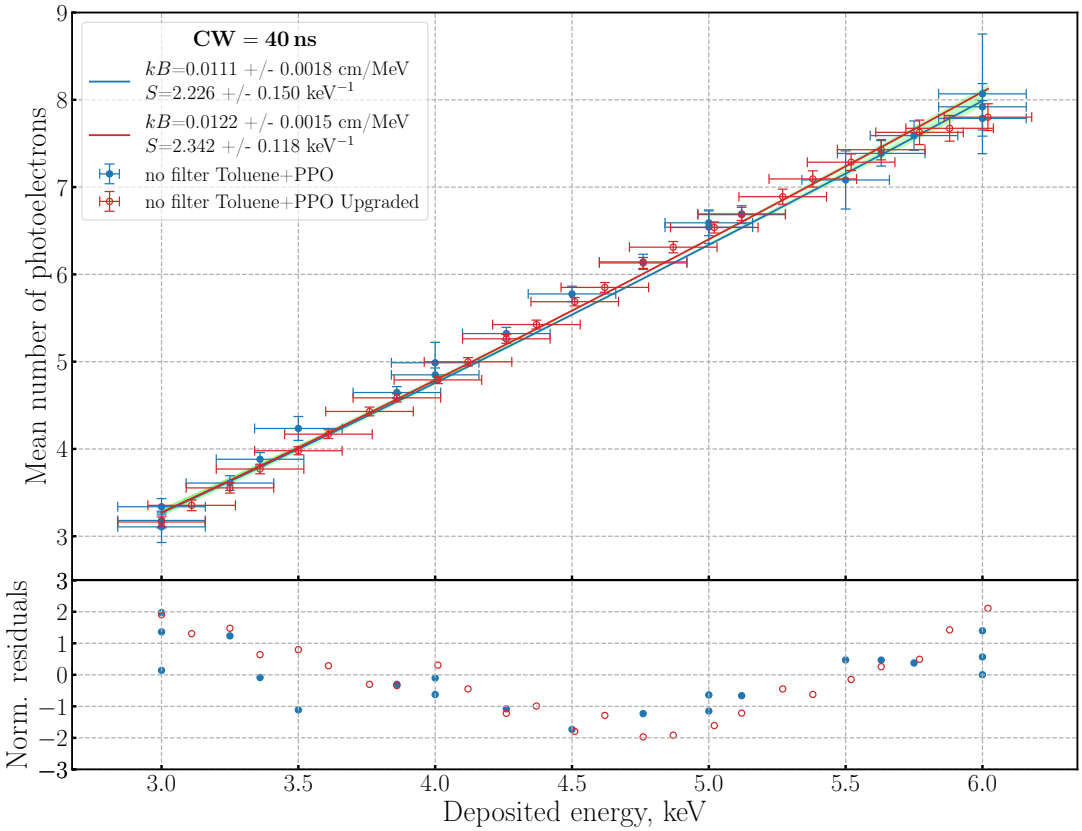

Figure 5.18: Dependence of the mean number of photoelectrons on the energy deposited in the scintillator before and after the upgrade of the CTDCR-SU system.

The results show good agreement between the *kB* values obtained before and after the upgrade, demonstrating that the multichannel acquisition mode reproduces the response measured with the initial single ROI setup. The *kB* value obtained after the upgrade is also in excellent agreement with the value (*kB* =0.0122(4) cm/MeV) determined independently by the efficiency variation method (see Section 6.1). This agreement confirms that the upgraded CTDCR-SU system provides consistent estimates of the scintillator non-linearity while substantially reducing the measurement time required to cover several Compton electron energies.

As an additional validation of the upgraded system, the *kB* parameter was also estimated separately for the three individual PMTs. In contrast to the results reported by Bignell *et al.* [163], where the Compton excitation source was placed inline with one of the PMTs, the *kB* values obtained here for the three PMTs are mutually consistent within their uncertainties. The scintillator response for the three PMT, shown in Figure 5.19, and the *kB* values given in the legend indicate that the three optical channels of the CTDCR-SU system provide coherent estimates of the ionization quenching parameter.

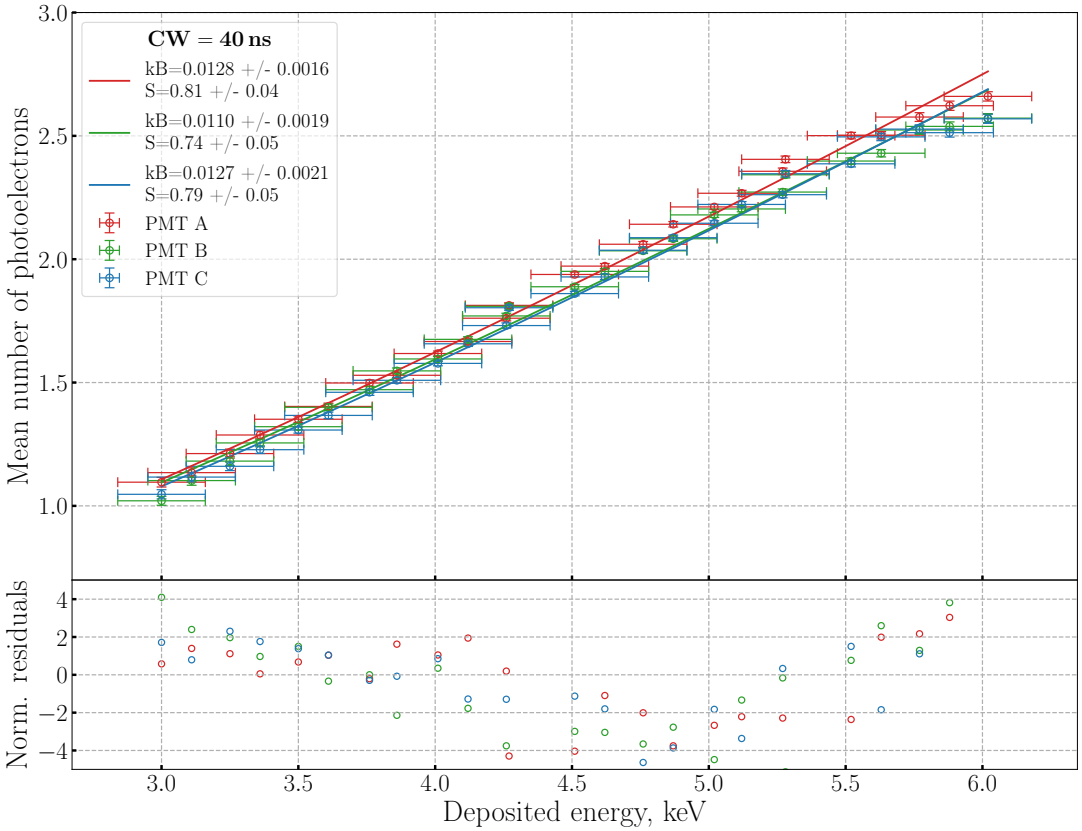

Figure 5.19: Dependence of the mean number of photoelectrons on the energy deposited in the scintillator for each of the PMTs.

After the characterization of the ^{3}H source in toluene+PPO, further Compton–TDCR measurements were performed using liquid scintillation samples with different radionuclides and scintillator compositions.

A ^{14}C sample was prepared from an acetone solution of ^{14}C-containing benzoic acid. Approximately 1 mL of this solution was added to 15 mL of Ultima Gold AB (UG AB) scintillation cocktail. The source was prepared in a 20 mL low-diffusion polyethylene vial fitted with a standard plastic cap. Polyethylene vials were selected because their light-diffusing walls improve the collection of scintillation photons and can therefore increase the detection efficiency of the TDCR channel (see Chapter 4).

The resulting Compton-TDCR light-response curve for the ^{14}C sample is shown in Figure 5.20.

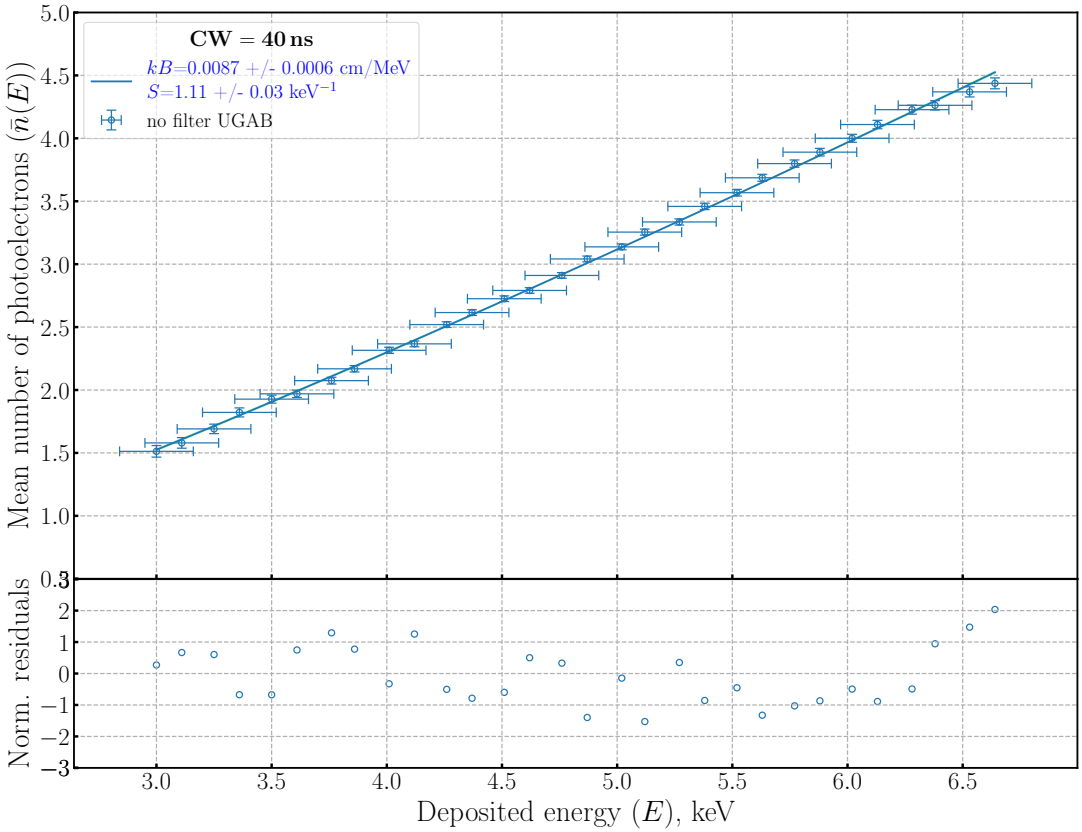

Figure 5.20: Mean number of detected photoelectrons as a function of deposited energy in UG AB for a ^{14}C sample, obtained from measurements with a 40 ns coincidence window (CW).

The *kB* value obtained from the Compton-TDCR fit for the ^{14}C/UG AB sample agrees, within its uncertainty, with the value determined by the TDCR efficiency variation method (*kB* =0.00080(6) cm/MeV; see Section 6.6). This agreement confirms the consistency of the two approaches for estimating the ionization quenching parameter of this scintillator.

After the study of the ^{14}C sample in UG AB, the measurements were continued with another radionuclide–scintillator combination in order to investigate the response of Ultima Gold (UG) cocktail. For this purpose, a ^{63}Ni source was prepared and measured with the Compton–TDCR system.

The ^{63}Ni sample was prepared from a (0.1) M HCl solution containing a $NiCl_2$ carrier. The stock solution was diluted, and approximately (0.1) mL of the resulting solution was mixed with 15 mL of Ultima Gold (UG) scintillation cocktail. The sample was prepared in a standard 20 mL glass vial fitted with a cap lined with aluminium foil. The vial walls were wrapped with diffusive adhesive tape in order to reduce the effects of internal reflection and improve the uniformity of light collection.

The resulting Compton-TDCR light-response curve, expressed as the mean number of detected photoelectrons as a function of the deposited Compton electron energy, is shown in Figure 5.21.

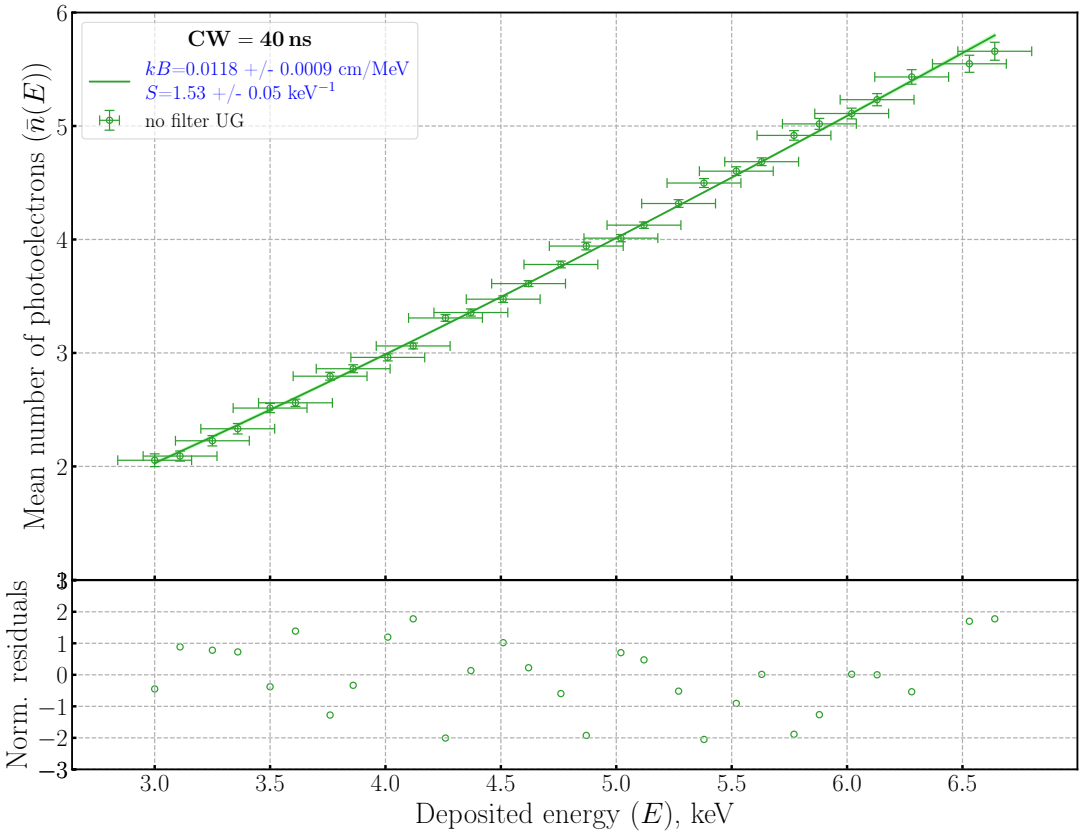

Figure 5.21: Mean number of detected photoelectrons as a function of deposited energy in UG for a ^{63}Ni sample, obtained from measurements with a 40 ns coincidence window (CW).

The *kB* value obtained from fitting the Compton–TDCR response of the ^{63}Ni/UG sample is consistent, within its uncertainty, with the value determined by the TDCR efficiency-variation method, (*kB* =0.00105(5) cm/MeV; see Section 6.7). This agreement provides another example where the ionization quenching parameter obtained from the directly measured scintillator response agrees with the value obtained from traditional TDCR analysis.

As a final radionuclide–scintillator combination, a ^{55}Fe sample in Ultima Gold was measured with the Compton-TDCR spectrometer. This measurement was of particular interest because UG was also used for the ^{63}Ni sample, allowing the Compton-TDCR results obtained for two different radionuclides prepared in the same commercial scintillation cocktail to be compared.

The ^{55}Fe sample was prepared from stock solution and approximately 0.7 g of it was added to 15 mL of UG scintillation cocktail. The sample was prepared in a standard 20 mL glass vial fitted with a foil-lined cap. As for the ^{63}Ni/UG sample, the vial walls were wrapped with diffusive adhesive tape in order to reduce internal reflection effects and improve light collection uniformity.

The Compton-TDCR response of the ^{55}Fe/UG sample was measured without an optical filter and with two grey filters. In contrast to earlier ^{3}H/toluene+PPO measurements, a larger number of experimental points was acquired, providing a more detailed sampling of the light response curve. The resulting dependence of the mean number of detected photoelectrons on the deposited Compton-electron energy is shown in Figure 5.22.

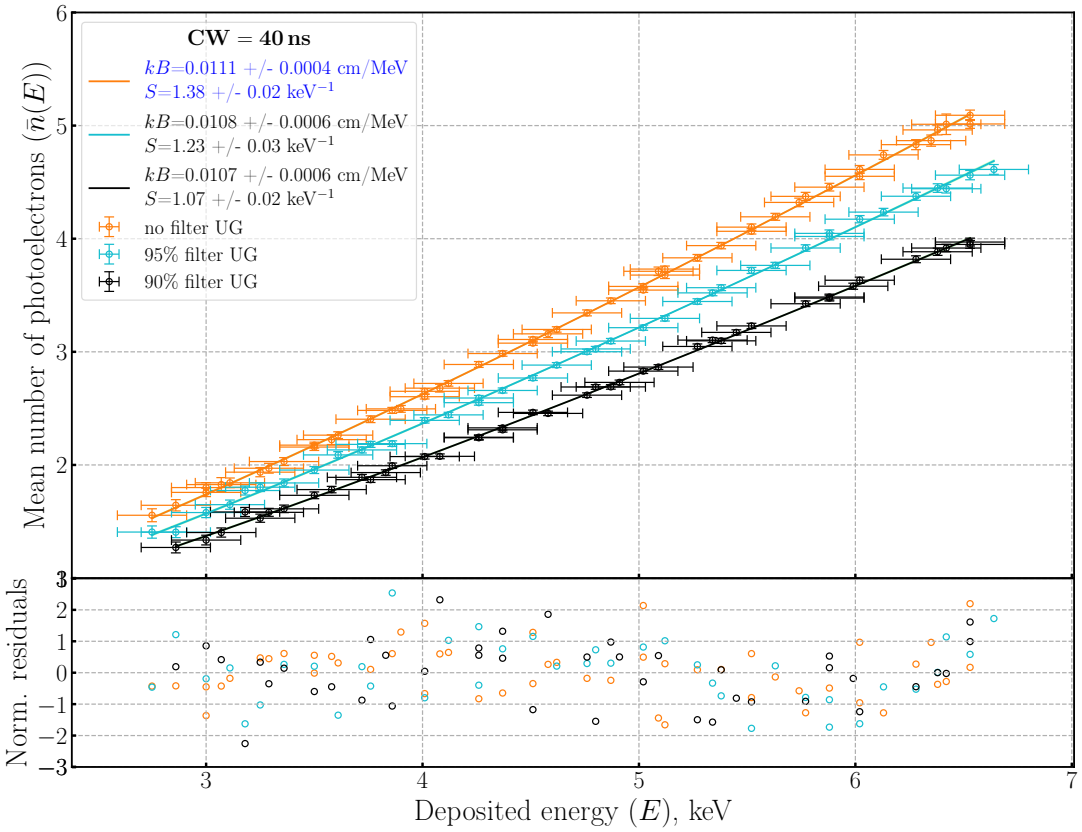

Figure 5.22: Mean number of detected photoelectrons as a function of deposited energy in UG for a ^{55}Fe sample, obtained from measurements with a 40 ns coincidence window (CW) and with no fileter and two different filters.

The fitted *kB* values obtained for the measurements without filter and with the two grey filters are coherent within their uncertainties. This confirms the ionization quenching parameter is related to the scintillator and should not change when the detected light level is reduced by optical filtering. By contrast, the fitted S parameter decreases systematically with increasing optical density of the filters, as expected from the reduced number of detected photoelectrons.

In the efficiency calculation code used for ^{55}Fe liquid-scintillation measurements, the Birks parameter is set to *kB* =0.01 cm/MeV. The values obtained from the Compton-TDCR fits are consistent with this default value, supporting its use as a reasonable choice for UG in the present measurement conditions. Furthermore, the *kB* values obtained for the ^{63}Ni/UG and ^{55}Fe/UG samples agree within the fit uncertainties. Since both samples were prepared in the same scintillation cocktail and with similar source chemistry, this agreement provides additional support for the reliability of the Compton-TDCR determination of the ionization quenching parameter in UG.

The Compton-TDCR measurements performed for the investigated scintillator-radionuclide combinations showed a consistent trend. The *kB* values obtained by fitting the measured Compton-electron light-response curves agree, within the corresponding uncertainties, with the values obtained independently by the TDCR efficiency-variation method, as summarized in Table 5.1. This agreement is good indication for correct *kB* determination, since the comparison is made using two experimentally different approaches: one based on the Compton-electron response, and the other on TDCR efficiency variation.

This result is particularly relevant in view of the study by Sabot *et al.* [16]. In that work the

kB values obtained from the Compton-TDCR measurements were approximately twice as large as values usually reported or expected for organic scintillators. The consistency achieved in the present work therefore represents a significant outcome of the CTDCR-SU measurements and supports the reliability of the obtained ionization quenching parameters.

Table 5.1: Comparison of the ionization quenching parameter *kB* obtained from Compton-TDCR measurements and from the TDCR efficiency variation method for the scintillator-radionuclide combinations studied in this thesis.

Radionuclide	Scintillator	*kB* from Compton-TDCR cm/MeV	*kB* from efficiency variation cm/MeV
^{3}H	toluene+PPO	0.0122(15)	0.0122(4)
^{14}C	Ultima Gold AB	0.0087(6)	0.0080(6)
^{63}Ni	Ultima Gold	0.0118(9)	0.0105(5)
^{55}Fe	Ultima Gold	0.0111(4)	0.0100

An important advantage of the Compton-TDCR method is that it provides direct experimental information on the scintillator response at low electron energies. This response does not necessarily have to be parameterized with the Birks equation. Instead, the measured scintillator response can be introduced directly into TDCR efficiency calculations. The ZoMBieS method [17]follows this idea by using Compton-TDCR data in a model free approach to determine the PMT detection efficiencies, thereby reducing the dependence on a specific quenching model.

The measurement of scintillator response by Compton-coincidence spectrometry is also of particular interest for plastic scintillators, since the efficiency variation method cannot be applied to these materials in the same way as to liquid scintillation sources. The measured response curve can either be fitted to estimate the ionization quenching parameter and the mean number of detected photoelectrons per unit deposited energy or used directly as an empirical scintillator response function.

Comparison between the TDCR counter systems at SU 6

This chapter presents an extensive comparison of all TDCR systems available at the Laboratory of Metrology of Ionizing Radiation at the Faculty of Physics, Sofia University. These systems are TDCR-SU, miniTDCR, μTDCR, and CTDCR-SU. The comparison is performed in order to evaluate the performance of the TDCR channel of the newly developed CTDCR-SU system against already established TDCR counters. Demonstrating agreement between CTDCR-SU and the reference systems is an essential validation step, since the Compton–TDCR method relies on the CTDCR-SU detector being capable of performing accurate and consistent TDCR measurements.

The main parameter in this comparison is the activity of each source, estimated based on measurements with each system. For the ^{3}H and ^{14}C sources, efficiency variation with grey filters (see Figure 6.1) was applied to obtain the efficiency for double and triple coincidence counting rates and the figure-of-merit (FOM) and these parameters are also included in the comparison as a measure of the quality of each counter. Last, the ionization quenching parameter kB , which results in the lowest slope in activity when changing detection efficiency is presented.

The grey filters used in the study were produced in-house using a standard laser printer by printing rectangles with different infill percentages onto transparent plastic sheets. During measurements, particular attention was paid to ensure that the glued section of each filter remained in a fixed position and did not obstruct any PMT window in the TDCR configuration.

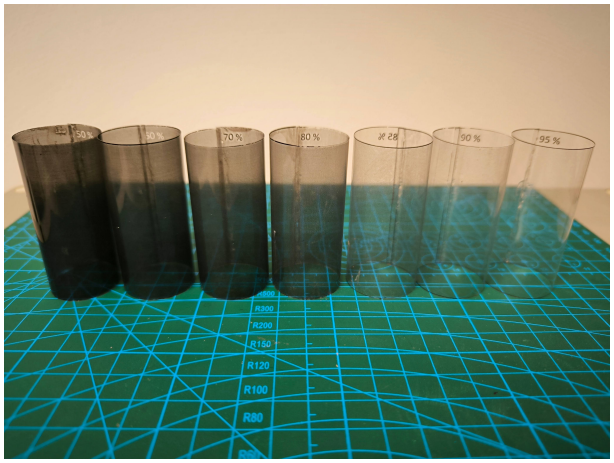

Figure 6.1: Grey filters used for efficiency-variation experiments [164].

In the analysis, the measurements were analyzed with 40 ns coincidence resolving time and 40 μs dead time. The counting rate of blank samples was subtracted to obtain the net counting rates of the sources. Accidental coincidences correction was applied [18] to the counting rates of the sources and blank samples.

Except the CTDCR-SU (described in Section 5.1), the other TDCR counters included in this comparison are portable counters meant for operation on-site. Therefore, they are equipped with miniature square Hamamatsu PMTs. The photocathode response of these PMTs is presented in Section 3.1.6.

The TDCR-SU counter [165] is equipped with three Hamamatsu R7600U-200 PMTs. The optical chamber is machined from a single white PTFE body. A nanoTDCR model TD9009 [152] was used as acquisition electronics. This system is long-established and has been used in international comparisons [154, 166].

The miniTDCR counter was designed and 3D-printed in LNHB, France [140]. The [149] reflective foil was used to cover the inner walls of the optical chamber. It also uses Hamamatsu R7600U-200 PMTs but their windows were covered with diffusive tape. For some of the LSC measurements, this counter was operated with a CAEN fast amplifier N978 [151] and the CAEN DT5751 digitizer but most of them were performed with a nanoTDCR model TD9010.

The μTDCR counter is also designed and 3D-printed in LNHB, France [140]. The inner walls of its optical chamber were also covered with reflective foil [149]. This counter utilizes Hamamatsu H11934-203 PMTs, which feature high gain and large effective area of the photocathode (see Section 3.1.6). A nanoTDCR model TD9010 was used to analyze the PMT signals.

Four unquenched LS sources and blank samples in sealed glass vials were used to compare the TDCR systems available at the MIL laboratory and to validate the LS part of the newly developed CTDCR-SU system. Two ^{3}H and one ^{14}C sources were originally control sources for the RackBeta 1219 liquid scintillation analyzer, which was manufactured by Wallac, Finland. One of the ^{3}H sources was standardized at LNHB, France and later will be refer to as "^{3}H LNHB". The forth source is a ^{14}C source produced by Amersham and together with its blank sample. All sources have a volume of 10 mL and a Toluene + PPO based cocktail. The walls of the vials were covered with diffusive adhesive tape in order to reduce the effect of total internal reflection of the light from the vial's walls [139].

6.1 ^{3}H Wallac source

Table 6.1 presents the efficiency variation results from measurements of ^{3}H Wallac source performed with the TDCR systems and the parameters used to compare their performance. Figure 6.2 shows the results from which the value of the kB parameter for each TDCR system was determined.

Table 6.1: Results obtained from efficiency variation measurements of ^{3}H Wallac source performed with on TDCR systems. The values in the brackets are the standard estimated uncertainties.

Detector	TDCR-SU	miniTDCR	μTDCR	CTDCR-SU
kB (cm/MeV)	0.0130(7)	0.0110(5)	0.0130(5)	0.0122(4)
TDCR	0.494	0.655	0.747	0.774
ε_D	0.5355(8)	0.6909(4)	0.7653(4)	0.7908(3)
ε_T	0.2647(8)	0.4526(6)	0.5714(7)	0.6117(4)
FOM (ph.e^{-}/keV)	0.877	1.448	2.235	2.505
A (Bq)	366.9(25)	367.1(18)	369.5(19)	368.1(16)

The results presented in Table 6.1 show that the efficiency for doubles and triples among the compared detectors is the highest for the CTDCR-SU system. The increase is about 3% in ε_D and about 7% in ε_T compared to the μTDCR. Compared to TDCR-SU system, the increase in the efficiency for doubles and triples are about 57% and 65%, respectively.

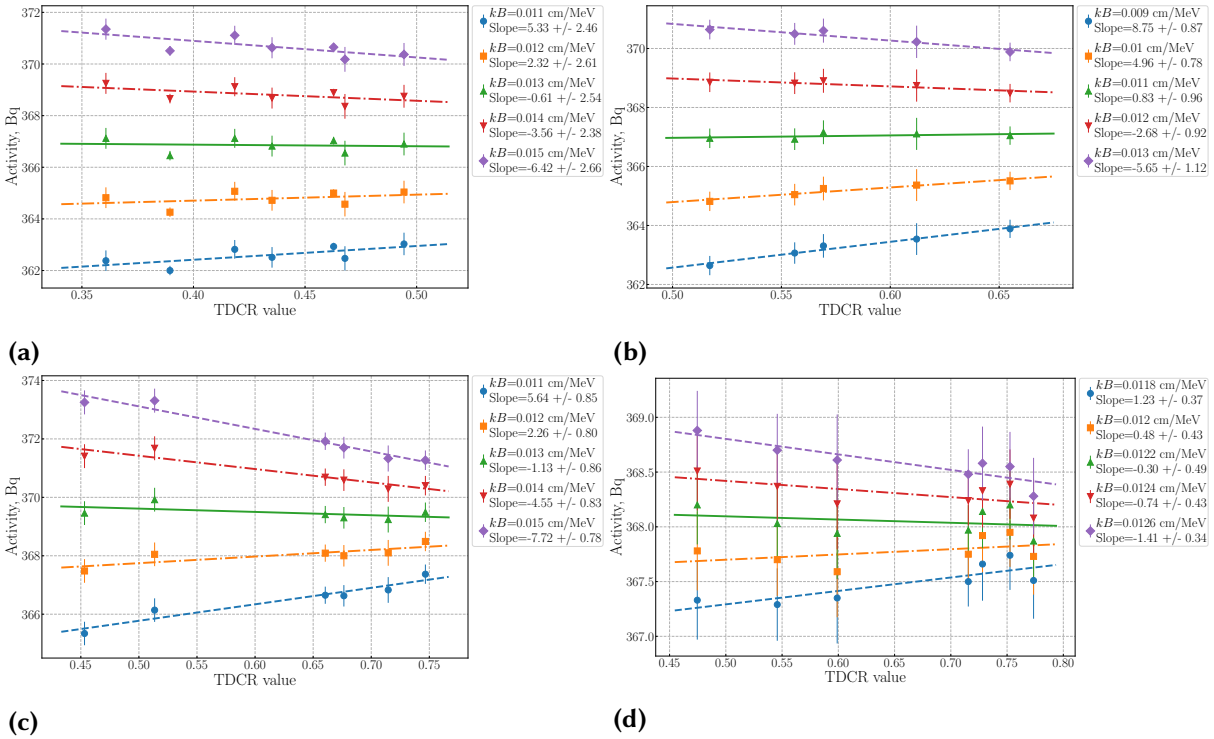

Figure 6.2: Efficiency variations of the Wallac ^{3}H source from measurements performed with (a) TDCR-SU, (b) miniTDCR , (c) μTDCR and the (d) CTDCR-SU system. The uncertainty bars represent only the statistical uncertainty of the double-coincidence counting rates [150].

The uncertainty of the *kB* parameter is estimated as the variance of a symmetrical triangular distribution, with interval bounds the first *kB* values for which the slope of the fitting line becomes non-zero within the estimated uncertainty.

The *kB* values presented in Table 6.1 are consistent within their estimated uncertainties, with the exception of the value obtained with the miniTDCR detector. This difference requires further investigation, since the same radionuclide was measured in the same scintillation cocktail. If the fitted *kB* parameter represented only the intrinsic ionization-quenching properties of the scintillator, compatible values would be expected for all detector systems. The observed discrepancy therefore suggests that the evaluated *kB* value may also be influenced by detector-specific effects, optical response differences, or assumptions in the TDCR efficiency model that are not satisfied for every detector. Nevertheless, the activities determined with the different systems remain in good agreement within their uncertainties, indicating that the TDCR model may partially compensate such differences through the *kB* parameter.

Important advantage of detectors with high double- and triple-coincidence detection efficiencies is that they can provide a better constrained determination of *kB* . This is illustrated in Figure 6.2 (d). Because the CTDCR-SU system has a higher initial detection efficiency, the efficiency variation measurements cover a wider useful range of TDCR values when grey filters are applied. As a result, the dependence of the calculated activity on TDCR can be examined over a broader interval, allowing the *kB* value to be varied with a smaller step and reducing the range of acceptable *kB* values used in the uncertainty estimate.

The efficiency is rarely reduced to very low TDCR values, typically below about 0.3, because in this region the calculated activity begins to decrease systematically. Under such conditions, the dependence A(TDCR) is no longer well described by a linear approximation, and the

corresponding points are not suitable for reliable *kB* determination. Therefore, a detector with high intrinsic efficiency is advantageous because it allows a sufficiently broad efficiency variation while still remaining within the region where the TDCR model provides a stable and approximately linear activity response.

6.2 ^{14}C Wallac source

Table 6.2 presents the efficiency variation results from measurements of ^{14}C Wallac source performed with TDCR systems and the parameters used to compare their performance. Figure 6.3 shows the results from which the value of the *kB* parameter for each TDCR system were determined.

Table 6.2: Results obtained from efficiency variation measurements of ^{14}C Wallac source performed on all TDCR systems. The values in the brackets are the standard estimated uncertainties.

Detector	TDCR-SU	miniTDCR	μTDCR	CTDCR-SU
kB (cm/MeV)	0.0098(3)	0.0070(4)	0.0078(4)	0.0110(4)
TDCR	0.947	0.969	0.978	0.980
ε_D	0.9509(2)	0.9708(3)	0.9782(1)	0.9794(1)
ε_T	0.9006(3)	0.9406(5)	0.9565(2)	0.9598(2)
FOM (ph.e$^-$/keV)	0.807	1.287	1.899	2.360
A (Bq)	1775.5(37)	1775.0(35)	1776.2(36)	1778.5(35)

Because ^{14}C emits higher-energy β particles than ^{3}H, the resulting scintillation light output is larger. The increased number of detected photons leads to higher double- and triple-coincidence efficiencies and therefore reduces the relative differences between the compared TDCR systems. Even under these counting conditions, the results presented in Table 6.2 show that the LS channel of the CTDCR-SU system provides the highest detection efficiency among the TDCR counters available in the MIL laboratory.

However, the *kB* values determined by the efficiency variation method again show differences between the compared TDCR counters. This observation is noteworthy because the present ^{14}C source and the ^{3}H source discussed in Section 6.1 were prepared in the same scintillation cocktail. Although the two radionuclides have different beta energy distributions, compatible *kB* values would generally be expected for the same cocktail if the fitted parameter represented only the intrinsic ionization quenching properties of the scintillator and if the efficiency model fully described the detector response. This consistency is observed for the CTDCR-SU system, whereas for the other counters the *kB* values obtained for the ^{14}C and ^{3}H sources are not compatible within their stated uncertainties. No correlation between the detector's efficiency and the estimated *kB* value could be observer from the experimental data.

This result again indicates that the *kB* value evaluated by the efficiency variation procedure may be influenced by factors beyond the intrinsic scintillator response. Possible contributions include detector-specific optical response, PMT detection efficiency, photocathode non-uniformity, differences in light collection, or limitations of the TDCR efficiency model. Nevertheless, despite the differences in the determined *kB* values, the final activities estimated with the compared TDCR counters remain coherent within about 0.2%. This suggests that, in the

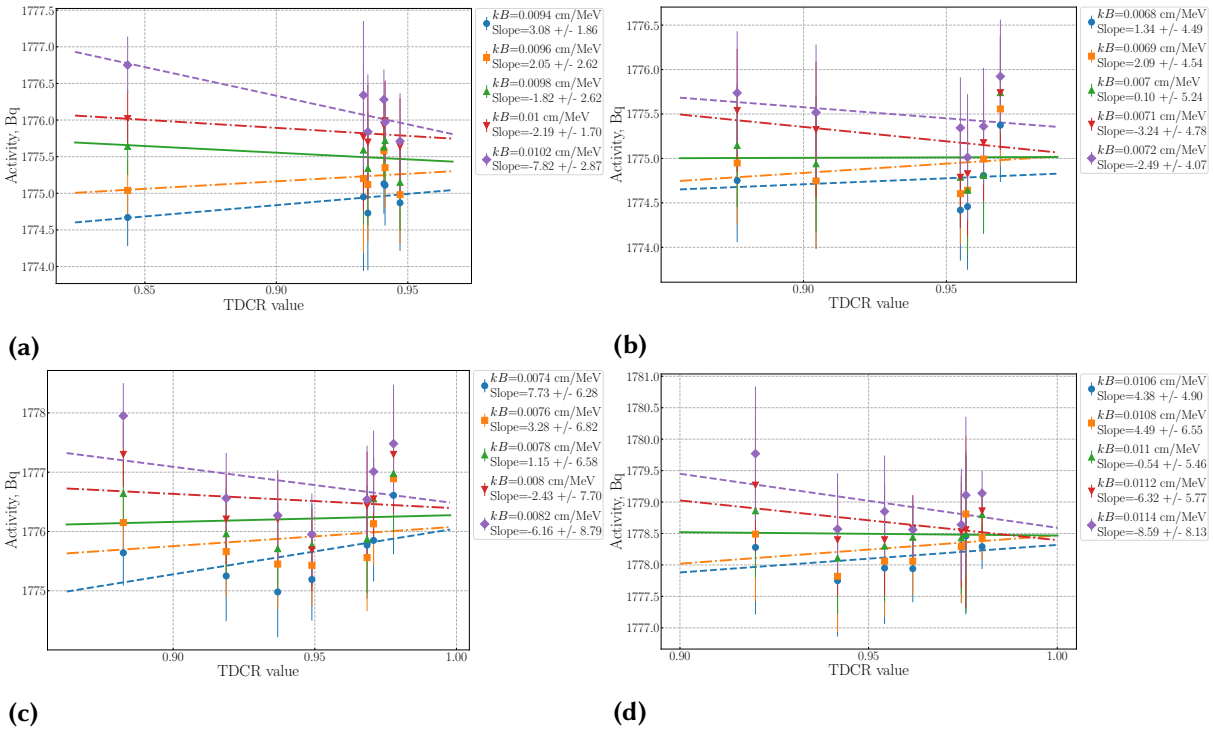

Figure 6.3: Efficiency variation of ^{14}C from measurements performed with the (a) TDCR-SU, (b) miniTDCR, (c) μTDCR and (d) CTDCR-SU system. The uncertainty bars represent only the statistical uncertainty of the double-coincidence counting rates [150].

practical application of the TDCR model, changes in the evaluated *kB* may partly compensate detector-specific response differences or model limitations, while still leading to consistent activity estimates.

6.3 ^{3}H LNHB source

Table 6.3 contains the efficiency variation results of the ^{3}H LNHB source with toluene+PPO cocktail performed with TDCR systems. Figure 6.4 shows the results from which the value of the *kB* parameter for each TDCR system was determined.

Table 6.3: Results obtained from efficiency variation measurements of ^{3}H LNHB source performed on all TDCR systems. The values in the brackets are the standard estimated uncertainties.

Detector	TDCR-SU	miniTDCR	μTDCR	CTDCR-SU
kB (cm/MeV)	0.0165(6)	0.0140(4)	0.0140(4)	0.0142(3)
TDCR	0.499	0.643	0.740	0.768
ε_D	0.5317(6)	0.6728(6)	0.7575(3)	0.7819(2)
ε_T	0.2654(6)	0.4324(9)	0.5603(5)	0.6005(3)
FOM (ph.e$^-$/keV)	0.965	1.501	2.231	2.579
A (Bq)	636.3(44)	635.9(45)	634.7(32)	634.3(32)

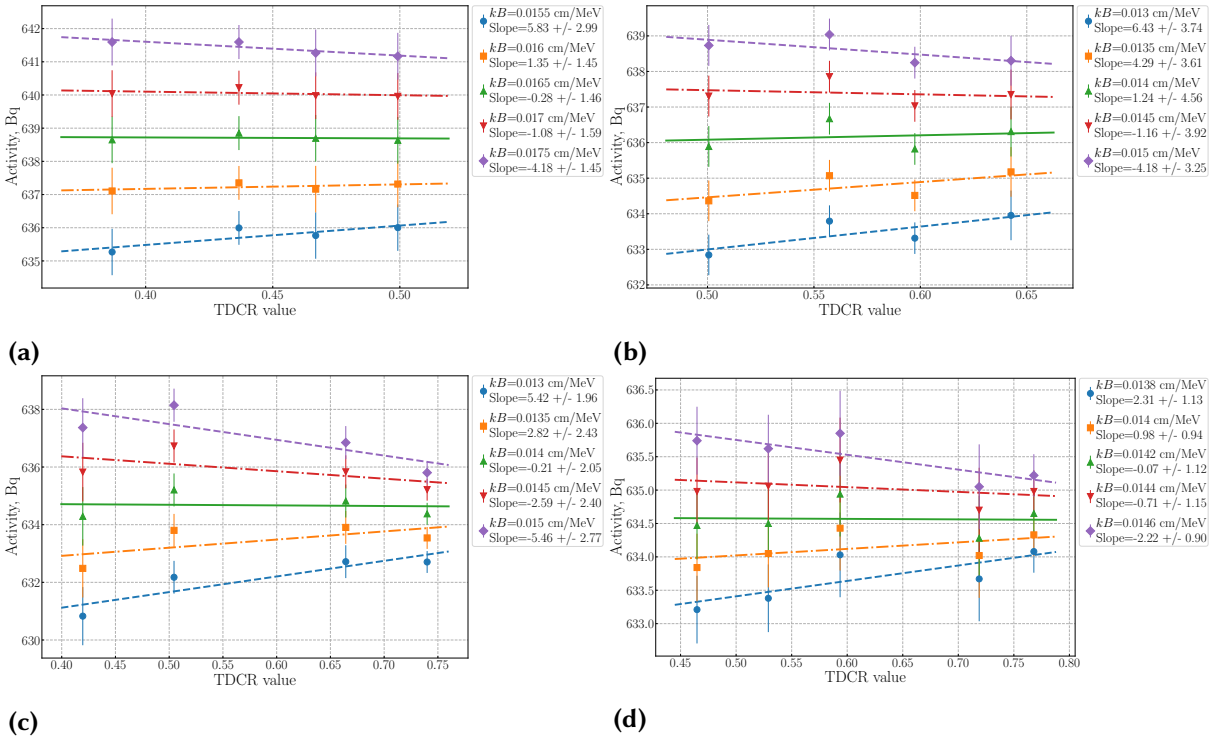

Figure 6.4: Efficiency variations of the LNHB ^{3}H source from measurements performed with (a) TDCR-SU, (b) miniTDCR, (c) μTDCR and the (d) CTDCR-SU system. The uncertainty bars represent only the statistical uncertainty of the double-coincidence counting rates.

The results presented in Table 6.3 show very good agreement between the activities determined with the miniTDCR, μTDCR, and CTDCR-SU systems. The corresponding *kB* values are also coherent, indicating that these systems provide compatible estimates of the ionization-quenching parameter for the ^{3}H LNHB source in toluene+PPO. Yet again, the CTDCR-SU system achieves the highest detection efficiency among the compared TDCR counters.

6.4 ^{14}C Amersham source

Table 6.4 shows the comparison between the efficiency variation results of the ^{14}C Amersham source. It shows the results from which the value of the *kB* parameter for each TDCR system were determined.

Table 6.4: Results obtained from efficiency variation measurements of ^{14}C Amersham source performed on all TDCR systems. The values given in brackets are the standard estimated uncertainties.

Detector	TDCR-SU	miniTDCR	μTDCR	CTDCR-SU
kB (cm/MeV)	0.0085(6)	0.0065(6)	0.0090(4)	0.0095(6)
TDCR	0.947	0.965	0.976	0.978
ε_D	0.9513(1)	0.9679(2)	0.9757(1)	0.9777(1)
ε_T	0.9005(2)	0.9340(5)	0.9518(3)	0.9561(2)
FOM (ph.e$^-$/keV)	0.777	1.141	1.783	2.005
A (Bq)	542.6(18)	542.0(16)	543.3(17)	543.1(15)

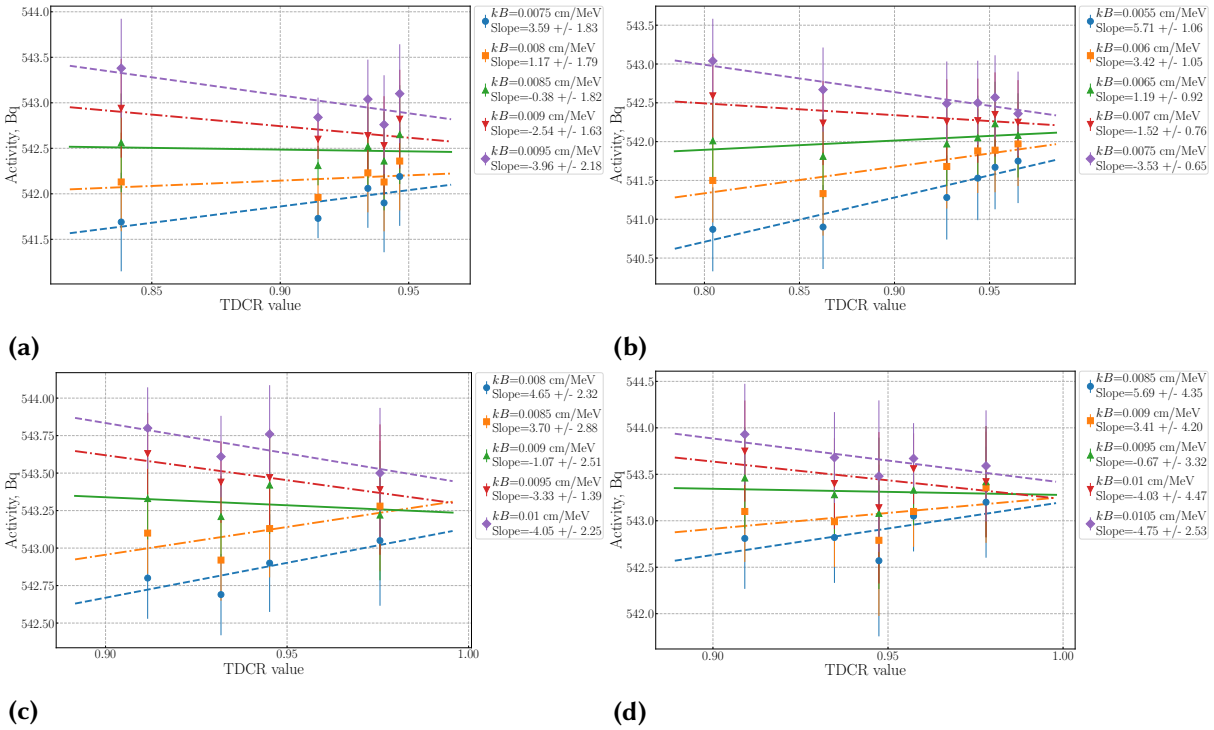

Figure 6.5: Efficiency variation of ^{14}C from measurements performed with the (a) TDCR-SU, (b) miniTDCR, (c) μTDCR and (d) CTDCR-SU system. The uncertainty bars represent only the statistical uncertainty of the double-coincidence counting rates.

The results presented in Table 6.4 show good agreement between the activities determined with the different TDCR systems. The corresponding kB values are also coherent within the estimated uncertainties. This level of agreement is expected for ^{14}C, since its higher β-particle energies produce a larger scintillation light output than ^{3}H. As a result, the detection efficiencies are higher and the influence of differences between the TDCR systems becomes less pronounced.

Taken together, the results presented in Table 6.1, Table 6.2, Table 6.3, and Table 6.4 demonstrate that the activities obtained for the measured ^{3}H and ^{14}C sources are coherent within their estimated uncertainties for all TDCR systems. Although the counters differ in detection efficiency and in the obtained values of the ionization quenching parameter kB , the TDCR

model accounts for these differences through the experimentally determined TDCR ratios and the corresponding calculated efficiencies which and delivers consistent activity estimates.

The observation that, the *kB* values obtained with different TDCR counters using the efficiency variation method are not the same is still to be explained. Possible explanations could be related to the underestimation of the *kB* value uncertainty or that it a consequence of the correlation between the figure of merit and the estimated kB value. This point deserves a more detailed study

6.5 ^{241}Am sources in Ultima Gold cocktails

Two ^{241}Am sources were prepared - one in Ultima Gold LLT and a second one in UltimaGold AB scintillator. About 20 mL of scintillator were used for the preparation of each source. The ^{241}Am was in a 1 M HCl solution, therefore 0.2 mL of H_2O was added to stabilize the source in the Ultima Gold LLT cocktail. The sources and the respective blank samples were prepared in high performance glass vials with aluminium foil lined caps to avoid evaporation. The low energy gamma-rays emitted by the ^{241}Am deposit small amount of energy in the scintillator in comparison to the high-energy alpha particles and with a TDCR value close to unity, the efficiency for double coincidence counting rate can be considered equal to the source activity, i.e. $\varepsilon_D = 1$ with an uncertainty of 0.4% [167]. Table 6.5 contains the results obtained with each system.

Table 6.5: Comparison of results obtained from the measurements of ^{241}Am performed on all TDCR systems. The values given in brackets are the standard estimated uncertainties.

Cocktail	Detector	TDCR-SU	miniTDCR	μTDCR	CTDCR-SU
UG AB	A (Bq)	1258.3(38)	1258.8(38)	1258.3(38)	1258.8(38)
UG LLT	A (Bq)	1255.3(38)	1254.9(38)	1251.5(38)	1251.5(38)

Results presented in Table 6.5 show excellent agreement between the activities of the source with the UG AB scintillator. The activities of the source with the UG LLT scintillator are also within the estimated uncertainties but with somewhat worse agreement. The measurements of the UG LLT sample with the μTDCR and the CTDCR-SU were performed 5 months after the measurements with the TDCR-SU and the miniTDCR. During its storage, the UG LLT sample could have undergone deterioration, explaining the heightened difference in the activities.

6.6 ^{14}C in Ultima Gold AB scintillator

This ^{14}C sample was prepared from an acetone solution of a standardized ^{14}C source (benzoic acid). Approximately 1 mL of the solution was added to 15 mL of Ultima Gold AB (UG AB) cocktail. The source was prepared in 20 mL low-diffusion polyethylene vials fitted with standard plastic caps. Polyethylene vials were selected because their light-diffusing walls enhance the collection of scintillation photons and thereby improve the detection efficiency (see Chapter 4). A blank sample with the same chemical composition was prepared as well. The results are presented in Table 6.6 and Figure 6.6.

Table 6.6: Results obtained from efficiency variation measurements of ^{14}C in Ultima Gold AB scintillator. The values in the brackets are the standard estimated uncertainties.

Detector	TDCR-SU	CTDCR-SU
kB (cm/MeV)	0.0085(6)	0.0080(6)
TDCR	0.889	0.959
ε_D	0.9059(1)	0.9609(1)
ε_T	0.8051(1)	0.9212(2)
FOM (ph.e$^-$/keV)	0.385	1.017
A (Bq)	2427.0(50)	2428.6(40)

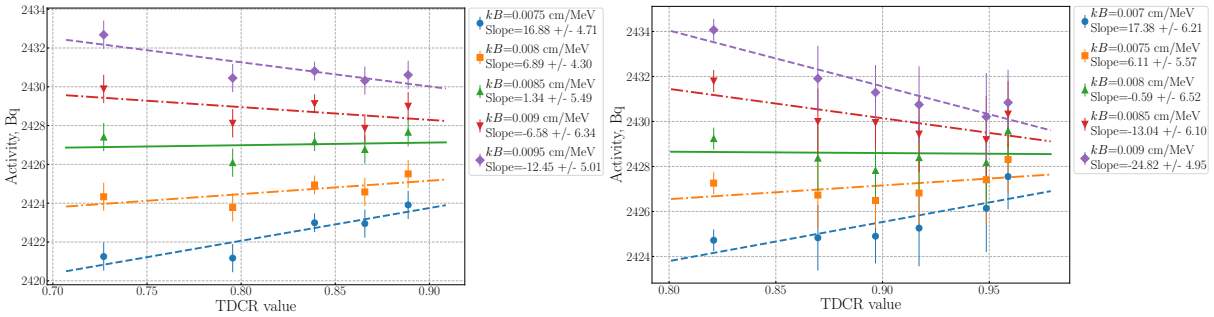

(a) **(b)**

Figure 6.6: Efficiency variation of ^{14}C in UGAB from measurements performed with the (a) TDCR-SU and (b) CTDCR-SU system. The uncertainty bars represent only the statistical uncertainty of the double-coincidence counting rates.

The results presented in Table 6.6 show good agreement between the activities determined with the TDCR-SU and CTDCR-SU systems. The kB values obtained from efficiency variation are also coherent within their uncertainties, indicating compatible estimates of the ionization quenching parameter for ^{14}C in UG AB.

The CTDCR-SU system shows substantially higher TDCR, double-, and triple-coincidence counting efficiencies. This is reflected in the larger FOM value, which is more than a 2.5 times higher than the value of the TDCR-SU, signifying the unmatched performance of the CTDCR-SU.

6.7 ^{63}Ni in Ultima Gold scintillator

The ^{63}Ni sample was prepared from a 0.1 M HCl solution containing a $NiCl_2$ carrier. The stock solution was diluted, and approximately 0.1 mL of the resulting solution was mixed with 15 mL of Ultima Gold (UG) scintillation cocktail. The sample was prepared in a standard 20 mL glass vial with aluminium-foil lined caps. The vial was wrapped with diffusive adhesive tape to reduce the effects of internal reflection. A blank sample with identical composition was also prepared. The results are presented in Table 6.7 and Figure 6.7.

Table 6.7: Results obtained from efficiency variation measurements of ^{63}Ni in Ultima Gold scintillator. The values in the brackets are the standard estimated uncertainties.

Detector	TDCR-SU	CTDCR-SU
kB (cm/MeV)	0.0110(6)	0.0105(4)
TDCR	0.712	0.872
ε_D	0.7101(1)	0.8616(9)
ε_T	0.5054(2)	0.7515(8)
FOM (ph.e$^-$/keV)	0.484	1.331
A (Bq)	3702.3(74)	3702.9(37)

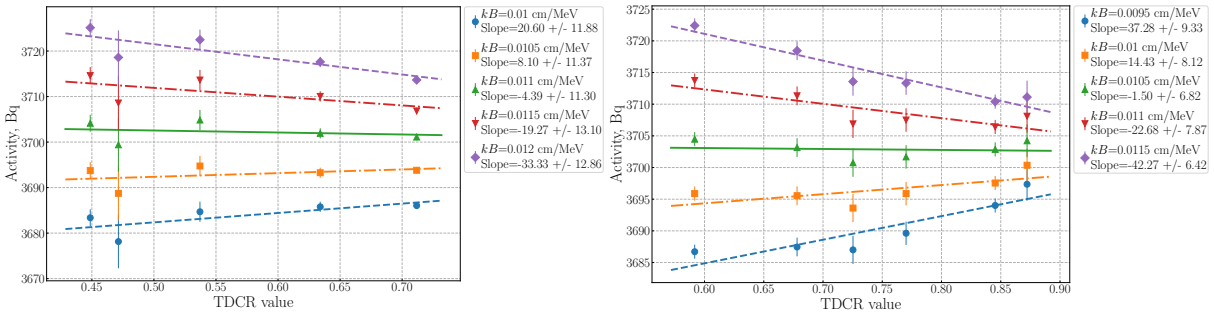

(a) **(b)**

Figure 6.7: Efficiency variation of ^{63}Ni in UG from measurements performed with the (a) TDCR-SU and (b) CTDCR-SU system. The uncertainty bars represent only the statistical uncertainty of the double-coincidence counting rates.

The results presented in Table 6.7 show excellent agreement between the activities determined with the TDCR-SU and CTDCR-SU systems. The kB values obtained by applying the efficiency variation method are also coherent within their standard uncertainties.

The higher efficiency of the CTDCR-SU system is clearly visible for this low-energy β-emitter. Compared with TDCR-SU, the double-coincidence efficiency of the CTDCR-SU is higher by about 18%, while the triple-coincidence efficiency is higher by about 33%. This improvement is also reflected in the larger FOM value, which indicates a higher detected photoelectron yield per unit deposited energy.

6.8 ^{55}Fe in Ultima Gold scintillator

Two samples were prepared - ^{55}Fe in Ultima Gold. The stock solution is 0.1 M HCl and the carrier is $FeCl_3$. The source was prepared by dilution of the stock solution and about 0.7 g of it was added to 15 mL of UG scintillator. The vials used were 20 mL glass vials with foil-lined caps and the vial walls were, again, wrapped in diffusive adhesive tape. Its corresponding blank sample was prepared with the same scintillator and chemical composition. The activity of the samples was calculated using the code written by Ph. Cassette `Fe55_6` using updated decay data of 19 March 2024 [105]. The activity estimated using this code is presented in Table 6.8.

Table 6.8: Results obtained from the measurements of ^{55}Fe performed with the TDCR systems. The values in the brackets are the standard estimated uncertainties.

Sample	Detector	TDCR-SU	miniTDCR	μTDCR	CTDCR-SU	Prep. method
Proba 4	A (Bq)	1129.7(57)	1138.7(57)	1150.1(57)	1159.0(57)	1153(18)
Proba 4	ε_D	0.3057(12)	0.4352(17)	0.6130(12)	0.7396(14)	—

Results presented in Table 6.8 show that the determination of ^{55}Fe activity might be influenced by the detection efficiency of the TDCR system.

The CTDCR-SU system has the highest detection efficiency, which is about 60% higher than that of TDCR-SU, about 41% higher than that of miniTDCR, and about 17% higher than that of μTDCR. This high efficiency is a substantial advantage for ^{55}Fe TDCR measurements.

The activity obtained with the two highest-efficiency systems, μTDCR and CTDCR-SU, are in agreement within their uncertainties.In contrast, the result obtained with the lower-efficiency TDCR-SU system is not consistent with the CTDCR-SU value or with the activity estimated from the preparation method. It should be noted that the preparation-based activity was calculated from the certified activity of the master solution, with reference date on 1 March 2018. The certificate was issued by PTB with specific activity $a = 572(9)$ kBq/g. The solution was prepared by a defined mixture of a parent solution of known specific activity and a carrier solution. The specific activity of the parent solution was determined by means of the TDCR method. At the time of certification, older decay data for ^{55}Fe were used. Therefore, recalculating the activity estimated by the preparation method using the newly evaluated decay data is expected to bring this value even closer to the activity obtained with the CTDCR-SU detector. The miniTDCR result is still not coherent with the activity estimated with the μTDCR and CTDCR-SU detectors, but is within the uncertainty of the activity estimated by the preparation method. Overall, the comparison demonstrates that the high detection efficiency of the CTDCR-SU system provides a clear advantage for the activity determination of very low-energy radionuclides such as ^{55}Fe.

The comparison presented in this chapter demonstrates that the TDCR channel of the CTDCR-SU system performs consistently with the established TDCR counters available in the MIL laboratory. For the investigated ^{3}H, ^{14}C, ^{63}Ni, and ^{55}Fe sources, the activities determined with CTDCR-SU were found to be consistent with those obtained using the other TDCR systems, within the corresponding uncertainties. This agreement verifies the metrological capability of the CTDCR-SU detector as an absolute liquid scintillation counting system.

The CTDCR-SU exhibits the highest detection efficiency among the compared counters. This is a particularly important advantage for low-energy radionuclides, where the scintillation light output is small and the activity determination becomes more sensitive to the detector efficiency. The benefit is especially evident for ^{55}Fe, for which the high efficiency of CTDCR-SU leads to improved coherence with the activity estimate by the preparation method.

These results confirm that the LS channel of the CTDCR-SU system is not only suitable for TDCR measurements, but also especially well matched to its intended role in the Compton-TDCR spectrometer. Its high detection efficiency is essential for measuring the scintillator response at very low Compton electron energies, where only a small number of photoelectrons is produced. The extensive comparison therefore establishes the TDCR channel of CTDCR-SU as a metrology-grade detector and validates its use for the low-energy scintillator response studies.

7 Influence of accidental coincidence corrections on *kB* determination by efficiency variation with grey filters

To the best of our knowledge, it was not studied whether this accidental coincidence correction has any impact on the selection of the *kB* parameter when performing efficiency variation measurements using grey filters. Because the counting rates vary when different grey filters are used, it is pertinent to investigate how accidental coincidences influence the determination of the *kB* value. This issue is especially important when evaluating the accuracy of previously reported *kB* values obtained at a time when accidental coincidence corrections were not yet available.

To explore this question, we re-examined experimental data collected with several TDCR systems and a range of radionuclides. For each data set, the *kB* parameter was determined both with and without applying analytical corrections for accidental coincidences. The outcomes of these two approaches are then compared and discussed.

7.1 Systems and Measurements

The TDCR detection systems used in Sofia University are presented in Chapter 6. The systems used in Laboratoire National Henri Becquerel (LNHB) are copies of the systems used in SU.

The data analysed in this work cover three radionuclides — ^{3}H, ^{63}Ni, and ^{14}C — measured in different scintillation cocktails. Specifically, ^{3}H in a toluene-based cocktail was measured with both the TDCR-SU and the miniTDCR-SU systems, while ^{3}H in Ultima Gold (UG) cocktail was analysed using the LNHB miniTDCR detector. Measurements of ^{14}C in a toluene-based cocktail were performed with the TDCR-SU and miniTDCR-SU systems, and ^{63}Ni in UG cocktail was studied with the LNHB microTDCR device. The ^{3}H and ^{14}C samples from the Wallac RackBeta standard set are described in Chapter 6. The ^{3}H and ^{63}Ni samples in UG cocktail were prepared using 10 mL of scintillator in sealed glass vials, which were wrapped in diffusive tape to reduce total internal reflection effects. It should be noted that the tape was replaced between the measurement campaigns performed in 2022 and 2023.

The TDCR data collected using the nanoTDCR acquisition system were processed with a dedicated software package — the TDCR analysis tool [119] — which allows the user to enable or disable accidental-coincidence (AC) corrections. This program also incorporates the TDCR17 code [168] to implement the TDCR evaluation procedure. Stopping-power values were computed either using the ICRU 37 formulation with linear extrapolation below 100 eV [160] or using the tabulated data of Tan and Xia [121] when available. The theoretical beta spectra were generated with the BETASHAPE code, which accounts for atomic effects [169].

The required variation of detection efficiency for determining the *kB* parameter was achieved by inserting grey filters, shown in Figure 6.1.

The analytical procedure for applying AC corrections followed the approach described in [18]. To examine the influence of the correction, each measurement was processed in two ways: first without applying the AC correction and then with the AC correction applied. This was done both for the radioactive source and for the corresponding blank sample.

The net counting rates were obtained by subtracting the blank counting rates from the corresponding source counting rates. In this way, two sets of net counting rates were produced:

one based on uncorrected source and blank data, and one based on AC corrected source and AC corrected blank data. These two sets were then processed independently with the TDCR analysis tool to determine the corresponding activity values and *kB* parameters.

Regarding acquisition settings, two coincidence resolving times were employed: 40 ns and 200 ns. The 40 ns window is widely used in TDCR activity measurements and represents a widely used value in the LS community. The 200 ns window, on the other hand, was selected to investigate whether collecting a greater fraction of the delayed scintillation component would influence the measured TDCR values. The base dead-time settings were 40 µs for measurements at SU and 50 µs for those conducted at LNHB.

7.2 Determination of *kB* for ^{3}H in a Toluene-Based Cocktail Using the miniTDCR-SU System

The results of the efficiency-variation measurements are presented in Figure 7.1. As shown in Figure 7.1 (a), the application of the accidental-coincidence correction does not affect the determination of the *kB* parameter for the investigated source and coincidence resolving time. Even when a finer step size is used for the *kB* variation (Figure 7.1 (b)), the values obtained with and without applying the accidental-coincidence correction remain identical, yielding *kB* =0.0136(2) cm/MeV.

7.3 Determination of *kB* for ^{3}H in Ultima Gold Cocktail Using the miniTDCR-LNHB System

The efficiency variation results are presented in Figure 7.2, covering measurements performed with coincidence windows of 40 ns and 200 ns. The findings indicate that the *kB* parameter remains unchanged whether or not the accidental-coincidence correction is applied. Even though the source activity in Figure 7.2 is 44 times larger than that in Figure 7.1, the influence of accidental coincidences is still too small to noticeably modify the estimate of the *kB* value. The *kB* parameter is 0.0122(10) cm/MeV for data collected with a 40 ns coincidence window (Figure 7.2 (a)), and 0.0126(10) cm/MeV when the coincidence window is 200 ns (Figure 7.2 (b)).

7.4 Determination of *kB* for ^{14}C in a Toluene-Based Cocktail Using the TDCR-SU System

The efficiency variation results of a ^{14}C in a toluene-based cocktail measured with the TDCR-SU system are presented in Figure 7.3. These data indicate that, for ^{14}C, the *kB* parameter evaluated without the accidental coincidence correction is consistent with the value obtained when the correction is applied. In both approaches, the resulting kB value is 0.0090(2) cm/MeV.

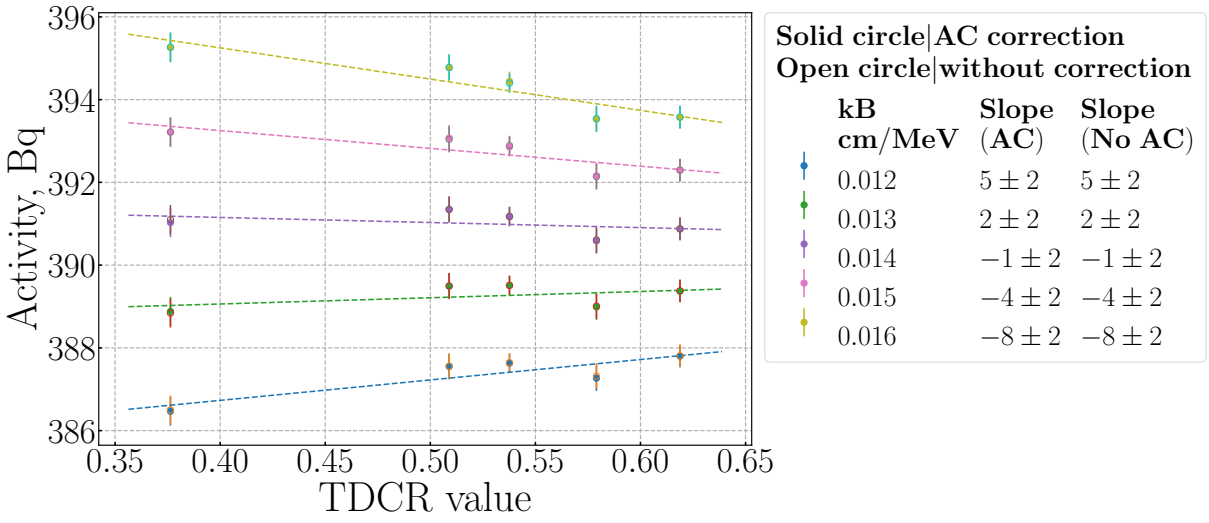

(a)

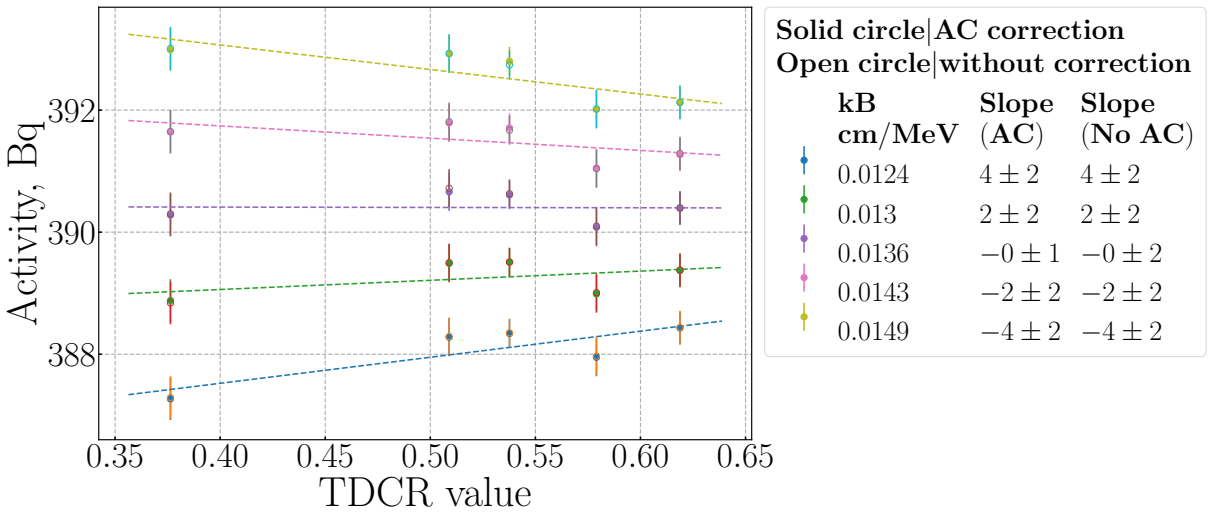

(b)

Figure 7.1: Efficiency-variation results for a ^{3}H sample in a toluene-based cocktail measured with the miniTDCR system at SU (a), and reanalysed with a reduced *kB* step size (b) [164].

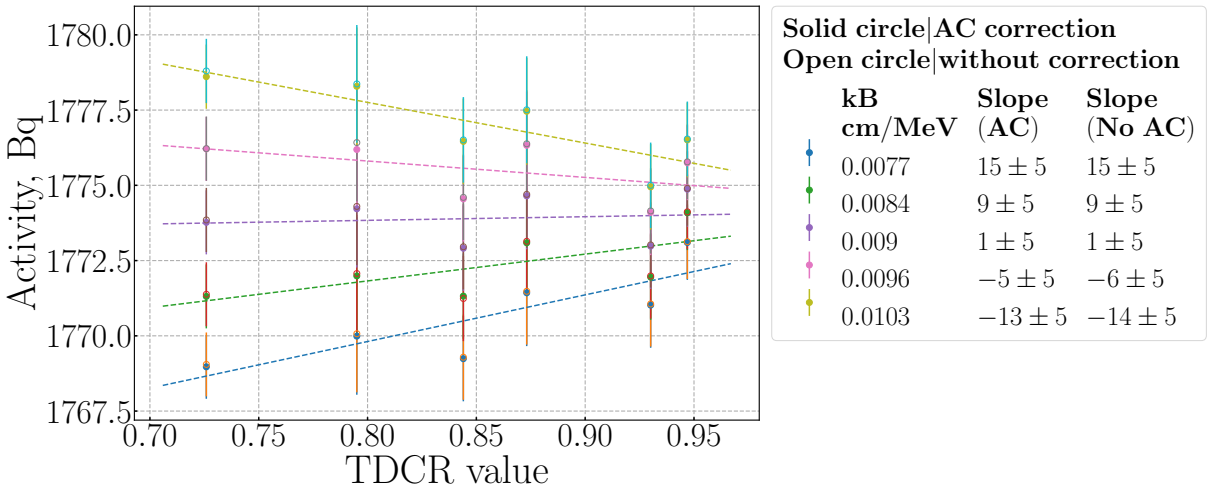

Figure 7.3: Efficiency variation results for a ^{14}C sample in a toluene-based cocktail measured with the TDCR-SU system at SU. The analysis is performed using a 40 ns coincidence window and a 40 μs dead time [164].

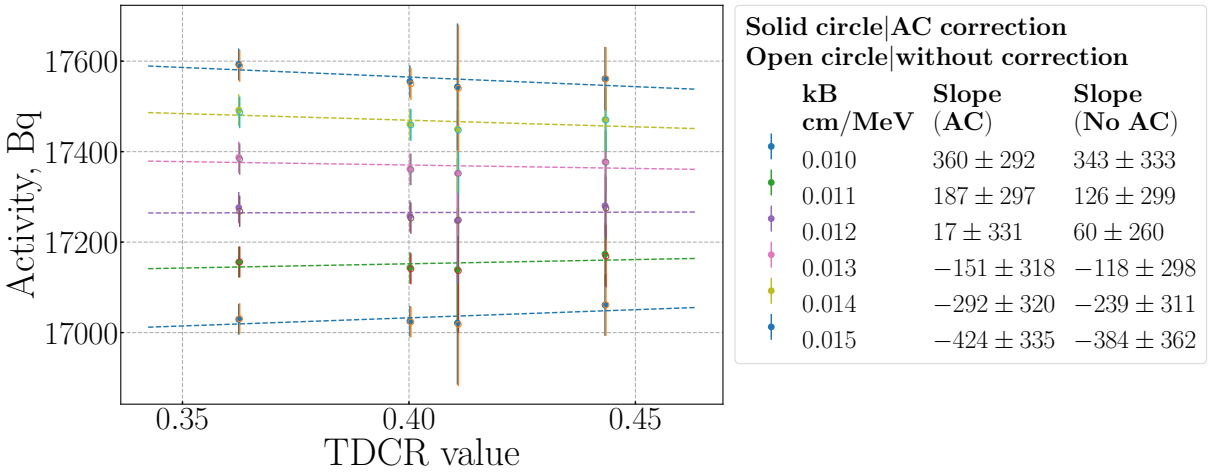

(a)

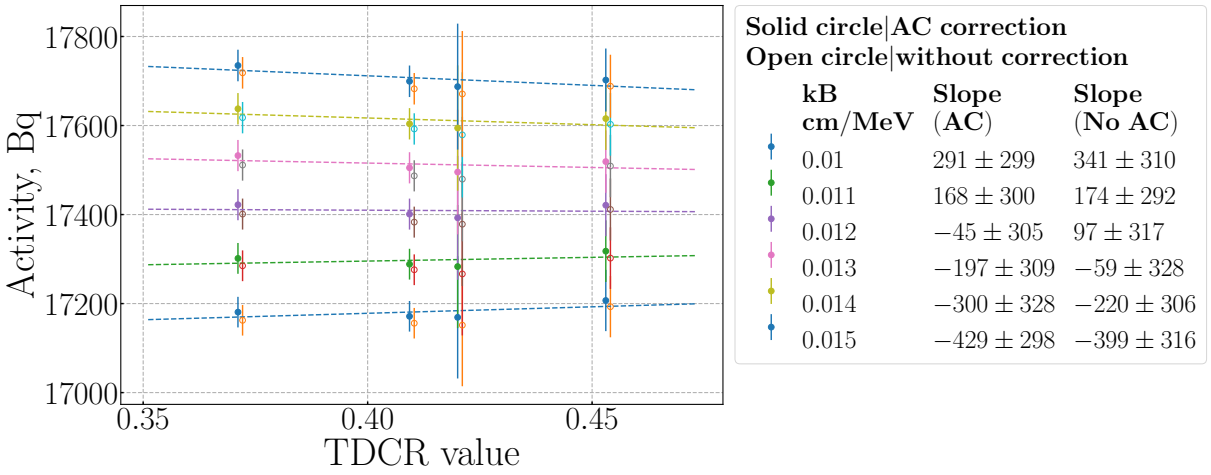

(b)

Figure 7.2: Efficiency-variation results for a ^{3}H sample prepared in UltimaGold scintillation cocktail, measured with the miniTDCR system at LNHB. The data are analysed using coincidence resolving times of 40 ns (a) and 200 ns (b), with a base dead time of 50 μs [164].

7.5 Determination of *kB* for ^{63}Ni in Ultima Gold Cocktail Using the microTDCR-LNHB System

The results of the efficiency-variation analysis are presented in Figure 7.4. These data further demonstrate that the contribution of the accidental-coincidence correction to the determination of the *kB* parameter is negligible; in both evaluation procedures, the obtained value is 0.0074(1) cm/MeV.

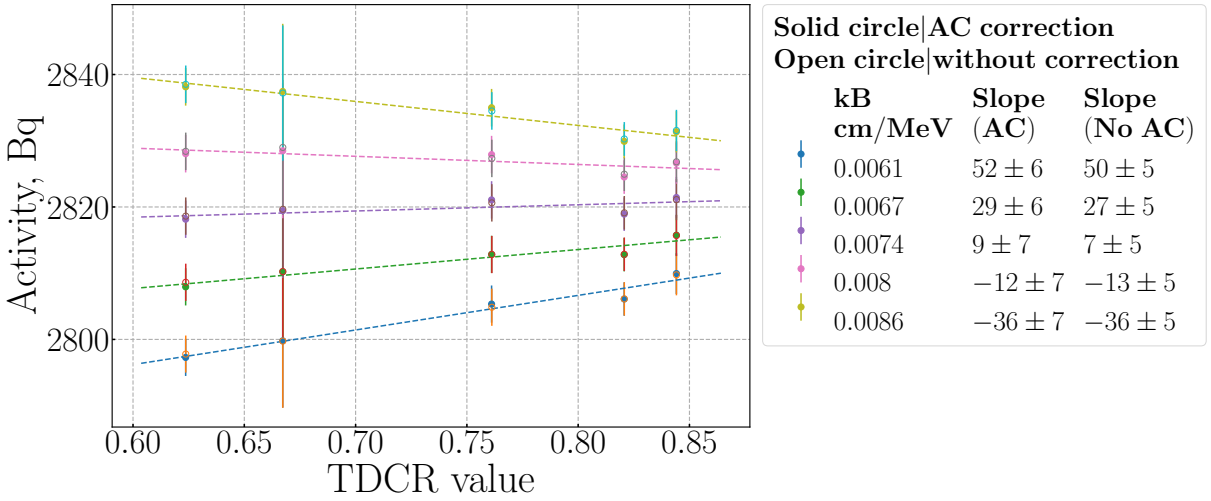

Figure 7.4: Efficiency variation results for a ^{63}Ni sample in a Ultima Gold cocktail measured with the microTDCR system at LNHB. The analysis is performed using a 40 ns coincidence window and a 50 μs dead time [164].

To sum up the analysis, Tables 7.1 and 7.2 report the doubles (D) and triples (T) counting rates, the T/D ratio, and the corresponding activity (A), all evaluated using the determined *kB* values. Table 7.1 refers to measurements acquired with a coincidence window of 40 ns, Table 7.2 corresponds to acquisitions performed with a 200 ns window. For both coincidence windows, the results show that the magnitude of the accidental coincidence correction is smaller than the statistical fluctuations of the measured counting rates.

A comparison of the *kB* values evaluated from efficiency variation measurements with coincidence windows of 40 ns and 200 ns is presented in Table 7.3. For ^{3}H, the use of the longer coincidence window leads, in most cases, to a lower evaluated *kB* value. A similar dependence of the *kB* parameter on the coincidence window setting has also been reported previously [12]. This behaviour should not be interpreted as a physical change of the Birks ionization quenching parameter.

The results also demonstrate that the determined *kB* values exhibit variations whose origin is not yet understood. For a given source and scintillation cocktail, the *kB* depends on the TDCR counting system but the estimated source activities remain consistent within the statistical uncertainties (see Tables 7.1 and 7.2).

The influence of the analytical accidental coincidence correction on the coincidence counting rates and estimated activity is small and remains within the statistical uncertainties and no influence on the *kB* determination is observed. This conclusion, however, is conditional on the tested measurement regime and should not be assumed to hold for other cocktails, activity levels, dead-time settings, or alternative efficiency variation techniques. These findings do not argue against applying the accidental coincidence correction. On the contrary, since an analytical correction is available and can be implemented easily, its use should be regarded as essential for TDCR data analysis [86].

The results presented in this chapter and the Compton-TDCR results presented in Section 5.3 indicate that further theoretical and experimental work is required to clarify the determination of the *kB* parameter and to improve the understanding of ionization quenching within the TDCR framework.

Table 7.1: Comparison of double D and triple T coincidence counting rates, T/D ratio and activity A of samples for 40 ns coincidence window acquisition [164].

Detector	Nuclide Cocktail	Case	D, s^{-1}	T, s^{-1}	T/D	A, Bq
TDCR-SU 2022	^{3}H	w/o AC	192.05 (25)	87.67 (14)	0.456 (2)	389.2 (15)
kB=0.0144 cm/MeV	toluene	w AC	192.05 (25)	87.66 (14)	0.456 (2)	389.2 (15)
		% corr.	0.002	0.003	0.001	0.002
miniTDCR-SU 2022	^{3}H	w/o AC	254.77 (19)	157.65 (20)	0.619 (1)	390.0 (9)
kB=0.0136 cm/MeV	toluene	w AC	254.77 (19)	157.65 (20)	0.619 (1)	389.9 (9)
		% corr.	0.003	0.003	0.0003	0.003
TDCR-SU 2023	^{3}H	w/o AC	206.19 (16)	101.55 (11)	0.493 (1)	386.4 (10)
kB=0.0130 cm/MeV	toluene	w AC	206.18 (16)	101.54 (11)	0.493 (1)	386.4 (10)
		% corr.	0.01	0.007	−0.002	0.003
miniTDCR-SU 2023	^{3}H	w/o AC	268.25 (14)	176.23 (18)	0.657 (1)	389.7 (12)
kB=0.0132 cm/MeV	toluene	w AC	268.24 (14)	176.23 (18)	0.657 (1)	389.7 (12)
		% corr.	0.003	0.004	0.001	0.003
miniTDCR-LNHB	^{3}H	w/o AC	8311 (28)	3686 (25)	0.443 (8)	17295 (122)
kB=0.0122 cm/MeV	UG	w AC	8308 (28)	3683 (25)	0.443 (8)	17298 (122)
		% corr.	0.03	0.08	0.05	−0.02
TDCR-SU 2023	^{14}C	w/o AC	1689 (1)	1599 (1)	0.947 (1)	1775 (3)
kB=0.009 cm/MeV	toluene	w AC	1689 (1)	1599 (1)	0.947 (1)	1775 (3)
		% corr.	0.002	0.002	0.0005	0.002
microTDCR-LNHB	^{63}Ni	w/o AC	2373 (3)	2003 (3)	0.844 (2)	2822 (16)
kB=0.0074 cm/MeV	UG	w AC	2373 (3)	2003 (3)	0.844 (2)	2822 (16)
		% corr.	0.007	0.010	0.003	0.007

Table 7.2: Comparison of double D and triple T coincidence counting rates, T/D ratio and activity A for a 200 ns coincidence window acquisition [164].

Detector	Nuclide Cocktail	Case	D, s^{-1}	T, s^{-1}	T/D	A, Bq
TDCR-SU 2022	^{3}H	w/o AC	198.65 (26)	93.40 (16)	0.470 (2)	390.3 (14)
kB=0.0138 cm/MeV	toluene	w AC	198.63 (26)	93.38 (16)	0.456 (2)	404.5 (20)
		% corr.	0.008	0.016	0.007	0.004
miniTDCR-SU 2022	^{3}H,	w/o AC	260.53 (21)	164.59 (23)	0.632 (2)	390.0 (10)
kB=0.0128 cm/MeV	toluene	w AC	260.49 (21)	164.55 (23)	0.627 (2)	394.2 (14)
		% corr.	0.014	0.016	0.002	0.008
TDCR-SU 2023	^{3}H	w/o AC	212.48 (17)	107.41 (12)	0.506 (1)	386.9 (13)
kB=0.0120 cm/MeV	toluene	w AC	212.38 (16)	107.32 (12)	0.498 (1)	392.8 (18)
		% corr.	0.04	0.03	0.010	0.018
miniTDCR-SU 2023	^{3}H	w/o AC	273.66 (17)	183.15 (18)	0.669 (1)	390.9 (13)
kB=0.0124 cm/MeV	toluene	w AC	273.62 (18)	183.11 (18)	0.663 (1)	394.3 (14)
		% corr.	0.02	0.02	0.003	0.009
miniTDCR-LNHB	^{3}H	w/o AC	8568 (30)	3890 (27)	0.454 (8)	17468 (133)
kB=0.0126 cm/MeV	UG	w AC	8555 (31)	3876 (27)	0.453 (8)	17482 (134)
		% corr.	0.15	0.37	0.23	−0.08
TDCR-SU 2023	^{14}C	w/o AC	1693 (1)	1606 (1)	0.949 (1)	1776 (3)
kB=0.0088 cm/MeV	toluene	w AC	1693 (1)	1599 (1)	0.947 (1)	1776 (3)
		% corr.	0.001	0.01	0.002	0
microTDCR-LNHB	^{63}Ni	w/o AC	2394 (3)	2013 (3)	0.848 (2)	2833 (15)
kB=0.0074 cm/MeV	UG	w AC	2394 (3)	2001 (3)	0.848 (2)	2835 (15)
		% corr.	0.03	0.05	0.002	0.02

Table 7.3: *kB* values obtained from measurements using 40 ns and 200 ns coincidence windows (CW) [164].

Detector system	Nuclide Cocktail	*kB* for 40 ns CW, cm/MeV	*kB* for 200 ns CW, cm/MeV
TDCR-SU 2022	^{3}H toluene	0.0144 (3)	0.0138 (3)
miniTDCR-SU 2022	^{3}H toluene	0.0136 (2)	0.0128 (2)
TDCR-SU 2023	^{3}H toluene	0.0130 (2)	0.0120 (1)
miniTDCR-SU 2023	^{3}H toluenel	0.0132 (3)	0.0124 (2)
miniTDCR-LNHB	^{3}H UG	0.0122 (10)	0.0126 (10)
TDCR-SU 2023	^{14}C toluene	0.0090 (2)	0.0088 (2)
microTDCR-LNHB	^{63}Ni UG	0.0074 (1)	0.0074 (4)

Study of *kB* selection with Monte Carlo simulated TDCR list-mode files

8

A major challenge in assessing the impact of the accidental coincidence correction on TDCR measurement results and on the subsequent application of the TDCR method is the absence of a reference (ground-truth) dataset against which the analysis can be validated. If such a reference were available, it would be possible not only to quantify the differences between uncorrected and corrected counting rates, but also to evaluate the residual deviation of the corrected rates from the true values. It would also enable a systematic evaluation of how the TDCR model performs on data analyzed with and without the accidental coincidence correction, and how this choice propagates to the final activity estimate. Moreover, such a reference would provide a more robust basis for investigating whether the accidental coincidence correction affects the selection of the *kB* parameter.

To address these limitations, investigations of the effect of the accidental coincidence correction on *kB* selection were performed using MC code developed by K. Mitev to simulate list-mode data files [170]. The principal advantage of applying the TDCR model to MC-simulated data is the availability of a known reference (the MC truth), enabling direct comparison of the estimated counting rates and activity with the corresponding simulated values. A detailed description of the simulation concept and implementation, together with its primary applications, is provided in [170]. The generated list-mode files were analyzed using the *cdt_logic* code developed by C. Dutsov [119].

The main objectives of this chapter are:

- to investigate the behavior of the accidental coincidence correction when the same MC-simulated list-mode file is analyzed using different coincidence resolving times;
- to evaluate the activity obtained from the TDCR model and the associated *kB* selection by comparison with the activity specified in the MC simulation.

Using the functionality of the code, two data set with different time distributions of the pulses between the PMTs were simulated. The input parameters used in the two simulations are the same, with the exception of the time-distribution width. The two time distributions are a convolution of Voigt and exponentially modified Gaussian distribution. In the first case, a realistic time distribution with parameters selected to resemble the time distribution between pulses of a real ^{3}H acquisition. In the second case, an artificial, non-physical distribution is adopted, with an extremely small width on the order of 10^{-15} s, included for verification purposes. The parameters of these two distributions are given in Table 8.1.

Table 8.1: Time distribution parameter values used in the simulations [170].

Input name	^{3}H-like time distribution	Narrow time distribution
Centroid of Voigt peak	0.0	0.0
Area of the Voigt peak	1.0	1.0
Gaussian Full Width Half Maximum (FWHM)	2.82E−9	2.82E−15
Lorentzian Half Widt Half Maximum (HWHM)	2.12E−9	2.12E−15
Centroid of Gaussian peak	0.0	0.0
Sigma of Gaussian peak	2.82E−9	2.82E−15
Area of Gaussian peak	0.141	0.141
Left exp. parameter	0.0E0	0.0E0
Right exp. parameter	862E−9	862E−15

The two output files produced with the input parameters listed in Table 8.1 were evaluated for several coincidence window settings, both with and without applying the analytical accidental coincidence correction proposed in [18]. The corresponding results are shown in Figure 8.1. The figure clearly indicates that a proper application of the TDCR method necessitates correction for accidental coincidences.

For the simulation employing the narrow time distribution, the correction is highly effective: once applied, all derived quantities agree closely with the Monte Carlo reference values (Figure 8.1 (b)). In contrast, for the simulation based on the realistic ^{3}H-like time distribution, the correction performance depends on the coincidence-window width. Specifically, agreement improves for larger coincidence windows and deteriorates for smaller ones (Figure 8.1 (a)), most likely as a consequence of missed events when narrow coincidence windows are used. Nevertheless, as summarized Table 8.2, the TDCR method appears to mitigate the impact of missed events in the final activity determination.

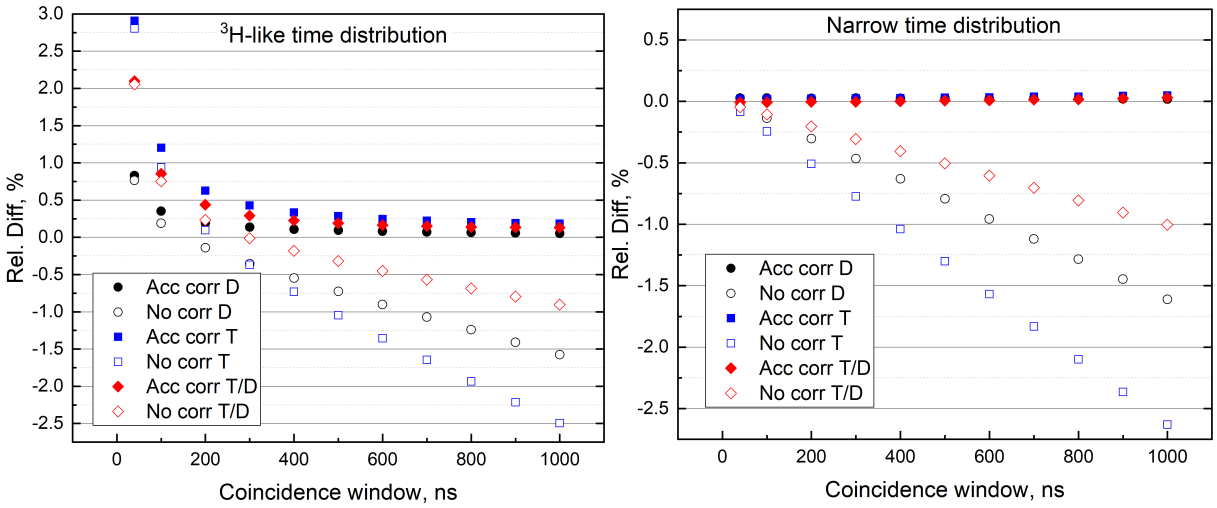

(a) (b)

Figure 8.1: Relative deviation between the simulated reference values and the calculated results as a function of the coincidence window (CW), for the realistic (Figure 8.1 (a)) and narrow (Figure 8.1 (b)) time distributions. Filled and open symbols denote results obtained with and without the accidental coincidence correction, respectively.

Table 8.2: Comparison of Monte Carlo (MC) simulated and estimated counting quantities for two time-distribution cases [170].

	^{3}H-like time distribution			Narrow time distribution		
Variable	MC simulated	Estimated	Δ	MC simulated	Estimated	Δ
A, cps	10680	10612	0.6%	10680	10682	−0.01%
B, cps	11914	11856	0.5%	11914	11915	−0.01%
C, cps	10619	10547	0.7%	10619	10620	−0.01%
AB, cps	6365	6262	1.6%	6365	6369	−0.05%
BC, cps	6221	6116	1.7%	6221	6225	−0.06%
AC, cps	5677	5568	1.9%	5677	5681	−0.07%
T, cps	4370	4248	2.8%	4370	4374	−0.09%
D, cps	9523	9450	0.8%	9523	9527	−0.04%
T/AB	0.687	0.678	1.2%	0.687	0.687	−0.03%
T/BC	0.703	0.695	1.1%	0.703	0.703	−0.02%
T/AC	0.770	0.763	0.9%	0.770	0.770	−0.02%
T/D	0.459	0.450	2.1%	0.459	0.459	−0.05%
Activity, Bq	19022	18998	0.1%	19022	19014	0.04%

Another application of the code is to demonstrate the role of accidental coincidence correction in the selection of the *kB* value in TDCR counting. Following the analysis of the list-mode files from the preceding example, the TDCR17 code [168] is applied to estimate the source activity for a range of *kB* values. The results for the narrow time distribution are presented in Figure 8.2. They show that, when the raw data are analyzed without correcting for accidental coincidences, the activity estimates exhibit a pronounced spread at each *kB* value, thereby complicating the identification of the appropriate *kB* (Figure 8.2 (a)). In contrast, once the accidental coincidence correction is applied, this spread is effectively removed and the correct *kB* value (0.012 cm/MeV in this case) can be readily identified (Figure 8.2 (b)).

A similar trend, albeit less pronounced, is observed for the ^{3}H-like time distribution Figure 8.3). The analysis of uncorrected data shows comparable dispersion in the deviations from the Monte Carlo reference for each *kB* value (Figure 8.3 (a)). Applying the accidental coincidence correction reduces the spread only modestly - most notably for larger coincidence windows - while a substantial dispersion remains (Figure 8.3 (a)). Notably, the correction has little influence on the 40 ns and 100 ns data points, whereas it markedly improves the clustering of results obtained with longer coincidence windows.

A plausible explanation is suggested in Figure 8.1 (a). For small coincidence windows, the T/D ratios corrected for accidental coincidences exhibit a significant bias. In contrast, for larger coincidence windows, the corrected T/D ratios do not show a comparable bias relative to the Monte Carlo values, even though the absolute number of accidental coincidences is higher. This behavior likely underlies the tighter grouping of points observed in Figure 8.3 (b) for CW $\geq$ 200 ns. The TDCR method appears to compensate for the effect of missed events in the final activity determination for a 40 ns coincidence window and *kB* =0.012 cm/MeV for the narrow distribution and *kB* =0.010 cm/MeV for the ^{3}H-like distribution.

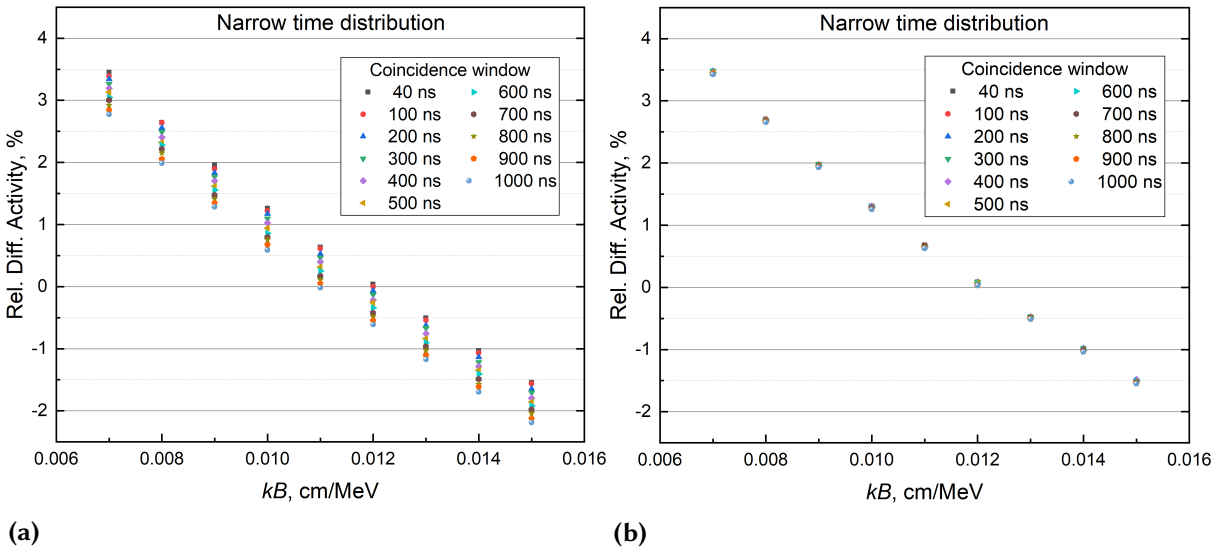

Figure 8.2: Relative deviation between the simulated reference activity and the calculated activity as a function of *kB* for the narrow time distribution, evaluated for several coincidence window settings, without (Figure 8.2 (a)) and with (Figure 8.2 (b)) accidental-coincidence correction [170].

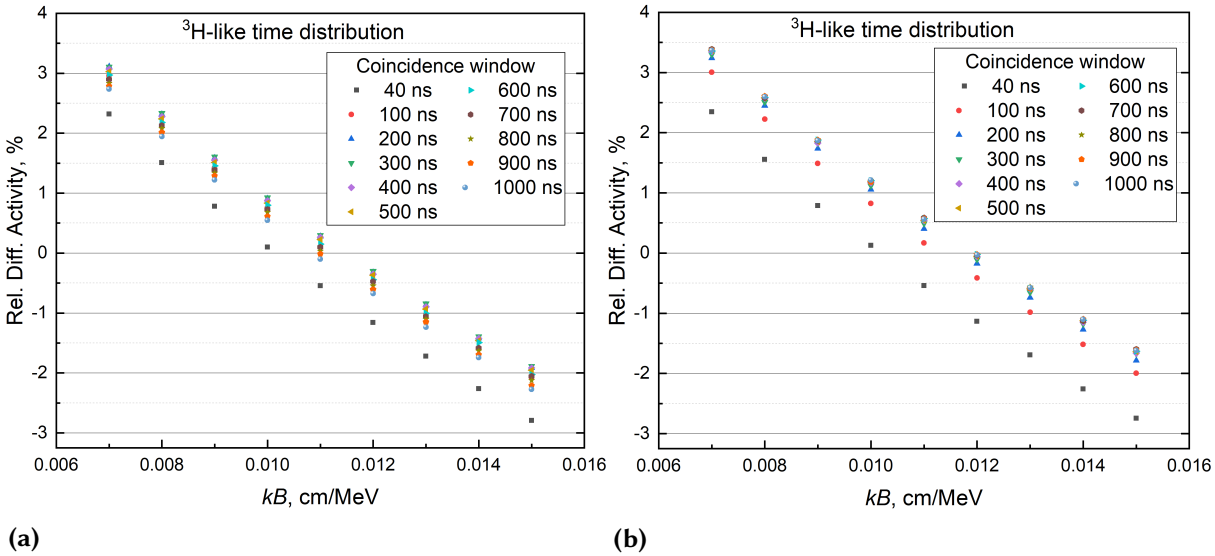

Figure 8.3: Relative deviation between the simulated reference activity and the calculated activity as a function of *kB* for the ^{3}H-like time distribution, evaluated for several coincidence window settings, without (Figure 8.3 (a)) and with (Figure 8.3 (b)) accidental-coincidence correction [170].

Two pulse-time distributions were investigated: an artificially narrow distribution and a realistic ^{3}H-like distribution. For the narrow distribution, the estimated counting rates agreed well with the Monte Carlo reference after applying the accidental coincidence correction. For the realistic ^{3}H-like distribution, larger deviations were observed at short coincidence windows, mainly due to missed true coincidences. The analysis code was validated and the importance of applying accidental coincidence correction was verified.

The simulations also showed that accidental coincidence correction can influence the determination of the *kB* parameter, although the strength of this effect depends on the time distribution and the coincidence window width. The effect was clear for the artificial narrow

distribution, whereas for the realistic ^{3}H-like distribution it was weaker and mainly improved the grouping of activity estimates for longer coincidence windows. Thus, the study confirms the usefulness of accidental coincidence correction, but also shows that the determination of *kB* remains a complex issue. Even with Monte Carlo reference data, the question of an unambiguous *kB* determination in TDCR measurements cannot be considered fully closed.

9 Conclusions & Outlook

The main objective of this thesis was to develop, validate, and apply a Compton–TDCR spectrometer for the experimental determination of the low-energy scintillation response of liquid scintillators. A new detection system was constructed at Sofia University, combining a three-PMT TDCR counter with an n-type planar HPGe detector for the energy selection of Compton-scattered photons. The system enables the scintillation light output to be measured for Compton electrons of known energy and therefore provides direct experimental characterization of the low-energy region that is most important for TDCR efficiency calculations.

The significance of this result lies in the fact that TDCR activity measurements, especially for low-energy β-emitting and electron-capture radionuclides, rely on an accurate description of the non-linear scintillator response. In TDCR efficiency calculations, this response is usually represented by the Birks' formula and a value of the ionization quenching parameter kB determined by efficiency variation. The Compton-TDCR spectrometer was successfully applied to the characterization of the light response of toluene+PPO, Ultima Gold AB, and Ultima Gold scintillation cocktails in the low-energy region of approximately 3–6 keV. The Compton-TDCR measurements demonstrated that experimentally measured response curves can be fitted with Birks' function and that the resulting kB values are consistent with values obtained independently by TDCR efficiency variation for the investigated scintillator–radionuclide combinations. This agreement confirms that the developed Compton-TDCR spectrometer provides physically meaningful scintillator-response data and validates its use as an independent experimental tool for studying ionization quenching in liquid scintillators.

The comparison between different TDCR counters showed that the estimated activities can agree within their uncertainties even when the evaluated kB values are not fully consistent. In principle, the ionization quenching parameter should characterize the scintillator response and should therefore not depend on the particular TDCR counter used for the measurement, provided that the same scintillator composition, decay data, and modelling assumptions are applied. The observed differences in the evaluated kB values therefore indicate that the determination of this parameter may be sensitive to features of the detection system and the assumptions used in the efficiency model that are not yet fully understood. However, the fact that the corresponding activity values remain consistent demonstrates that the TDCR efficiency calculation can still provide reliable activity estimates, even when the selected kB value is not identical across different detector systems.

Dependence of the evaluated kB value on the coincidence window width is was observed. From the efficiency variation of the ^{3}H sources, the kB values determined for a 40 ns coincidence window was systematically higher than those obtained with a 200 ns window. The same was observed in the Compton-TDCR measurements, where scintillation response acquired with different coincidence windows led to different fitted kB values. This indicates that the coincidence window changes what part of the scintillation emission contributes to the measured signal. A short coincidence window is dominated mainly by the prompt scintillation component, whereas a longer window also increases the contribution of the delayed fluorescence. Since Birks' formula describes ionization quenching of the prompt scintillation response and does not explicitly account for delayed emission or the full scintillation kinetics, kB values obtained

with longer coincidence windows should be interpreted as "effective", acquisition-dependent parameters.

A central limitation of the TDCR approach for low-energy radionuclides is the reliance on a parametric description of non-linearity. The Compton-TDCR measurements indicate that the obtained *kB* values are correlated with the intrinsic scintillation efficiency, implying that multiple parameter combinations can describe the same experimental curve. A practical mitigation is to use the experimentally determined response function directly in the TDCR model. This direction naturally connects to zero-model concepts such as ZoMBieS, where the PMT detection efficiency curve as a function of the energy deposited in the scintillator is measured experimentally and is approximated with appropriate function without necessarily having a physical meaning. Work on the implementation of the ZoMBieS method has begun and in its current state shows promising results.

The preparatory PMT studies were also essential to the reliability of the developed spectrometer. The Hamamatsu R331-05 PMTs selected for the TDCR channel were shown to have a sufficiently uniform response over most of the effective photocathode area, supporting their use in the LS channel of the Compton-TDCR system. The broader study of PMT photocathode response demonstrated that spatial non-uniformity can increase the uncertainty of TDCR efficiency estimates, particularly under low light conditions. This is important for low-energy radionuclides and for efficiency variation measurements, where the detected number of photoelectrons is small. The observation that PMT defocusing can increase spatial non-uniformity shows that defocusing is not a good way of reducing detection efficiency, because it may change the spatial distribution of photon detection probability of the system.

The TDCR performance of the new system was also confirmed through comparison with established TDCR counters using ^{3}H, ^{14}C, ^{63}Ni, and ^{55}Fe sources. The activity values obtained with the Compton-TDCR channel were consistent with those obtained using the other systems, demonstrating that the detector operates reliably as a primary liquid scintillation counter. The new system exhibited the highest detection efficiency among the compared counters. This result is particularly significant for the main objective of the thesis, because low-energy Compton electrons produce only a small number of detected photoelectrons. The high efficiency of the TDCR channel therefore makes the Compton-TDCR system especially suitable for studying scintillator response at very low deposited energies.

The investigation of accidental-coincidence correction clarified the conditions under which this correction affects TDCR efficiency calculations. For the experimental efficiency variation measurements performed at moderate activities, the analytical correction produced no changes in the evaluated *kB* values compared with their uncertainties. Monte Carlo list-mode simulations showed that the correction can strongly influence the *kB* selection for an artificially narrow, non-physical time distribution, whereas for a realistic ^{3}H-like time distribution the effect is more limited and mainly improves the grouping of estimated activities at coincidence windows larger than 100 ns. It was shown that the accidental-coincidence correction is an essential part of accurate TDCR analysis, especially for high counting rates and long coincidence windows.

The thesis also demonstrated the applicability of TDCR counting beyond the Compton-TDCR development through the primary standardization of ^{222}Rn in water. A practical source-preparation procedure was implemented, and TDCR measurements were used to prepare standardized radon-in-water sources. These sources were then used to calibrate secondary instruments, thereby providing a traceability chain for routine radon-in-water measurements. This application confirms that the TDCR methodology developed and used in the thesis has

direct relevance for practical radionuclide metrology and environmental radioactivity measurements.

Scientific contributions, for which the author has a leading role, are:

- Design, assembly, and commissioning of a Compton–TDCR system for low-energy scintillator-response measurements; geometric characterization of the nHPGe detector for Monte Carlo modelling; optimization of the setting of the coincidence acquisition chain; validation of the TDCR channel using low-energy β emitters and an electron-capture radionuclide through cross-comparisons with established TDCR systems.
- Measurement of scintillator response in multiple scintillator–radionuclide combinations; development of analysis software for fitting Birks' ionization quenching function; comparison of Compton-TDCR kB estimates with those obtained from efficiency variation measurements.
- Analysis of TDCR efficiency variation data for ^{3}H, ^{14}C, and ^{63}Ni liquid scintillation sources with and without analytical accidental coincidence correction; analysis of Monte Carlo generated list-mode files to benchmark accidental coincidence corrected and uncorrected results against the Monte Carlo ground truth; demonstration of the conditions under which accidental coincidence correction is critical for accurate counting rate estimation and for robust kB selection.
- Development and validation of an automated scanning-stage system for measuring PMT photocathode response; measurement of five PMTs and concurrent monitoring of heat transfer from the high-voltage divider; demonstration that PMT defocusing can substantially increase non-uniformity and may therefore be unsuitable (or require strict validation) as an efficiency-variation technique in TDCR counting.
- Implementation of TDCR counting for the primary standardization of ^{222}Rn-in-water in the MIL laboratory and calibration of secondary instruments.

Articles in refereed journals

[A.1] V. Todorov, P. Cassette, S. Georgiev, B. Sabot, and K. Mitev. **Automatic system for testing PMT photocathode homogeneity**. *Journal of Radioanalytical and Nuclear Chemistry* (Mar. 2025). ISSN: 1588-2780. DOI: 10.1007/s10967-025-10028-y. URL: http://dx.doi.org/10.1007/s10967-025-10028-y.

[A.2] P. Cassette, V. Todorov, B. Sabot, S. Georgiev, and K. Mitev. **Uncertainties in TDCR measurement revisited: Contribution of optical effects**. *Applied Radiation and Isotopes* 201 (Nov. 2023), 110992. ISSN: 0969-8043. DOI: 10.1016/j.apradiso.2023.110992. URL: http://dx.doi.org/10.1016/j.apradiso.2023.110992.

[A.3] V. Todorov, P. Cassette, V. Jordanov, S. Ivanov, H. Stoycheva, S. Georgiev, B. Sabot, and K. Mitev. **Design of a new Compton-TDCR spectrometer at Sofia University for the characterization of Liquid Scintillation cocktails**. *Applied Radiation and Isotopes* 226 (2025), 112194. ISSN: 0969-8043. DOI: https://doi.org/10.1016/j.apradiso.2025.112194. URL: https://www.sciencedirect.com/science/article/pii/S0969804325005391.

[A.4] V. Todorov, K. Mitev, P. Cassette, and B. Sabot. **Investigation of the possible effect of the accidental coincidences correction on the determination of kB value by efficiency variation with grey filters**. *Journal of Radioanalytical and Nuclear Chemistry* 334:9 (May 2025), 5943–5950. ISSN: 1588-2780. DOI: 10.1007/s10967-025-10173-4. URL: http://dx.doi.org/10.1007/s10967-025-10173-4.

[A.5] K. Mitev, V. Todorov, P. Cassette, and B. Sabot. **MCLTDCR: A Monte Carlo code for generation of list mode TDCR files**. *Applied Radiation and Isotopes* 226 (Dec. 2025), 112094. ISSN: 0969-8043. DOI: 10.1016/j.apradiso.2025.112094. URL: http://dx.doi.org/10.1016/j.apradiso.2025.112094.

Articles in refereed conference proceedings

[P.1] V. Todorov, P. Cassette, S. Georgiev, H. Stoycheva, R. Vasileva, and K. Mitev. **Application of TDCR Counting for Primary Standardization of Radon-in-Water Samples**. In: *2024 XXXIV International Scientific Symposium Metrology and Metrology Assurance (MMA)*. 2024, 1–6. DOI: 10.1109/MMA62616.2024.10817679.

Other articles related to the thesis

[O.1] V. Todorov, C. Dutsov, P. Cassette, and K. Mitev. **Effects of the photocathode non-uniformity on radon measurements by plastic scintillation spectrometry**. *Journal of Radioanalytical and Nuclear Chemistry* (June 2022). DOI: 10.1007/s10967-022-08362-6.

[O.2] V. Todorov, P. Cassette, Ch. Dutsov, B. Sabot, S. Georgiev, and K. Mitev. **A study of the non-uniformity of the PMT photocathode response and its influence on the results obtained in different scintillation counting experiments**. *Nuclear Instruments and Methods in Physics Research Section A: Accelerators, Spectrometers, Detectors and Associated Equipment* 1046 (Jan. 2023), 167719. ISSN: 0168-9002. DOI: 10.1016/j.nima.2022.167719. URL: http://dx.doi.org/10.1016/j.nima.2022.167719.

Application of TDCR counting to measuring ^{222}Rn in water

A

Radon-222 is widely regarded as the most significant natural radioisotope in terms of radiological impact on human health. According to [171], exposure to ^{222}Rn and its short-lived progeny in indoor air constitutes the leading cause of lung cancer among non-smokers.

In residential environments, the dominant entry pathway for radon is migration from soil gas into buildings. Radon dissolved in drinking water has also been recognized as a public health concern [172]. Because ^{222}Rn readily transfers from water to air during agitation and use, routine consumption and household use of radon-bearing water can elevate indoor radon levels. Consequently, several countries have introduced reference levels for radon in drinking water. Within the European Union, the reference level for ^{222}Rn in water is 100 Bq/L [173], whereas the United States Environmental Protection Agency specifies a level below 148 Bq/L [174].

Liquid scintillation counting is among the most commonly applied techniques for measuring ^{222}Rn in water. Calibration of this method has typically relied on standardized ^{226}Ra solutions. However, this approach has notable limitations, primarily because ^{210}Pb gradually accumulates in the radium solution as it ages [175]. The resulting ingrowth can interfere with liquid-scintillation sample measurements and complicate the establishment of a robust and reliable calibration.

Primary standardization of ^{222}Rn by TDCR counting was first proposed in 2006 by Cassette et al. [19]. This approach avoided technical difficulties associated with calibrating liquid-scintillation sources prepared from ^{226}Ra solutions in equilibrium with ^{222}Rn. [176, 175]

A primary standard for radon in water [177] was established at LNHB and implemented a dedicated production system to generate radon-in-water samples with concentrations traceable to the primary radon standard [178]. The proposed approach largely eliminates sampling-related radon losses and the associated variability in measurement results [177]. Comparisons have shown that the specific activity determined by the TDCR method is consistent with the primary standard and agrees with measurements performed using a commercial liquid scintillation counter. [177].

The method described in [19] relies on measuring liquid-scintillation samples in which ^{222}Rn is in radioactive equilibrium with its short-lived progeny. In the ^{222}Rn decay chain, three nuclides emit α particles (^{222}Rn, ^{218}Po, and ^{214}Po), while two progeny (^{214}Pb and ^{214}Bi) are high-energy β emitters. Secular equilibrium of the chain down to ^{210}Pb ($T_{1/2}$ = 22.2 years) is established after approximately 5 hours.

Because ^{214}Po has a very short half-life (162.3(12) μs), its decay may occur within the detector dead time that follows a ^{214}Bi decay. This effect lowers the effective detection efficiency for ^{214}Po [19]. The corresponding counting rate obtained during the live time and including the correction for ^{214}Po decays occurring during the detector dead time τ, is given in [19]:

$$R = \varepsilon_{^{222}\mathrm{Rn}}\, S_{^{222}\mathrm{Rn}}\, A_{^{222}\mathrm{Rn}} + \varepsilon_{^{218}\mathrm{Po}}\, S_{^{218}\mathrm{Po}}\, A_{^{218}\mathrm{Po}} + \varepsilon_{^{214}\mathrm{Pb}}\, S_{^{214}\mathrm{Pb}}\, A_{^{214}\mathrm{Pb}} + \varepsilon_{^{214}\mathrm{Bi}}\, S_{^{214}\mathrm{Bi}}\, A_{^{214}\mathrm{Bi}} + \varepsilon_{^{214}\mathrm{Po}}\, S_{^{214}\mathrm{Po}}\, A_{^{214}\mathrm{Po}}\, e^{-\lambda_{^{214}\mathrm{Po}}\,\tau} \tag{A.1}$$

where ε denotes the detection efficiencies of the respective radionuclides - equal to 100% for the α emitters and approximately 100% for the high-energy β emitters, S represents the corresponding emission probabilities, and A the radionuclides' activity.

By considering the activity relationships between ^{222}Rn and its progeny under secular equilibrium [179]:

$$\frac{A_{^{218}\mathrm{Po}}}{A_{^{222}\mathrm{Rn}}} = 1.001, \frac{A_{^{214}\mathrm{Pb}}}{A_{^{222}\mathrm{Rn}}} = 1.005, \frac{A_{^{214}\mathrm{Bi}}}{A_{^{222}\mathrm{Rn}}} = 1.009, \frac{A_{^{214}\mathrm{Po}}}{A_{^{222}\mathrm{Rn}}} = 1.009. \tag{A.2}$$

Equation (A.1) can be expressed in the form

$$R = A_{^{222}\mathrm{Rn}}\left(2.001 + 1.005\,\varepsilon_{^{214}\mathrm{Pb}} + 1.009\,\varepsilon_{^{214}\mathrm{Bi}} + 1.009\,e^{-\lambda_{^{214}\mathrm{Po}}\,\tau}\right), \tag{A.3}$$

where the numerical coefficients follow from the secular equilibrium activity ratios.

Within the TDCR, the detection efficiencies of the β emitters (^{214}Pb and ^{214}Bi) can be computed from their corresponding β-energy spectra. Since these efficiencies are close to unity, the inferred activity is only weakly dependent on the choice of the *kB* parameter. By contrast, an accurate determination of the ^{222}Rn activity requires the correction for ^{214}Po decays occurring during the detector dead time [19].

For the purposes of absolute standardization of ^{222}Rn in water, a dedicated `radon222` code to calculate the detection efficiencies in TDCR counting has been developed by P. Cassette. As input, `radon222` requires the β spectra of ^{214}Bi and ^{214}Pb, the TDCR value of the measurement and the detector dead time. The β spectra are derived from Monte Carlo simulations of the energy deposited in the liquid scintillator using the PENELOPE code [180], with initial β-emission spectra generated by the BETASHAPE code [104]. The outputs of `radon222` are the detection efficiencies of ^{222}Rn for double- and triple-coincidence counting.

TDCR counting is generally not optimal for the quantification of low-activity samples; however, it is well suited for the primary standardization of high-^{222}Rn activity water sources. Such standards can subsequently be used to calibrate detectors intended for measurements at or below regulatory reference levels.

In the MIL laboratory, a series of LSC sources with progressively decreasing ^{222}Rn concentrations in water was prepared and standardized using two TDCR systems. These sources were then employed to calibrate a Wallac RackBeta 1219 liquid scintillation counter for low-activity measurements and an HPGe detector.

A detailed description of the source preparation is given in [181]. In short the process is as follows:

- using a pump, circulate ^{222}Rn air and dissolve part of it in a water 10 L tank;
- mix six different ratios of the radonated and distilled water in 2 L bottles, resulting in water with different specific activity. One of the bottles was filled with undiluted radonated water. The bottle with the highest activity is labeled '6' and the bottle with the lowest activity is labeled '1'. The same labeling principle was used for the LSC samples;
- prepare LS sources in 20 mL high performance glass vials (Perkin Elmer) with 10 mL of water from the 2 L bottles and approximately 14 mL of UltimaGold LLT LS cocktail. Two LS sources with the highest activity water were prepared in order to check reproducibility. After mixing, water and cocktail result in a homogeneous phase and most of the Rn is transferred to the cocktail.

Two TDCR systems were employed in this study — the TDCR-SU and the miniTDCR with the CAEN DT5751 digitizer (see Chapter 6 for more details on the systems). The dominant

contributions to the uncertainty associated with the calculated specific activity are given in Table A.1.

Table A.1: Uncertainty budget of the specific activity measurement [181].

Uncertainty component	Relative standard uncertainty, %
Counting rates	0.3 – 0.7
kB parameter	0.001
Po-214 half-life	0.04
TDCR value	0.05
Spectrum calculation	0.6
Weighing	0.1
H_2O density	0.1
Final value	**0.7 – 1.0**

All LS samples were measured using both TDCR systems, with the exception of the vials with the highest activities which were measured with only one TDCR counter.

For most samples, measurements were performed on two consecutive days (named 'Meas 1' and 'Meas 2') with the two TDCR systems. Repeating the measurements verified the stability of the LS cocktail and confirmed that radon loss by diffusion from the cocktail to the air in the vial was not significant. The corresponding results are summarized in Table A.2.

Table A.2: Volume activity A_s (Bq/L) of the LSC samples obtained from two consecutive measurements with the TDCR-SU and miniTDCR systems; values are reported with standard uncertainties in parentheses [181].

	TDCR-SU: A_s,Bq/L		**miniTDCR: A_s, Bq/L**	
Vial	**Meas. 1**	**Meas. 2**	**Meas. 1**	**Meas. 2**
LSC 1	1232(10)	1238(13)	1237(18)	1226(12)
LSC 2	2554(18)	2567(24)	2561(23)	2553(23)
LSC 3	3787(28)	3791(28)	3778(25)	3783(37)
LSC 4	5129(47)	5136(32)	5127(32)	5111(43)
LSC 5	6378(42)	6376(46)	6376(49)	6367(47)
LSC 6-1	7538(52)	7548(57)	—	—
LSC 6-2	—	—	7525(52)	—

Table A.2 show that, for each sample, the volumic activities obtained on the two measurement days agree within their estimated uncertainties. Since the two measurements were performed with more than 15 hour delay, the samples can be considered stable over one day period, with radon largely retained in the liquid phase.

During the preparation procedure, the mass ratio of radonated water to distilled water was determined for each 2 L bottle. If no radon loss occurred during preparation and storage, the ratio of the measured volume activities of the corresponding LSC samples should therefore be equal to the ratio of radonated-water masses used for their preparation. The measured activity ratios and the corresponding mass ratios are reported in Table A.3.

Table A.3: Ratios of LSC sample volume activities relative to LSC6-1, compared with the corresponding radonated-to-distilled water mass ratios; relative standard uncertainties and the relative difference between the two ratios are also given [181].

Sample / LSC6-1	R_{LSC}	$u_{\mathrm{rel}}(R_{\mathrm{LSC}})$	R_{mass}	$u_{\mathrm{rel}}(R_{\mathrm{mass}})$	**Rel. diff.**
LSC5/LSC6-1	0.845	1.0%	0.833	0.3%	−1.4%
LSC4/LSC6-1	0.680	1.0%	0.666	0.4%	−2.1%
LSC3/LSC6-1	0.502	1.1%	0.493	0.5%	−1.9%
LSC2/LSC6-1	0.340	1.2%	0.334	0.8%	−1.9%
LSC1/LSC6-1	0.164	1.3%	0.165	1.5%	0.5%

The relative differences shown in Table A.3 suggest a loss of activity in the undiluted 2 L bottle (bottle labeled '6'). A plausible explanation is that, when the bottle was filled only with radonated water, no layer of distilled water was present at the bottom during filling. This may have facilitated the transfer of ^{222}Rn from the water phase to the air volume in the bottle. In contrast, in the diluted bottles, the radonated water was introduced below the surface of the distilled water, reducing direct contact with air and therefore limiting radon loss.

The small positive deviation observed for the ratio LSC1/LSC6-1 is likely related to minor spillage during preparation. Since this occurred for the bottle with the lowest activity, the spilled liquid was predominantly distilled water, which would slightly increase the final activity concentration and explain the observed positive difference.

The obtained specific activities and the comparison in the activity to mass ratios were used in two ways:

- the Wallac RackBeta 1219 detector was calibrated for LS counting. The HPGe detector in the same laboratory was also calibrated for measuring ^{222}Rn-in-water in LS vial geometry;
- we updated our source preparation procedure to have small amount of distilled water in each bottle and prevent activity loss.

These results demonstrate that TDCR-based standardization of ^{222}Rn-in-water provides a practical and metrologically sound basis for in-house calibration. The validated procedure has now been transferred to routine practice in the laboratory and can be used in future calibration campaigns for both LS counters and HPGe detectors, ensuring traceable measurements of ^{222}Rn activities in water.

Bibliography

[1] J. B. Birks. **The Theory and Practice of Scintillation Counting**. Oxford: Pergamon Press, 1964 (see pages 1, 5, 7, 8, 10, 13–16, 39, 76).

[2] von Immanuel Broser and Hartmut Kallmann. **Über die Anregung von Leuchtstoffen durch schnelle Korpuskularteilchen L (Eine neue Methode zur Registrierung und Energiemessung schwerer geladener Teilchen)**. *Zeitschrift Naturforschung Teil A* 2 (1947), 439 (see pages 1, 4).

[3] George T. Reynolds, F. B. Harrison, and G. Salvini. **Liquid Scintillation Counters**. *Phys. Rev.* 78 (4 1950), 488. DOI: 10.1103/PhysRev.78.488. URL: https://link.aps.org/doi/10.1103/PhysRev.78.488 (see page 1).

[4] D. L. Horrocks. **Applications of Liquid Scintillation Counting**. 1974. URL: http://gen.lib.rus.ec/book/index.php?md5=AEC337237738642FC1E09F533E5600F1 (see pages 1, 4).

[5] F.D. Brooks. **Development of organic scintillators**. *Nuclear Instruments and Methods* 162:1 (1979), 477–505. ISSN: 0029-554X. DOI: https://doi.org/10.1016/0029-554X(79)90729-8. URL: https://www.sciencedirect.com/science/article/pii/0029554X79907298 (see pages 1, 9, 13).

[6] G. F. Knoll. **Radiation Detection and Measurement**. 4th ed. Wiley, 2010. ISBN: 9780470131480 (see pages 1, 21).

[7] M. F. L'Annunziata. **Editor, Handbook of Radioactivity Analysis.** Third. Amsterdam, The Netherlands: Academic Press, Elsevier., 2012 (see pages 1, 14, 21, 23).

[8] M. Koshimizu. **Fundamental processes and recent development of organic scintillators**. *Journal of Luminescence* 278 (2025), 121008. ISSN: 0022-2313. DOI: https://doi.org/10.1016/j.jlumin.2024.121008. URL: https://www.sciencedirect.com/science/article/pii/S0022231324005726 (see page 1).

[9] V. Kolarov, Y. Le Gallic, and R. Vatin. **Mesure absolue directe de l'activité des emetteurs β purs par scintillation liquide**. *The International Journal of Applied Radiation and Isotopes* 21:8 (Aug. 1970), 443–452. DOI: 10.1016/0020-708x(70)90090-6 (see pages 1, 4).

[10] K. Pochwalski and T. Radoszewski. **Disintegration Rate Determination by Liquid Scintillation Counting Using the Triple to Double Coincidence Ratio (TDCR) Method**. Tech. rep. INR 1848/OPiDI/E/A. Warsaw: Institute of Nuclear Research, 1979 (see pages 2, 24).

[11] Ryszard Broda, Philippe Cassette, and Karsten Kossert. **Radionuclide metrology using liquid scintillation counting**. *Metrologia* 44:4 (2007), S36 (see pages 2, 19, 24–32, 39, 53).

[12] Chavdar Dutsov, Philippe Cassette, Krasimir Mitev, and Benoît Sabot. **In quest of the optimal coincidence resolving time in TDCR LSC**. *Nuclear Instruments and Methods in Physics Research Section A: Accelerators, Spectrometers, Detectors and Associated Equipment* (Nov. 2020), 164846. DOI: 10.1016/j.nima.2020.164846 (see pages 2, 24, 105).

[13] M. Péron and P. Cassette. **COCO, a Compton coincidence experiment to study liquid scintillator response in the 1–20 keV energy range**. *Nuclear Instruments Meth. Phys. Res. Section A: Accelerators, Spectrometers, Detectors and Associated Equipment* 353:1-3 (1994), 41–45. DOI: 10.1016/0168-9002(94)91598-9 (see pages 2, 35, 61).

[14] M.N. Peron and P. Cassette. **A Compton coincidence study of liquid scintillator response to low-energy electrons**. *Nuclear Instruments and Methods in Physics Research Section A: Accelerators, Spectrometers, Detectors and Associated Equipment* 369:2–3 (Feb. 1996), 344–347. ISSN: 0168-9002. DOI: 10.1016/s0168-9002(96)80006-4. URL: http://dx.doi.org/10.1016/S0168-9002(96)80006-4 (see pages 2, 35).

[15] P. Cassette and P. Do. **The Compton source efficiency tracing method in liquid scintillation counting: A new standardization method using a TDCR counter with a Compton spectrometer**. *Applied Radiation and Isotopes* 66:6-7 (2008), 1026–1032. DOI: 10.1016/j.apradiso.2008.02.062 (see pages 2, 36–38, 61, 76).

[16] Benoit Sabot, Chavdar Dutsov, Philippe Cassette, Krasimir Mitev, Matthieu Hamel, Guillaume H. V. Bertrand, Kheirreddine Lebbou, and Christophe Dujardin. **A compact detector system for simultaneous measurements of the light yield non-linearity and timing properties of scintillators**. *Scientific Reports* 14:1 (Mar. 2024). ISSN: 2045-2322. DOI: 10.1038/s41598-024-57186-9. URL: http://dx.doi.org/10.1038/s41598-024-57186-9 (see pages 2, 36, 70, 78, 88).

[17] L. J. Bignell, L. Mo, T. Steele, and S. Reza Hashemi-Nezhad. **The Zero Model by Using Coincidence Scintillation (ZoMBieS) Method of Absolute Radioactivity Measurement**. *IEEE Transactions on Nuclear Sci.* 60:5 (2013), 4007–4014. DOI: 10.1109/tns.2013.2275990 (see pages 2, 38, 89).

[18] Chavdar Dutsov, Philippe Cassette, Benoît Sabot, and Krasimir Mitev. **Evaluation of the accidental coincidence counting rates in TDCR counting**. *Nuclear Instruments and Methods in Physics Research Section A: Accelerators, Spectrometers, Detectors and Associated Equipment* 977 (Oct. 2020), 164292. DOI: 10.1016/j.nima.2020.164292 (see pages 3, 24, 33–35, 61, 90, 101, 109).

[19] P. Cassette, M. Sahagia, L. Grigorescu, M. C. Lepy, and J. L. Picolo. **Standardization of 222Rn by LSC and comparison with alpha- and gamma-spectrometry.** *Applied Radiation and Isotopes.* 64 (2006), 1465–1470 (see pages 3, 118, 119).

[20] J A B Gibson and H J Gale. **Absolute standardization with liquid scintillation counters**. *J. Phys. E: Sci. Instrum.* 1:2 (Feb. 1968), 99–106. DOI: 10.1088/0022-3735/1/2/305 (see page 4).

[21] Ryszard Broda, Krzysztof Pochwalski, and Tomasz Radoszewski. **Calculation of liquid-scintillation detector efficiency**. *International Journal of Radiation Applications and Instrumentation. Part A. Applied Radiation and Isotopes* 39:2 (1988), 159–164. DOI: 10.1016/0883-2889(88)90161-x (see page 4).

[22] A. Grau Malonda and Bert M. Coursey. **Calculation of beta-particle counting efficiency for liquid-scintillation systems with three phototubes**. *International Journal of Radiation Applications and Instrumentation. Part A. Applied Radiation and Isotopes* 39:12 (Jan. 1988), 1191–1196. DOI: 10.1016/0883-2889(88)90098-6 (see page 4).

[23] Jie Ren, Peng Wang, Aotian Gu, Chunhui Gong, Kaiwei Chen, Ping Mao, Yan Jiao, Kai Chen, and Yi Yang. **A Review of Recent Improvements in Novel Liquid Scintillator Materials**. *Processes* 12:6 (2024). ISSN: 2227-9717. DOI: 10.3390/pr12061223. URL: https://www.mdpi.com/2227-9717/12/6/1223 (see page 5).

[24] Mordechai Bixon and Joshua Jortner. **Intramolecular Radiationless Transitions**. *The Journal of Chemical Physics* 48:2 (Jan. 1968), 715–726. ISSN: 1089-7690. DOI: 10.1063/1.1668703. URL: http://dx.doi.org/10.1063/1.1668703 (see pages 5, 7).

[25] R. Voltz, J. Lopes da Silva, G. Laustriat, and A. Coche. **Influence of the Nature of Ionizing Particles on the Specific Luminescence of Organic Scintillators**. *The Journal of Chemical Physics* 45:9 (Nov. 1966), 3306–3311. DOI: 10.1063/1.1728106 (see pages 6, 17).

[26] R. Voltz and G. Laustriat. **Radioluminescence des milieux organiques I. Étude cinétique**. *Journal de Physique* 29:2-3 (1968), 159–166. DOI: 10.1051/jphys:01968002902-3015900 (see pages 6, 8–10).

[27] R. Voltz, H. Dupont, and G. Laustriat. **Radioluminescence des milieux organiques. II. Vérification expérimentale de l'étude cinétique**. *Journal de Physique* 29:4 (1968), 297–305. DOI: 10.1051/jphys:01968002904029700 (see pages 6, 9).

[28] G. Laustriat. **The luminescence decay of organic scintillators**. *Molecular Crystals* 4:1-4 (June 1968), 127–145. DOI: 10.1080/15421406808082905 (see pages 6, 7, 10–13).

[29] Daniel Blanc, Francis Cambou, and Yann Gervais de Lafond. **Étude cinétique de la scintillation dans les cristaux organiques purs**. *Journal de Physique* 25:3 (1964), 319–325. DOI: 10.1051/jphys:01964002503031900. URL: https://hal.science/jpa-00205779 (see pages 8, 10, 17).

[30] C. A. Parker and C. G. Hatchard. **Triplet-singlet emission in fluid solutions. Phosphorescence of eosin**. *Trans. Faraday Soc.* 57 (0 1961), 1894–1904. DOI: 10.1039/TF9615701894. URL: http://dx.doi.org/10.1039/TF9615701894 (see page 8).

[31] Chavdar Dutsov, Benoît Sabot, Philippe Cassette, and Krasimir Mitev. **Measurement of the half-life of excited nuclear states using liquid scintillation counting**. *Applied Radiation and Isotopes* 176 (Oct. 2021), 109845. ISSN: 0969-8043. DOI: 10.1016/j.apradiso.2021.109845. URL: http://dx.doi.org/10.1016/j.apradiso.2021.109845 (see pages 8, 48).

[32] T. A. King and R. Voltz. **The time dependence of scintillation intensity in aromatic materials**. *Proceedings of the Royal Society of London. Series A. Mathematical and Physical Sciences* 289:1418 (Jan. 1966), 424–439. DOI: 10.1098/rspa.1966.0021 (see pages 10, 11).

[33] F. D. Brooks. **Organic Scintillators**. *Progress in Nuclear Physics* 5 (1956). Ed. by O. R. Frisch, 284–311 (see page 13).

[34] G. T. Wright. **Scintillation Decay Times of Organic Crystals**. *Proceedings of the Physical Society. Section B* 69:3 (1956), 358–372. DOI: 10.1088/0370-1301/69/3/311 (see page 13).

[35] R B Owen. **The Decay Times of Organic Scintillators and Their Application to the Discrimination between Particles of Differing Specific Ionization**. *IRE Trans. Nuclear Sci.* Vol: NS-5 (Dec. 1958). DOI: 10.1109/TNS2.1958.4315657. URL: https://www.osti.gov/biblio/4265230 (see page 13).

[36] R. B. Owen. **The Variation of Phosphor Decay Time With Specific Ionization and its Applications**. In: *Nuclear Electronics: Proceedings of the International Symposium on Nuclear Electronics, Paris, 1958*. Vol. 1. Vienna: International Atomic Energy Agency, 1959, 27 (see page 14).

[37] L. M. Bollinger and G. E. Thomas. **Measurement of the Time Dependence of Scintillation Intensity by a Delayed-Coincidence Method**. *Review of Scientific Instruments* 32:9 (Sept. 1961), 1044–1050. ISSN: 0034-6748. DOI: 10.1063/1.1717610. eprint: https://pubs.aip.org/aip/rsi/article-pdf/32/9/1044/19034510/1044_1_online.pdf. URL: https://doi.org/10.1063/1.1717610 (see page 14).

[38] P E Gibbons, D C Northrop, and O Simpson. **The Scintillation Phenomenon in Anthracene: II. Scintillation Pulse Shape**. *Proceedings of the Physical Society* 79:2 (1962), 373. DOI: 10.1088/0370-1328/79/2/316. URL: https://doi.org/10.1088/0370-1328/79/2/316 (see page 14).

[39] F. D. Brooks. **A scintillation counter with neutron and gamma-ray discriminators**. *Nuclear Instruments and Methods* 4:3 (Apr. 1959), 151–163. DOI: 10.1016/0029-554X(59)90067-9 (see page 14).

[40] R. B. Owen. **Pulse-Shape Discrimination Identifies Particle Types**. *Nucleonics* 17:9 (Sept. 1959), 92–95. URL: https://www.osti.gov/biblio/4238076 (see page 15).

[41] M.L. Roush, M.A. Wilson, and W.F. Hornyak. **Pulse shape discrimination**. *Nuclear Instruments and Methods* 31:1 (1964), 112–124. ISSN: 0029-554X. DOI: https://doi.org/10.1016/0029-554X(64)90333-7. URL: https://www.sciencedirect.com/science/article/pii/0029554X64903337 (see page 15).

[42] T.K. Alexander and F.S. Goulding. **An amplitude-insensitive system that distinguishes pulses of different shapes**. *Nuclear Instruments and Methods* 13 (1961), 244–246. ISSN: 0029-554X. DOI: https://doi.org/10.1016/0029-554X(61)90198-7. URL: https://www.sciencedirect.com/science/article/pii/0029554X61901987 (see page 15).

[43] Valentin T. Jordanov. **Pile-up Real Time Pulse-Shape Discrimination Based on Ballistic Deficit Measurement and Digital Time-Invariant Pulse Shaping**. In: *2018 IEEE Nuclear Science Symposium and Medical Imaging Conference Proceedings (NSS/MIC)*. IEEE, Nov. 2018. DOI: 10.1109/nssmic.2018.8824502 (see page 15).

[44] Yantel. *nanoPSD, product information*. URL: https://www.yantel.com/products/nanopsd/ (see pages 15, 40).

[45] Tessa E. Maurer, Leah. M. Clark, Shaun D. Clarke, and Sara A. Pozzi. **Pulse Shape Discrimination of Shielded and Unshielded 252Cf in Organic Glass Scintillators**. In: *2022 IEEE Nuclear Science Symposium and Medical Imaging Conference (NSS/MIC)*. 2022, 1–3. DOI: 10.1109/NSS/MIC44845.2022.10399197 (see page 15).

[46] Leah M. Clark, Tessa E. Maurer, Stefano Marin, Nathan P. Giha, Shaun D. Clarke, and Sara A. Pozzi. **Time and Energy Resolution of Organic Glass Scintillators for Radionuclide Monitoring**. In: *2021 IEEE Nuclear Science Symposium and Medical Imaging Conference (NSS/MIC)*. 2021, 1–4. DOI: 10.1109/NSS/MIC44867.2021.9875704 (see page 15).

[47] Miguel Astrain, Mariano Ruiz, Adam. V. Stephen, Rashed Sarwar, Antonio Carpeño, Sergio Esquembri, Andrea Murari, Francesco Belli, and Marco Riva. **Real-Time Implementation of the Neutron/Gamma Discrimination in an FPGA-Based DAQ MTCA Platform Using a Convolutional Neural Network**. *IEEE Transactions on Nuclear Science* 68:8 (2021), 2173–2178. DOI: 10.1109/TNS.2021.3090670 (see page 15).

[48] Urmila Shirwadkar, Edgar van Loef, Tawan Jamdee, Lakshmi Soundara Pandian, Nathaniel Kaneshige, Jarek Glodo, Patrick L. Feng, Lucas Nguyen, Annabelle Benin, Remco G. T. Zegers, Jorge Pereira, Cavan Maher, and Kanai S. Shah. **Development of Multi-mode Organic Glass Scintillators for Nuclear Physics Applications**. In: *2021 IEEE Nuclear Science Symposium and Medical Imaging Conference (NSS/MIC)*. 2021, 1–4. DOI: 10.1109/NSS/MIC44867.2021.9875655 (see page 15).

[49] Dimitris Papanikolaou, Agatino Musumarra, Maria Grazie Pellegriti, and Nikolaos Patronis. **Neutron capture reactions for nuclear astrophysics: Development; characterization of an innovative detection setup based on trans-Stilbene organic scintillators**. *HNPS Advances in Nuclear Physics* 31 (2025), 1–7. DOI: 10.12681/hnpsanp.7995. URL: https://eproceedings.epublishing.ekt.gr/index.php/hnps/article/view/7995 (see page 15).

[50] Colton Graham, Ethan Todd, Caryanne Wilson, Shaun Clarke, Sara Pozzi, and Igor Jovanovic. **Light output-dependent integration gating for optimized pulse shape discrimination**. *Nuclear Instruments and Methods in Physics Research Section A: Accelerators, Spectrometers, Detectors and Associated Equipment* 1088 (2026), 171521. ISSN: 0168-9002. DOI: https://doi.org/10.1016/j.nima.2026.171521. URL: https://www.sciencedirect.com/science/article/pii/S0168900226002470 (see page 15).

[51] Willem G. J. Langeveld, Michael J. King, John Kwong, and Daniel T. Wakeford. **Pulse Shape Discrimination Algorithms, Figures of Merit, and Gamma-Rejection for Liquid and Solid Scintillators**. *IEEE Transactions on Nuclear Science* 64:7 (2017), 1801–1809. DOI: 10.1109/TNS.2017.2681654 (see page 15).

[52] Willem G. J. Langeveld, Andrew Glenn, Steven A. Sheets, Dan A. Strellis, and Natalia P. Zaitseva. **Comparison of pulse shape discrimination performance of stilbene and liquid scintillator under high count-rate active interrogation conditions**. *Nuclear Instruments & Methods in Physics Research Section A-accelerators Spectrometers Detectors and Associated Equipment* 954 (2020), 161204. URL: https://api.semanticscholar.org/CorpusID:116058313 (see page 15).

[53] Haoran Liu, Yihan Zhan, Mingzhe Liu, Yanhua Liu, Peng Li, Zhuo Zuo, Bingqi Liu, and Runxi Liu. **Pulse shape discrimination algorithms: Survey and benchmark**. *Radiation Measurements* 193 (2026), 107653. ISSN: 1350-4487. DOI: https://doi.org/10.1016/j.radmeas.2026.107653. URL: https://www.sciencedirect.com/science/article/pii/S1350448726000508 (see page 15).

[54] *Estar — stopping power and range tables for electrons*. URL: https://physics.nist.gov/PhysRefData/Star/Text/ESTAR.html (see page 16).

[55] J B Birks. **Scintillations from Organic Crystals: Specific Fluorescence and Relative Response to Different Radiations**. *Proceedings of the Physical Society. Section A* 64:10 (1951), 874. DOI: 10.1088/0370-1298/64/10/303. URL: https://doi.org/10.1088/0370-1298/64/10/303 (see page 16).

[56] C. N. Chou. **Saturation Effect of Plastic Scintillators**. *Phys. Rev.* 87:5 (Sept. 1952), 903–904. DOI: 10.1103/physrev.87.903 (see page 16).

[57] G. T. Wright. **Scintillation Response of Organic Phosphors**. *Phys. Rev.* 91:5 (Sept. 1953), 1282–1283. DOI: 10.1103/physrev.91.1282.2 (see page 16).

[58] J. Hong, W. W. Craig, P. Graham, C. J. Hailey, N. J. C. Spooner, and D. R. Tovey. **The scintillation efficiency of carbon and hydrogen recoils in an organic liquid scintillator for dark matter searches**. *Astropart. Phys.* 16 (2002), 333–338. DOI: 10.1016/S0927-6505(01)00114-1 (see page 16).

[59] S. Yoshida, T. Ebihara, T. Yano, A. Kozlov, T. Kishimoto, I. Ogawa, R. Hazama, S. Umehara, K. Mukaida, K. Ichihara, Y. Hirano, I. Murata, J. Datemichi, and H. Sugimoto. **Light output response of KamLAND liquid scintillator for protons and 12C nuclei**. *Nuclear Instruments and Methods in Physics Research Section A: Accelerators, Spectrometers, Detectors and Associated Equipment* 622:3 (2010), 574–582. ISSN: 0168-9002. DOI: https://doi.org/10.1016/j.nima.2010.07.087. URL: https://www.sciencedirect.com/science/article/pii/S0168900210017018 (see page 17).

[60] Thibault A. Laplace, Bethany L. Goldblum, Joshua A. Brown, Glenn LeBlanc, Tianyue Li, Juan J. Manfredi, and Erik Brubaker. **Modeling ionization quenching in organic scintillators**. *Mater. Adv.* 3 (14 2022), 5871–5881. DOI: 10.1039/D2MA00388K. URL: http://dx.doi.org/10.1039/D2MA00388K (see pages 17, 19, 20).

[61] Jeppe Brage Christensen and Claus E Andersen. **Relating ionization quenching in organic plastic scintillators to basic material properties by modelling excitation density transport and amorphous track structure during proton irradiation**. *Physics in Medicine & Biology* 63:19 (2018), 195010. DOI: 10.1088/1361-6560/aadf2d. URL: https://doi.org/10.1088/1361-6560/aadf2d (see page 17).

[62] H. Bethe. **Bremsformel für Elektronen relativistischer Geschwindigkeit**. *Zeitschrift für Physik* 76:5-6 (May 1932), 293–299. ISSN: 1434-601X. DOI: 10.1007/bf01342532. URL: http://dx.doi.org/10.1007/BF01342532 (see page 18).

[63] *Liquid scintillation cocktail elementary composition*. URL: http://www.lnhb.fr/pdf/2010_LSC_cocktails_elementary_composition.pdf (see page 19).

[64] James F. Ziegler, M.D. Ziegler, and J.P. Biersack. **SRIM – The stopping and range of ions in matter (2010)**. *Nuclear Instruments and Methods in Physics Research Section B: Beam Interactions with Materials and Atoms* 268:11 (2010). 19th International Conference on Ion Beam Analysis, 1818–1823. ISSN: 0168-583X. DOI: https://doi.org/10.1016/j.nimb.2010.02.091. URL: https://www.sciencedirect.com/science/article/pii/S0168583X10001862 (see page 19).

[65] M. J. Berger, J. S. Coursey, M. A. Zucker, and J. Chang. *ESTAR, PSTAR, and ASTAR: Computer Programs for Calculating Stopping-Power and Range Tables for Electrons, Protons, and Helium Ions*. Version 1.2.3. National Institute of Standards and Technology. 2005. URL: http://physics.nist.gov/Star (visited on 05/13/2026) (see page 19).

[66] Helmut Paul and Andreas Schinner. **Empirical stopping power tables for ions from 3Li to 18Ar and from 0.001 to 1000 MeV/nucleon in solids and gases**. *Atomic Data and Nuclear Data Tables* 85 (2003), 377–452. URL: https://api.semanticscholar.org/CorpusID:94518226 (see page 19).

[67] Hamamatsu. *Photomultiplier tubes - basics and applications*. Fourth edition. Hamamatsu photonics. 2017. URL: https://www.hamamatsu.com/resources/pdf/etd/PMT_handbook_v4E.pdf (see pages 21–23, 32, 44).

[68] Kodai Matsuoka. **Expression for the angular dependence of the quantum efficiency of a thin multi-alkali photocathode and its optical properties**. *Progress of Theoretical and Experimental Physics* 2018:12 (Dec. 2018). ISSN: 2050-3911. DOI: 10.1093/ptep/pty123. URL: http://dx.doi.org/10.1093/ptep/pty123 (see page 22).

[69] A. G. Wright. **Method for the determination of photomultiplier collection efficiency, F**. *Applied Optics* 49:11 (Apr. 2010), 2059. ISSN: 1539-4522. DOI: 10.1364/ao.49.002059. URL: http://dx.doi.org/10.1364/AO.49.002059 (see page 23).

[70] A. W. Schardt and W. Bernstein. **Resolution of the Scintillation Spectrometer**. *Review of Scientific Instruments* 22:12 (Dec. 1951), 1020–1021. DOI: 10.1063/1.1745805. URL: https://doi.org/10.1063/1.1745805 (see page 23).

[71] T. F. Godlove and W. G. Wadey. **Photocathode Uniformity and Resolution of Scintillation Spectrometers**. *Review of Scientific Instruments* 25:1 (Jan. 1954), 1–4. DOI: 10.1063/1.1770874. URL: https://doi.org/10.1063/1.1770874 (see page 23).

[72] P. S. Takhar. **Resolution and Cathode Uniformity in Scintillation Counters**. *IEEE Transactions on Nuclear Science* 14 (1967), 438–442. ISSN: 0018-9499. DOI: 10.1109/tns.1967.4324451. URL: http://dx.doi.org/10.1109/tns.1967.4324451 (see pages 23, 45).

[73] B. Leskovar and C. C. Lo. **Performance Studies of Photomutipliers Having Dynodes with GaP(Cs) Secondary Emitting Surface**. *IEEE Transactions on Nuclear Science* 19:3 (1972), 50–62. DOI: 10.1109/tns.1972.4326702. URL: https://doi.org/10.1109/tns.1972.4326702 (see page 23).

[74] M. Mottaghian, R. Koohi-Fayegh, N. Ghal-Eh, and G. R. Etaati. **Photocathode non-uniformity contribution to the energy resolution of scintillators**. *Radiation Protection Dosimetry* 140:1 (Feb. 2010), 16–24. DOI: 10.1093/rpd/ncq041. URL: https://doi.org/10.1093/rpd/ncq041 (see page 23).

[75] J.M. Paul. **Studies concerning the behaviour of photomultiplier with large photocathode**. *Nuclear Instruments and Methods* 89 (Dec. 1970), 285–287. DOI: 10.1016/0029-554x(70)90836-0. URL: https://doi.org/10.1016/0029-554x(70)90836-0 (see page 23).

[76] H. Kume, S. Sawaki, M. Ito, K. Arisaka, T. Kajita, A. Nishimura, and A. Suzuki. **20 inch diameter photomultiplier**. *Nuclear Instruments and Methods in Physics Research* 205:3 (Feb. 1983), 443–449. DOI: 10.1016/0167-5087(83)90007-8. URL: https://doi.org/10.1016/0167-5087(83)90007-8 (see page 23).

[77] M.A. Unland Elorrieta, R.S. Busse, L. Classen, and A. Kappes. **Homogeneity of the photocathode in the Hamamatsu R15458-02 Photomultiplier Tube**. *Journal of Instrumentation* 16:11 (Nov. 2021), P11038. DOI: 10.1088/1748-0221/16/11/p11038. URL: https://doi.org/10.1088/1748-0221/16/11/p11038 (see page 23).

[78] N. Anfimov. **Large photocathode 20-inch PMT testing methods for the JUNO experiment**. *Journal of Instrumentation* 12:06 (June 2017), C06017–C06017. ISSN: 1748-0221. DOI: 10.1088/1748-0221/12/06/c06017. URL: http://dx.doi.org/10.1088/1748-0221/12/06/C06017 (see page 23).

[79] Feng Gao, Sen Qian, Yichao Ma, Jingkai Xia, Zhe Ning, Zhigang Wang, Lishuang Ma, Qi Wu, and Shuo Peng. **Research and development of 20-inch PMT uniformity scanning platform**. *Nuclear Instruments and Methods in Physics Research Section A: Accelerators, Spectrometers, Detectors and Associated Equipment* 1027 (Mar. 2022), 166257. DOI: 10.1016/j.nima.2021.166257. URL: https://doi.org/10.1016/j.nima.2021.166257 (see page 23).

[80] S Korpar, I Bizjak, A Gorišek, P Križan, R Pestotnik, M Starič, and A Stanovnik. **Surface sensitivity of multianode photomultiplier tubes**. *Nuclear Instruments and Methods in Physics Research Section A: Accelerators, Spectrometers, Detectors and Associated Equipment* 478:1–2 (Feb. 2002), 391–394. ISSN: 0168-9002. DOI: 10.1016/s0168-9002(01)01780-6. URL: http://dx.doi.org/10.1016/S0168-9002(01)01780-6 (see page 23).

[81] V. Vasileiou, R. W. Ellsworth, and A. J. Smith. *Photocathode-Uniformity Tests of the Hamamatsu R5912 Photomultiplier Tubes Used in the Milagro Experiment*. 2007. DOI: 10.48550/ARXIV.0711.1910. URL: https://arxiv.org/abs/0711.1910 (see page 23).

[82] L. Baudis, S. D'Amato, G. Kessler, A. Kish, and J. Wulf. **Measurements of the position-dependent photo-detection sensitivity of the Hamamatsu R11410 and R8520 photomultiplier tubes** (Sept. 2015). arXiv: 1509.04055 [physics.ins-det] (see page 23).

[83] R. Kossakowski, J.C. Audemer, J.M. Dubois, D. Fougeron, R. Hermel, R. Sottile, and J.P. Vialle. **Study of the photomultiplier R7600-00-M4 for the purpose of the electromagnetic calorimeter in the AMS-02 experiment**. Tech. rep. 2002, 1–20. URL: https://in2p3.hal.science/in2p3-00021475 (see page 23).

[84] Y. Ren, X. Yang, Y. Wang, Z. Deng, Z. Qin, A. Olshevskiy, W. Wang, N. Anfimov, Z. Wang, and G. Cao. *Development of a comprehensive PMT optical model for the JUNO experiment*. 2026. arXiv: 2601.19081 [hep-ex]. URL: https://arxiv.org/abs/2601.19081 (see page 23).

[85] ORDELA Inc. *PERALS® Simplified Environmental Alpha Spectrometry*. Online; accessed 01-Aug-2022. 2017. URL: https://ordelacom.files.wordpress.com/2017/01/peralsc2ae-color-brochure-revised.pdf (see page 23).

[86] Karsten Kossert and Marcell Péter Takács. **Study of a method to correct for accidental coincidences in TDCR measurements**. *Applied Radiation and Isotopes* 226 (Dec. 2025), 112176. ISSN: 0969-8043. DOI: 10.1016/j.apradiso.2025.112176. URL: http://dx.doi.org/10.1016/j.apradiso.2025.112176 (see pages 24, 35, 61, 105).

[87] *Tritium and carbon-14 activity in gaseous effluents and gas discharges of nuclear installations — Part 2: Determination of tritium and carbon-14 activities sampled by bubbling technique*. Accessed 2026-05-14. International Organization for Standardization, Sept. 2025. URL: https://www.iso.org/standard/78795.html (see page 24).

[88] **Lesson 7: Tritium and C-14 Monitoring**. Tech. rep. Training material (PDF), accessed 2026-05-14. International Atomic Energy Agency (IAEA), 2021. URL: https://www.iaea.org/sites/default/files/21/12/7_tritium_and_c-14_monitoring.pdf (see page 24).

[89] *Water quality — Tritium — Test method using liquid scintillation counting*. Accessed 2026-05-14. International Organization for Standardization, May 2019. URL: https://www.iso.org/standard/69649.html (see page 24).

[90] *Water quality — Carbon 14 — Test method using liquid scintillation counting*. Accessed 2026-05-14. International Organization for Standardization, June 2021. URL: https://www.iso.org/standard/75821.html (see page 24).

[91] A. G. Hogg. **Liquid scintillation counting (LSC)—past, present, and future**. *Radiocarbon* 64:3 (2022), 541–554. DOI: 10.1017/RDC.2021.91 (see page 24).

[92] Lino Miramonti. **Borexino: A real time liquid scintillator detector for low energy solar neutrino study** (2002). arXiv: hep-ex/0206063. URL: https://arxiv.org/abs/hep-ex/0206063 (see page 24).

[93] F. Suekane, T. Iwamoto, H. Ogawa, O. Tajima, and H. Watanabe. **An Overview of the KamLAND 1-kiloton Liquid Scintillator** (2004). arXiv: physics/0404071. URL: https://arxiv.org/abs/physics/0404071 (see page 24).

[94] R Broda. **A review of the triple-to-double coincidence ratio (TDCR) method for standardizing radionuclides**. *Applied Radiation and Isotopes* 58:5 (May 2003), 585–594. DOI: 10.1016/s0969-8043(03)00056-3 (see pages 24, 29, 33).

[95] Karsten Kossert, Ryszard Broda, Philippe Cassette, Guy Ratel, and Brian E. Zimmerman. **Uncertainty determination for activity measurements by means of the TDCR method and the CIEMAT/NIST efficiency tracing technique**. *Metrologia* 52:3 (2015), S172–S190. DOI: 10.1088/0026-1394/52/3/S172 (see page 24).

[96] P Cassette, J Bouchard, and B Chauvenet. **Standardization of iodine-129 by the TDCR liquid scintillation method and $4\pi\beta$–γ coincidence counting**. *Nuclear Instruments and Methods in Physics Research Section A: Accelerators, Spectrometers, Detectors and Associated Equipment* 339:1 (1994), 339–342. ISSN: 0168-9002. DOI: https://doi.org/10.1016/0168-9002(94)91828-7. URL: https://www.sciencedirect.com/science/article/pii/0168900294918287 (see page 24).

[97] Agustín Grau Malonda and Eduardo Garcia-Toraño. **Evaluation of counting efficiency in liquid scintillation counting of pure β-ray emitters**. *The International Journal of Applied Radiation and Isotopes* 33:4 (1982), 249–253. ISSN: 0020-708X. DOI: https://doi.org/10.1016/0020-708X(82)90022-9. URL: https://www.sciencedirect.com/science/article/pii/0020708X82900229 (see page 24).

[98] P Cassette, R Broda, D Hainos, and T Terlikowska. **Analysis of detection-efficiency variation techniques for the implementation of the TDCR method in liquid scintillation counting**. *Applied Radiation and Isotopes* 52:3 (Mar. 2000), 643–648. DOI: 10.1016/s0969-8043(99)00224-9 (see pages 24, 34).

[99] A. G. Malonda. **Free Parameter Models in Liquid Scintillation Counting**. Colección Documentos CIEMAT. CIEMAT, 1999. ISBN: 978-8478-34-3-5-0-8. URL: https://books.google.bg/books?id=YR5EQwAACAAJ (see page 27).

[100] P.Grau Carles and A.Grau Malonda. **Free parameter, figure of merit and ionization quench in liquid scintillation counting**. *Applied Radiation and Isotopes* 54:3 (2001), 447–454. ISSN: 0969-8043. DOI: https://doi.org/10.1016/S0969-8043(00)00272-4. URL: https://www.sciencedirect.com/science/article/pii/S0969804300002724 (see page 27).

[101] C. Bobin, C. Thiam, B. Chauvenet, and J. Bouchard. **On the stochastic dependence between photomultipliers in the TDCR method**. *Applied Radiation and Isotopes* 70:4 (Apr. 2012), 770–780. DOI: 10.1016/j.apradiso.2011.12.035 (see page 27).

[102] Eduardo Garcia-Toraño and Agustín Grau Malonda. **EFFY, a new program to compute the couting efficiency of beta particles in liquid scintillators**. *Computer Physics Communications* 36:3 (1985), 307–312. ISSN: 0010-4655. DOI: https://doi.org/10.1016/0010-4655(85)90057-8. URL: https://www.sciencedirect.com/science/article/pii/0010465585900578 (see page 28).

[103] Philippe Cassette. **SPEBETA, programme de calcul du spectre en énergie des électrons émis par des radionucléides émetteurs bêta**. Note Technique LPRI/92/307. Laboratoire de Préparations Microanalytiques des Radionucleides (LPRI), 1992 (see pages 28, 34).

[104] Xavier Mougeot. **BetaShape: A new code for improved analytical calculations of beta spectra**. *EPJ Web of Conferences* 146 (2017). Ed. by A. Plompen, F.-J. Hambsch, P. Schillebeeckx, W. Mondelaers, J. Heyse, S. Kopecky, P. Siegler, and S. Oberstedt, 12015. ISSN: 2100-014X. DOI: 10.1051/epjconf/201714612015. URL: http://dx.doi.org/10.1051/epjconf/201714612015 (see pages 28, 119).

[105] M. A. Kellett and O. Bersillon. **The Decay Data Evaluation Project (DDEP) and the JEFF-3.3 radioactive decay data library: Combining international collaborative efforts on evaluated decay data**. *EPJ Web Conferences* 146 (2017). Ed. by A. Plompen, F.-J. Hambsch, P. Schillebeeckx, W. Mondelaers, J. Heyse, S. Kopecky, P. Siegler, and S. Oberstedt, 02009. DOI: 10.1051/epjconf/201714602009 (see pages 28, 99).

[106] Leendert Hayen, Nathal Severijns, Kazimierz Bodek, Dagmara Rozpedzik, and Xavier Mougeot. **High precision analytical description of the allowed β spectrum shape**. *Rev. Mod. Phys.* 90 (1 2018), 015008. DOI: 10.1103/RevModPhys.90.015008. URL: https://link.aps.org/doi/10.1103/RevModPhys.90.015008 (see page 28).

[107] Karsten Kossert and Xavier Mougeot. **The importance of the beta spectrum calculation for accurate activity determination of 63Ni by means of liquid scintillation counting**. *Applied Radiation and Isotopes* 101 (2015), 40–43. ISSN: 0969-8043. DOI: https://doi.org/10.1016/j.apradiso.2015.03.017. URL: https://www.sciencedirect.com/science/article/pii/S0969804315000950 (see page 28).

[108] Philippe Cassette. **Evaluation of the influence of wall effects on the liquid scintillation counting detection efficiency for the standardization of high-energy beta and alpha radionuclides**. In: *LSC 2001, Advances in Liquid Scintillation Spectrometry*. Tucson, Arizona: Radiocarbon, 2002, 45–55 (see page 28).

[109] X. Mougeot. **Improved calculations of electron capture transitions for decay data and radionuclide metrology**. *Applied Radiation and Isotopes* 134 (2018). ICRM 2017 Proceedings of the 21st International Conference on Radionuclide Metrology and its Applications, 225–232. ISSN: 0969-8043. DOI: https://doi.org/10.1016/j.apradiso.2017.07.027. URL: https://www.sciencedirect.com/science/article/pii/S0969804317304372 (see page 29).

[110] P. Cassette and R. Vatin. **Experimental evaluation of TDCR models for the 3 PM liquid scintillation counter**. *Nuclear Instruments and Methods in Physics Research Section A: Accelerators, Spectrometers, Detectors and Associated Equipment* 312:1-2 (Feb. 1992), 95–99. DOI: 10.1016/0168-9002(92)90135-q (see page 29).

[111] J. Bouchard and P. Cassette. **MAC3: an electronic module for the processing of pulses delivered by a three photomultiplier liquid scintillation counting system**. *Applied Radiation and Isotopes* 52:3 (Mar. 2000), 669–672. DOI: 10.1016/s0969-8043(99)00228-6 (see page 30).

[112] Ole Nähle, Qi Zhao, Carsten Wanke, Mathias Weierganz, and Karsten Kossert. **A portable TDCR system**. *Applied Radiation and Isotopes* 87 (2014). Proceedings of the 19th International Conference on Radionuclide Metrology and its Applications 17–21 June 2013, Antwerp, Belgium, 249–253. ISSN: 0969-8043. DOI: https://doi.org/10.1016/j.apradiso.2013.11.084. URL: https://www.sciencedirect.com/science/article/pii/S0969804313005332 (see page 30).

[113] Yantel. *nanoTDCR Triple-to-double coincidence ratio liquid scintillation counting system (TDCR) and MCA manual*. http://www.labzy.com/pdf/nanoTDCR_Data_Sheet_Rev_01a.pdf. labZY, 2017 (see page 30).

[114] Giuliano Mini, Francesco Pepe, Carlo Tintori, and Marco Capogni. **A full digital approach to the TDCR method**. *Applied Radiation and Isotopes* 87 (May 2014), 166–170. DOI: 10.1016/j.apradiso.2013.11.103 (see page 30).

[115] W. H. Press, S. A. Teukolsky, B. P. Flannery, and W. T. Vetterling. **Numerical Recipes in FORTRAN 77: The Art of Scientific Computing**. Vol. 1. Cambridge University Press, 1992. ISBN: 052143064X (see page 31).

[116] O. Nähle, K. Kossert, and J. Brunzendorf. **Study of the light emission process for the design of liquid scintillation counters**. *LSC 2008, Advances in liquid scintillation spectrometry* (2009), 87–95. URL: http://citeseerx.ist.psu.edu/viewdoc/download?doi=10.1.1.658.1144 (see page 32).

[117] Philippe Cassette and Jacques Bouchard. **The design of a liquid scintillation counter based on the triple to double coincidence ratio method**. *Nuclear Instruments and Methods in Physics Research Section A: Accelerators, Spectrometers, Detectors and Associated Equipment* 505:1-2 (June 2003), 72–75. DOI: 10.1016/s0168-9002(03)01023-4 (see page 33).

[118] Chavdar Dutsov, Benoît Sabot, Philippe Cassette, and Krasimir Mitev. **Significance of the corrections for accidental coincidences in liquid scintillation counting measurements**. *Journal of Radioanalytical and Nuclear Chemistry* 331:8 (Apr. 2022), 3303–3311. ISSN: 1588-2780. DOI: 10.1007/s10967-022-08316-y. URL: http://dx.doi.org/10.1007/s10967-022-08316-y (see pages 33, 35).

[119] Chavdar Dutsov. **Studies on the applications of the triple-to-double coincidence ratio method for primary activity standardization using liquid scintillation counting**. PhD Thesis. Sofia, Bulgaria: Sofia University "St. Kliment Ohridski", July 2021. URL: https://physica.dev/files/phd_thesis.pdf (see pages 33, 34, 101, 108).

[120] Ch Dutsov, K. Mitev, P. Cassette, and V. Jordanov. **Study of two different coincidence counting algorithms in TDCR measurements**. *Applied Radiation and Isotopes* 154 (Dec. 2019), 108895. DOI: 10.1016/j.apradiso.2019.108895 (see pages 33, 63).

[121] Zhenyu Tan and Yueyuan Xia. **Stopping power and mean free path for low-energy electrons in ten scintillators over energy range of 20–20, 000eV**. *Applied Radiation and Isotopes* 70:1 (Jan. 2012), 296–300. DOI: 10.1016/j.apradiso.2011.08.012 (see pages 34, 101).

[122] A. Grau Carles. **MICELLE, the micelle size effect on the LS counting efficiency**. *Computer Physics Communications* 176:4 (2007), 305–317. ISSN: 0010-4655. DOI: https://doi.org/10.1016/j.cpc.2006.11.002. URL: https://www.sciencedirect.com/science/article/pii/S001046550600395X (see page 34).

[123] C. Dutsov. **Study on the applications of the Triple-to-Double Coincidences Ratio method**. Sofia University 'St. Kliment Ohridski', 2018 (see page 34).

[124] Romain Coulon and Jialin Hu. **TDCRPy: A python package for TDCR measurements**. *Applied Radiation and Isotopes* 214 (2024), 111518. ISSN: 0969-8043. DOI: https://doi.org/10.1016/j.apradiso.2024.111518. URL: https://www.sciencedirect.com/science/article/pii/S0969804324003464 (see page 34).

[125] John D. Valentine and Brian D. Rooney. **Design of a Compton spectrometer experiment for studying scintillator non-linearity and intrinsic energy resolution**. *Nuclear Instruments and Methods in Physics Research Section A: Accelerators, Spectrometers, Detectors and Associated Equipment* 353:1–3 (Dec. 1994), 37–40. ISSN: 0168-9002. DOI: 10.1016/0168-9002(94)91597-0. URL: http://dx.doi.org/10.1016/0168-9002(94)91597-0 (see page 35).

[126] J.D. Valentine, B.D. Rooney, and J. Li. **The light yield nonproportionality component of scintillator energy resolution**. *IEEE Transactions on Nuclear Science* 45:3 (June 1998), 512–517. ISSN: 1558-1578. DOI: 10.1109/23.682438. URL: http://dx.doi.org/10.1109/23.682438 (see page 35).

[127] W.-S. Choong, K. M. Vetter, W. W. Moses, G. Hull, S. A. Payne, N. J. Cherepy, and J. D. Valentine. **Design of a Facility for Measuring Scintillator Non-Proportionality**. *IEEE Transactions on Nuclear Science* 55:3 (June 2008), 1753–1758. ISSN: 0018-9499. DOI: 10.1109/tns.2008.921491. URL: http://dx.doi.org/10.1109/TNS.2008.921491 (see page 35).

[128] Larry Ahle, Gregory Bizarri, Nerine Cherepy, Woon-Seng Choong, William W. Moses, S A Payne, Steven Sheets, and Benjamin W. Sturm. **Studies of Non-Proportionality in Alkali Halide and Strontium Iodide Scintillators Using SLYNCI**. *MRS Proceedings* 1164 (2009). ISSN: 1946-4274. DOI: 10.1557/proc-1164-l07-04. URL: http://dx.doi.org/10.1557/PROC-1164-L07-04 (see page 35).

[129] V. Todorov, C. Dutsov, P. Cassette, and K. Mitev. **Effects of the photocathode non-uniformity on radon measurements by plastic scintillation spectrometry**. *Journal of Radioanalytical and Nuclear Chemistry* (June 2022). DOI: 10.1007/s10967-022-08362-6 (see pages 39, 45).

[130] V. Todorov, P. Cassette, Ch. Dutsov, B. Sabot, S. Georgiev, and K. Mitev. **A study of the non-uniformity of the PMT photocathode response and its influence on the results obtained in different scintillation counting experiments**. *Nuclear Instruments and Methods in Physics Research Section A: Accelerators, Spectrometers, Detectors and Associated Equipment* 1046 (Jan. 2023), 167719. ISSN: 0168-9002. DOI: 10.1016/j.nima.2022.167719. URL: http://dx.doi.org/10.1016/j.nima.2022.167719 (see pages 39, 43–45).

[131] V. Todorov, P. Cassette, S. Georgiev, B. Sabot, and K. Mitev. **Automatic system for testing PMT photocathode homogeneity**. *Journal of Radioanalytical and Nuclear Chemistry* (Mar. 2025). ISSN: 1588-2780. DOI: 10.1007/s10967-025-10028-y. URL: http://dx.doi.org/10.1007/s10967-025-10028-y (see pages 40, 44–51, 62).

[132] TOPDON. *TOPDON TC001 Product Profile*. [Online; accessed 17-Nov-2025]. 2025. URL: https://web-file.topdon.com/topdon-web/information_download/TC001-Product-Profile-V2.pdf (see page 40).

[133] Hamamatsu. *Hamamatsu R9779 photomultiplier tube datasheet*. [Online; accessed 17-Nov-2025]. 2025. URL: https://www.artisantg.com/info/Hamamatsu_R9779_Datasheet_201727162455.pdf (see page 43).

[134] Hamamatsu. *Hamamatsu R331-05 photomultiplier tube datasheet*. [Online; accessed 17-Nov-2025]. 2025. URL: https://www.hamamatsu.com/content/dam/hamamatsu-photonics/sites/documents/99_SALES_LIBRARY/etd/R331-05_TPMH1209E.pdf (see pages 43, 62).

[135] Philips. *Philips XP2020Q photomultiplier tube datasheet.* [Online; accessed 17-Nov-2025]. 2025. URL: http://bitsavers.org/components/philips/_dataBooks/1987_T09_Philips_Photo_and_Electron_Multipliers.pdf (see page 43).

[136] F. Bauer, M. Aykac, M. Loope, C.W. Williams, L.A. Eriksson, and M. Schmand. **Performance Study of the new Hamamatsu R9779 and Photonis XP20D0 fast 2" Photomultipliers**. In: *IEEE Nuclear Science Symposium Conference Record, 2005.* Vol. 5. IEEE, 2920–2923. DOI: 10.1109/nssmic.2005.1596942. URL: http://dx.doi.org/10.1109/nssmic.2005.1596942 (see page 48).

[137] Ch. Bobin and J. Bouchard. **A 4π(LS)β–γ coincidence system using a TDCR apparatus in the β-channel**. *Applied Radiation and Isotopes* 64 (Jan. 2006), 124–130. ISSN: 0969-8043. DOI: 10.1016/j.apradiso.2005.06.008. URL: http://dx.doi.org/10.1016/j.apradiso.2005.06.008 (see page 48).

[138] Valentin T. Jordanov. **Double and Triple Coincidence Counter With More Than Three Photosensors and Independent Coincidence Counting**. *IEEE Transactions on Nuclear Science* 71 (Jan. 2024), 88–95. ISSN: 1558-1578. DOI: 10.1109/tns.2023.3334189. URL: http://dx.doi.org/10.1109/tns.2023.3334189 (see page 50).

[139] P. Cassette, V. Todorov, B. Sabot, S. Georgiev, and K. Mitev. **Uncertainties in TDCR measurement revisited: Contribution of optical effects**. *Applied Radiation and Isotopes* 201 (Nov. 2023), 110992. ISSN: 0969-8043. DOI: 10.1016/j.apradiso.2023.110992. URL: http://dx.doi.org/10.1016/j.apradiso.2023.110992 (see pages 51–60, 91).

[140] Benoît Sabot, Chavdar Dutsov, Philippe Cassette, and Krasimir Mitev. **Performance of portable TDCR systems developed at LNE-LNHB**. *Nuclear Instruments and Methods in Physics Research Section A: Accelerators, Spectrometers, Detectors and Associated Equipment* 1034 (July 2022), 166721. ISSN: 0168-9002. DOI: 10.1016/j.nima.2022.166721. URL: http://dx.doi.org/10.1016/j.nima.2022.166721 (see pages 57, 91).

[141] V. Jordanov, P. Cassette, Ch. Dutsov, and K. Mitev. **Development and applications of a miniature TDCR acquisition system for in-situ radionuclide metrology**. *Nuclear Instruments and Methods in Physics Research Section A: Accelerators, Spectrometers, Detectors and Associated Equipment* 954 (Feb. 2020), 161202. DOI: 10.1016/j.nima.2018.09.037 (see page 57).

[142] Matthieu Hamel, ed. **Plastic Scintillators: Chemistry and Applications. Topics in Applied Physics, vol 140. Springer**. Cham: Springer International Publishing, 2021, XXIII, 638. ISBN: 978-3-030-73488-6. DOI: 10.1007/978-3-030-73488-6. URL: https://doi.org/10.1007/978-3-030-73488-6 (see page 61).

[143] Karsten Kossert and Ole J. Nähle. **Activity determination of 59Fe**. *Applied Radiation and Isotopes* 93 (Nov. 2014), 33–37. ISSN: 0969-8043. DOI: 10.1016/j.apradiso.2014.01.013. URL: http://dx.doi.org/10.1016/j.apradiso.2014.01.013 (see page 62).

[144] Karsten Kossert, Hendrik Bauer, Marcell Péter Takács, and Ole Nähle. **A custom-built liquid scintillation counter for the simultaneous application of CIEMAT/NIST and TDCR methods**. *Journal of Radioanalytical and Nuclear Chemistry* (Feb. 2025). ISSN: 1588-2780. DOI: 10.1007/s10967-025-10027-z. URL: http://dx.doi.org/10.1007/s10967-025-10027-z (see page 62).

[145] Romain Coulon, Ryszard Broda, Philippe Cassette, Sammy Courte, Aldo Dupire, Simon Jerome, Steven Judge, Karsten Kossert, Haoran Liu, Carine Michotte, and Manuel Nonis. **The new international reference system for pure α- and pure β-emitting radionuclides and some electron capture decaying radionuclides by liquid scintillation counting**. *Journal of Radioanalytical and Nuclear Chemistry* 331:8 (June 2022), 3221–3230. ISSN: 1588-2780. DOI: 10.1007/s10967-022-08337-7. URL: http://dx.doi.org/10.1007/s10967-022-08337-7 (see page 62).

[146] Hamamatsu. *D-type socket assemblies*. [Online; accessed 18-Mar-2025]. 2025. URL: https://www.hamamatsu.com/content/dam/hamamatsu-photonics/sites/documents/99_SALES_LIBRARY/etd/D-type_socket_assemblies_TPMZ0002E02_p88-99.pdf (see page 62).

[147] P. Cassette, M. Capogni, L. Johansson, K. Kossert, O. Nahle, J. Sephton, and P. De Felice. **Development of portable Liquid Scintillation counters for on-site primary measurement of radionuclides using the Triple-To-Double Coincidence Ratio method**. In: *2013 3rd International Conference on Advancements in Nuclear Instrumentation, Measurement Methods and their Applications (ANIMMA)*. IEEE, June 2013, 1–7. DOI: 10.1109/animma.2013.6727876. URL: http://dx.doi.org/10.1109/ANIMMA.2013.6727876 (see page 62).

[148] CAEN. *CAEN DT1470ET 4 Ch Reversible Desktop HV Power Supply Module*. https://www.caen.it/products/dt1470et/. [Online; accessed 18-Mar-2025]. CAEN, 2025 (see page 62).

[149] 3M. *3M Enhanced Specular Reflector Film (ESR)*. [Online; accessed 18-Mar-2025]. 2025. URL: https://multimedia.3m.com/mws/media/1245089O (see pages 62, 91).

[150] V. Todorov, P. Cassette, V. Jordanov, S. Ivanov, H. Stoycheva, S. Georgiev, B. Sabot, and K. Mitev. **Design of a new Compton-TDCR spectrometer at Sofia University for the characterization of Liquid Scintillation cocktails**. *Applied Radiation and Isotopes* 226 (2025), 112194. ISSN: 0969-8043. DOI: https://doi.org/10.1016/j.apradiso.2025.112194. URL: https://www.sciencedirect.com/science/article/pii/S0969804325005391 (see pages 63, 65, 67–69, 71, 73, 74, 78, 79, 81, 83, 92, 94).

[151] CAEN. *CAEN N978 4 Channel Variable Gain Fast Amplifier*. https://www.caen.it/products/n978/. [Online; accessed 18-Mar-2025]. CAEN, 2025 (see pages 63, 91).

[152] Yantel. *Triple-To-Double Coincidence Ratio Liquid Scintillation Counting System (TDCR) and a digital multichannel analyzer (MCA)*. https://www.yantel.com/products/nanotdcr/. [Online; accessed 18-Mar-2025]. YANTEL, 2025 (see pages 63, 91).

[153] CAEN. *CAEN DT5751 digitizer manual*. https://www.caen.it/products/dt5751/. CAEN, 2020 (see page 63).

[154] P Cassette, A Arinc, M Capogni, P De Felice, C Dutsov, R Galea, E Garcia-Toraño, K Kossert, J Liang, K Mitev, O Nähle, Y Nedjadi, P Oropesa Verdecia, M Takács, and T Ziemek. **Results of the CCRI(II)-K2. H-3 key comparison 2018: measurement of the activity concentration of a tritiated-water source**. *Metrologia* 57:1A (Jan. 2020), 06004. ISSN: 1681-7575. DOI: 10.1088/0026-1394/57/1a/06004. URL: http://dx.doi.org/10.1088/0026-1394/57/1A/06004 (see pages 63, 91).

[155] Chavdar Dutsov. *TDCR CAEN Digitizer logic*. https://gitlab.com/cdutsov/cdt_logic. [Online; accessed 18-Mar-2025]. 2025 (see page 64).

[156] Yantel. *Ultra Low Noise Real-Time Digital Pulse Processor (DPP) and Digital MCA*. https://www.yantel.com/products/nanomcaii/. [Online; accessed 18-Mar-2025]. YANTEL, 2025 (see page 65).

[157] H. Stefanova. **Study of n-type planar HPGe detector for applications in radionuclide methrology**. Sofia University 'St. Kliment Ohridski', 2023 (see pages 65, 66, 75, 78).

[158] Valentin T. Jordanov. **Unfolding-synthesis technique for digital pulse processing. Part 1: Unfolding**. *Nuclear Instruments and Methods in Physics Research Section A: Accelerators, Spectrometers, Detectors and Associated Equipment* 805 (2016). Special Issue in memory of Glenn F. Knoll, 63–71. ISSN: 0168-9002. DOI: https://doi.org/10.1016/j.nima.2015.07.040. URL: https://www.sciencedirect.com/science/article/pii/S0168900215008694 (see page 69).

[159] Maryla Aleksandra Olszewska-Wasiolek and David Romaine. **Unexpected Neutron Emissions from New Sealed Am-241 Sources.** In: Sandia National Lab. (SNL-NM), Albuquerque, NM (United States). Mar. 2018. URL: https://www.osti.gov/biblio/1502279 (see page 72).

[160] ICRU. **Stopping powers for electrons and positrons: ICRU Report 37**. Tech. rep. Bethesda, MD., USA: ICRU, 1984 (see pages 77, 101).

[161] Pauli Virtanen, Ralf Gommers, Travis E. Oliphant, Matt Haberland, Tyler Reddy, David Cournapeau, Evgeni Burovski, Pearu Peterson, Warren Weckesser, Jonathan Bright, Stéfan J. van der Walt, Matthew Brett, Joshua Wilson, K. Jarrod Millman, Nikolay Mayorov, Andrew R. J. Nelson, Eric Jones, Robert Kern, Eric Larson, C J Carey, İlhan Polat, Yu Feng, Eric W. Moore, Jake VanderPlas, Denis Laxalde, Josef Perktold, Robert Cimrman, Ian Henriksen, E. A. Quintero, Charles R. Harris, Anne M. Archibald, Antônio H. Ribeiro, Fabian Pedregosa, Paul van Mulbregt, and SciPy 1.0 Contributors. **SciPy 1.0: Fundamental Algorithms for Scientific Computing in Python**. *Nature Methods* 17 (2020), 261–272. DOI: 10.1038/s41592-019-0686-2. URL: https://rdcu.be/b08Wh (see page 77).

[162] Paul T Boggs, Richard H Byrd, Janet E Rogers, and Robert B Schnabel. *User's reference guide for ODRPACK version 2.01:: software for weighted orthogonal distance regression*. 1992. DOI: 10.6028/nist.ir.4834. URL: http://dx.doi.org/10.6028/NIST.IR.4834 (see pages 77, 78).

[163] L.J. Bignell. **Can the ZoMBieS method be used to characterise scintillator non-linearity?** *Applied Radiation and Isotopes* 87 (May 2014), 265–268. ISSN: 0969-8043. DOI: 10.1016/j.apradiso.2013.11.006. URL: http://dx.doi.org/10.1016/j.apradiso.2013.11.006 (see page 84).

[164] V. Todorov, K. Mitev, P. Cassette, and B. Sabot. **Investigation of the possible effect of the accidental coincidences correction on the determination of kB value by efficiency variation with grey filters**. *Journal of Radioanalytical and Nuclear Chemistry* 334:9 (May 2025), 5943–5950. ISSN: 1588-2780. DOI: 10.1007/s10967-025-10173-4. URL: http://dx.doi.org/10.1007/s10967-025-10173-4 (see pages 90, 103–107).

[165] K. Mitev, P. Cassette, V. Jordanov, H. R. Liu, and Ch. Dutsov. **Design and performance of a miniature TDCR counting system**. *Journal of Radioanalytical and Nuclear Chemistry* 314:2 (Sept. 2017), 583–589. DOI: 10.1007/s10967-017-5451-3 (see page 91).

[166] V Jobbagy and M Hult. **Performance evaluation of a European scale proficiency test on radon-in-water measurements in Europe**. *Applied Radiation and Isotopes* 160 (2020), 109111. ISSN: 0969-8043 (online). DOI: 10.1016/j.apradiso.2020.109111(online) (see page 91).

[167] Denis E. Bergeron, Jeffrey T. Cessna, Ryan P. Fitzgerald, Lizbeth Laureano-Pérez, Leticia Pibida, and Brian E. Zimmerman. **Primary standardization of 212Pb activity by liquid scintillation counting**. *Applied Radiation and Isotopes* 190 (Dec. 2022), 110473. ISSN: 0969-8043. DOI: 10.1016/j.apradiso.2022.110473. URL: http://dx.doi.org/10.1016/j.apradiso.2022.110473 (see page 97).

[168] Philippe Cassette. *TDCR17 code*. [Online; accessed 18-Mar-2025]. 2025. URL: http://www.lnhb.fr/home/conferences-publications/icrm_lsc_wg/icrm_lsc_software/ (see pages 101, 110).

[169] X. Mougeot. **Reliability of usual assumptions in the calculation of β and ν spectra**. *Physical Review C* 91:5 (May 2015). DOI: 10.1103/physrevc.91.055504 (see page 101).

[170] K. Mitev, V. Todorov, P. Cassette, and B. Sabot. **MCLTDCR: A Monte Carlo code for generation of list mode TDCR files**. *Applied Radiation and Isotopes* 226 (Dec. 2025), 112094. ISSN: 0969-8043. DOI: 10.1016/j.apradiso.2025.112094. URL: http://dx.doi.org/10.1016/j.apradiso.2025.112094 (see pages 108–111).

[171] World Health Organization. *WHO Handbook on Indoor Radon - A Public Health Perspective*. 2009. URL: https://www.who.int/publications/i/item/9789241547673 (see page 118).

[172] United Nations Scientific Committee on the Effects of Atomic Radiation. **UNSCEAR 2000 Report to the General Assembly, with Scientific Annexes. Sources and effects of ionizing radiation.** New York, NY, USA: UN Publications, 2000 (see page 118).

[173] **Council Directive 2013/51/Euratom of 22 October 2013 laying down requirements for the protection of the health of the general public with regard to radioactive substances in water intended for human consumption**. *Official Journal of the European Union* L 296 (2013), 12–21. URL: https://eur-lex.europa.eu/legal-content/EN/TXT/PDF/?uri=CELEX:02013L0051-20131022 (see page 118).

[174] U.S. Environmental Protection Agency. **National Primary Drinking Water Regulations; Radon-222**. *Federal Register* 64 (Nov. 1999), 59246–59378 (see page 118).

[175] Laina Salonen. **Calibration of the direct LSC method for radon in drinking water: Interference from 210Pb and its progenies accumulated in 226Ra standard solution**. *Applied Radiation and Isotopes* 68:1 (2010), 131–138. ISSN: 0969-8043. DOI: https://doi.org/10.1016/j.apradiso.2009.08.006. URL: https://www.sciencedirect.com/science/article/pii/S0969804309005090 (see page 118).

[176] M. E. Kitto. **Characteristics of liquid scintillation analysis of radon in water**. *Journal of Radioanalytical and Nuclear Chemistry Articles* 185:1 (Nov. 1994), 91–99. ISSN: 1588-2780. DOI: 10.1007/bf02042955. URL: http://dx.doi.org/10.1007/BF02042955 (see page 118).

[177] Krasimir Mitev, Benoit Sabot, Sylvie Pierre, Marie-Christine Lépy, and Philippe Cassette. **Towards a radon-in-water primary standard at LNHB**. *Applied Radiation and Isotopes* 201 (Nov. 2023), 111013. ISSN: 0969-8043. DOI: 10.1016/j.apradiso.2023.111013. URL: http://dx.doi.org/10.1016/j.apradiso.2023.111013 (see page 118).

[178] J.L. Picolo. **Absolute measurement of radon 222 activity**. *Nuclear Instruments and Methods in Physics Research Section A: Accelerators, Spectrometers, Detectors and Associated Equipment* 369:2–3 (Feb. 1996), 452–457. ISSN: 0168-9002. DOI: 10.1016/s0168-9002(96)80029-5. URL: http://dx.doi.org/10.1016/S0168-9002(96)80029-5 (see page 118).

[179] LNHB. *Library for gamma and alpha emissions*. [Online; accessed 20-Jan-2026]. 2026. URL: http://www.lnhb.fr/Laraweb/ (see page 119).

[180] **PENELOPE 2018: A code system for Monte Carlo simulation of electron and photon transport: Workshop Proceedings, Barcelona, Spain, 28 January – 1 February 2019**. OECD, Sept. 2019. ISBN: 9789264489950. DOI: 10.1787/32da5043-en. URL: http://dx.doi.org/10.1787/32da5043-en (see page 119).

[181] V. Todorov, P. Cassette, S. Georgiev, H. Stoycheva, R. Vasileva, and K. Mitev. **Application of TDCR Counting for Primary Standardization of Radon-in-Water Samples**. In: *2024 XXXIV International Scientific Symposium Metrology and Metrology Assurance (MMA)*. 2024, 1–6. DOI: 10.1109/MMA62616.2024.10817679 (see pages 119–121).